Université catholique de Louvain

Faculté des bioingénieurs

Earth and Life Institute

Fonctionnement et altérations hydrologiques du bassin d'Ankavia (Madagascar) dans une perspective de Gestion Intégrée des Ressources en Eau (GIRE)

Zonirina Ramahaimandimby

Novembre 2024

Thèse présentée en vue de l'obtention du grade de :

Docteur en sciences agronomiques

et ingénierie biologique

Membres du jury

Président	:	Prof. Emmanuel HANERT
		UCLouvain, Belgique
Promoteur	:	Prof. Charles L. BIELDERS
		UCLouvain, Belgique
Co-promoteur	:	Dr. Alain RANDRIAMAHERISOA
		Université d'Antananarivo, Madagascar
Lecteurs	:	Prof. Marnik VANCLOOSTER
		UCLouvain, Belgique
		Prof. François JONARD
		Université de Liège, Belgique
		Prof. Sandra Soarez FRAZAO
		UCLouvain, Belgique
		Dr. Quentin GOOR
		Chargé de cours invité à l'UCLouvain, Belgique

Crédits

Cette thèse a été réalisée dans le cadre du projet GIRE SAVA : « Renforcement des capacités en gestion intégrée des ressources en eau de la région SAVA, Madagascar ». Le projet a été entièrement financé par l'Académie de Recherche et d'Enseignement Supérieur (ARES) de la Fédération Wallonie-Bruxelles.

« I can do all things through Christ who strengthens me. » Phil 4,13

For Your glory.

“The supreme goodness is like water.
It benefits all things without contention.
In dwelling, it stays grounded.
In being, it flows to depths.
In expression, it is honest.
In confrontation, it stays gentle.
In governance, it does not control.
In action, it aligns to timing.
It is content with its nature,
and therefore cannot be faulted.”

Lao-Tzu, Tao Te Ching

Remerciements

Je tiens à exprimer ma gratitude envers Celui qui m'a accordé non seulement l'opportunité d'entreprendre cette thèse, mais aussi la force, la persévérance et la bénédiction d'avoir croisé des personnes extraordinaires tout au long de ce parcours enrichissant.

Comme le souligne si justement le proverbe malgache « Tao-trano tsy efa irery » (littéralement : « On ne peut construire une maison seul »), toute réalisation d'envergure nécessite une collaboration. Ce travail est le fruit d'efforts collectifs, et je tiens à exprimer ma profonde reconnaissance envers toutes les personnes, institutions et organisations qui ont contribué à sa réalisation.

Sans la vision du Dr Joseph Benitsiafantoka, Coordonnateur Sud (2017-2021), le projet GIRE SAVA n'aurait pas vu le jour. Je le remercie pour sa clairvoyance dans l'identification et la priorisation des besoins urgents des communautés. Nos vifs remerciements s'adressent également au Dr Christophe Manjaribe, qui a repris le rôle de Coordonnateur Sud du projet depuis 2021.

J'adresse mes plus sincères remerciements au Prof. Marnik Vanclooster, qui a assumé le double rôle de Coordonnateur Nord du projet GIRE SAVA et de lecteur de cette thèse. Sa bienveillance et son accompagnement ont été déterminants, particulièrement dans l'optimisation de mes conditions de travail lors de mes séjours en Belgique tout au long de ces années de recherche. Je lui exprime ma profonde reconnaissance pour son soutien inestimable.

Cette thèse a été menée sous la direction du Prof. Charles L. Bielders, dont l'engagement et le dévouement ont été déterminants dans l'aboutissement de ce travail. Malgré un emploi du temps chargé, il a assumé avec une remarquable disponibilité son rôle de directeur de thèse, m'accordant un encadrement scientifique rigoureux et bienveillant. Sa confiance indéfectible et son soutien, tant sur le plan intellectuel que matériel, m'ont permis de mener à bien cette recherche. Je lui suis particulièrement reconnaissant pour m'avoir transmis une méthodologie scientifique rigoureuse et une éthique professionnelle exemplaire. Au-delà de son rôle de directeur de thèse, ses qualités humaines exceptionnelles et son mentorat bienveillant ont profondément marqué mon parcours doctoral.

Je tiens à exprimer ma profonde gratitude au Dr Alain Randriamaherisoa, co-directeur de cette thèse, dont l'expertise pointue en hydrologie malgache s'est révélée précieuse et déterminante pour la réalisation de ce travail. Ses analyses pertinentes, ses critiques constructives et sa connaissance approfondie du terrain ont significativement enrichi cette recherche. Son accompagnement scientifique a grandement contribué à la qualité et à la rigueur de cette étude.

J'exprime ma gratitude au Prof. Emmanuel Hanert qui m'a fait l'honneur de présider ce jury de thèse. Je souhaite témoigner également ma reconnaissance aux membres du jury : Prof. François Jonard, Prof. Sandra Soares Frazao et Dr Quentin Goor, pour

leur lecture attentive de ce manuscrit. Leurs observations pertinentes et leurs suggestions éclairées ont contribué à enrichir la qualité de ce travail.

J'adresse mes remerciements chaleureux :

- à Tsirinasy et Carlos Totomalaza de la Direction Régionale de l'Eau, de l'Assainissement et de l'Hygiène (DREAH Sambava), pour leur collaboration précieuse. Leur expertise et leur engagement ont permis une synergie fructueuse avec le projet GIRE SAVA, enrichissant significativement la portée de cette recherche.

- à l'équipe du CURSA (Centre Universitaire Régional de la SAVA) : Tombozafy, Romaric Benitsiafantoka et Landry Indrianaharivelo, pour leur précieuse collaboration. Une pensée particulière va également à Sabrina et Fabricia, dont l'accueil et le soutien durant mon séjour à Antalaha ont grandement facilité la réalisation des travaux de terrain.

- au personnel administratif de l'UCLouvain, en particulier Carine Demeyer, Sabine Finné et Jasmine De Wulf, pour leur soutien constant et leur assistance précieuse tout au long de ce parcours doctoral. Leur professionnalisme et leur efficacité ont grandement facilité les démarches administratives inhérentes à cette thèse.

- au personnel de l'ARES (Académie de Recherche et d'Enseignement Supérieur), et tout particulièrement à Lucie Petillon et Gabriela Bidegain. Leur accompagnement bienveillant et leur gestion efficace des aspects administratifs liés à ma bourse de recherche ont été déterminants dans la réussite de ce projet. Leur disponibilité et leur sympathie ont grandement facilité mon séjour d'études en Belgique.

- aux techniciens qui ont contribué de manière significative à cette recherche. Ma gratitude va particulièrement à Sébastien François et Arnaud Willems pour leur expertise technique indispensable dans l'approvisionnement et la gestion du matériel hydrologique, ainsi que pour leur précieux accompagnement dans les travaux de laboratoire. Je tiens également à exprimer ma profonde reconnaissance à Christian Sabe pour son engagement exemplaire dans la collecte des données de terrain. Son professionnalisme et sa présence ont rendu les relevés mensuels, nécessitant des déplacements de 50 km, à la fois efficaces et enrichissants.

- aux membres des comités de bassin versant d'Ankavia pour leur contribution essentielle à cette recherche. Mes remerciements s'adressent tout particulièrement à Mr Olivier Bodimena, Président des comités de bassin, pour son leadership exemplaire, ainsi qu'aux coordonnateurs locaux de chaque sous-bassin versant pour leur engagement rigoureux dans la collecte des données hydrométéorologiques. Leur expertise locale et leur implication constante ont été déterminantes pour la qualité et la fiabilité des données recueillies.

- à mes collègues doctorants : Aristide Benitsiafantoka, Hélène Voahanginirina et Michael Bejoma, avec qui j'ai partagé les défis du travail de terrain et de précieux moments tant à Antalaha qu'en Belgique. Notre collaboration étroite et notre soutien mutuel face aux challenges de la recherche ont créé des liens professionnels et amicaux durables qui ont enrichi cette aventure scientifique.

- à mes collègues chercheurs du GERU, avec qui j'ai eu le privilège de partager ces années de recherche. Ma gratitude va particulièrement au Dr Kadir Mokrane, Dr Jean-Baptiste Got, Dr Raed Fehri, Dr Axelle Koch, Victorine Djago, Dr Kaijun Wu, Dr Jean-Claude Maki Mateso, Alousseynou Bah et à Abdoulaye Guindo. La richesse de nos échanges scientifiques, l'entraide constante et l'atmosphère collaborative qui ont caractérisé notre parcours commun ont significativement contribué à l'aboutissement de ce projet.

- à mes collègues de l'École Polytechnique, Prof. Faneva Manambina et Dr Njara Andriamanantena, qui ont poursuivi avec excellence leur carrière dans le monde de la recherche. Leur parcours et leur soutien constant ont été une source d'inspiration et d'émulation tout au long de ce cheminement doctoral. Qu'ils trouvent ici l'expression de ma sincère reconnaissance - Misaotra betsaka zalah a !

- à mes anciens directeurs de recherche, Pr Fano Andriamahefazafy et Dr Georges Serpantié, qui m'ont fait découvrir cette opportunité de bourse doctorale et ont ravivé ma passion pour la recherche.

- à ma famille bien-aimée : à mes très chers parents, dont les prières m'accompagnent et me guident chaque jour, à mon frère jumeau, Docteur et mentor, qui partage généreusement avec moi ses précieuses techniques de recherche, à mon petit frère et ma petite sœur, qui complètent ce cercle familial si cher à mon cœur.

- à ma belle-famille, et tout particulièrement à toi, chère mamie, dont le dévouement et les sacrifices me touchent profondément. Mon cœur déborde de gratitude pour tout l'amour que tu déverses sans compter sur tes petits-enfants. Ta tendresse infinie et ton abnégation font de toi une grand-mère exceptionnelle. Je remercie également de tout cœur tonton Rafa pour son soutien inestimable et son aide précieuse.

- à ma précieuse épouse, meilleure amie et mère admirable de mes enfants : ton courage face aux épreuves m'inspire chaque jour. Les mots ne suffisent pas pour exprimer ma gratitude devant tes sacrifices quotidiens et tes prières qui m'ont accompagné tout au long de cette aventure doctorale.

- à mes chers enfants, mon courageux Niaiko et ma vaillante Tsifoiko : ces périodes d'absence ont été nécessaires, même si elles n'ont pas toujours été faciles. Votre patience et votre compréhension m'ont donné la force d'aller jusqu'au bout.

- à toutes les personnes bienveillantes qui m'ont soutenu sur ce chemin et dont les noms, bien que gravés dans mon cœur, ne peuvent tous être cités ici : recevez l'expression de ma plus profonde gratitude.

Résumé

Les milieux tropicaux humides, notamment la région SAVA au nord-est de Madagascar, font face à des défis cruciaux en matière de gestion des ressources hydriques, exacerbés par les changements d'occupation des sols et les modifications climatiques. L'opérationnalisation efficace de la Gestion Intégrée des Ressources en Eau (GIRE) s'avère impérative pour développer des approches durables conciliant les besoins actuels et la préservation des ressources pour les générations futures. Toutefois, sa mise en œuvre effective est entravée par une pénurie de données hydrométéorologiques fiables et une compréhension insuffisante des processus hydrologiques locaux. L'étude se concentre sur le bassin versant d'Ankavia, représentatif de la région SAVA, pour élucider son fonctionnement hydrologique et analyser ses altérations face aux changements environnementaux. Une approche méthodologique multiscalaire et interdisciplinaire a été adoptée, intégrant des analyses à différentes échelles spatiales et temporelles, du micro-bassin au grand-bassin versant, et couvrant des périodes allant des événements pluvieux isolés aux tendances climatiques à long terme. Cette démarche combine des méthodes et des connaissances issues de l'hydrologie, de la climatologie, de la géologie et de la pédologie, permettant une compréhension holistique des interactions entre les systèmes naturels et anthropiques.

Les principaux résultats de cette étude sont : (1) l'identification des produits satellitaires IMERG comme la source la plus fiable de données pluviométriques pour servir d'alternatives aux données des pluviomètres au sol ; (2) la mise en évidence de l'occupation du sol, des propriétés pédologiques et géologiques comme principaux facteurs influençant les débits, avec un rôle prépondérant de la couverture forestière dans la régulation du cycle hydrologique ; (3) la prédominance de l'écoulement de subsurface en milieu forestier et probablement le ruissellement de surface dans les zones de pâturage, les terres cultivées et les jachères lors d'épisodes pluvieux intenses ou prolongés ; (4) la nécessité de poursuivre les mesures des précipitations au sol pour des observatoires hydrologiques fiables, en particulier pour les suivis des débits de pointe et des étiages ; (5) l'évaluation de l'impact futur des changements d'utilisation des terres et du climat, montrant que le changement climatique aura un impact prédominant sur l'hydrologie du bassin, surpassant largement les effets des changements d'utilisation des terres.

Cette recherche a contribué à améliorer la compréhension des dynamiques hydrologiques et de leurs altérations en milieu tropical humide, offrant ainsi une perspective utile pour la mise en œuvre effective d'une GIRE adaptée aux spécificités locales de la région SAVA et d'autres régions tropicales humides similaires.

Abstract

Humid tropical environments, particularly the SAVA region in northeastern Madagascar, face critical challenges in water resource management, exacerbated by land-use changes and climate modifications. The enhancement and effective operationalization of Integrated Water Resources Management (IWRM) are imperative to develop sustainable approaches that reconcile current needs with resource preservation for future generations. However, its effective implementation is hampered by a scarcity of reliable hydrometeorological data and insufficient understanding of local hydrological processes. This study focuses on the Ankavia watershed, representative of the SAVA region, to elucidate its hydrological functioning and analyze its alterations in response to environmental changes. A multiscalar and interdisciplinary methodological approach was adopted, integrating analyses at various spatial and temporal scales, from micro-basin to global watershed, and covering periods ranging from isolated rainfall events to long-term climate trends. This approach combines methods and knowledge from hydrology, climatology, geology, and pedology, enabling a holistic understanding of the interactions between natural and anthropogenic systems.

The main findings of this study are: (1) the identification of IMERG satellite products as the most reliable source of rainfall data to serve as alternatives to ground rain gauge data; (2) the demonstration of land cover, pedological, and geological properties as primary factors influencing streamflow, with forest cover playing a predominant role in regulating the hydrological cycle; (3) the predominance of subsurface flow in forested areas and the likely dominance of surface runoff in pasture areas, croplands, and fallows during intense or prolonged rainfall events; (4) the necessity to continue ground precipitation measurements for reliable hydrological observatories, particularly for monitoring peak flows and low flows; (5) the assessment of future impacts of land-use and climate changes, indicating that climate change will have a predominant impact on basin hydrology, far surpassing the effects of land-use changes.

This research has contributed to improving the understanding of hydrological dynamics and their alterations in humid tropical environments, thus offering a valuable perspective for the effective implementation of Integrated Water Resources Management (IWRM) adapted to the local specificities of the SAVA region and other similar humid tropical regions.

Fintina

Ny tontolo mando sy mafana, indrindra fa ny faritra SAVA any avaratra atsinanan'i Madagasikara, dia miatrika olana lehibe amin'ny fitantanana ny rano, noho ny fiovana amin'ny fampiasana ny tany sy ny fiovan'ny toetr'andro. Ny fanatsarana sy ny fampiharana mahomby ny Fitantanana Mirindra ny Loharanonkarenan'ny Rano (GIRE) dia ilaina maika mba hamolavola fomba maharitra mampiray ny filàna ankehitriny sy ny fiarovana ny loharano ho an'ny taranaka ho avy. Na izany aza, ny fampiharana izany dia tsy tomombana noho ny tsy fahampian'ny angon-drakitra azo antoka momba ny rano sy ny toetr'andro ary ny tsy fahalalana tsara ny fomba fiasan'ny rano eo an-toerana. Ity fikarohana ity dia mifantoka amin'ny faritra Ankavia, izay maneho ny faritra SAVA, mba hanazavana ny fomba fiasan'ny rano sy ny fiovany manoloana ny fiovana eo amin'ny tontolo iainana. Fomba fiasa maro samy hafa sy mifampiankina no nampiasaina, ka nampiditra fanadihadiana amin'ny haavon-toerana sy fotoana isan-karazany, manomboka amin'ny sahandriaka kely ka hatramin'ny sahandriaka lehibe, ary mandrakotra ny vanim-potoana manomboka amin'ny orana iray ka hatramin'ny fiovan'ny toetr'andro maharitra. Ity fomba fiasa ity dia manakambana ny fomba sy fahalalana avy amin'ny fiasan'ny rano, ny toetr'andro, ny firafitry ny tany, ary ny karazan-tany, ahafahan'ny olona mahazo fahalalana feno momba ny fifandraisana eo amin'ny rafitra voajanahary sy ataon'olombelona.

Ireto avy ny vokatra lehibe hita tamin'ity fikarohana ity: (1) ny famantarana fa ny vokatra azo avy amin'ny zanabolana IMERG no loharanom-baovao azo antoka indrindra momba ny orana mba ho solon'ny angon-drakitra avy amin'ny fitaovana mandrefy orana eny an-tany; (2) ny fanehoana fa ny fampiasana ny tany, ny toetoetr'ny tany ary ny firafitry ny tany no singa lehibe mamaritra ny fikoriana, ka ny ala no manana anjara toerana lehibe amin'ny fitantanana ny fihodinan'ny rano; (3) ny fikorian'ny rano ao ambanin'ny tany amin'ny faritra misy ala, fa ny fikorian'ny rano eny ambonin'ny tany amin'ny tany fiandrasana biby fiompy, ny tanimboly ary ny savoka rehefa misy orana be na maharitra; (4) ny filana ny hanohy ny fandrefesana ny orana eny an-tany mba hahazoana antontan'isa azo antoka momba ny rano, indrindra fa ho an'ny fanaraha-maso ny fiakaran'ny rano sy ny fihenan'ny rano; (5) ny fanombanana ny fiantraikan'ny fiovana amin'ny fampiasana ny tany sy ny toetr'andro amin'ny ho avy, izay maneho fa ny fiovan'ny toetr'andro no hisy fiantraikany lehibe indrindra amin'ny fikorian'ny rano amin'ny faritra, mihoatra lavitra ny vokatry ny fiovana amin'ny fampiasana ny tany.

Ity fikarohana ity dia nanampy tamin'ny fanatsarana ny fahatakarana ny fomba fiasan'ny rano sy ny fiovany amin'ny tontolo mando sy mafana, ka manome fomba fijery azo ampiasaina amin'ny fampiharana mahomby ny Fitantanana Mirindra ny Loharanonkarenan'ny Rano (GIRE) mifanaraka amin'ny toe-javatra misy eo an-toerana any amin'ny faritra SAVA sy any amin'ny faritra hafa mitovy amin'izany.

Table des matières

Remerciements ..... **vii**

Résumé ..... **xi**

Abstract ..... **xii**

Fintina ..... **xiii**

Table des matières ..... **xv**

Liste des figures ..... **xxiii**

Liste des tableaux ..... **xxxv**

Liste des annexes ..... **xxxvii**

Liste des acronymes ..... **xxxix**

1. Chapitre 1 : Introduction générale **1**

1.1. Contexte et enjeux 1

1.2. Aperçu de la thèse 6

2. Chapitre 2 : Etat de l'art **11**

2.1. Rappel théorique du cycle hydrologique d'un bassin versant 11

2.1.1. Bassin versant et son fonctionnement 11

2.1.2. Processus hydrologique à l'échelle du bassin versant 13

2.2. Spécificités du contexte tropical 25

2.2.1. Les milieux tropicaux 25

2.2.2. Caractéristiques générales des climats tropicaux humides 27

2.2.3. Processus hydrologiques en milieu tropical humide 27

2.2.4. Limites et défis des études de bassin versant en climat tropical humide 35

2.3. Scénarios climatiques globaux et leurs impacts sur les milieux tropicaux 37

2.4. Modélisation hydrologique adaptée aux environnements changeants 39

2.4.1. Modélisation hydrologique 39

2.4.2. Types de modèles hydrologiques 40

2.4.3. Sélection et description du modèle hydrologique 44
2.5. Le modèle SWAT 46
2.6. La recherche hydrologique à Madagascar 51
2.6.1. L'évolution de la recherche hydrologique à Madagascar 51
2.6.2. Enjeux liés à la recherche hydrologique 53
2.7. Hypothèses et objectifs de la recherche 61
2.7.1. Hypothèses 61
2.7.2. Objectifs 62
3. Chapitre 3 : Zone d'études 63
3.1. L'île de Madagascar 63
3.1.1. Localisation 63
3.1.2. Relief 63
3.1.3. Fonctionnement climatique 65
3.1.4. Tendance climatique 67
3.1.5. Hydrographie 68
3.2. Cadre de l'étude : Région SAVA 75
3.2.1. Géographie 75
3.2.2. Relief et occupation de sol 75
3.2.3. Fonctionnement climatique 75
3.2.4. Géologie 76
3.2.5. Pédologie 77
3.2.6. Hydrologie 77
3.3. Bassin versant d'Ankavia 80
3.3.1. Localisation 80
3.3.2. Relief 82
3.3.3. Climat 83
3.3.4. Géologie 83
3.3.5. Pédologie 84

3.3.6. Couvertures végétales et activités de conservation 86
3.3.7. Les sous-bassins versants de l'Ankavia 87
3.4. Stations de mesure 88
3.4.1. Mesure des précipitations et paramètres climatiques 88
3.4.2. Mesure du niveau d'eau 90
3.4.3. Mesure de débits faibles et moyens 92
3.4.4. Mesure de hauts débits 98
4. Chapitre 4 : Reliability of Gridded Precipitation Products for Water Management Studies : The Case of the Ankavia River Basin in Madagascar 101
4.1. Introduction 102
4.2. Materials and Methods 106
4.2.1. Study area 106
4.2.2. Ground-based precipitation data 108
4.2.3. Gridded precipitation products 109
4.2.4. Data comparison methodology 112
4.3. Results 118
4.3.1. Overall GPP performance at daily time scale 118
4.3.2. GPP performance at daily time scale across the watershed 120
4.3.3. Daily rainfall probability distribution function 122
4.3.4. Precipitation detection ability 123
4.3.5. Different time scales assessment (hourly to yearly) 125
4.3.6. Event scale assessment 128
4.4. Discussion 130
4.5. Conclusion 135
5. Chapitre 5 : Driving Factors of the Hydrological Response of a Tropical Watershed : The Ankavia River Basin in Madagascar 137
5.1. Introduction 138
5.2. Materials and Methods 141
5.2.1. Study area 141

5.2.2. Watershed attributes 143
5.2.3. Hydrometeorological datasets 148
5.2.4. Catchment descriptors (CD) analysis 148
5.2.5. Streamflow analysis 155
5.2.6. Hydrological signatures (HS) Analysis 155
5.2.7. Hydrological signatures analysis 157
5.2.8. Linking hydrological signature and catchment descriptors 160
5.3. Results 161
5.3.1. Catchment descriptors characteristics 161
5.3.2. Hydrological signatures and their spatial patterns 165
5.3.3. Correlation between selected CDs and HSs 170
5.4. Discussion 172
5.4.1. General hydrological characteristics 172
5.4.2. Catchment Descriptors 174
5.4.3. Which catchment descriptors are the best predictors for each hydrological signature? 175
5.5. Conclusion 178
6. Chapitre 6 : How Tropical Land Cover Shapes Streamflow: Insights from the Ankavia River Basin, Madagascar 179
6.1. Introduction 180
6.2. Materials and Methods 183
6.2.1. Study area 183
6.2.2. Methodology 187
6.3. Results 193
6.3.1. Rainfall characteristics 193
6.3.2. Soil characteristics 195
6.3.3. Event-based hydrological characteristics of micro-catchments 202
6.3.4. Curve Number for each land cover 202
6.4. Discussion 204

6.4.1. Spatial variation in soil physical characteristics across land cover types 204

6.4.2. Effect of land cover on runoff processes 206

6.4.3. Effect of spatial configuration of land cover on hydrological responses 208

6.5. Conclusion 210

7. Chapitre 7 : Raingauge vs IMERG precipitation data : Balancing Accuracy and Cost for a Reliable Hydrological Observatory in a Tropical River Basin 213

7.1. Introduction 214

7.2. Materials and Methods 218

7.2.1. Study area 218

7.2.2. Data collection 220

7.2.3. Rainfall spatial variability 221

7.2.4. Hydrological modelling: SWAT semi-distributed model 223

7.3. Results 227

7.3.1. Rainfall characteristics 227

7.3.2. Streamflow characteristics 230

7.3.3. Rainfall-runoff model performances 230

7.4. Discussion 236

7.4.1. Rainfall characteristics 236

7.4.2. Hydrological usefulness of precipitation data 236

7.4.3. Implication of the selection of precipitations datasets in streamflow simulation 238

7.5. Conclusion 239

8. Chapitre 8 : Unraveling the impacts of land cover and climate changes on hydrological response of a tropical river basin: the case of Sahafihitry catchment, Madagascar 241

8.1. Introduction 242

8.2. Materials and Methods 245

8.2.1. Study area 245

8.2.2. Data collection 246
8.2.3. Scenarios analysis 248
8.2.4. Hydrological alterations analysis 253
8.3. Results 256
8.3.1. Climate model performance/ Projected climate change 256
8.3.2. CA Markov model performance and land use/land cover change projections 261
8.3.3. Hydrological model performance 267
8.3.4. Hydrological alterations 270
8.4. Discussion 273
8.4.1. Climate change modelling 273
8.4.2. Land cover modelling 273
8.4.3. Hydrological model performance 275
8.4.4. Hydrological alterations 276
8.5. Conclusion 278
9. Chapitre 9 : Discussion et conclusion générales 281
9.1. Synthèses des résultats 281
9.1.1. Fiabilité des produits satellitaires pour une étude de gestion des ressources en eau dans le milieu tropical 281
9.1.2. Facteurs déterminants les réponses hydrologiques à l'échelle des méso-bassins 282
9.1.3. Facteurs de contrôle hydrologiques à l'échelle des micro-bassins 283
9.1.4. Importance des réseaux de mesure au sol 284
9.1.5. Impacts du changement climatique versus changements d'utilisation des terres. 284
9.2. Limites et forces méthodologiques 285
9.2.1. Limites 285
9.2.2. Forces 288
9.3. Implications et perspectives de recherche 288

9.3.1. Implications pour la gestion des ressources en eau 288
9.3.2. Perspectives de recherche 290
10. Références bibliographiques..... 293
11. Annexes I

Liste des figures

Figure 1. Principaux cheminements de la thèse : titre de chaque chapitre et les échelles d'études. 9

Figure 2. 1. Schéma d'un bassin versant et d'un sous-bassin versant avec leurs exutoires et les lignes de partage des eaux. Source : adaptée à partir de Charlton (2008). 12

Figure 2. 2. Principaux processus hydrologiques au sein d'un bassin versant. Source : modifiée à partir de Charlier, 2007. 14

Figure 2. 3. Polygones de Thiessen pour une série de pluviomètres (r_i) dans un bassin versant imaginaire où a_i est la superficie de chaque polygone ; les emplacements des pluviomètres sont indiqués par des points noirs. 16

Figure 2. 4. Evolution générale du régime d'infiltration et de l'infiltration cumulative au cours du temps (Ks = conductivité hydraulique à saturation). Source : Musy, 2004. 19

Figure 2. 5. Processus hydrologiques de surface (modifiée à partir de Charlier, 2007). 20

Figure 2. 6. Processus hydrologique de subsurface et souterrain (modifiée à partir de Charlier, 2007). 21

Figure 2. 7. Représentation des différents processus de génération de l'écoulement en fonction du milieu naturel (D'après Dunne, 1983). 24

Figure 2. 8. Climats tropicaux selon Koppen (1936) : climat tropical humide (Af), la mousson tropicale (Am) et le climat tropical de savane (Aw). 25

Figure 2. 9. Position de la Zone de Convergence Inter Tropicale (ZCIT) en fonction des saisons. Source : Baumman, 2011. 26

Figure 2. 10. Distribution mondiale des stations synoptiques. Source : WMO, 2022. 28

Figure 2. 11. Le spectre des cheminements hydrologiques dans les forêts tropicales humides (d'après Elsenbeer, 2001). 31

Figure 2. 12. Evolution de la température moyenne globale selon différents scénarios d'émissions (1950 – 2100). Ligne noire : données historiques observées jusqu'en 2005 ; ligne bleue : scénario RCP2.6 (scénario d'atténuation stricte) ; ligne rouge scénario RCP8.5 (scénario à fortes émissions). Source : GIEC, 2021. 37

Figure 2. 13. Changements projetés de température (a) et de précipitations (b) selon les scénarios RCP 2.6 (atténuation stricte) et RCP 8.5 (émissions élevées) (1986 – 2005 à 2081 – 2100). Source : GIEC, 2021. 38

Figure 2. 14. Structure typique et variables d'un modèle hydrologique. Source : Musy, 2004. 40

Figure 2. 15. Représentation schématique de la classification des modèles hydrologiques. Source : Singh et Woolhiser, 2002. 41

Figure 2. 16. Conceptualisation du cycle hydrologique dans le modèle SWAT. Source: Soil and Water Assessment Tool, Theoretical documentation, Version 2009. http://twri.tamu.edu/reports/2011/tr406.pdf, consulté en Juin 2024..... 47

Figure 2. 17. Données spatiales d'entrée requises pour le modèle SWAT. Source: Soil and Water Assessment Tool, Theoretical documentation, Version 2009. http://twri.tamu.edu/reports/2011/tr406.pdf, consulté en Juin 2024..... 47

Figure 3. 1. Carte de localisation de Madagascar (à gauche) et de la région SAVA (à droite). Source : OpenStreetMap 64

Figure 3. 2. Schématisation des principaux centres d'action réglant le climat à Madagascar. Source : Chaperon et al. (1993)..... 66

Figure 3. 3. Carte de Madagascar avec isohyètes (A : Température moyenne annuelle ; B : Précipitations moyennes annuelles). Les données ont été obtenues à partir de la base de données WORLDCLIM (Hijmans et al. 2005). 70

Figure 3. 4. Carte de classification climatique de Köppen-Geiger pour Madagascar (1980 - 2016). Source : Beck et al. 2018 71

Figure 3. 5. Valeurs minimales (a) et maximales (b) des projections de l'augmentation de la température moyenne annuelle (°C) obtenues à partir de 13 modèles climatiques globaux et pour la période centrée en 2055 (Source : DGM, 2008). 72

Figure 3. 6. Changements (Médiane) des précipitations mensuelles (mm/mois) obtenus à partir de la mise à l'échelle de 6 modèles globaux (période centrée en 2055). Les régions où 3 modèles ont donné des augmentations des précipitations et les 3 autres des diminutions sont laissées en blanc. Il en est de même pour les régions où les augmentations sont <10 mm/mois (Source : DGM, 2008). 73

Figure 3. 7. Principaux régimes hydrologiques de Madagascar. Source : World Bank Group, ESMAP, SHER (2017). 74

Figure 3. 8. Géologie et lithologie – Partie Nord de Madagascar, Source : cartothèque IRD (http://sphaera.cartographie.ird.fr/, mai 2024) 78

Figure 3. 9. Pédologie – Partie Nord de Madagascar, Source : cartothèque IRD (http://sphaera.cartographie.ird.fr/, mai 2024) 79

Figure 3. 10. Localisation du bassin versant d'Ankavia. Source : BD 100 FTM 81

Figure 3. 11. Topographie du bassin versant d'Ankavia et le réseau hydrographique. Source : Digital Elévation Model (Earth Resources Observation And Science (EROS) Center 2017) 82

Figure 3. 12. Moyenne mensuelle des paramètres climatiques dans le bassin versant d'Ankavia, à partir des données recueillies au niveau de la station climatique de Marofinaritra pendant la période 2018-2020. Source : GIRE SAVA 83

Figure 3. 13. Géologie du bassin versant d'Ankavia. Source : PGRM, 2018 (https://www.brgm.fr/fr/reference-projet-acheve/synthese-geologique-miniere-madagascar) 84

Figure 3. 14. Pédologie du bassin versant d'Ankavia. Source : SoilGRID, (Hengl et al. 2017) 85

Figure 3. 15. Couvertures végétales en 2020 avec les aires protégées dans le bassin d'Ankavia. Source : Globcover 2020, (Bontemps et al. 2009) 86

Figure 3. 16. Localisation des stations de mesures hydrométéorologiques dans le bassin versant d'Ankavia. Source : SRTM (Earth Resources Observation And Science (EROS) Center 2017), GIRE SAVA. 89

Figure 3. 17. Equipements météorologiques : (a) Pluviomètre et (b) station climatique de Marofinaritra. 89

Figure 3. 18. Capteurs de pression et échelles limnimétriques installés à l'exutoire de chaque sous-bassin : (a) Sahafihitry, (b) Ankaviabe, (c) Antsahovy, (d) Ankavia. 91

Figure 3. 19. Photographie de la sonde du courantomètre électromagnétique (à gauche) et appareil d'affichage des résultats (à droite). 93

Figure 3. 20. Sections en travers représentatives des exutoires des sous-bassins versants, accompagnées des photographies correspondantes. (Crédit photo : Ramahaimandimby). 94

Figure 3. 21. Représentation de la section en travers avec intervalles et méthodes de mesure des vitesses ponctuelles d'écoulement (1 ou 2 points) au courantomètre électromagnétique. Source : modifiée à partir de Castermans (2019). 95

Figure 3. 22. Courbes de tarage de chaque cours d'eau du bassin versant, avec les hauteurs maximales enregistrées dépendant de la date d'acquisition des données. (a) Sahafihitry : 3 ans de données (08/2018 – 07/2021). (b) Ankaviabe, (c) Antsahovy et (d) Ankavia : 10 mois de données (09/2018 – 06/2019). 97

Figure 4. 1. Location of the Ankavia watershed in northeastern Madagascar with rain gauge network (rain gauges numbered A to N). 107

Figure 4. 2. Data processing with two different approaches: (a) point-to-grid, (b) point-gridded. 115

Figure 4. 3. Comparison of ground-based precipitation data with 6 GPPs at a daily time scale from September 2018 to August 2020 based on 4 indicators: (a)

Coefficient of determination, (b) Slope of linear regression, (c) Root Mean Square Error, (d) Mean Absolute Error. Each box plot is based on 2 years of data from 14 rain gauges in the Ankavia watershed. 'A' refers to the point-to-grid approach (grey boxes and whiskers) and 'B' to the point-gridded approach (red boxes and whiskers) (see Figure 2). Box edges correspond to the 25th (Q1) and 75th (Q3) percentiles. Whiskers extend to Q1-1.5IQR (lower bound) and Q3+1.5IQR (upper bound), with IQR = Q3-Q1 (Inter-Quartile Range). Points outside the box are outliers. 120
Figure 4. 4. Spatial distribution of the statistical evaluation metrics across the Ankavia watershed based on the point-gridded approach at a daily time scale from September 2018 to August 2020. 121
Figure 4. 5. Probability distribution function (PDF) of daily rainfall intensities based on GPP and rain gauge data from September 2018 to August 2020. Note logarithmic (Log10) scale for Y axis. 122
Figure 4. 6. Precipitation detection ability of the six GPPs based on daily rainfall: (a) Probability of detection (POD), (b) False alarm ratio (FAR), (c) Critical success index (CSI). Ground-based rain gauge data from September 2018 to August 2020 are used as reference. Note logarithmic (Log10) scale for X axis. 124
Figure 4. 7. Comparison of ground-based precipitation data with IMERG at different time scales: (**a**) yearly, (**b**) monthly, (**c**) daily, (**d**) hourly, (**e**) barplot of monthly rainfall with standard deviation. R^2 value is determined for regression passing through (0,0). 128
Figure 4. 8. Probability distribution function of (**a**) rainfall duration, (**b**) rainfall depth, and (**c**) rainfall intensity at event time scale for ground-based rain gauges and IMERG data from September 2018 to August 2020. 130

Figure 5. 1. Location of the Ankavia catchment (WS1) and its sub-catchments (WS2, WS3, and WS4). The map includes the location of the weather station, rain gauges, and stream gauges, as well as the grids of IMERG (a gridded rainfall dataset). 142
Figure 5. 2. (**a**) 2019 land cover of Ankavia catchment, (**b**) soil texture, (**c**) dominant soil orders, (**d**) hydrological soil group, (**e**) modified geological map. Data sources are listed in Table 5.1. 147

Figure 5. 3. Event identification and hydrograph separation. 156
Figure 5. 4. Hypsometric curves: (**a**) slope–area (**b**) elevation–area. 162
Figure 5. 5. Correlation plot between (**a**) all catchment descriptors, and (**b**) selected catchment descriptors, based on Pearson's coefficient r. The catchment descriptors are color-coded according to their generic group: topographic (T), land cover (LC), soil (S), and geology (G). The size of the circles indicates the strength of the correlation, with red corresponding to positive and green to negative correlations. Gray circles mean poor correlation (r < |0.5|). 164
Figure 5. 6. Cumulative rainfall (IMERG) over the 10-month study period (September 2018–June 2019). Date on X-axis in MM/DD/YYYY format. 165
Figure 5. 7. Streamflow characteristics of sub-catchments (%): (**a**) cumulative streamflow, (**b**) cumulative runoff (quickflow), (**c**) cumulative baseflow from September 2018 to June 2019. All values are expressed relative to the total rainfall of each sub-catchment (Figure 6). Date in X-axis in MM/DD/YYYY format. 166
Figure 5. 8. Flow duration curve of the four sub-catchment rivers. Note logarithmic (Log10) scale for Y axis. 167
Figure 5. 9. Boxplots of hydrological signatures of the Ankavia catchment sub-watersheds over the 10-month study period. (a) Baseflow index (-), (b) runoff coefficient (-), (c) peak discharge (mm h^{-1}), (d) runoff event time scale (h km^{-1}), (e) high flows Q5, mean discharge and low flows Q95 (mm day^{-1}). Box lower and upper edges correspond to the 25th (Q1) and 75th (Q3) percentiles. Whiskers extend to Q1 − 1.5IQR (lower bound) and Q3 + 1.5IQR (upper bound), with IQR = Q3 − Q1 (inter-quartile range). Points outside the box are outliers. 169
Figure 5. 10. Correlation plot between hydrological signatures using Pearson's coefficient r. The size of the circles indicates the strength of the correlation, with red corresponding to positive and green to negative correlations. Gray circles mean poor correlation (r < |0.5|). 170
Figure 5. 11. Correlation plot between HSs and CDs using Pearson's coefficient r. The catchment descriptors are color-coded according to their generic group: topography (T), land cover (LC), soil (S), and geology (G). The size of the circles indicates the strength of the correlation, with red corresponding to positive and green to negative

correlations. Gray circles mean poor correlation (r < |0.5|). '*' indicates a robust correlation. 171

Figure 6. 1. Location of the three micro-catchments and their respective land cover distribution, stream networks, instrumentation (section 6.2.2), and soil sampling sites..... 186

Figure 6. 2. Illustration of dominant land cover types: A) forested land, B) fallowed land, C) cropland, D) pasture (former irrigated rice field). 187

Figure 6. 3. View of the type of modified San Dimas weir used to gauge streamflow at the micro-catchment outlets: (a) dimensions of San Dimas flume, (b) San Dimas flume installed at the outlet of the FAL micro-catchment. 189

Figure 6. 4. (a) Correlations between hourly rainfall from the R1 and the R2 or R3 rain gauges (see Figure 6.1 for location of gauges). (b) average cumulative rainfall for each discharge monitoring period: in black, cumulative rainfall during the rainy period when both the MIX and FAL discharge flumes were operational (upper X axis, Feb-June 2020); in grey, cumulative rainfall during the rainy period when both the MIX and FOR discharge flumes were operational (lower X axis, Dec 2020 – April 2021). Period in X-axis is in MM/DD/YYYY format (c) distribution of rainfall intensity. 194

Figure 6. 5. (a) Profile description of SOIL 1 found under forest, fallow and cropland covers; (b) Profile description of SOIL 2 found under the pasture cover. The rulers in the photo measure 30 cm. 196

Figure 6. 6. Texture of the soil samples for the two soil types identified in the micro-catchments and different horizons, according to the National Resources Conservation Service (NRCS) textural diagram..... 197

Figure 6. 7. Soil characteristics: (a) proportion of sand (%); (b) proportion of clay (%); (c) Organic carbon content; sand and clay content are differentiated by soil type, while pH and OC are differentiated by land use..... 198

Figure 6. 8. Soil bulk density under each respective soil and land cover type (Soil 1: forest (frst), fallow land (fall), cropland (crop); Soil 2: pasture (past)). A indicates A horizon; B indicates B or B1 horizon. Box edge corresponds to the 25th (Q1) and 75th (Q3) percentiles. Whiskers extend to Q1-1.5QR (lower bound) and Q3+1.5QR (upper bound), with IQR = Q3 – Q1 (Inter-Quantile Range).....199

Figure 6. 9. Soil water retention curve for each land cover type. Note logarithmic (Log10) scale for X axis. Matric head values should be understood as being negative. 200

Figure 6. 10. Infiltration rate as measured by double ring infiltrometer under each land cover type. Box edges correspond to the 25th (Q1) and 75th (Q3) percentiles. Whiskers extend to Q1-1.5QR (lower bound) and Q3+1.5QR (upper bound), with IQR = Q3 – Q1 (Inter-Quantile Range). Points outside the box are outliers. Note logarithmic (Log10) scale for Y axis. The blue lines represent the percentiles of the 5-min rainfall intensity recorded at rain gauge R2: 55th (4.8 mm h^{-1}, bold solid line), 75th (7.2 mm h^{-1}, medium bold solid line), 90th (16.8 mm h^{-1}, thin solid line), 95th (28.8 mm h^{-1}, dashed line), 99th (62.4 mm h^{-1}, dotted line). 201

Figure 6. 11. Hydrological signatures of the three micro-catchments: (a) Runoff coefficient (rc) and (b) normalized lag time (t_lag). Box edge corresponds to the 25th (Q1) and 75th (Q3) percentiles. Whiskers extend to Q1-1.5QR (lower bound) and Q3+1.5QR (upper bound), with IQR = Q3 – Q1 (Inter-Quantile Range). Points outside the box are outliers. Each pair of signatures corresponds to a specific rainy period: the MIX/FAL comparison extends over the period from February 2020 to June 2020, while the MIX/FOR comparison relates to the period from December 2020 to April 2021 (see materials and methods section for further details). 203

Figure 7. 1. Geographical context of the Sahafihitry catchment in Northeastern Madagascar: topography and location of weather station, additional rain gauges and river discharge monitoring station within the watershed. Rain gauge No. 1 is located

at the weather station in Marofinaritra. Grids correspond to the grid of the IMERG gridded precipitation dataset. 219

Figure 7. 2. Characteristics of the Sahafihitry catchment: (a) 2020 Land cover, (b) Soil properties, (c) Slope. 222

Figure 7.3. Mean cumulative rainfall for one rain gauge (1RG), two rain gauges (2RG), five rain gauges (5RG) and IMERG satellite-based precipitation data. The date on the X-axis is in MM/DD/YYYY format. 227

Figure 7.4. Cumulative rainfall for one rain gauge (1RG), two rain gauges (2RG), five rain gauges (5RG) and IMERG satellite-based precipitation data based on 'wet' rainy season (RS) and 'dry' rainy season (DS). The date on the X-axis is in MM/DD/YYYY format. 229

Figure 7.5. Cumulative rainfall (5RG) and discharge (Q_OBS) curves of the Sahafihitry watershed over (a) the entire study period and (b) on an annual basis. 231

Figure 7.6. Plots of observed and simulated daily flows for the 5 rainfall-runoff scenarios (from the left to the right: 1RG, 2RG, 5RG, IMERG) for the calibration period (top, from 08/2018 to 07/2020) and validation period (bottom, 08/2020 – 07/2021). The last scenario (IMERG_in_5RG) corresponds to the model calibrated using 5 rain gauges but run with IMERG data for the validation period. Note logarithmic (Log10) scale for Y and X axis. 232

Figure 7.7. Comparison of observed (Q_OBS) and simulated hydrographs for the validation period (08/2020-07/2021) at the Sahafihitry station for the 5 rainfall-runoff scenarios. Model calibrated using one rain gauge (Q_1RG), 2 gauges (Q_2RG), 5 gauges (Q_5RG) or IMERG data (Q_IMERG). The last scenario corresponds to the model calibrated using 5 rain gauges but run with IMERG data for the validation period (IMERG_in_5RG). 234

Figure 7.8. (a) Root Mean Square Error (RMSE), (b) Nash Sutcliffe Efficiency coefficient (NSE) and (c) Kling-Gupta efficiency (KGE) for various classes of discharge for the 5 rainfall-runoff scenarios. Model calibrated using one rain gauge (1RG), 2 gauges (2RG), 5 gauges (5RG) or IMERG data (IMERG). The last scenario corresponds

to the model calibrated using 5 rain gauges but run with IMERG data for the validation period (IMERG_in_5RG). Square markers refer to the calibration period, triangular markers refer to the validation period. 235

Figure 8. 1. Land use and land cover (LULC) alterations from 1992 to 2020 in the Sahafihitry catchment. Derived from GlobCover images (section 8.2.2.). 247

Figure 8. 2. Alignment of monthly simulated historical precipitation (CCLM4, HIRHAM, RACMOT22T, REMO2009, RCA4) and their ensemble mean over a twenty-year period (1980-2000) with monthly IMERG precipitation over a twenty-year period (2001-2021) (a) before and (b) after bias correction. 258

Figure 8. 3. Frequency distribution of daily precipitation intensities based on IMERG (2001-2021) and the ensemble mean of five regional climate model-generated precipitation for the mid-term (2040-2060) and long-term (2080-2100) periods under RCP 4.5 and RCP 8.5 scenarios. Note the logarithmic scale for the Y-axis. ... 259

Figure 8. 4. Projected precipitation patterns: (a) Monthly precipitation totals for IMERG baseline (2001-2021) and ensemble means of regional climate models for medium-term (2040-2060) and long-term (2080-2100) under RCP 4.5 and RCP 8.5; (b) Monthly mean (across climate models) precipitation changes (mm) relative to IMERG baseline for future scenarios. Error bars in (a) correspond to standard deviation across the five climate models. 260

Figure 8. 5. Alignment of monthly simulated historical temperature max and min (CCLM4, HIRHAM, RACMOT22T, REMO2009, RCA4) and their ensemble mean (1980-2000) with monthly observed temperature (2001-2021) (a,b) before and (c) after bias correction. See Table 8.1 for details. 262

Figure 8. 6. Projected monthly temperature changes (°C) relative to climate station baseline for future scenarios (a) maximum temperature, (b) minimum temperature. Error bars are not shown due to their negligible magnitude. 264

Figure 8. 7. Observed land use/land cover in the Sahafihitry catchment in 1992 and 2010; and predicted LULC for 2050 and 2090. 266

Figure 8. 8. Comparison of observed and simulated mean daily discharge using SWAT model: (a) Calibration period (08/2018 – 07/2020) and (b) Validation period (08/2020 – 07/2021). 95 PPU indicates the 95th percentile prediction uncertainty. 268

Figure 8. 9. Observed (Qobs) and simulated (Qsim) daily discharge obtained from the hydrological model for the (a) calibration period (08/2018 to 07/2020) and (b) the validation period (08/2020 – 07/2021). Note logarithmic (Log10) scale for X and Y axis. For metrics of model performance, see Table 8.3. Metrics are calculated on actual discharge values (not log-transformed). 269

Figure 8. 10. (a) Root Mean Square Error (RMSE), (b) Nash Sutcliffe Efficiency coefficient (NSE) and (c) Kling-Gupta efficiency (KGE) for different classes of discharge for the SWAT model by IMERG rainfall data. Square markers refer to the calibration period (08/2018 to 07/2020), triangular markers refer to the validation period (08/2020 – 07/2021). 270

Figure 8. 11. Projected changes in streamflow characteristics based on simulations twenty hydrological years: (a) Q95 (95th percentile flow); (b) q_mean (mean daily discharge); (c) Q5 (5th percentile flow), under three scenarios: Scenario 1 : effect of land cover change only; Scenario 2 : effect of climate change only; Scenario 3 : combined effect of land cover and climate changes. Refer to Table 4 for details. Box edges correspond to the 25th (Q1) and 75th (Q3) percentiles. Whiskers extend to Q1-1.5QR (lower bound) and Q3+1.5IQR (upper bound), with IQR = Q3-Q1 (Inter-Quartile Range). Points outside the box are outliers. 271

Liste des tableaux

Table 2. 1. Produits satellitaires fréquemment utilisés pour étudier les caractéristiques des climats tropicaux. 29

Table 2. 2. Comparaison de bilans hydrologiques annuels et des principaux processus pour des micro-bassins tropicaux avec un sol perméable, modifié à partir de Charlier, 2007. 33

Table 2. 3. Synthèse des recherches hydrologiques à Madagascar après les années 1990. 56

Table 3. 1. Caractéristiques des sous-bassins versants de l'Ankavia 87

Table 3. 2. Estimation des paramètres nécessaires au calcul du coefficient de rugosité de Manning. 99

Table 4. 1. Selected gridded precipitation products. 113

Table 4. 2. Statistical metrics used to quantify GPP performance. 117

Table 4. 3. Summary of IMERG assessment studies in tropical environments at a daily time scale. 133

Table 5. 1. Summary of the gridded products and maps used to characterize the Ankavia catchment. 144

Table 5. 2. Descriptors and calculation of catchment descriptors. 149

Table 5. 3. Hydrological signatures of runoff events used in the present study. ... 159

Table 6. 1. Morphometric characteristics of the three headwater micro-catchments (FOR, MIX and FAL) and the upstream forested sub-catchment of MIX (MIX-frst). 185

Table 6. 2. Properties of the two identified soil types.....195

Table 6. 3. Curve Number of each land cover type. (LS = Least Square method)...202

Table 7. 1. Description of the parameters used in the calibration process, their possible range, the initial value as well as the optimum values after calibration using the 1RG, 2RG, 5RG and IMERG rainfall scenarios (see section Scenarios below). . 224
Table 7. 2. Statistical metrics used for evaluating the SWAT model performance. 226
Table 7. 3. Cumulative rainfall and average coefficients of variation (CV) between the five ground-based rain gauges (5RG) and eight IMERG grids across the Sahafihitry watershed for three successive years. 228

Table 8. 1. Summary of spatial data and temporal data used to assess hydrological alterations in Sahafihitry catchment. 250
Table 8. 2. Description of the parameters used in the calibration process, their possible range, the initial value as well as the optimum values after calibration using IMERG rainfall (see section 8.2.3)..... 254
Table 8. 3. Statistical metrics to evaluate the hydrological model performance. .. 255
Table 8. 4. Separate or combined land cover and climate change scenarios considered in the present study. 256
Table 8. 5. Land use and land cover in 1992, 2010, 2050 and 2090 and changes in LULC relative to 1992..... 265

Liste des annexes

Annexe A : Modèle SWAT (Chapitre 2) I

Annexe B : Descripteurs de bassin versant (Chapitres 3 et 5) VIII

Annexe C : Localisation géographique des pluviomètres au sol et des exutoires (Chapitre 3) IX

Annexe D : Grille de corrélation entre les pluviomètres (Chapitres 4 et 7) X

Annexe E : Matrice des distances entre les pluviomètres (Chapitres 3, 4 et 7). XI

Annexe F : Méthode de polygone de Thiessen (Chapitre 4) XII

Annexe G : Séparation du débit de base (échelle journalière) (Chapitre 5) WS1 = Ankavia ; WS2 = Ankaviabe ; WS3 = Sahafihitry ; WS4 = Antsahovy XIII

Annexe H : Signatures hydrologiques (Chapitre 5) XIV

Annexe I : Corrélation entre les CD et les HS sélectionnés WS1 (Ankavia) = vert ; WS2 (Ankaviabe) = rouge ; WS3 (Sahafihitry) = bleu ; WS4 (Antsahovy) = gris (Chapitre 5) XV

Annexe J : La charte des couleurs de Munsell (Chapitre 6) XVI

Annexe K : Séparation linéaire de l'hydrogramme telle que mise en œuvre dans l'outil Visuhydro (Rocha 2014) (Chapitre 6) XVII

Annexe L : pH du sol sous chaque type de couvert végétal : prairie (ancienne rizière irriguée), jachère, forêt, terre cultivée (Chapitre 6) XVIII

Liste des acronymes

AFD	:	Agence Française de Développement
ANN	:	Artificial Neural Network
ARC-2	:	African Rainfall Estimate Climatology
CCD	:	Cold Cloud Duration
CD	:	Catchment Descriptors
CDF	:	Cumulative Distrubution Function
CDS	:	Climate Data Store
CFS	:	Climate Forecast System
CHIRPS	:	Climate Hazards Group InfraRed Precipitation with Station data
CHPclim	:	CHIRPS precipitation climatology
CHRS	:	Center for Hydrometeorology and Remote Sensing
CORDEX	:	Coordinated Regional Climate Downscaling Experiment-Africa
CPC	:	Climate Prediction Center
CPGU	:	Cellule de Prévention et Gestion des Urgences
CREAM	:	Centre de Recherches, d'Etudes et d'Appui à l'Analyse Economique à Madagascar
CREAMS	:	Chemicals, Runoff, and Erosion from Agricultural Management Systems
CSI	:	Critical Success Index
DFFITS	:	Difference in Fits
DPR	:	Dual-frequency Precipitation Radar
ECMWF	:	European Centre Medium-Range Weather Forecasts
EPIC	:	Erosion Productivity Impact Calculator
ERA5	:	ECMWF Re-Analysis 5
EROS	:	Earth Resources Observation and Science
ESGF	:	Earth System Grid Federation
EUMETSAT	:	European Organization for the Exploitation of Meteorological Satellites
FAO	:	Food and Agriculture Organization
FAR	:	False Alarm Ratio
FDC	:	Flow Duration Curves
GIEC	:	Groupe d'experts intergouvernemental sur l'évolution du climat
GIRE	:	Gestion Intégrée des Ressources en Eau
GLEAMS	:	Groundwater Loading Effects of Agricultural Management Systems
GMI	:	GPM Microwave Imager
GOES	:	Geostationary Operational Environmental Satellite
GPCC	:	Global Precipitation Climatology Centre
GPCP-1DD	:	Global Precipitation Climatology Project
GPI	:	GOES precipitation index
GPP	:	Gridded Precipitation Products

GRACE	:	Gravity Recovery And Climate Experiment
GTS	:	Global Telecommunications System
HOF	:	Hortonian Overlan Flow
HRU	:	Hydrological Reponse Unit
HS	:	Hydrological Signature
IHACRES	:	Identification of unit Hydrographs And Component flows from Rainfall, Evaporation and Streamflow data
IMERG GPM	:	Integrated Multi-satellitE Retrievals for Global Precipitation Measurement Mission
IR	:	InfraRed
IRD	:	Institut de Recherche pour le Développement
IRSM	:	Institut de Recherche Scientifique de Madagascar
JAXA	:	Japan Aerospace Exploration Agency
JIRAMA	:	Jiro sy Rano Malagasy (Eau et Electricité de Madagascar)
KGE	:	Kling Gupta Efficiency
LAI	:	Leaf Area Index
LS	:	Least Square fitting method
LULC	:	Land Use Land Cover
MAE	:	Mean Absolute Error
MBG	:	Missouri Botanical Garden
MCE	:	Multi-Criteria Evaluation
MED	:	Median fitting method
MNP	:	Madagascar National Parks
MNT	:	Modèle Numérique de Terrain
MODIS	:	Moderate Resolution Imaging Spectroradiometer
MRBM	:	Major River Basin of Madagascar
MSWEP	:	Multi-Source Weighted-Ensemble Precipitation
NASA	:	National Aeronautics and Space Administration
NCDC	:	National Climate Data Center
NOAA	:	National Oceanic and Atmospheric Administration
NRT	:	Near Real-Time
NSE	:	Nash Sutcliffe model Efficiency coefficient
OC	:	Organic Carbon Content
ORSTOM	:	Office de la Recherche Scientifique et Technique Outre-Mer (ancien nom de l'IRD)
PDF	:	Probability Distribution Function
PERSIANN-CCS	:	Precipitation Estimation from Remotely Sensed Information using Artificial Neural Networks Cloud Classification System
PERSIANN-CDR	:	Precipitation Estimation from Remotely Sensed Information using Artificial Neural Networks - Climate Data Record
POD	:	probability of detection
RCA4	:	Rossby Center Regional Atmospheric model
RCP	:	Representative Concentration Pathways
RG	:	Rain gauge
RMSE	:	Root Mean Square Error
SCS CN	:	Soil Conservation Service - Curve Number

SOF	:	Saturated excess Overland Flow
SRTM	:	Shuttle Radar Topography Mission
SSF	:	Subsurface flow
SSP	:	Shared Socioeconomic Pathway
SWAT	:	Soil and Water Assessment Tool
SWRRB	:	Simulator for Water Resources in Rural Basins
TRMM	:	Tropical Rainfall Measuring Mission
USDA	:	United States Department of Agriculture
WHAT	:	Web-based Hydrograph Analysis Tool
WMO	:	World Meteorological Organization
ZCIT	:	Zone de Convergence Intertropicale

1. Chapitre 1 : Introduction générale

1.1. Contexte et enjeux

L'eau douce ne représente qu'une infime partie de l'eau présente sur Terre, soit seulement 2,5% (Musy 2004). Cette faible proportion est répartie de la manière suivante : 69% est stockée sous forme de glace ou de neige dans les calottes glaciaires et les régions polaires, 30% se trouve dans les aquifères souterrains profonds, et seulement 1% est facilement accessible en surface, sous forme de cours d'eau, de fleuves, de rivières et de lacs. Bien que cette dernière catégorie ne constitue qu'une fraction minuscule des ressources en eau douce totales, elle revêt une importance cruciale pour la vie, l'agriculture, l'élevage et la santé humaine.

Les eaux de surface sont indispensables aux économies et au bien-être social des populations, en particulier dans les régions tropicales où elles constituent souvent la seule source d'eau douce disponible (Baumann 2011). Cependant, l'accès à ces ressources vitales est inégalement réparti à travers le monde en raison des variations des conditions climatiques et environnementales (Baumann 2011; Bonell 2005). Certaines régions arides, comme en Afrique subsaharienne, connaissent des niveaux d'accès extrêmement préoccupants, avec une disponibilité inférieure à 1 000 m^3 par habitant et par an, bien en deçà du seuil international recommandé de 1 700 m^3 (Ntouda et al. 2013; Dos Santos 2012). Cette pénurie d'eau chronique touche de manière disproportionnée les populations vulnérables, notamment les femmes et les enfants (Tallman et al. 2023; Hrdinka et al. 2012). À l'opposé, d'autres régions comme certaines parties de l'Amérique du Sud et de l'Asie du Sud-Est sont relativement bien pourvues en ressources en eau douce (Caravaggio Iorio 2016; Lathuillière et al. 2016; Karthe et al. 2015). Néanmoins, même dans ces zones plus favorisées, l'accès à l'eau potable reste précaire, particulièrement dans les zones rurales et les bidonvilles (Slater 2019). De plus, ces régions sont particulièrement exposées aux phénomènes météorologiques extrêmes, notamment les cyclones tropicaux, qui perturbent gravement l'approvisionnement en eau. Les conséquences sont dramatiques : inondations massives, comme celles ayant touché 7,2 millions de

Bangladais en 2022, ou au contraire, pénuries d'eau dues à de longues sécheresses (Islam et al. 2024; Rana et al. 2024). Ces catastrophes naturelles fragilisent la production agricole, aggravant l'insécurité alimentaire et la malnutrition. Elles favorisent également la propagation de maladies hydriques mortelles telles que le choléra et la diarrhée. Selon l'Organisation Mondiale de la Santé, ces maladies sont responsables d'environ 1,5 million de décès d'enfants de moins de 5 ans chaque année (Bertolina et al. 2023).

Face aux défis critiques et complexes liés à la gestion hydrique, le concept de la Gestion Intégrée des Ressources en Eau (GIRE) a attiré l'attention croissante des gestionnaires et décideurs depuis les conférences de Dublin et de Rio en 1992 (Mdee et al. 2024). Cette approche vise à coordonner le développement et la gestion de l'eau, des terres et des ressources connexes, en impliquant tous les acteurs concernés dans un processus participatif. L'objectif principal est de maximiser le bien-être socio-économique des populations tout en préservant la durabilité des écosystèmes vitaux (Telle 2024; Godinez-Madrigal et al. 2019). De plus, la GIRE encourage la coopération entre différents secteurs et parties prenantes, assurant ainsi une gestion efficace, équitable et durable de l'eau. Elle cherche également à améliorer les infrastructures hydrauliques et sanitaires, tout en promouvant une bonne gouvernance, des réformes politiques adaptées et la participation active des communautés locales (Mdee et al. 2024).

Malgré ses nombreux avantages théoriques, la mise en œuvre de la GIRE reste largement un défi dans de nombreux milieux tropicaux. Son approche intégrée et holistique exige d'abord de comprendre les forces motrices qui exercent des pressions sur les ressources en eau, ainsi que leurs impacts sur les propriétés physiques et le fonctionnement quantitatif de ces ressources (Godinez-Madrigal et al. 2019; PNUD 2015). Ce n'est qu'à partir de cette compréhension approfondie que les stratégies de gestion les plus efficaces peuvent être développées et mises en place, en tenant compte des spécificités locales et en impliquant toutes les parties prenantes concernées.

L'une des principales pressions à prendre en compte est la croissance démographique galopante dans les régions tropicales. Avec une population mondiale devant augmenter de 2 à 3 milliards de personnes d'ici 25 ans, dont plus de 75% dans les zones tropicales, l'eau, déjà une ressource rare, apparaît comme un facteur limitant majeur pour assurer la sécurité alimentaire et risque d'engendrer des conflits sérieux avec d'autres usages humains et environnementaux (Ling 2022). Une autre pression majeure est le changement d'occupation des sols résultant de la conversion des forêts en terres agricoles (Agarwal et al. 2005). Au Pérou, par exemple, la perte de 20% de la couverture forestière peut réduire jusqu'à 60% la capacité des sols à retenir l'eau, favorisant le ruissellement et entravant la recharge des nappes phréatiques (Zubieta et al. 2017). Cela pourrait entraîner une baisse inquiétante des niveaux d'eau en période sèche et accentuer les risques d'inondations dévastatrices lors de fortes pluies. Cependant, les constats sur l'impact de la déforestation sur les ressources en eau sont parfois contradictoires. Certaines études démontrent en effet une influence négligeable sur le débit suite à la conversion de forêts en terres agricoles (Arias et al. 2018a; Wilk et al. 2001). Ces disparités peuvent être attribuées aux différences d'échelle spatio-temporelle considérées, ainsi qu'aux différents contextes climatiques et aux complexités des bassins versants tropicaux étudiés.

Le changement climatique constitue également une pression majeure, intensifiant le cycle hydrologique mondial et entraînant des événements extrêmes plus fréquents et plus variables. Selon les projections du Groupe d'experts Intergouvernemental sur l'Evolution du Climat (GIEC), certaines régions connaîtront une hausse significative des précipitations annuelles moyennes, tandis que d'autres subiront des réductions importantes à long terme (Bates et al. 2008). Dans les régions tropicales comme l'Afrique de l'Est, une augmentation des précipitations de 20% à 45% est attendue, pouvant entraîner des inondations plus fréquentes et plus sévères (Aragaw et al. 2022; Abe et al. 2018). Des études en Ouganda corroborent ces projections, prévoyant des hausses de 7% à 22% selon les scénarios choisis, qui engendrerait une augmentation de 37% à 52% du ruissellement de surface (Gabiri et al. 2020). À l'inverse, dans d'autres zones comme l'Afrique australe et le sud de

Madagascar, les scénarios climatiques mettent en avant des réductions significatives des précipitations, aggravant les conditions de sécheresse et la pression sur des ressources en eau déjà limitées. Une diminution de 12% du débit de la rivière Zambezi au Mozambique (Uamusse et al. 2020) et une baisse pouvant atteindre 17% du débit annuel moyen de la rivière Mzingwane au Zimbabwe sont prévues d'ici 2050 (Arnell et al. 2003). De même, une réduction de 4% du ruissellement de la rivière Mangoky est anticipée au sud de Madagascar (Rabezanahary et al. 2021). Ces contrastes soulignent que les impacts du changement climatique sur les ressources en eau diffèrent grandement d'une zone à l'autre, en fonction des conditions environnementales et climatiques locales. Ainsi, pour assurer une gestion durable des ressources hydriques face aux environnements changeants, il est crucial de prendre en compte les réalités et contraintes locales spécifiques à chaque région d'études (Ademe et al. 2024 ; Sales and Parrott 2024).

Bien que la GIRE présente des avantages pour faire face à ces pressions complexes, prédire avec précision leurs impacts demeure un défi de taille, particulièrement dans les régions tropicales. La complexité intrinsèque des systèmes hydrologiques tropicaux, combinée au manque criant de données fiables et à haute résolution dans de nombreuses régions, entrave considérablement la compréhension des processus hydrologiques à toutes les échelles et, par conséquent, la mise en place efficace de la GIRE (Baumann 2011; Sivapalan et al. 2003). En effet, on estime que près de 60% du réseau de stations climatiques dans ces régions ne fournit que des données partielles, obsolètes ou de qualité insuffisante (WMO 2022; Sivapalan et al. 2003), creusant davantage l'écart avec les connaissances acquises en milieu tempéré. Ce manque de données adéquates contraint de nombreux acteurs à recourir à des approches de modélisation, qui sont toutefois basées sur des hypothèses réductrices et une connaissance imparfaite des facteurs qui régissent le fonctionnement précis de ces systèmes complexes (WMO 2022). L'utilisation de telles méthodes simplifiées peut engendrer des erreurs importantes dans les estimations des bilans hydrologiques, aggravant les problèmes de pénurie d'eau et d'inondations auxquels sont déjà confrontées près de 2 milliards de personnes (Ali and Othman 2018).

L'intégration de technologies innovantes, telles que les systèmes basés sur la télédétection, représente une opportunité majeure pour améliorer la couverture des observations hydrométéorologiques (Sun et al. 2018). Ces technologies permettent de collecter des données dans des zones difficiles d'accès ou présentant une faible densité de stations de mesure au sol. Elles offrent également une résolution temporelle et spatiale accrue, favorisant une meilleure compréhension des processus hydrologiques et facilitant une prise de décision plus éclairée en matière de GIRE (Huffman et al. 2020). Actuellement, plusieurs missions ont été entamées, tels que MODIS (*Moderate Resolution Imaging Spectroradiometer*), TRMM (*The Tropical Rainfall Measuring Mission*) et IMERG GPM (*Integrated Multi-satellitE Retrievals for Global Precipitation Measurement Mission*) (Huffman et al. 2020). Cependant, leur fiabilité et leur précision, en particulier pour les données liées au climat, dépendent étroitement de leur validation par des observations au sol. Il est d'ailleurs problématique d'utiliser ces données génériques comme alternatives sans connaître leur niveau de confiance ni identifier les éventuels biais (Mei et al. 2014). Des études ont démontré que le choix des produits satellitaires a un impact significatif sur l'estimation du ruissellement, soulignant la nécessité d'une évaluation rigoureuse à l'aide d'observations in situ préalablement à leur application dans la recherche sur le cycle de l'eau (Van Soesbergen et Mulligan 2018). En somme, bien que prometteuses, ces technologies doivent être utilisées avec précaution et toujours accompagnées de validations appropriées pour garantir leur efficacité dans la gestion des ressources en eau.

Madagascar, une île renommée pour l'immense richesse de ses ressources naturelles, illustre parfaitement les défis complexes liés à la gestion durable de l'eau en milieu tropical (McConnell 2002). Abritant des écosystèmes d'une grande diversité, elle bénéficie de services environnementaux essentiels tels que des réservoirs de biodiversité, des sources d'eau potable, des terres fertiles pour l'agriculture et un potentiel prometteur pour la production d'énergie hydroélectrique (Chaperon et al. 1993; Aldegheri 1972). Cependant, ces services vitaux sont gravement menacés par les pressions conjuguées du changement climatique et de l'expansion rapide des activités humaines, comme les cultures sur

brûlis (Puri and Puri 2022; Hannah et al. 2008; Egashira et al. 2006; Agarwal et al. 2005). La région du Nord-Est malgache est particulièrement vulnérable, subissant des variations notables des régimes de précipitations, ainsi que des assauts fréquents de cyclones dévastateurs et de sécheresses sévères (Puri and Puri 2022; Rabefitia 2008). Ces aléas climatiques extrêmes perturbent fortement la productivité agricole et les moyens de subsistance des populations locales, tout en exacerbant les problèmes d'accès déjà précaire à une eau potable de qualité (CPGU 2012). Cette situation engendre des déséquilibres dans le fonctionnement de la société et fait peser des risques importants sur les perspectives de gestion durable des ressources de la région (CPGU 2012).

En dépit de la mise en place de cadres réglementaires pour une GIRE à Madagascar, leur application efficace se heurte à un cruel manque de données hydrométéorologiques fiables et à une compréhension encore limitée des processus hydrologiques locaux jugés complexes (PNUD 2015; Randriamaherisoa et al. 1993). Cette carence compromet gravement la capacité à modéliser avec précision l'évolution future des ressources en eau de l'île, pourtant cruciales pour assurer son développement durable et préserver ses trésors naturels uniques au monde.

1.2. Aperçu de la thèse

La thèse est structurée en neuf chapitres interdépendants (Figure 1). Le **premier chapitre** sert d'introduction générale à l'étude, établissant le cadre contextuel global. Il aborde également les enjeux spécifiques liés à la mise en place de la GIRE dans les pays tropicaux, en accordant une attention particulière à la situation de Madagascar.

Le chapitre 2 offre une synthèse des connaissances actuelles sur les processus hydrologiques en milieu tropical. Il examine les différentes composantes du cycle de l'eau, les facteurs qui les influencent, ainsi que les diverses projections de scénarios climatiques. S'ensuit une analyse des modèles pluie-débit adaptés aux environnements en mutation. Le chapitre propose ensuite une synthèse des études

hydrologiques menées à Madagascar. Il se termine par l'énoncé des hypothèses et des objectifs de la recherche.

Le chapitre 3 se focalise sur la zone d'étude, débutant par un aperçu de la Grand Ile, puis en affinant l'analyse vers la région SAVA (Nord-Est de Madagascar), pour finalement détailler le bassin versant d'Ankavia et ses sous-bassins. Cette section commence par une exploration approfondie de la topographie, du climat, de la couverture végétale, de la pédologie et des données géologiques de la région, ainsi que du bassin étudié. Pour conclure, le chapitre dresse l'inventaire des instruments de mesure déployés dans le cadre de cette recherche.

Le chapitre 4 analyse la fiabilité de six produits satellitaires de précipitations (largement utilisés en Afrique) sur la base de leur capacité à reproduire les caractéristiques pluviométriques mesurées dans le bassin. Des produits de précipitations maillés à haute résolution spatio-temporelle sont évalués par rapport aux données des 14 pluviographes situés au sol distants de 5-10 km. Le produit le plus performant sera utilisé dans les **chapitres 5, 7 et 8**.

Le chapitre 5 identifie les principaux facteurs régissant le fonctionnement hydrologique du bassin versant. Il vise à comprendre les liens entre différentes caractéristiques du bassin (topographie, morphométrie, couverture végétale, pédologie et géologie) et certaines signatures hydrologiques (dérivées des hydrogrammes), en se basant sur les données de débit mesurées aux quatre stations hydrométriques du bassin d'Ankavia.

Le chapitre 6 traite les effets des occupations du sol sur les réponses hydrologiques à l'échelle des trois micro-bassins spatialement très proches, à couvertures plus ou moins homogènes mais contrastées (cultures, forêts, jachères, pâturages). Cette analyse ciblée permet d'approfondir la compréhension des caractéristiques des écoulements générés par des bassins supposés similaires du point de vue climatique et géologique, mais différents en termes d'occupation des sols et de propriétés pédologiques. Cette approche a pour objectif de réduire l'hétérogénéité des caractéristiques abordées dans le **Chapitre 5**.

Le chapitre 7 explore des méthodes permettant d'estimer de manière économique le débit des cours d'eau dans les environnements tropicaux. Il compare les performances du modèle Soil and Water Assessment Tool (SWAT) en évaluant deux sources de données : les données des pluviomètres au sol, configurés selon différents dispositifs (un, deux ou cinq pluviomètres), et les données de télédétection jugées performantes dans le **chapitre 4**. Il s'agit également d'évaluer la fiabilité des produits satellitaires de précipitation sur les observatoires hydrologiques.

Le chapitre 8 examine les impacts à moyen et long terme des changements d'occupation des sols et/ou climatiques, individuellement et combinés, sur les processus hydrologiques, tout en analysant leurs altérations. Les processus hydrologiques sont modélisés en utilisant le même modèle pluie-débit que celui présenté dans le **chapitre 7**. À partir des paramètres générés lors de la construction du modèle, celui-ci est utilisé pour simuler les réponses hydrologiques passées (2001-2021) ainsi que futures à moyen terme (2040-2060) et à long terme (2080-2100), en prenant en compte les changements d'occupation des sols et/ou du climat (températures et précipitations). Les altérations hydrologiques sont évaluées à l'aide de quelques signatures hydrologiques couramment utilisées.

Finalement**, le chapitre 9** expose les discussions et conclusions générales, les contributions scientifiques, les limitations, les forces ainsi que les recommandations pour les recherches futures.

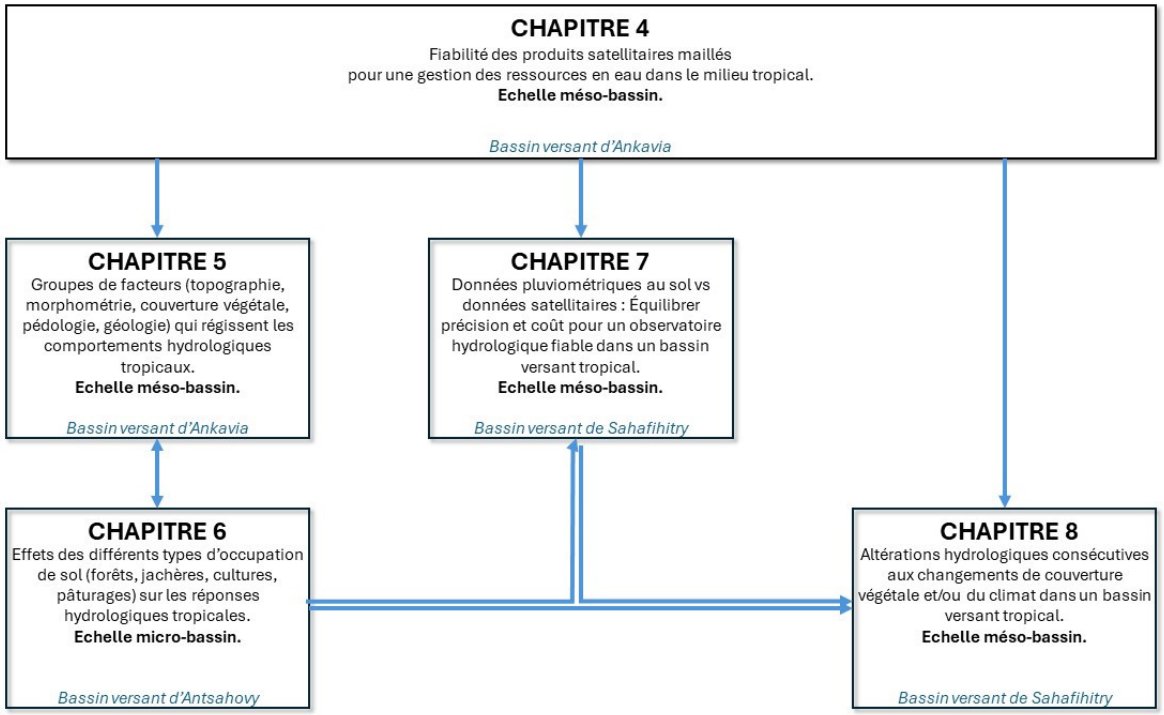

Figure 1. Principaux cheminements de la thèse : titre de chaque chapitre et les échelles d'études.

2. Chapitre 2 : Etat de l'art

Cette section examine les processus hydrologiques à l'échelle du bassin versant, en mettant l'accent sur le fonctionnement des systèmes hydrologiques en climat tropical en général, et en milieu tropical humide en particulier. Elle présente également les modèles hydrologiques adaptés pour caractériser les milieux tropicaux tout en tenant compte des changements environnementaux. L'analyse se poursuit par un aperçu des recherches hydrologiques menées à Madagascar, illustrant les défis et les opportunités spécifiques à ce contexte insulaire tropical.

2.1. Rappel théorique du cycle hydrologique d'un bassin versant

2.1.1. Bassin versant et son fonctionnement

En introduction, deux concepts clés sont définis : le bassin versant et son fonctionnement hydrologique. En sciences de l'eau, un bassin versant est une zone géographique délimitée par une ligne de partage des eaux, où les eaux de surface (ruissellement) convergent vers un exutoire commun, généralement un cours d'eau, un lac ou un océan (Figure 2.1) (Musy 2004). La ligne de crête topographique est généralement considérée comme la limite du bassin versant, ce qui est également le cas dans ce mémoire.

Il convient de souligner que l'écoulement des eaux souterraines (nappes phréatiques) ne suit pas toujours les mêmes chemins que les eaux de surface et peut traverser les limites du bassin versant topographique. Néanmoins, malgré la possibilité d'infiltration et de transfert souterrain de l'eau vers d'autres bassins, la définition du bassin versant basée sur la topographie demeure privilégiée pour sa praticité dans l'étude des flux d'eau de surface.

Selon l'emplacement de l'exutoire, la taille d'un bassin versant peut varier considérablement, allant de quelques hectares à des milliers de km². On distingue généralement trois échelles spatiales : (i) l'échelle macro, désignant les très grands bassins versants couvrant plus de 20 000 km² ; (ii) l'échelle micro, concernant les

petits bassins de moins de 50 km², (iii) l'échelle méso, intermédiaire entre les deux, englobant les bassins de taille moyenne allant de 50 km² à 20 000 km² (FAO et UNEP 2020).

Ainsi, le fonctionnement hydrologique d'un bassin versant est caractérisé par des processus ou des combinaisons de processus dominants qui varient dans l'espace (selon les caractéristiques du milieu) et dans le temps (selon les saisons et les événements météorologiques). Déterminer ce fonctionnement consiste à associer ces processus dominants à des compartiments spécifiques du bassin versant (sols, végétation, aquifères, etc.), en tenant compte des caractéristiques du milieu (topographie, géologie, climat, etc.) et de leurs périodes d'occurrence (Musy 2004).

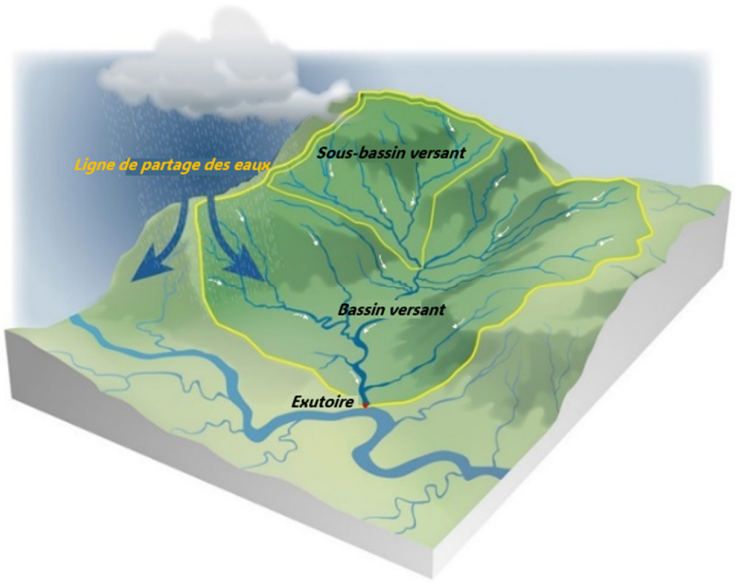

Figure 2. 1. Schéma d'un bassin versant et d'un sous-bassin versant avec leurs exutoires et les lignes de partage des eaux. Source : adaptée à partir de Charlton (2008).

2.1.2. Processus hydrologique à l'échelle du bassin versant

Le cycle hydrologique décrit le mouvement perpétuel de l'eau dans l'environnement, transitant entre différents réservoirs terrestres, atmosphériques et souterrains. À l'échelle d'un bassin versant, ce cycle prend une forme plus détaillée et complexe, impliquant de multiples processus hydrologiques interdépendants. Cette échelle permet de comprendre la répartition et les chemins empruntés par les précipitations tombant sur cette zone, depuis leur arrivée jusqu'à leur sortie à l'exutoire du bassin. De manière simplifiée, le processus peut se décomposer comme suit (Figure 2.2).

Avec
- P : les précipitations ;
- E_I : l'interception ;
- ET : l'évapotranspiration ;
- I : l'infiltration ;
- OF : le ruissellement de surface (*Surface Runoff – Overland Flow*) ;
- SSF : les écoulements hypodermiques (*Subsurface flow*) ;
- Q : le ruissellement total (*Total runoff*) ;
- W_S : le stock d'eau du sol (*Soil water storage*) ;
- W_{SA} : le stock de la nappe superficielle (*Shallow Aquifer*) ;
- W_{DA} : le stock de la nappe profonde (*Deep Aquifer*) ;
- D : le drainage profond (*Deep percolation*) ;
- B : le drainage latéral de la nappe ou débit de base (*Baseflow*) ;
- O_{SA} : les pertes latérales de la nappe superficielle (*Outflows*) ;
- I_{DA} : les apports amont de la nappe profonde (*Inflows*) ;
- O_{DA} : les pertes latérales de la nappe profonde.

Le bilan hydrique peut être modélisé par des équations différentielles représentant la conservation de la masse, de l'énergie ou de la quantité de mouvement.

- En surface $\Delta W_S/\Delta t = P - E_I - ET - OF - SSF - I$ (2.1)
- Dans l'aquifère superficiel $\Delta W_{SA}/\Delta t = I - B - O_{SA} - D$ (2.2)
- Dans l'aquifère profond $\Delta W_{DA}/\Delta t = D + I_{DA} - O_{DA}$ (2.3)

Les processus mentionnés ci-dessus sont décrits en détail dans les sections suivantes.

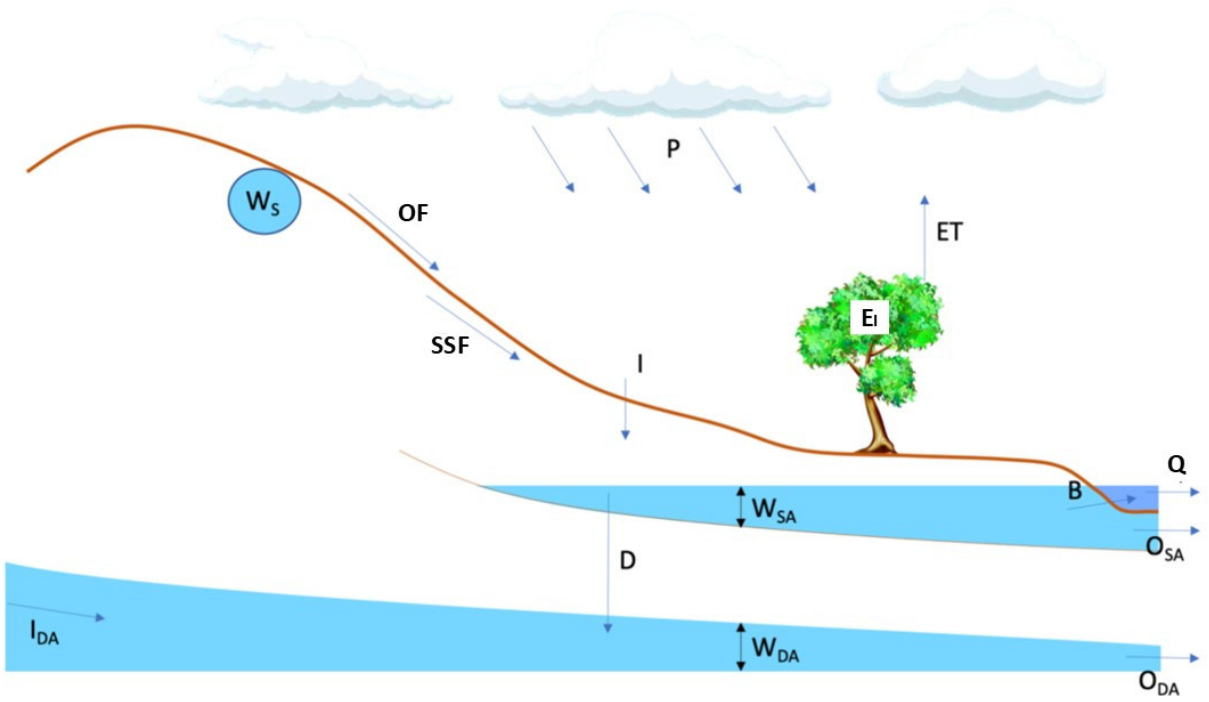

Figure 2. 2. Principaux processus hydrologiques au sein d'un bassin versant. Source : modifiée à partir de Charlier, 2007.

2.1.2.1. Précipitations

Les précipitations (**P**) constituent l'apport principal d'eau dans le cycle hydrologique, se présentant sous forme liquide (bruine, pluie, averse), solide (neige, grésil, grêle), ou occulte (rosée, gelée blanche, givre). Quantifiées par leur intensité (mm h^{-1}) et leur hauteur (mm), les précipitations liquides sont mesurées principalement par des pluviomètres et pluviographes.

Pour estimer les précipitations sur l'ensemble d'un bassin versant à partir de mesures ponctuelles, une interpolation spatiale est souvent nécessaire. Une méthode couramment utilisée est celle des polygones de Thiessen. Cette méthode consiste à associer chaque pluviomètre à une zone représentative, délimitée par les médiatrices des lignes reliant les pluviomètres adjacents. La moyenne spatiale des précipitations est alors calculée en pondérant les mesures de chaque pluviomètre par la surface de son polygone correspondant.

$$P = \sum_{i=1}^{n} ri \frac{ai}{A} \tag{2.4}$$

Où r_i représente les précipitations au pluviomètre i, a_i est la superficie du polygone entourant le pluviomètre i, et A la surface totale du bassin versant. Le terme (a_i/A) désigne la proportion du bassin versant occupée par un polygone donné, aussi appelé coefficient de Thiessen (Figure 2.3).

La télédétection, via radars météorologiques et satellites, a révolutionné également la mesure des précipitations en permettant une observation à grande échelle (Kidd et Levizzani 2011). Les radars météorologiques fournissent des données à haute résolution sur les précipitations locales, comme le réseau ARAMIS (Application Radar à la Météorologie Infra-Synoptique) en France qui permet de détecter les pluies intenses et les orages (Tabary et al. 2012). Les satellites, tels que le Global Precipitation Measurement (GPM) de la NASA et de la JAXA, permettent aussi une observation globale des systèmes météorologiques, couvrant près de 90% de la surface terrestre (Hou et al. 2014).

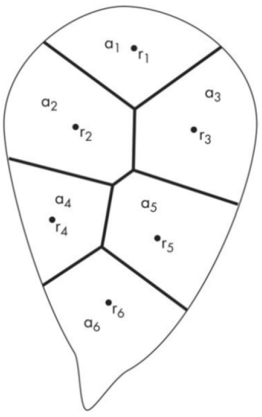

Figure 2. 3. Polygones de Thiessen pour une série de pluviomètres (r_i) dans un bassin versant imaginaire où a_i est la superficie de chaque polygone ; les emplacements des pluviomètres sont indiqués par des points noirs.

2.1.2.2. Interception/ stockage dans les dépressions

Les précipitations, qu'elles soient sous forme de pluie dans les climats tropicaux ou de neige dans les régions tempérées, subissent une redistribution complexe lors de leur chute, notamment en présence de végétation. Une partie est interceptée (**E_I**) par le couvert végétal. Par la suite, l'eau qui n'est pas interceptée atteint le sol, où elle peut être stockée temporairement dans les micro-dépressions du terrain. La quantité d'eau retenue dépend de la topographie du sol, de sa rugosité et de l'intensité des précipitations, qui peuvent être particulièrement intenses dans les milieux tropicaux pendant la saison des pluies. Bien que ces processus soient parfois négligés dans certains modèles hydrologiques simplifiés, leur prise en compte est cruciale pour une modélisation précise du cycle de l'eau, particulièrement à l'échelle du bassin versant (Savenije 2004).

2.1.2.3. Evaporation/Evapotranspiration

L'évaporation se définit comme le passage de l'eau de l'état liquide à l'état gazeux. Ce phénomène, principalement régi par la radiation solaire, concerne essentiellement les plans d'eau et la couverture végétale, mais aussi les surfaces de sol nu (Allen et al. 1998). Le concept d'évapotranspiration (**ET**), englobant à la fois l'évaporation et la transpiration des plantes, se décline en plusieurs types principaux : l'évapotranspiration réelle (ETR) qui représente la somme effective des quantités de vapeur d'eau évaporées par le sol et transpirées par les plantes dans des conditions spécifiques d'humidité du sol et de développement végétal (Rana et Katerji 2000) ; l'évapotranspiration potentielle (ETP) qui représente la demande évaporative maximale de l'atmosphère pour un couvert végétal donné dans des conditions d'alimentation en eau non limitantes, et l'évapotranspiration de référence (ET_0) qui mesure la demande évaporative de l'atmosphère pour un couvert végétal de référence standardisé (généralement du gazon ou de la luzerne) bien alimenté en eau. Cette dernière est utilisée comme référence pour estimer l'ET d'autres cultures (FAO, 1998). L'ET_0 peut être estimée en utilisant l'équation de Penman-Monteith (Equation 2.5).

$$\mathrm{ET0} = \frac{0.408\Delta\,(Rn - Rg) + \gamma\,\frac{900}{T+273}\,u\,\delta e}{\Delta + \gamma(1 + 0.34u)} \qquad (2.5)$$

avec ET_0 : evapotranspiration de référence [mm]

Rn : rayonnement net à la surface du couvert végétal [MJ m^{-2} $jour^{-1}$]

Rg : densité de flux thermique du sol [MJ m^{-2} $jour^{-1}$]

T : température moyenne journalière de l'air à 2 m de hauteur [°C]

u : vitesse du vent à 2 m de hauteur [m s^{-1}]

δe : déficit de pression de vapeur saturante [kPa]

Δ : pente de la courbe de pression de vapeur [kPa $°C^{-1}$]

γ : constante psychométrique [kPa $°C^{-1}$]

2.1.2.4. Infiltration/ Percolation

L'infiltration (**I**) désigne le mouvement de l'eau pénétrant dans les couches superficielles du sol sous l'action de la gravité et des effets de pression matricielle et hydrostatique. Ce phénomène, distinct de la percolation qui concerne l'infiltration profonde vers la nappe phréatique, est crucial pour le renouvellement des réserves d'eau du sol et des aquifères (Beven 2004). Le taux d'infiltration, exprimé en mm h^{-1} ou m^3 m^{-2} s^{-1}, représente la quantité d'eau s'infiltrant par unité de temps à un instant donné (i(t) ; Equation 2.6), tandis que la capacité d'infiltration ou infiltrabilité définit le taux potentiel d'infiltration dans des conditions données (en général pour un sol saturé en régime permanent) (Figure 2.4). L'infiltration cumulative, intégrale temporelle du régime d'infiltration, quantifie le volume total d'eau infiltrée sur une période spécifique (Hillel & Debacker 1988). Plusieurs facteurs influencent ce processus, notamment les propriétés du sol (structure, texture, porosité), la compaction de surface, la couverture végétale, la topographie, l'intensité des précipitations et l'humidité initiale du sol. La végétation, en particulier, joue un rôle positif en ralentissant l'écoulement superficiel et en améliorant la perméabilité du sol via le système racinaire (Beven et Germann 2013).

$$I(t) = \int_{t=t0}^{t} i(t)dt \qquad (2.6)$$

avec I(t) : infiltration cumulative au temps t [mm]

i(t) : régime ou taux d'infiltration au temps t [mm h^{-1}]

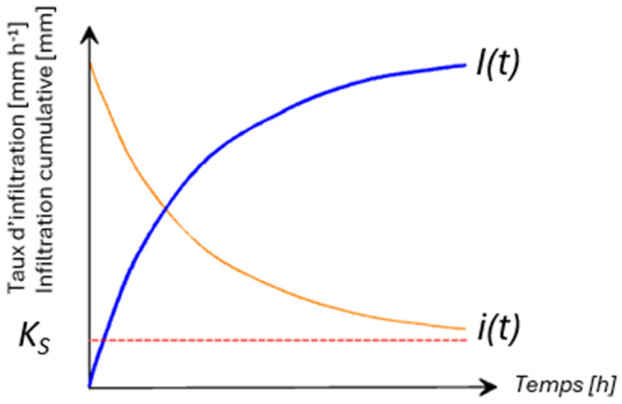

Figure 2. 4. Evolution générale du régime d'infiltration et de l'infiltration cumulative au cours du temps (Ks = conductivité hydraulique à saturation). Source : Musy, 2004.

2.1.2.5. Ecoulements

Les écoulements hydrologiques se caractérisent par une grande diversité, se répartissant principalement entre écoulements rapides et lents. Les écoulements rapides, cruciaux pour la formation des crues, comprennent le ruissellement de surface **OF** et l'écoulement de subsurface ou hypodermique **SSF**. Les écoulements lents, quant à eux, comprennent principalement l'écoulement souterrain ou de base **B**, qui conditionne le débit des cours d'eau en période d'étiage.

Ecoulements de surface

Les cours d'eau sont alimentés par diverses sources, notamment les précipitations (**P**) tombant directement sur leur surface libre (**CP**). Toutefois, une part significative de l'apport en eau provient du ruissellement, qui se manifeste sous deux formes principales (Figure 2.5). (1) Le ruissellement hortonien (**HOF**), décrit par Horton (1932), se produit lorsque l'intensité des précipitations dépasse la capacité d'infiltration du sol, un phénomène particulièrement fréquent dans les régions semi-arides ou lors de fortes pluies. (2) Le ruissellement sur surfaces saturées (**SOF**),

identifié par Dunne et Black (1970), survient quand le sol atteint sa capacité maximale de stockage et de transmission latérale d'eau. Ce type de ruissellement est courant dans les zones de convergence topographique ou sur les sols peu profonds, où même des précipitations de faible intensité peuvent générer un écoulement important. Ces deux mécanismes contribuent significativement à l'alimentation des cours d'eau, leur importance relative variant selon les caractéristiques du terrain, le type de sol et les conditions climatiques locales.

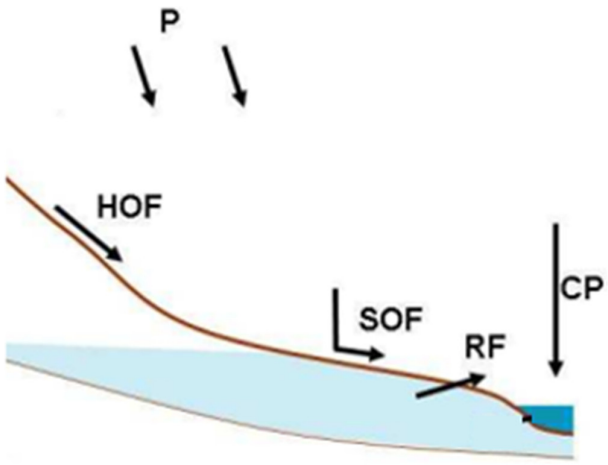

Figure 2. 5. Processus hydrologiques de surface (modifiée à partir de Charlier, 2007).

*Avec **P** les précipitations, **HOF** le ruissellement hortonien (Horton Overland Flow), **SOF** le ruissellement de surface saturée (Saturated Overland Flow), **RF** l'exfiltration (Return Flow, voir section suivante), **CP** la précipitation directe (Channel Precipitation)*

Ecoulements hypodermiques

L'écoulement de subsurface (**SSF**), ou hypodermique implique le mouvement quasi-horizontal de l'eau dans les couches supérieures du sol, contribuant rapidement au gonflement des crues (Whipkey 1978) (Figure 2.6). L'importance de l'écoulement de subsurface dépend largement de la structure du sol, notamment de la présence de macropores et de la conductivité hydraulique latérale. Les macropores, définis comme des pores où les phénomènes de capillarité sont négligeables, peuvent être d'origine biologique (faune du sol, racines), physique (fissures) ou anthropique (pratiques culturales) (Beven et Germann 1982). Leur présence peut accélérer significativement l'infiltration et le drainage du sol. D'autres mécanismes, tels que l'effet piston, l'intumescence de la nappe et l'écoulement de retour (**RF**) (Figure 2.5), contribuent également à la complexité des processus hydrologiques de subsurface (Sklash et Farvolden 1979).

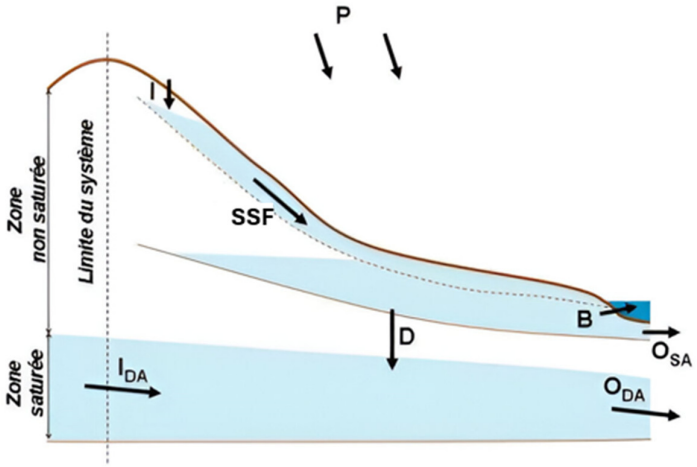

Figure 2. 6. Processus hydrologique de subsurface et souterrain (modifiée à partir de Charlier, 2007).

*Avec **P** les précipitations, **I** l'infiltration, **SSF** les écoulements hypodermiques (Subsurface flow), **B** le drainage latéral ou débit de base (Baseflow), O_{SA} les pertes latérales de la nappe superficielle (Outflows), **D** le drainage profond (Deep percolation), I_{DA} les apports amont de la nappe profond (Inflows), O_{DA} les pertes latérales de la nappe profonde*

Ecoulements souterrains

L'écoulement souterrain, également connu sous le nom d'écoulement de base, nécessite la présence d'une nappe phréatique. Celle-ci est alimentée par l'infiltration (**I**) jusqu'à la nappe phréatique, tandis que les percolations profondes (**D**) alimentent exclusivement les aquifères plus profonds (Figure 2.2 et Figure 2.6) (Freeze et Cherry 1979). L'importance de cet apport dépend de plusieurs facteurs, notamment la structure et la géologie du sous-sol, ainsi que le volume des précipitations. Une fois dans l'aquifère, l'eau transite à des densités de flux variables, allant de quelques mètres par jour à quelques millimètres par an, avant de rejoindre le cours d'eau, souvent par résurgence (Sophocleous 2002). En raison de ces faibles vitesses, l'écoulement de base (**B**) ne contribue généralement que faiblement aux débits de crue, mais joue un rôle essentiel dans le maintien des débits d'étiage et l'alimentation des rivières en période sèche. Cependant, la contribution de l'eau souterraine à l'écoulement total peut varier considérablement selon les conditions hydrogéologiques et climatiques. Dans certains cas, notamment dans les régions semi-arides à arides, la nappe peut être déconnectée du cours d'eau, voire drainer celui-ci (Winter 2000).

2.1.2.6. Synthèse de genèse de crue

Dans sa synthèse des processus hydrologiques, Dunne (1983) propose une analyse approfondie des mécanismes en jeu lors des épisodes pluvieux, en les associant aux conditions pédoclimatiques et géomorphologiques (Figure 2.7). Son travail met en lumière un continuum de processus entre deux extrêmes : d'un côté, le milieu aride ou semi-aride, dominé par le ruissellement Hortonien (**HOF**) et principalement contrôlé par les états de surface ; de l'autre, le milieu humide, caractérisé par le ruissellement sur surfaces saturées (**SOF**) et le ruissellement de subsurface (**SSF**), où la dynamique interne du sol prédomine.

À l'échelle du micro-bassin, plusieurs déterminants clés des processus hydrologiques émergent : la structure du couvert végétal influence la répartition spatiale de la pluie au sol ; les états de surface conditionnent le partage entre ruissellement et infiltration, contrôlant ainsi le processus hortonien ; la topographie et les propriétés hydrodynamiques du profil superficiel régissent les processus souterrains; enfin, les propriétés hydrodynamiques souterraines et la géométrie des dépôts déterminent les processus de recharge et les écoulements de nappe.

Dans le cas des grands bassins versants, la complexité s'accroît avec l'hétérogénéité spatiale et temporelle des processus. Selon Blöschl et al. (2007), l'échelle spatiale influence significativement la dominance relative des différents processus hydrologiques. Par exemple, l'importance du stockage dans les plaines d'inondation et les interactions entre les eaux de surface et les eaux souterraines augmentent avec la taille du bassin (Sophocleous 2002). De plus, la variabilité climatique à grande échelle peut entraîner des réponses hydrologiques non linéaires et des effets de seuil, comme l'ont démontré Eltahir et Yeh (1999) dans leur étude sur les grands bassins fluviaux. Cette analyse souligne la complexité des interactions entre les facteurs environnementaux et les processus hydrologiques à différentes échelles, mettant en évidence la nécessité d'une approche intégrée et multi-échelle dans l'étude des bassins versants.

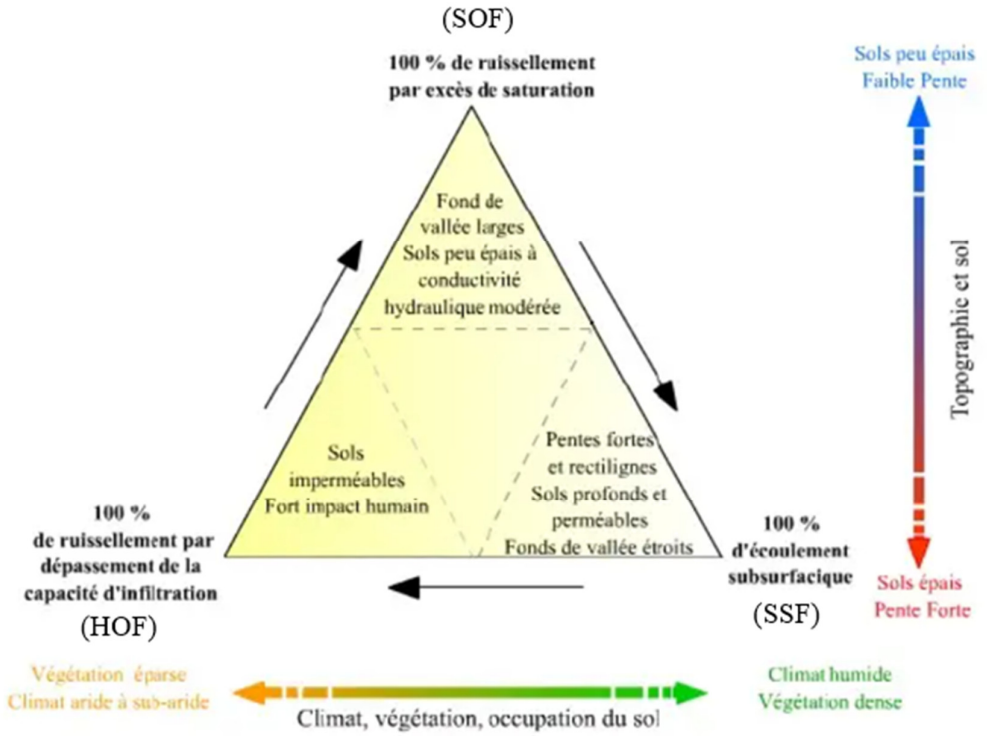

Figure 2. 7. Représentation des différents processus de génération de l'écoulement en fonction du milieu naturel (D'après Dunne, 1983).

2.2. Spécificités du contexte tropical

2.2.1. Les milieux tropicaux

Les milieux tropicaux correspondent à la zone s'étendant entre les deux tropiques, le Tropique du Cancer (23°26' N) et le Tropique du Capricorne (23°26' S) (Baumann 2011). Cette ceinture intertropicale, située de part et d'autre de l'équateur, se caractérise par un climat chaud où les températures moyennes dépassent 18°C toute l'année (Koppen 1936). On y distingue trois grands types de climats tropicaux : le climat tropical humide, aussi appelé climat de forêt équatoriale humide (Af), le climat de mousson tropicale (Am) et le climat tropical de savane (Aw) (Figure 2.8). L'humidité varie selon le type de climat tropical. Les climats tropicaux humides (ou équatoriaux) se caractérisent par d'importantes précipitations tout au long de l'année. En revanche, les climats tropicaux de savane ainsi que les climats de mousson tropicale connaissent des variations saisonnières marquées des régimes pluviométriques.

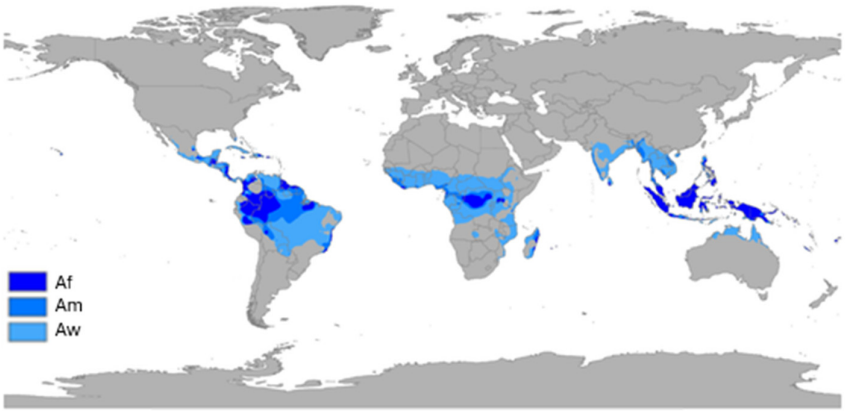

Figure 2. 8. Climats tropicaux selon Koppen (1936) : climat tropical humide (Af), la mousson tropicale (Am) et le climat tropical de savane (Aw).

Le contrôle climatique le plus important pour les types de climat tropical est lié à la position de la zone de convergence intertropicale (ZCIT) (Figure 2.9). La ZCIT est une

zone de basse pression qui marque le point de convergence des vents alizés. Ces deux caractéristiques en font un élément essentiel de la circulation atmosphérique et lui confèrent un rôle crucial dans la formation de la cellule de Hadley (Baumann 2011). Bien qu'elle reste proche de l'équateur, la ZCIT sur les terres s'écarte plus au nord ou au sud que celle sur les océans, en raison des variations plus importantes des températures terrestres. Son emplacement peut varier jusqu'à 40° à 45° de latitude au nord ou au sud de l'équateur, selon la configuration des terres et des océans. Malgré ces variations, elle est étroitement liée à la position du soleil et marque généralement la zone où le soleil est au zénith. Aux latitudes tropicales, c'est elle qui est responsable de la migration des basses pressions et des changements saisonniers des pluies tropicales.

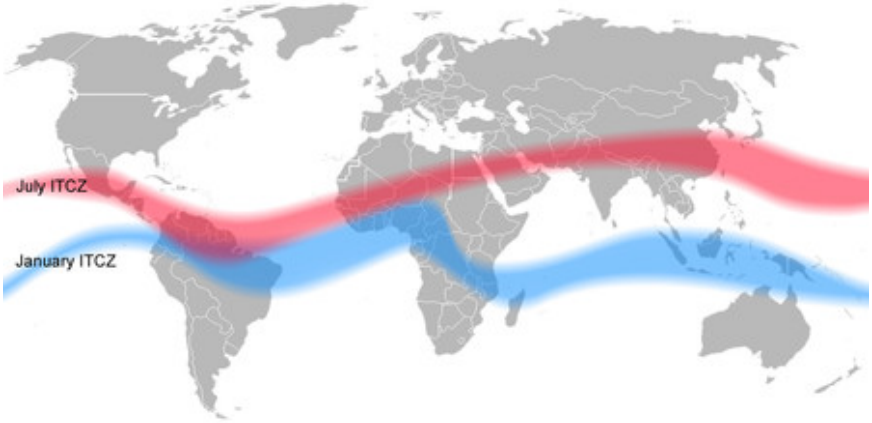

Figure 2. 9. Position de la Zone de Convergence Inter Tropicale (ZCIT) en fonction des saisons. Source : Baumman, 2011.

Après cette mise en contexte nécessaire du milieu tropical, il convient de se concentrer sur le sujet central de ce mémoire : les milieux tropicaux humides, qui caractérisent la zone d'étude de ce travail.

2.2.2. Caractéristiques générales des climats tropicaux humides

Le climat tropical humide (Af), est un type de climat intertropical que l'on trouve principalement autour de l'Équateur (Figure 2.8). Outre les caractéristiques communes aux climats tropicaux (température moyenne annuelle supérieure à 18°C, précipitations annuelles dépassant 2 000 mm), ce climat se différencie par l'absence de véritable saison sèche : les précipitations mensuelles restent supérieures à 60 mm même durant les mois les moins pluvieux (Koppen 1936). Ces conditions climatiques spécifiques favorisent le développement d'une végétation luxuriante, en particulier des forêts tropicales humides, et contribuent à la formation de sols évolués caractérisés par une forte perméabilité (Tan et al. 2019).

2.2.3. Processus hydrologiques en milieu tropical humide

2.2.3.1. Précipitations

Dans les milieux tropicaux humides, les précipitations (**P**) présentent des caractéristiques particulières. Tan et al. (2019) soulignent l'importance des processus convectifs dans ces zones, engendrant des averses intenses presque quotidiennes, particulièrement en fin d'après-midi. De plus, comme l'expliquent Sun (2024), l'humidité atmosphérique constamment élevée favorise la formation rapide de nuages et de précipitations. Bien que moins marquée que dans d'autres régions tropicales, une certaine variabilité saisonnière existe, influencée par des phénomènes climatiques à grande échelle tels qu'El Niño (Cai et al. 2020).

Les régions tropicales en général, et les régions tropicales humides en particulier souffrent toutefois d'une pénurie d'installations de suivi pluviométrique. Comparées aux zones tempérées, elles disposent d’un réseau moins dense de stations météorologiques et de radars pluviométriques, comme le montre la distribution mondiale des stations synoptiques (Figure 2.10). Cette faible densité entraîne la rareté, voire une absence, de rapports synoptiques fiables dans ces zones.

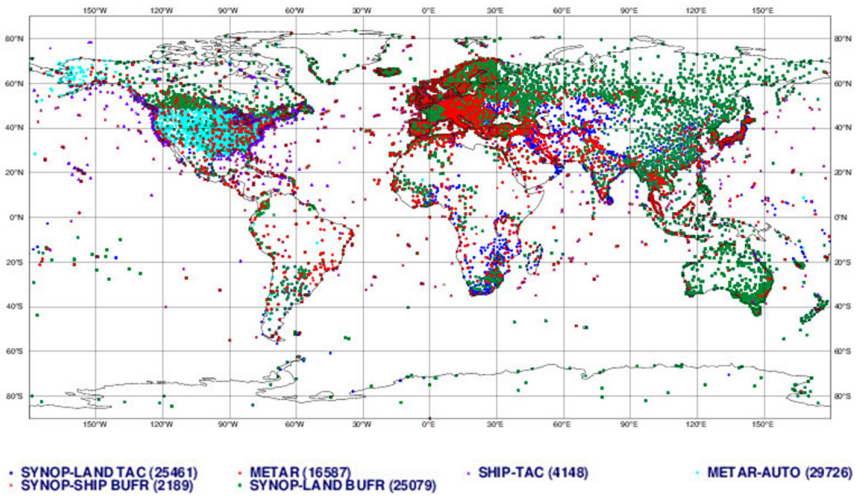

Figure 2. 10. Distribution mondiale des stations synoptiques. Source : WMO, 2022.

Face à ce défi, les estimations de précipitations par satellite sont devenues une alternative précieuse pour les pays tropicaux (Sun et al. 2018). Ces produits, parmi tant d'autres, offrent une couverture spatiale étendue et une résolution temporelle fine, comblant ainsi les lacunes des réseaux d'observation au sol. Plusieurs produits satellitaires et de réanalyse ont été développés et utilisés avec succès dans les études hydrologiques en milieu tropical. Le tableau 2.1 ci-dessous présente un aperçu des principaux produits utilisés, leurs caractéristiques, ainsi que leurs références. Ces produits ont permis d'améliorer considérablement notre compréhension des régimes de précipitations dans les régions tropicales. Par exemple, le TRMM (Tropical Rainfall Measuring Mission) et son successeur GPM (Global Precipitation Measurement) ont fourni des données précieuses sur la structure verticale des précipitations et la distribution des systèmes convectifs dans les tropiques (Kidd et al. 2017). Les produits de réanalyse comme ERA5 intègrent des observations satellitaires et au sol avec des modèles numériques, offrant une représentation cohérente de l'atmosphère sur de longues périodes.

Table 2. 1. Produits satellitaires fréquemment utilisés pour étudier les caractéristiques des climats tropicaux.

Produit	Nom complet	Couverture spatiale	Résolution spatiale	Résolution temporelle	Références
TRMM 3B42	Tropical Rainfall Measuring Mission 3B42	50°N – 50°S	0.25° x 0.25°	3 heures	Huffman et al. (2007)
GPM IMERG	Global Precipitation Measurement Integrated Multi-satellitE Retrievals for GPM	60°N – 60°S	0.1° x 0.1°	30 minutes	Huffman et al. (2020)
PERSIANN-CDR	Precipitation Estimation from Remotely Sensed Information using Artificial Neural Networks – Climate Data Record	60°N – 60°S	0.25° x 0.25°	Quotidien	Ashouri et al. (2015)
CHIRPS	Climate Hazards Group InfraRed Precipitation with Station data	50°N – 50°S	0.05° x 0.05°	Quotidien	Funk et al. (2015)
ERA5	ECMWF Reanalysis v5	Global	0.25° x 0.25°	Horaire	Hersbach et al. (2020)
MSWEP	Multi-Source Weighted-Ensemble Precipitation	Global	0.1° x 0.1°	3 heures	Beck et al. (2019b)

2.2.3.2. Processus hydrologiques influencés par le couvert végétal

Interception et redistribution des précipitations

L'interception (**E_I**) et la redistribution de la pluie par le couvert végétal varient considérablement selon le type de végétation et les conditions climatiques. Une revue récente par Carlyle-Moses et al. (2018) montre que l'interception en zone tropicale humide peut représenter entre 5 et 60% de la pluie totale, selon la structure de la végétation.

Les forêts tropicales, avec leur surface foliaire importante et leur canopée dense, sont particulièrement efficaces dans l'interception des précipitations et peut atteindre jusqu'à 60% de la pluie incidente annuelle, soit environ 2000 mm an^{-1} dans certains cas (Teale et al. 2014). D'autres types de couvertures végétales comme les jachères ont aussi fait l'objet d'études récentes en raison de leur importance dans les systèmes agricoles tropicaux. Awessou et al. (2017) ont étudié l'interception dans différents types de jachères en Afrique de l'Ouest et ont constaté qu'elle variait entre 5 et 20% de la pluie totale, selon l'âge et la composition de la jachère. Dans les savanes et les prairies, l'interception est généralement plus faible que dans les forêts, mais reste significative. Une étude de Wang et al. (2012) dans une savane semi-aride a montré que l'interception par la strate herbacée pouvait atteindre 15% de la pluie annuelle. Les cultures agricoles présentent également des taux d'interception variables. Une étude de Wang et al. (2024) sur des cultures de maïs en Chine a montré que l'interception pouvait atteindre jusqu'à 30% de la pluie totale pendant la période de croissance maximale. Pour les cultures en rangs comme le soja, ils ont rapporté des taux d'interception allant de 10 à 25% selon le stade de croissance.

Evapotranspiration

L'évapotranspiration (**ET**), qui combine l'évaporation de l'eau du sol et la transpiration des plantes, représente une part considérable des précipitations annuelles, allant de 50% à 80% (Gentine et al. 2019). La transpiration constitue la

composante principale de l'ET, pouvant atteindre jusqu'à 70% du total dans les forêts tropicales (Schlesinger et Jasechko 2014). Par ailleurs, l'évaporation directe de l'eau interceptée par la canopée n'est pas négligeable, comptant pour 10% à 20% des précipitations annuelles (Benzaghta et al. 2012). L'ET n'est pas constante et varie selon les conditions locales. En effet, elle peut diminuer significativement pendant les périodes de sécheresse.

2.2.3.3. Processus d'écoulement à l'échelle des micro-bassins

Elsenbeer (2001) a proposé une classification des types d'écoulement d'eau en forêt tropicale basée sur deux types de sols évolués : les acrisols et les ferrasols, selon la classification WRB (World Reference Base for Soil Resources). Les acrisols sont des sols acides caractérisés par une accumulation d'argile dans le sous-sol et un faible capacité d'échange cationique, tandis que les ferrasols sont des sols tropicaux profondément altérés, riches en oxydes de fer et d'aluminium, avec une structure grumeleuse stable. Cette typologie a été par la suite affinée et élargie à d'autres types de sols tropicaux (Negishi et al. 2007; Bonell 2005) (Figure 2.11, Table 2.2). Dans ce cadre, les acrisols favorisent les écoulements latéraux de subsurface (**SSF**), tandis que les ferralsols privilégient les écoulements verticaux de percolation. Cette classification demeure une généralisation, et que les processus hydrologiques peuvent varier de manière significative en fonction du type de couvert végétal, de la topographie et des propriétés locales du sol (Zimmermann et Elsenbeer 2009).

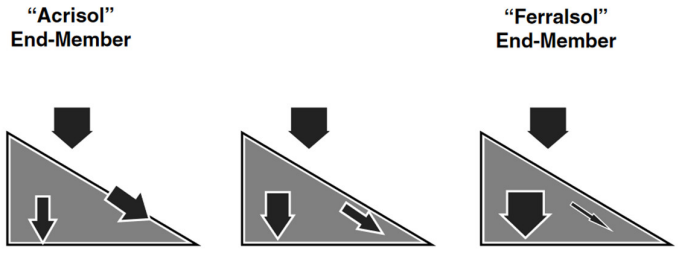

Figure 2. 11. Le spectre des cheminements hydrologiques dans les forêts tropicales humides (d'après Elsenbeer, 2001).

Par ailleurs, au-delà des forêts tropicales, d'autres écosystèmes et occupations du sol présentent des dynamiques hydrologiques distinctes. Les savanes arborées sont souvent caractérisées par une combinaison de **SSF** et de **SOF**, avec une tendance au **HOF** pendant les précipitations intenses en raison de la couverture herbacée discontinue (Bonell and Williams 1986). Les prairies tropicales ont une tendance au **SOF** dans les zones de bas-fond, avec une occurrence possible de **HOF** sur les sols compactés ou pendant les événements pluvieux intenses (Zimmermann et al. 2006). Les mangroves sont dominées par **SOF** en raison de la proximité de la nappe phréatique et des inondations tidales régulières (Furukawa et al. 1997). Dans les zones agricoles, les processus peuvent varier selon les pratiques, présentant tous les types d'écoulement : le labour peut favoriser le **HOF**, tandis que l'irrigation peut conduire à **SOF**, et **SSF** peut être important dans les systèmes agroforestiers (Bruijnzeel 2004). Enfin, les zones de déforestation récente ont tendance à passer de **SSF** dominant à **HOF** dominant, en raison de la compaction du sol et de la perte de couverture végétale (Giertz et al. 2005).

2.2.3.4. Processus d'écoulement à l'échelle des méso et macro-bassins

À l'échelle méso et macro, les processus hydrologiques en milieu tropical humide se révèlent particulièrement complexes. Ils englobent notamment la réinfiltration du ruissellement de surface sur les versants, la formation de nappes perchées temporaires, ainsi qu'une contribution significative des écoulements de subsurface (**SSF**) et du ruissellement sur surfaces saturées (**SOF**) dans la génération des crues. Comme l'ont souligné Bonell (2005); Levia et al. (2020), ces processus sont fortement influencés par les caractéristiques spécifiques du bassin versant, telles que la géologie, les sols, la végétation, ainsi que par l'intensité et la distribution des précipitations. Bien que la compréhension de ces mécanismes hydrologiques en milieu tropical humide ait considérablement progressé ces dernières années, des zones d'ombre persistent. Kayitesi et al. (2022) et Wohl et al. (2012) ont notamment mis en évidence les incertitudes qui subsistent quant à l'impact des changements d'utilisation des terres et du changement climatique sur ces processus.

Table 2. 2. Comparaison de bilans hydrologiques annuels et des principaux processus pour des micro-bassins tropicaux avec un sol perméable, modifié à partir de Charlier, 2007.

Sites	Surface	Végétation	Sol[a]	K_s de surface	Horizon limitant la percolation	P[b]	ET/P	Q/P	ΔW/P	D/P	Principaux processus de crue	OF/P annuel[c]	OF/P crue[c]	Auteurs
	[ha]	[-]	[-]	[mm h^{-1}]	[-]	[mm]	[%]	[%]	[%]	[%]		[%]	[%]	
Amazonie péruvienne	2.5	Culture sur brûlis (1ère année)	Acrisol	35-95	oui	2800	35	60	1	4	HOF et SOF	3	05 -12	Alegre and Cassel (1996)
Vietnam du Nord	3.1	Culture sur brûlis (2ème année)	Acrisol	103	non	1800					HOF			Ziegler (2004)
Indonésie (Kali Mondo)	19	Eucalyptus	Andosol	955	selon la profondeur du substratum	4668	26.1	74.1	-0.2	0	SSF (<7.7%), HOF sur chemins (0.9%), CP (1.3%)	4.7	1.7 - 8	Bruijnzeel (1983)
Malaisie (Bornéo)	308	Jungle vierge	Ultisol	1500	non	2500		1			SSF			Nainar et al. (2017)
Brésil (Amazonie)	93	Forêt primaire	Oxisol		non	1190	46	48	0.03		SOF		12	Guzha et al. (2015)
Panama (Lutz creek)	9.7	Forêt tropicale	Acrisol	29 - 65	oui	2100		20-80			SOF			Godsey et al. (2004)
Pérou (La Cuenca)	0.7	Forêt tropicale	Ferralsol	300	oui	3300					SSF et SOF			Elsenbeer and Vertessy (2000)

[a]D'après la classification de WRB (2006), [b]calculé à partir de l'équation 2.1, [c]OF/P est le coefficient de ruissellement de crue

Table 2.2. (Suite) Comparaison de bilans hydrologiques annuels et des principaux processus pour des micro-bassins tropicaux avec un sol perméable, modifié à partir de Charlier, 2007.

Sites	Surface	Végétation	Sol[a]	K_S de surface	Horizon limitant la percolation	P[b]	ET/P	Q/P	ΔW/P	D/P	Principaux processus de crue	OF/P annuel[c]	OF/P crue[c]	Auteurs
	[ha]	[-]	[-]	[mm h^{-1}]	[-]	[mm]	[%]	[%]	[%]	[%]		[%]	[%]	
Guyane Fr. (ECEREX B)	1.5	Forêt tropicale	Ferralsol	-	oui	3380	36	18	0	45	SSF	15	30-49	Fritsch (1992)
Guyane Fr. (ECEREX F)	1.4	Forêt tropicale	Ferralsol		oui	3143	46.8	43.9	0	9.3	SSF	25.6		Fritsch (1992)
Madagascar (Andasibe)		Forêt tropicale	Ferralsol	724	oui	1650					SSF et HOF			Zwartendijk et al. (2017)
Costa Rica (La Selva)	1	Forêt tropicale	Inceptisol	100-200	non	4000	35	60			HOF et CP			Gómez-Delgado et al. (2011)
Côte d'Ivoire	0.8	Jachère (10 ans)	Ferralsol	60-150	non	1800	48	47			SSF et SOF			Kassin et al. (2008)
Amazonie brésilienne	1.2	Jachère (5 ans)	Oxisol	40-100	oui	2300	42	53	2	3	HOF et SSF	6	10 -18	Davidson et al. (2007)
Brésil (Amazonie)	6.6	Pâturage	Oxisol	30-80	oui	2200	40	55	1	4	HOF et SOF	3	05 -12	Guzha et al. (2015)

[a]D'après la classification de WRB (2006), [b]calculé à partir de l'équation 2.1, [c]OF/P est le coefficient de ruissellement de crue

2.2.4. Limites et défis des études de bassin versant en climat tropical humide

2.2.4.1. Caractéristiques pluviométriques locales

Les mesures locales de pluie dans les milieux tropicaux humides présentent des défis considérables, principalement dus à la forte variabilité spatiale des précipitations, l'intensité élevée des pluies, l'accessibilité limitée des terrains et les conditions climatiques extrêmes (Houze 2012 ; Michaelides et al. 2009). Face à ces limitations, la télédétection par satellite et les produits de réanalyse offrent des alternatives prometteuses. Ces produits combinent souvent des observations satellitaires, des mesures au sol et des modèles climatiques pour offrir une couverture globale, particulièrement utile dans les régions où les données in situ sont rares. Cependant, Kidd et al. (2017) soulignent que ces méthodes nécessitent toujours une validation au sol, mettant en évidence l'importance continue des mesures in situ.

2.2.4.2. Besoin d'approfondir les études dans les milieux autres que forestiers

Dans le contexte des paysages tropicaux dominés par les jachères et les terres cultivées, notamment l'agriculture sur brûlis, la dynamique hydrologique présente des particularités importantes. Bien que la figure de Dunne (1983) offre une vue d'ensemble des processus hydrologiques (Figure 2.7), elle ne reflète pas pleinement la complexité des milieux tropicaux modifiés par l'homme. En effet, la majorité des études en climat tropical humide se concentre sur les écosystèmes forestiers, laissant un vide dans la compréhension des milieux cultivés et des jachères. Pourtant, les effets de la déforestation et de la mise en culture à l'échelle du bassin versant sont significatifs, comme le montrent de nombreuses études (Table 2.2) (Bruijnzeel 2004; Bosch and Hewlett 1982). Ces changements d'occupation du sol modifient profondément les flux hydrologiques, augmentant souvent le coefficient de ruissellement durant les crues. Des recherches récentes soulignent l'importance de la végétation dans la redistribution de la pluie au sol (Gordon et al. 2019), avec des

implications particulières pour les systèmes d'agriculture sur brûlis où la couverture végétale varie considérablement au fil du temps.

De plus, la conversion des forêts en terres agricoles est fréquemment associée à une réduction de l'infiltrabilité des sols (Lozano-Baez et al. 2019; Zimmermann et al. 2006), ce qui peut amplifier le ruissellement de surface. Les conséquences hydrologiques de ces changements sont substantielles : Peña-Arancibia et al. (2019) ont observé des augmentations significatives des débits annuels suite à la déforestation dans diverses régions tropicales, bien que l'ampleur de ces effets puisse varier selon les caractéristiques locales du bassin versant. Ces modifications du régime hydrologique peuvent persister pendant plusieurs années après le défrichement, avec une tendance progressive vers un nouvel équilibre qui peut différer significativement du régime forestier initial (Lacombe et al. 2016). La compréhension de ces dynamiques complexes dans les paysages tropicaux dominés par l'agriculture itinérante et les jachères est cruciale pour une gestion durable des ressources en eau et l'adaptation aux changements climatiques dans ces régions.

2.2.4.3. Nécessité d'une approche par modélisation

Au sein des bassins versants méso-échelle, cruciaux pour la gestion des ressources en eau, les défis sont amplifiés par les changements rapides d'utilisation des terres et la forte variabilité climatique (Guzha et al. 2018; Malhi et al. 2009). Campling et al. (2002) soulignent le besoin de modèles hydrologiques adaptés à ces environnements uniques. Malgré ces obstacles, les avancées en télédétection, en réanalyse climatique et en modélisation hydrologique ouvrent de nouvelles perspectives pour améliorer la compréhension et la gestion des ressources en eau dans les régions tropicales humides. L'intégration de ces diverses sources de données, combinée à des techniques d'assimilation et de fusion de données, offre des opportunités prometteuses pour surmonter les limitations des mesures traditionnelles, tout en réaffirmant l'importance cruciale des données de terrain fiables pour la calibration et la validation des modèles et des produits dérivés.

2.3. Scénarios climatiques globaux et leurs impacts sur les milieux tropicaux

Les défis hydrologiques rencontrés dans les milieux tropicaux sont exacerbés par les scénarios climatiques globaux, élaborés par le GIEC, qui prévoient des changements significatifs pour les régions tropicales au cours du XXIe siècle. Ces projections sont basées sur différents scénarios d'émissions de gaz à effet de serre, incluant les Trajectoires socioéconomiques partagées (SSP) (O'Neill et al. 2016) et les profils représentatifs d'évolution de concentration (RCP) (van Vuuren et al. 2011). Les scénarios RCP ont été développés pour le cinquième rapport d'évaluation du GIEC en 2014. Parmi eux, le RCP 4.5 et le RCP 8.5 sont fréquemment utilisés dans les études climatiques :

- RCP 4.5 : Scénario de stabilisation où le forçage radiatif total est stabilisé à environ 4,5 W m^{-2} avant 2100.
- RCP 8.5 : Scénario à fortes émissions, avec un forçage radiatif atteignant 8,5 W m^{-2} en 2100.

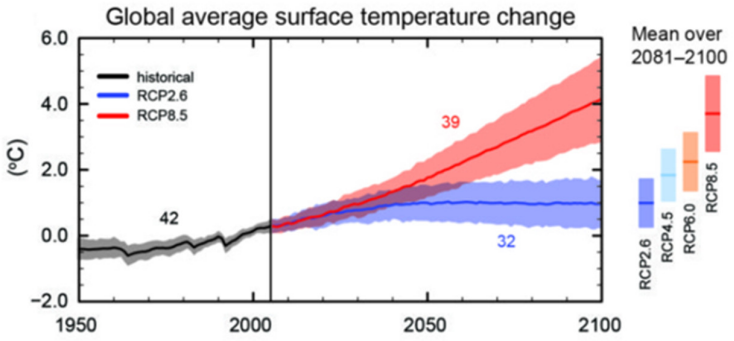

Figure 2. 12. Evolution de la température moyenne globale selon différents scénarios d'émissions (1950 – 2100). Ligne noire : données historiques observées jusqu'en 2005 ; ligne bleue : scénario RCP2.6 (scénario d'atténuation stricte) ; ligne rouge scénario RCP8.5 (scénario à fortes émissions). Les chiffres 42, 39, 32 indiquent les nombres de modèles utilisés. Source : GIEC, 2021.

Selon le dernier rapport du GIEC (Masson-Delmotte et al. 2021), les températures moyennes dans les régions tropicales pourraient augmenter de 1,5°C à plus de 4°C d'ici 2100, selon le scénario considéré. Dans le cadre du RCP 4.5, l'augmentation moyenne globale de température est estimée entre 1,1°C et 2,6°C ; tandis que pour le RCP 8.5, elle pourrait atteindre 2,6°C à 4,8°C (Figure 2.12).

Les modèles climatiques prévoient également des changements importants dans les régimes de précipitations des régions tropicales, avec une intensification probable du cycle hydrologique (Chadwick et al. 2016) (Figure 2.13). Ces changements varient selon les scénarios RCP :

- RCP 4.5 : Augmentation modérée des précipitations dans certaines régions tropicales, avec des variations régionales importantes.
- RCP 8.5 : Changements plus prononcés, avec une augmentation significative des précipitations dans certaines zones tropicales et une aridification accrue dans d'autres.

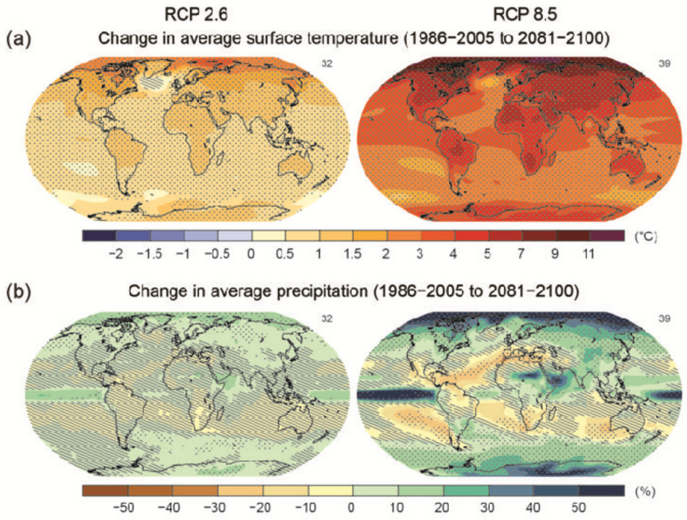

Figure 2. 13. Changements projetés de température (a) et de précipitations (b) selon les scénarios RCP 2.6 (atténuation stricte) et RCP 8.5 (émissions élevées) (1986 – 2005 à 2081 – 2100). Source : GIEC, 2021.

Les écosystèmes tropicaux, notamment les forêts tropicales, sont particulièrement vulnérables aux changements climatiques projetés par les scénarios RCP. Dans les forêts tropicales, les changements climatiques pourraient entraîner des modifications significatives de la composition des espèces et de la structure de la végétation. Sous le scénario RCP 8.5, certains modèles prédisent un risque accru de "savanisation" de parties de l'Amazonie si les seuils critiques de températures et de précipitations sont dépassés (Nobre et al. 2016). Cette transformation pourrait entraîner des conséquences dramatiques sur la biodiversité et le cycle du carbone à l'échelle mondiale. Ces impacts varient en intensité selon les scénarios RCP considérés, soulignant l'importance cruciale des efforts de réduction des émissions de gaz à effet de serre pour la préservation de ces écosystèmes uniques et vitaux.

2.4. Modélisation hydrologique adaptée aux environnements changeants

Pour étudier les altérations hydrologiques consécutives à un environnement changeant (modifications rapides de l'occupation des sols et changements climatiques), les modèles hydrologiques s'avèrent essentiels. Cependant, le choix d'un modèle approprié, en particulier pour les bassins versants tropicaux, nécessite une compréhension approfondie des différents types de modèles disponibles et de leurs caractéristiques (Musy 2004). Avant de sélectionner un modèle, il est important de faire un bref rappel des principaux types de modèles hydrologiques et de leurs particularités. Cette revue aidera à mieux comprendre les critères de sélection et à justifier notre choix final.

2.4.1. Modélisation hydrologique

Un modèle est d'abord une représentation simplifiée d'un phénomène physique, visant à comprendre les processus qui le régissent. La modélisation hydrologique est, par conséquent, un domaine fondamental de l'hydrologie qui vise à représenter et prédire le comportement de l'eau dans l'environnement (Figure 2.14). Elle consiste

à créer des représentations mathématiques des processus hydrologiques afin de comprendre et de simuler le cycle de l'eau à différentes échelles spatiales et temporelles.

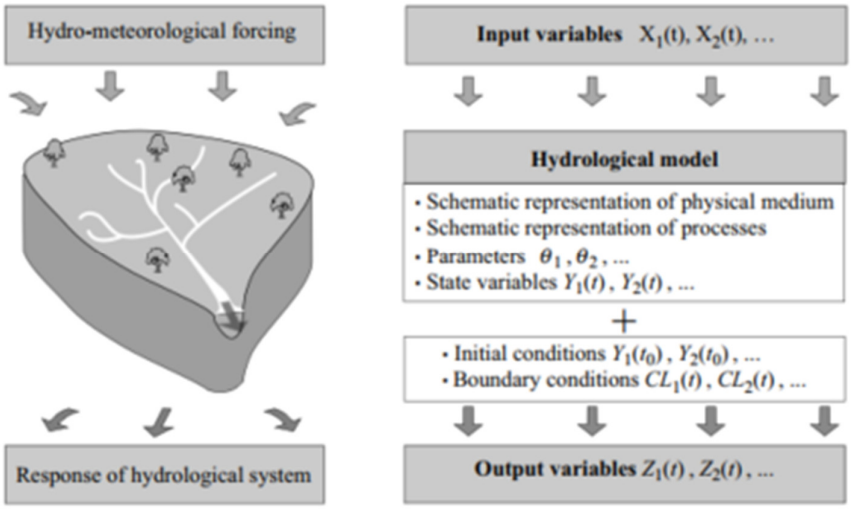

Figure 2. 14. Structure typique et variables d'un modèle hydrologique. Source : Musy, 2004.

2.4.2. Types de modèles hydrologiques

L'évolution de la modélisation hydrologique a engendré une pléthore de modèles, chacun conçu pour répondre à des besoins spécifiques. Cette diversité d'approches a donné naissance à un large éventail d'outils, chacun possédant ses propres domaines d'application et limites de validité (Musy 2004). Ces modèles se distinguent principalement par leur approche de la discrétisation spatiale, pouvant être soit globale, soit distribuée. De plus, ils varient dans leur manière de représenter les phénomènes hydrologiques : certains s'appuient sur des équations empiriques, d'autres sur des équations physiques, tandis que d'autres encore adoptent une approche conceptuelle, simplifiant à divers degrés les équations physiques (Figure 2.15) (Perrin 2002).

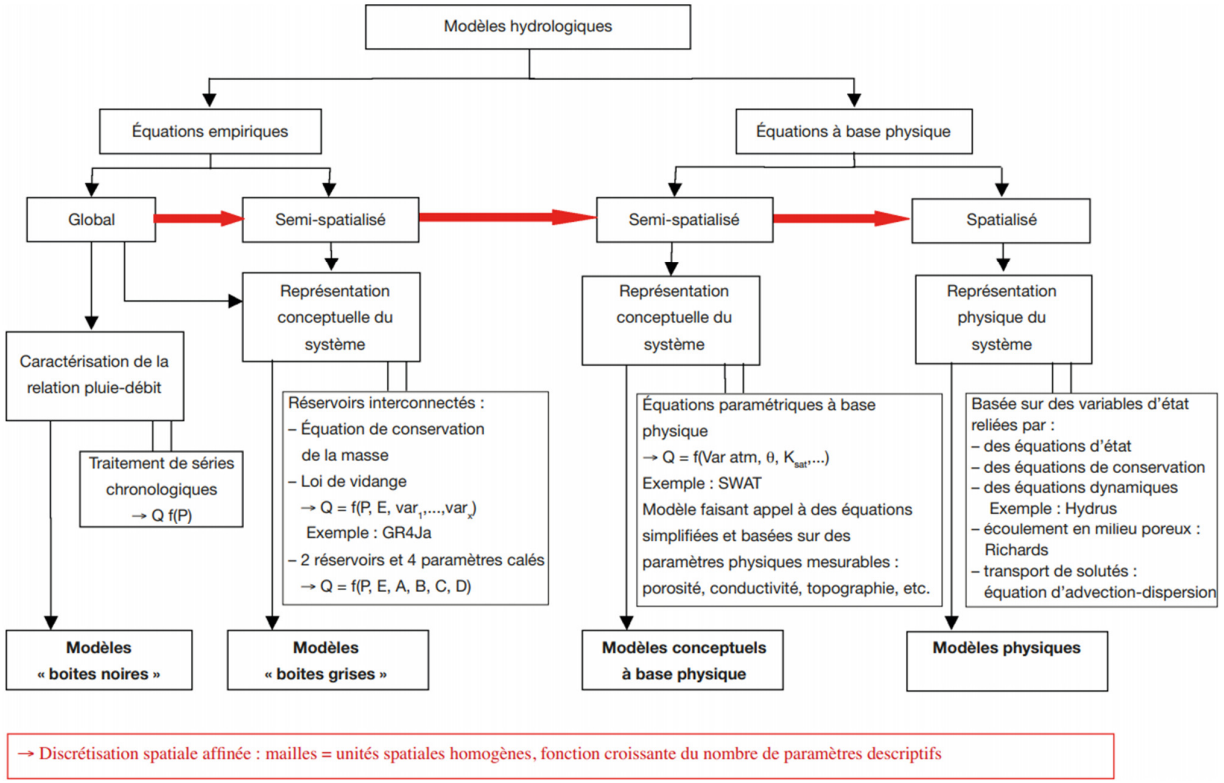

Figure 2. 15. Représentation schématique de la classification des modèles hydrologiques. Source : Singh et Woolhiser, 2002.

La classification des modèles hydrologiques peut être divisée en quatre catégories principales, selon leur représentation du bassin versant et leur lien avec les paramètres physiques : (i) Les modèles empiriques ou "boîtes noires", constituent la catégorie la plus simple des modèles hydrologiques. Leur principe repose sur une relation directe entre la pluie P entrant dans le bassin versant et le débit à l'exutoire Q, exprimée par la fonction Q = f(P). Ces modèles se caractérisent par leur approche simplifiée, ne tenant pas compte du cheminement de l'eau dans le bassin ni des paramètres physiques. Malgré leur utilisation limitée dans la recherche, ils s'avèrent particulièrement efficaces pour les prévisions de crue en bassin jaugé, grâce à leur simplicité opérationnelle (Perrin 2002). La méthode rationnelle est un exemple emblématique de cette catégorie de modèles. Les principaux avantages des modèles empiriques résident dans leur simplicité d'utilisation et leur rapidité d'exécution. Cependant, ils présentent des limites significatives, notamment un manque de représentation des processus physiques et une applicabilité restreinte aux bassins jaugés, ce qui limite leur capacité à être transposés à des contextes hydrologiques différents.

(ii) Les modèles conceptuels empiriques, aussi connus sous le nom de "boîtes grises", représentent une avancée par rapport aux modèles empiriques simples. Ils conceptualisent le bassin versant comme un ensemble de réservoirs interconnectés, dont les paramètres de vidange sont calibrés sur les débits observés à l'exutoire, plutôt que basés sur des caractéristiques physiques réelles (Birkel et Barahona 2019). Un exemple typique de cette approche est le modèle GR4J (Perrin et al. 2003), largement utilisé en hydrologie. Ces modèles offrent une meilleure représentation des processus hydrologiques que leurs homologues purement empiriques, tout en restant relativement simples à mettre en œuvre. Cependant, ils présentent certaines limites : ils nécessitent une calibration rigoureuse et peuvent rencontrer des difficultés lors de l'extrapolation à des conditions non observées. Malgré ces contraintes, les modèles conceptuels empiriques constituent un compromis intéressant entre la simplicité des modèles empiriques et la complexité des modèles physiques plus avancés.

(iii) Les modèles conceptuels à base physique, également appelés modèles capacitifs, représentent une évolution significative dans le domaine de la modélisation hydrologique. Ces modèles intègrent les différents éléments du cycle de l'eau dans une représentation simplifiée mais basée sur des principes physiques. Leur développement a marqué une transition des modèles globaux vers des modèles distribués, permettant une division du bassin versant en sous-unités homogènes (HRU) ou selon un maillage régulier. Cette approche offre la possibilité d'analyser les écoulements au sein du bassin et d'étudier la variabilité du système hydrologique de manière plus détaillée (Ayral et Sauvagnargues 2005). Des exemples notables de cette catégorie incluent TOPMODEL (Beven and Kirkby 1979) et SWAT (Arnold et al. 2012). Les avantages principaux de ces modèles résident dans leur capacité à bien représenter les processus hydrologiques et à simuler les flux internes du bassin. Cependant, ils présentent également des limites, notamment une complexité accrue par rapport aux modèles plus simples et un besoin important en données spatiales détaillées pour leur paramétrage et leur validation.

(iv) Les modèles physiques représentent l'approche la plus avancée et la plus complexe en modélisation hydrologique. Ils se distinguent par leur fondement sur des lois physiques fondamentales, telles que l'équation de Darcy (1856) pour le domaine saturé et l'équation de Richards (1931) pour le domaine insaturé. Ces modèles offrent une représentation tridimensionnelle des processus hydrologiques, permettant une analyse détaillée des flux d'eau dans le bassin versant. Cependant, cette sophistication s'accompagne d'exigences importantes en termes de puissance de calcul et de données descriptives du sol (Payraudeau 2002; Ambroise 1999). Des exemples notables de ces modèles incluent MIKE SHE (Abbott et al. 1986) et SHETRAN (Ewen et al. 2000). Bien que ces modèles offrent une représentation très détaillée des processus physiques, leur complexité élevée et leurs besoins importants en données et en ressources informatiques constituent des limites significatives à leur utilisation généralisée. Néanmoins, ils restent des outils précieux pour la recherche avancée en hydrologie et pour des applications nécessitant une compréhension approfondie des mécanismes hydrologiques.

2.4.3. Sélection et description du modèle hydrologique

L'étude des altérations hydrologiques dans les bassins versants tropicaux représente un enjeu crucial face aux changements globaux (Wohl et al. 2012). Ces milieux se caractérisent par des propriétés uniques qui influencent significativement les processus hydrologiques. Les sols tropicaux, riches en argile et dotés d'une structure macroporeuse (Wohl et al. 2012; Bruijnzeel 2004), favorisent les écoulements de subsurface (**SSF**) et sur surface saturée (**SOF**) comme processus dominants (Elsenbeer 2001; Bonell 1993). La forte variabilité spatiale et temporelle des précipitations (Houze 2012), marquée par des événements intenses et localisés tels que les orages convectifs, engendre des réponses hydrologiques rapides et hétérogènes à l'échelle du bassin versant (Moron et al. 2009). De plus, la topographie accidentée des bassins versants tropicaux, caractérisée par des pentes abruptes, joue un rôle crucial dans la redistribution de l'eau et la formation des écoulements (Chappell et al. 2007). L'interaction entre ces caractéristiques topographiques, les propriétés du sol et la couverture végétale crée des motifs complexes de génération et de propagation des écoulements. Cette complexité nécessite une représentation fine et détaillée dans les modèles hydrologiques pour capturer adéquatement la dynamique des bassins versants tropicaux (Nobre et al. 2011).

Pour étudier efficacement ces altérations, il est nécessaire d'utiliser un modèle hydrologique capable d'évaluer les impacts des changements d'occupation des sols et des changements climatiques, d'intégrer ces processus hydrologiques spécifiques aux régions tropicales, de s'adapter à différentes échelles spatiales et temporelles, et de gérer la variabilité des données disponibles en termes de quantité et de qualité.

Les modèles hydrologiques traditionnels comme TOPMODEL ou IHACRES (Identification of unit Hydrographs And Component flows from Rainfall, Evaporation and Streamflow data) présentent certaines limitations substantielles mais variables selon les contextes pour la modélisation des bassins versants tropicaux. TOPMODEL, basé principalement sur l'indice topographique comme facteur dominant du comportement hydrologique (Beven and Kirkby 1979), suppose une relation directe

entre la topographie et les zones saturées qui s'avère trop simpliste pour les régions tropicales. IHACRES, bien que flexible dans sa structure, reste limité par sa conception empirique et sa difficulté à représenter explicitement les processus physiques complexes des milieux tropicaux. Ces modèles ne peuvent pas intégrer efficacement la forte hétérogénéité spatiale des sols tropicaux, l'impact des changements rapides d'occupation des sols, ni les processus hydrologiques spécifiques tels que l'interception importante par la canopée dense et les écoulements préférentiels le long des racines profondes typiques des forêts tropicales (Nobre et al. 2011). Par contre, le modèle SWAT (http://swat.tamu.edu/software/, consulté en Juin 2024) (Arnold et al. 2012), qui est un modèle à base physique et semi-distribué, offre la flexibilité nécessaire pour représenter la dynamique des surfaces contributives saturées et les débits dans ces environnements complexes.

SWAT a été appliqué avec succès dans diverses régions tropicales. En Amazonie brésilienne, Pereira et al. (2016) ont évalué les impacts hydrologiques de la déforestation dans le bassin de la rivière Xingu. Dans le bassin inférieur du Mekong en Asie du Sud-Est, Piman et al. (2013) ont étudié l'impact des changements climatiques et de l'utilisation des terres. En Afrique, Mpanano (2019) ont appliqué le modèle au bassin du fleuve Congo pour évaluer sa sensibilité aux paramètres d'entrée. Cependant, l'utilisation de SWAT en milieu tropical peut nécessiter des ajustements. Tan et al. (2019), dans leur étude sur le bassin de la rivière Kelantan en Malaisie, ont souligné l'importance d'adapter le modèle aux processus de ruissellement et d'érosion spécifiques à ces environnements. De même, Akoko et al. (2021), travaillant sur le bassin de la rivière Nyando au Kenya, ont montré que la représentation des dynamiques d'écoulement par les seuls processus **SSF** et **SOF** n'est pas toujours suffisante, même sur des sols perméables. En conclusion, SWAT offre des possibilités intéressantes pour la modélisation hydrologique en milieu tropical, tout en nécessitant une compréhension détaillée des processus hydrologiques locaux et potentiellement des adaptations pour refléter au mieux les spécificités de ces environnements.

2.5. Le modèle SWAT

Le modèle SWAT (Soil and Water Assessment Tool) est le fruit de plus de 30 ans de développement continu par l'United States Department of Agriculture (USDA) Agricultural Research Service (Arnold et al. 2012) (Figure 2.16). Conçu pour simuler les cycles de l'eau, des sédiments, des nutriments et des pesticides à l'échelle du bassin versant, SWAT est un modèle distribué à base physique, fonctionnant à un pas de temps journalier (Neitsch et al. 2011). C'est un modèle continu à long terme, non conçu pour simuler des événements ponctuels détaillés. Il intègre des composantes de plusieurs modèles précédents, notamment SWRRB (Simulator for Water Resources in Rural Basins), CREAMS (Chemicals, Runoff, and Erosion from Agricultural Management Systems), GLEAMS (Groundwater Loading Effects of Agricultural Management Systems) et EPIC (Erosion Productivity Impact Calculator) (Gassman et al. 2007). Cette approche composite lui confère une grande flexibilité et une capacité à traiter une large gamme de problématiques environnementales.

Le modèle a considérablement évolué depuis sa création initiale dans les années 1990. La version SWAT2012 représente une amélioration significative, avec des mises à jour dans plusieurs composantes du modèle (Arnold et al. 2012). Plus récemment, SWAT+ a été développé comme une restructuration complète du code SWAT, offrant une plus grande flexibilité dans la configuration des unités spatiales et des processus simulés (Bieger et al. 2017). Malgré les avancées de SWAT+, nous avons choisi d'utiliser SWAT2012 pour cette étude en raison de sa stabilité éprouvée, de sa large base d'utilisateurs et de la disponibilité importante de documentation et de ressources de support. De plus, l'interface graphique pour SWAT2012, ArcSWAT, est une extension pour ArcGIS bien établie. Elle facilite l'intégration des données d'entrée telles que le modèle numérique de terrain (MNT), les données climatiques, le réseau hydrographique, ainsi que les cartes de sols et d'occupation des sols. ArcSWAT permet également l'extraction des paramètres d'entrée, la configuration du modèle et la visualisation des résultats (Moriasi et al. 2019), ce qui est particulièrement avantageux pour notre contexte d'étude (Figure 2.17).

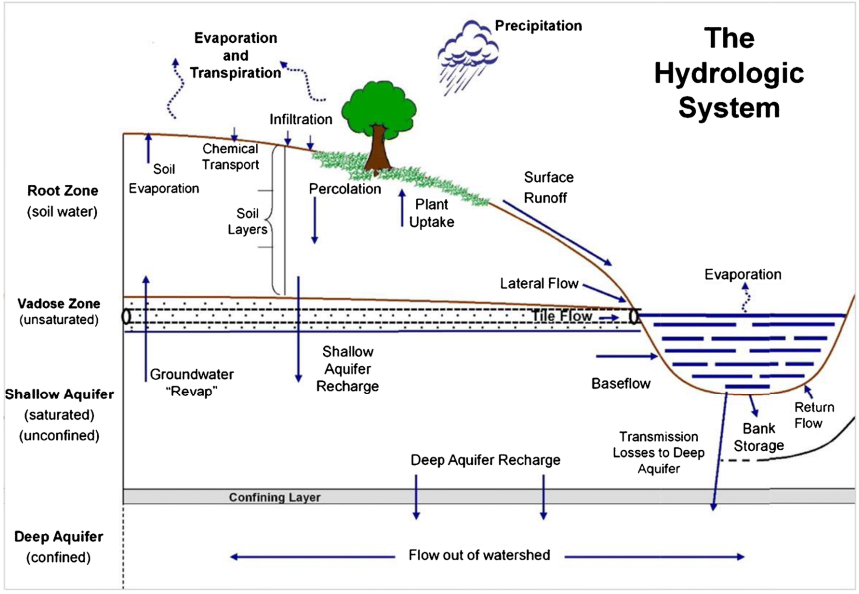

Figure 2. 16. Conceptualisation du cycle hydrologique dans le modèle SWAT. Source: Soil and Water Assessment Tool, Theoretical documentation, Version 2009. http://twri.tamu.edu/reports/2011/tr406.pdf, consulté en Juin 2024.

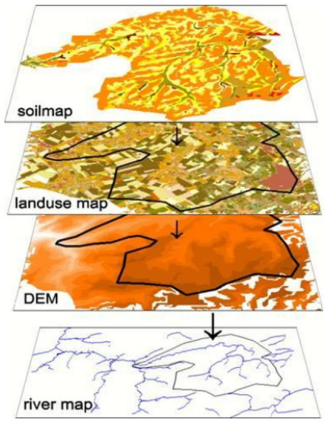

Figure 2. 17. Données spatiales d'entrée requises pour le modèle SWAT. Source: Soil and Water Assessment Tool, Theoretical documentation, Version 2009. http://twri.tamu.edu/reports/2011/tr406.pdf, consulté en Juin 2024.

SWAT est un modèle hydrologique continu à base physique. Il a été développé pour prédire l'impact des pratiques de gestion des terres sur l'eau ainsi que sur les rendements en sédiments et en produits chimiques agricoles dans de grands bassins versants complexes présentant différentes conditions de sol, d'utilisation des terres et de gestion sur de longues périodes (Eckhardt et al. 2002). Le modèle hydrologique fonctionne en divisant le bassin versant en sous-bassins. Chaque sous-bassin est ensuite discrétisé en une série d'unités de réponse hydrologique (HRU), qui sont des combinaisons uniques de sol et d'utilisation des terres. La teneur en eau du sol, le ruissellement de surface, les cycles des nutriments, la production de sédiments, la croissance des cultures et les pratiques de gestion sont simulés pour chaque HRU, puis agrégés pour le sous-bassin par une moyenne pondérée. Le bilan hydrologique est calculé sur la base de l'équation suivante (Equation 2.7) :

$$SWt = SWo + \sum_{i=1}^{t} (\mathrm{Rday} - \mathrm{Qsurf} - \mathrm{Ea} - \mathrm{Wseep} - \mathrm{Qgw}) \quad (2.7)$$

Avec :
SW_t et SW_O sont respectivement le contenu final et initial en eau du sol [mm H_2O],
t est le temps [jours],
R_{day} est la quantité de précipitations le jour i [mm H_2O],
Q_{surf} est la quantité de ruissellement de surface le jour i [mm H_2O],
E_a est la quantité d'évapotranspiration le jour i [mm H_2O],
W_{seep} est la quantité d'eau s'infiltrant du profil de sol vers la zone vadose sous-jacente le jour i [mm H_2O],
et Q_{gw} est la quantité d'écoulement de retour (écoulement latéral souterrain) le jour i [mm H_2O].

Dans chaque HRU du SWAT, l'eau est stockée dans quatre volumes de stockage : la neige, le profil du sol, l'aquifère peu profond et l'aquifère profond. Toutefois, avant d'atteindre ces compartiments, une partie des précipitations est interceptée par la canopée végétale. L'interception, qui est la première composante du cycle hydrologique simulée par SWAT, est estimée en fonction du type de végétation, de son stade de développement et de la quantité de précipitations (Neitsch et al. 2011). SWAT utilise l'équation de stockage de la canopée pour calculer la quantité maximale

d'eau pouvant être retenue par la végétation, qui varie selon l'indice de surface foliaire (LAI). L'eau interceptée peut ensuite s'évaporer directement de la canopée ou atteindre le sol par égouttement.

Le modèle calcule ensuite l'évaporation des sols et des plantes de manière séparé. L'évapotranspiration potentielle peut être modélisée avec trois options disponibles dans SWAT, à savoir les méthodes de Penman-Monteith, Priestley-Taylor et Hargreaves (Neitsch et al. 2011), selon la disponibilité des données. L'évaporation potentielle de l'eau du sol est estimée en fonction de l'ET potentielle et de l'indice de surface foliaire. L'évaporation réelle du sol est estimée en utilisant des fonctions exponentielles de la profondeur du sol et de la teneur en eau. Par contre, l'évaporation de l'eau des plantes est simulée comme une fonction linéaire de l'évapotranspiration potentielle, de l'indice de surface foliaire et de la profondeur des racines, et peut être limitée par la teneur en eau du sol.

Le ruissellement de surface provenant des précipitations quotidiennes est estimé à l'aide de la méthode du Curve Number (CN) du Soil Conservation Service (Boughton 1989) ou du modèle d'infiltration de Green et Ampt (Rawls et al. 1983). La méthode CN estime la quantité de ruissellement en fonction de l'utilisation locale des terres, du type de sol et des conditions d'humidité antécédentes, tandis que le modèle de Green et Ampt offre une approche plus physique basée sur les propriétés hydrauliques du sol. Le débit calculé, la production de sédiments et la charge en nutriments obtenus pour chaque sous-bassin sont ensuite acheminés à travers le cours d'eau en utilisant la méthode du stockage variable ou de Muskingum. Le temps de concentration du bassin versant est estimé à l'aide de l'équation cinématique de Manning, en tenant compte à la fois de l'écoulement terrestre et de l'écoulement en canal.

Le profil du sol est subdivisé en plusieurs couches qui supportent les processus hydrologiques du sol, notamment l'infiltration, l'évaporation, l'absorption par les plantes, l'écoulement latéral et la percolation vers les couches inférieures (Douglas-Mankin et al. 2010). La composante de percolation du sol dans SWAT utilise une technique de capacité de stockage d'eau pour prédire l'écoulement à travers chaque

couche de sol dans la zone racinaire. L'écoulement vers le bas se produit lorsque la capacité au champ d'une couche de sol est dépassée et que la couche inférieure n'est pas saturée (Arnold et al. 2012). La percolation à partir du fond du profil du sol recharge l'aquifère peu profond. La quantité d'eau entrant dans l'aquifère peu profond est fonction du volume total d'eau sortant du profil du sol et d'une fonction de décroissance exponentielle pour tenir compte du délai de recharge. Ce dernier dépend des formations géologiques sus-jacentes. Si la profondeur de l'aquifère peu profond augmente au-dessus de la valeur seuil définie par l'utilisateur, on suppose qu'il y a décharge des eaux souterraines et contribution au cours d'eau (Arnold et al. 1998). Le mouvement ascendant vers les couches de sol non saturées sus-jacentes est simulé en acheminant l'eau du composant de stockage de l'aquifère peu profond vers le sol par pression capillaire ou par absorption directe par les racines des plantes (Neitsch et al. 2011).

Les écoulements de subsurface sont simulés dans SWAT à travers deux composantes principales : l'écoulement hypodermique dans le sol et l'écoulement de base provenant des aquifères. L'écoulement de subsurface ou hypodermique, est modélisé simultanément avec la percolation grâce à un modèle de stockage cinématique (Sloan and Moore 1984), qui prend en compte la pente du terrain, la conductivité hydraulique et la porosité du sol. Ce processus se produit dans la couche de sol saturée au-dessus d'une couche imperméable ou semi-perméable, contribuant au débit du cours d'eau dans le sous-bassin. L'écoulement de base, issu de l'aquifère peu profond, est estimé à l'aide d'une constante de récession dépendant des caractéristiques hydrogéologiques du bassin versant (Arnold et al. 1998). SWAT intègre également la simulation de la recharge de l'aquifère profond, considérée comme une perte du système, sauf en cas d'activation de l'option de pompage des eaux souterraines (Neitsch et al. 2011). Cette approche globale permet à SWAT de représenter de manière exhaustive les différentes composantes des écoulements de subsurface et leur contribution au débit des cours d'eau. Des descriptions plus détaillées du modèle peuvent être trouvées dans Neitsch et al. (2011) [Annexe A].

Pour conclure, on peut affirmer que le modèle SWAT s'avère être un outil particulièrement adapté pour traiter les altérations hydrologiques des bassins versants tropicaux, en général, et les bassins versant tropicaux humides, en particulier. Sa capacité à simuler de manière détaillée les différents processus hydrologiques, depuis l'interception des précipitations intenses par la canopée dense jusqu'aux écoulements souterrains, en passant par le ruissellement de surface rapide/ subsurface, l'infiltration dans des sols souvent altérés et l'évapotranspiration élevée, en fait un modèle robuste pour l'analyse des changements hydrologiques en milieu tropical. La flexibilité du SWAT dans la prise en compte des variations spatiales des caractéristiques du bassin versant (topographie accidentée, sols hétérogènes, occupation des sols diversifiée) et sa capacité à intégrer les pratiques de gestion agricole tropicale et les aménagements hydrauliques permettent une représentation fidèle des conditions spécifiques tropicales. De plus, sa capacité à simuler les impacts à long terme des changements d'utilisation des terres, des pratiques de gestion et du climat tropical sur l'hydrologie du bassin en fait un outil précieux pour l'évaluation et la gestion durable des ressources en eau dans ces régions. Ainsi, le modèle SWAT offre une plateforme complète et fiable pour analyser, comprendre et prédire les altérations hydrologiques dans le contexte particulier des bassins versants tropicaux, caractérisés par une forte variabilité saisonnière et des écosystèmes sensibles.

2.6. La recherche hydrologique à Madagascar

2.6.1. L’évolution de la recherche hydrologique à Madagascar

L'île de Madagascar, avec ses caractéristiques physiques uniques et sa vulnérabilité aux phénomènes météorologiques extrêmes, a toujours présenté des défis particuliers en matière de gestion des ressources en eau. Dès les premiers projets d'aménagement hydraulique, les problèmes hydrologiques se sont manifestés, nécessitant une compréhension approfondie des processus hydrologiques du pays (Danloux 1983). C'est dans ce contexte que les recherches hydrologiques ont pris son essor à Madagascar, s'adaptant aux besoins et aux contextes changeants au fil des décennies.

Les prémices de la recherche hydrologique à Madagascar remontent au début du XXe siècle, menées par les Travaux Publics. Cependant, c'est l'implication de l'Office de la Recherche Scientifique et Technique Outre-Mer (ORSTOM) à partir des années 1940 qui a marqué un tournant majeur. L'Orstom a contribué à l'expansion du réseau hydrologique et à l'amélioration des connaissances sur les ressources en eau du pays. Cette période a vu la mise en place de stations de mesure hydrologique et la réalisation d'études sur les régimes hydriques des principales rivières de Madagascar.

Les années 1960 et 1970 ont été marquées par une réorganisation majeure du réseau hydrologique et par des études approfondies sur les crues cycloniques, fréquentes à Madagascar. Cette période a également connu la création de l' Institut de Recherche Scientifique de Madagascar (IRSM), qui a joué un rôle crucial dans la coordination et la promotion de la recherche hydrologique dans le pays (Aldegheri 1972, 1960).

En 1993, après 90 ans d'efforts cumulés, une synthèse importante des connaissances hydrologiques à Madagascar a été publiée dans l'ouvrage "Fleuves et rivières de Madagascar" (Chaperon et al. 1993). Cette publication a servi de base solide pour les recherches ultérieures et a permis de mettre en lumière les défis et les opportunités liés à la gestion des ressources en eau dans le pays. S'appuyant sur cet ouvrage, plusieurs organismes internationaux, tels que l'Institut de Recherche pour le Développement (IRD), l'Agence Française de Développement (AFD), l'Organisation pour l'Alimentation et l'Agriculture (FAO) et la Banque mondiale, ont développé leurs propres programmes de recherche hydrologique à Madagascar. Ces initiatives ont intégré des technologies modernes telles que la télédétection et des modèles de prévision avancés, permettant d'améliorer la précision et l'efficacité des études hydrologiques. De plus, un accent particulier a été mis sur la formation des hydrologues locaux et le renforcement des capacités des communautés face aux risques hydrologiques.

2.6.2. Enjeux liés à la recherche hydrologique

L'étude des ressources en eau à Madagascar bénéficie d'une base historique solide grâce au travail de Ferry (1995, 1987) qui a compilé une liste bibliographique exhaustive des recherches hydrologiques, climatologiques et des aménagements hydrauliques de 1923 à 1990. Cette compilation offre un aperçu précieux de l'évolution des études hydrologiques dans le pays. Le tableau 2.3 complète cette perspective en présentant une synthèse des recherches hydrologiques menées après 1990, mettant en lumière une diversité d'échelles temporelles et de thématiques abordées. Cependant, bien que des avancées significatives aient été réalisées, des lacunes persistent dans notre compréhension des systèmes hydrologiques malgaches. Cette situation souligne la nécessité de nouvelles orientations de recherche pour améliorer la compréhension et la gestion des ressources en eau du pays.

On observe une concentration des études hydrologiques sur plusieurs zones critiques de Madagascar, chacune présentant des enjeux spécifiques :

(1) Le corridor Ankeniheny-Zahamena, important pour son écologie et sa biodiversité, fait l'objet de recherches sur l'impact de la déforestation sur les ressources en eau et la biodiversité (Van Soesbergen and Mulligan 2018; Zwartendijk et al. 2017).

(2) Le Grand Sud, confronté à un stress hydrique sévère et à des épisodes de sécheresse récurrents, nécessite des études sur la gestion de l'eau en conditions arides (Carrière et al. 2021).

(3) La plaine d'Antananarivo, zone urbaine densément peuplée, est au cœur de recherches portant sur la gestion des inondations et l'assainissement (Li et al. 2023).

(4) Le lac Alaotra, considéré comme le grenier à riz de Madagascar, est l'objet d'études se concentrant sur l'irrigation et la gestion durable des ressources en eau pour l'agriculture (Ferry et al. 2009). Ces travaux, souvent menés à l'échelle régionale, offrent une compréhension globale des systèmes hydrologiques et

apportent des informations précieuses pour la gestion durable des ressources en eau dans ces zones prioritaires.

Malgré cette concentration sur des zones critiques, on note un manque relatif d'études locales, ce qui pourrait limiter la compréhension des processus hydrologiques à petite échelle et la prise en compte des spécificités locales dans les stratégies de gestion de l'eau. De plus, certaines régions comme le Nord-Est de Madagascar semblent sous-représentées, avec une seule étude hydrologique mentionnée (Randriamaherisoa and Binard 1992). Cette disparité géographique reflète probablement les priorités dictées par les défis hydrologiques les plus urgents, mais souligne également la nécessité d'élargir la couverture géographique des recherches pour obtenir une image plus complète de l'hydrologie malgache.

Il convient de souligner également que les Grands Bassins Versants de Madagascar (MRBM) et le bassin versant de Mangoky ont récemment fait l'objet d'une modélisation hydrologique utilisant le modèle SWAT (Rakotoarimanana et al. 2024c, Rabezanahary et al. 2021) (Table 2.3). Ces études, orientées vers la simulation des réponses hydrologiques à moyen et long terme, se sont focalisées uniquement sur l'impact des changements climatiques sans considérer les modifications d'occupation des sols. Conduites à un pas de temps annuel et sur des macro-bassins, leurs résultats, bien qu'ils constituent une avancée, restent limités pour une application pratique à l'échelle locale. En effet, cette résolution temporelle ne permet pas de capturer les dynamiques hydrologiques à court terme, particulièrement importantes dans un contexte d'événements climatiques extrêmes fréquents.

Dans la progression des recherches hydrologiques, trois axes d'amélioration se dégagent désormais. Le premier axe concerne l'application du modèle SWAT à des échelles spatiales plus fines (méso-bassins ~1000 km²). Il s'agit d'adapter et d'affiner le modèle pour qu'il puisse prendre en compte les spécificités locales des sous-bassins versants.

Le second axe porte sur l'adaptation du modèle pour une simulation à pas de temps journalier. Cette orientation consiste à évaluer et à optimiser la capacité du modèle SWAT à simuler de manière fiable les processus hydrologiques à une échelle temporelle plus fine, notamment pour les bassins versants présentant une réponse hydrologique rapide. Une telle adaptation, bien qu'exigeante en termes de précision des données et de puissance de calcul, permettrait une analyse plus détaillée des dynamiques hydrologiques à court terme, offrant ainsi des possibilités accrues en termes de prévision et de gestion des événements hydrologiques extrêmes.

Le troisième axe vise à intégrer les changements d'occupation des sols dans la modélisation, un facteur particulièrement crucial en milieu tropical. Cette considération permettrait une analyse plus complète des altérations hydrologiques, prenant en compte à la fois les impacts climatiques et anthropiques sur les ressources en eau.

Les avancés dans ces axes de recherche pourraient considérablement enrichir notre compréhension de l'hydrologie malgache, tout en fournissant des outils plus précis pour la gestion durable des ressources en eau du pays.

Table 2. 3. Synthèse des recherches hydrologiques à Madagascar après les années 1990.

Thématiques	Titre/ Méthodologie	Echelle[1]	Zone d'études	Area	Pas de Temps[2]	Références
Processus hydrologiques	Madagascar : étude et gestion de la ressource en eau : analyse bibliographique des travaux récents (1968-1989).	N	Madagascar	587 041 km²		(Danloux and Danloux 1990)
	Approche des échanges surface-souterrain en milieu cristallin altéré aquifère.	L	Madagascar			(Grillot and Ferry 1990)
	Etude hydrologie l'Onilahy à Tongobory	L	Rivière Onilahy		J	(Lamagant 1990)
	Géodynamique de l'hydrosphère continentale	N	Madagascar			(Olivry 1990)
	Madagascar, programme eaux continentales (PEC) : connaissance protection et gestion.	N	Madagascar			(Rakotovao, 1990)
	Les données d'observations et estimation des débits maximums à Madagascar	N	Madagascar			(Danloux 1991)
	Bilan des eaux, typologie des bas-fonds, érosion et modélisation sur des bassins emboîtés des Hautes Terres de Madagascar	N	Hautes Terres centrales			(Dussarat 1991)
	Inventaire des eaux de surface malgache	N	Madagascar			(Elouart 1991)
	Banque de données hydroclimatologiques de Madagascar	N	Madagascar			(Ferry 1995)
	Reconnaissance hydrologique et géologique dans la région de Manombo/Ranozaza (Madagascar)	L	Ville de Ranozaza			(Ferry 1991)

[1] Echelle : N : Nationale ; R : Régionale ; L : Locale ; [2] Pas de temps : A : Annuel ; M : Mensuel ; J : Journalier : H : Horaire

Table 2.3. (Suite) Synthèse des recherches hydrologiques à Madagascar après les années 1990.

Thématiques	Titre/ Méthodologie	Echelle[1]	Zone d'études	Area	Pas de Temps[2]	Références
Processus hydrologiques (suite)	Etalonnage de cinq stations limnigraphiques dans la région d'Andapa. Antananarivo	L	Bassin versant de la Lokoho. Bassin versant de l'Ikopa		M	(Ferry 1991)
	Fleuves et rivières de Madagascar	N	Madagascar			(Chaperon et al. 1993)
	Un enregistrement environnemental de 36 000 ans dans les tropiques du sud	L	Lac Tritrivakely			(Gasse et al. 1994)
	Bilan des eaux, typologie des bas-fonds, érosion et modélisation sur des bassins emboîtés des Hautes Terres de Madagascar	N	Hautes Terres		M	(Dussarrat 1994)
	Le lac Alaotra à Madagascar	L	Lac Alaotra	900 km²		(Ferry et al. 2009)
	Comparaison des propriétés hydrologiques du sol entre zones de tavy et forêts	L	Southern part CAZ		5'	(Zwartendijk et al. 2017)
	Mesure de l'humidité du sol et du ruissellement sur des versants d'agriculture sur brûlis	L	Marolaona catchment	31.7 ha	5 '	(Zwartendijk et al. 2023)
	Comparaison d'algorithmes automatisés de cartographie des inondations en quasi-temps réel utilisant des données satellitaires et des méthodes basées sur le MNT	R	Plaine d'Antananarivo		M	(Li et al. 2023)
	Surveillance des flux d'eau du sol et du ruissellement dans un bassin versant tropical	L	Marolaona catchment	31.7 ha	5'	(Zwartendijk et al. 2020)
	Caractéristiques hydrographiques et géomorphologiques d'Antananarivo	R	Colline d'Antananarivo	86.4 km²		(Frodella et al. 2021)
Interception	Mesure et modélisation de l'interception des précipitations dans des forêts secondaires	R	Corridor Ankeniheny-Zahamena (CAZ)		J	(Ghimire et al. 2017)

[1] Echelle : N : Nationale ; R : Régionale ; L : Locale ; [2] Pas de temps : A : Annuel ; M : Mensuel ; J : Journalier : H : Horaire

Table 2.3.(Suite) Synthèse des recherches hydrologiques à Madagascar après les années 1990.

Thématiques	Titre/ Méthodologie	Echelle[1]	Zone d'études	Area	Pas de Temps[2]	Références
Modèle pluie-débit	Test de méthodes de calibration pour des modèles hydrologiques multi-jauges	R	Major River Basins in Madagascar (MRBM)	320 373 km²	M	(Rakotoarimanana et al. 2024b)
	Analyse des isotopes du corail pour la reconstruction du ruissellement historique des rivières	R	Onilahy RB/ Antainambalana RB		A	(Maina et al. 2012)
	Application d'un modèle hydrologique à un lac fermé pour reconstructions paléoclimatiques	L	Lac Ihotry	3000 km²	M	(Vallet-Coulomb et al. 2006)
	Utilisation de modèles hydrologiques pour la quantification des propriétés des bassins versants	N	Madagascar			(Stampoulis et al. 2014)
	Modélisation hydrologique du bassin versant de l'Ikopa à Antananarivo : application d'un modèle à discrétisation spatiale.	R	Bassin versant de l'Ikopa	24 000 km²	M	(Razafimanjato 1992)
Evapotranspiration	Calcul de l'évapotranspiration de référence à partir de données météorologiques sur 30 ans	N	Madagascar		A/ M	(Djaman et al. 2018)
	Comparaison des estimations d'évapotranspiration par télédétection avec mesures au sol	N	Madagascar		A/ M	(Carrière et al. 2024)
	Modélisation des effets du reboisement sur le bilan hydrique d'un bassin versant	R	Corridor Ankeniheny-Zahamena (CAZ)		J	(Ghimire et al. 2015)
Précipitations	Carte des isohyètes de Madagascar	N	Madagascar			(Ferry 1991)
	Précipitations dans le Sud-Ouest de Madagascar	R	Sud de Madagascar			(Ferry 1998)
	Variabilité interannuelle des caractéristiques des précipitations dans le sud-ouest de Madagascar	R	Sud-Ouest de Madagascar			(Randriamahefasoa and Reason 2017)
	Évaluation statistique de plusieurs ensembles de données de précipitations maillées	N	Madagascar			(Randriatsara et al. 2022a)

[1] Echelle : N : Nationale ; R : Régionale ; L : Locale ; [2] Pas de temps : A : Annuel ; M : Mensuel ; J : Journalier : H : Horaire

Table 2.3. (Suite) Synthèse des recherches hydrologiques à Madagascar après les années 1990.

Thématiques	Titre/ Méthodologie	Echelle[1]	Zone d'études	Area	Pas de Temps[2]	Références
Précipitations (suite)	Comparaison des sorties de modèles climatiques avec observations de précipitations	N	Madagascar		A	(Randriatsara et al. 2023)
	Combinaison de jeux de données pour des estimations de précipitations améliorées	N	Madagascar		M	(Ollivier et al. 2023)
	Analyse de séries chronologiques d'événements hydrométéorologiques extrêmes	N	Madagascar			(Vecchia and Eunhea 2019)
	Intégration de données CHIRPS et GRACE pour l'étude de la variabilité hydroclimatique	R	Betsiboka river basin	49 000 km²	M	(Bigot et al. 2021)
Débits	Combinaison d'imagerie satellite et modélisation pour l'estimation des débits de petits bassins	R	Tsiribihina river	49 800 km²	M	(Andriambeloson et al. 2020)
	Analyse de la vulnérabilité aux inondations par approche multi-agents	R	Sud de Madagascar			(Rakotoarisoa et al. 2018)
Ecoulements souterrains	Reconnaissance hydrogéologique par méthode électrique et électromagnétique	L	Lac Ihotry, Sud-Ouest de Madagascar			(Rasolomanana 1997)
	Utilisation de traceurs isotopiques et mesures piézométriques pour l'étude des aquifères	L	Plateau de Mahafaly		H	(Carrière et al. 2023)
	Mise en place d'un réseau de surveillance des eaux souterraines à long terme	L	Bassin versant d'Ankazomanga/ Mandrare		H	(Carrière et al. 2021)
	Application de techniques de cartographie hydrogéologique avec données limitées	R	North of Madagascar		M	(Davies 2009)
	Utilisation de techniques SIG pour la cartographie du potentiel en eau souterraine	R	Great South of Madagascar			(Serele et al. 2020)
	Évaluation rapide des risques géologiques et hydrologiques en milieu urbain	L	Antananarivo	86.4 km²	E	(Ciampalini et al. 2019)

[1] Echelle : N : Nationale ; R : Régionale ; L : Locale ; [2] Pas de temps : A : Annuel ; M : Mensuel ; J : Journalier : H : Horaire

Table 2.3. (Suite) Synthèse des recherches hydrologiques à Madagascar après les années 1990.

Thématiques	Titre/ Méthodologie	Echelle[1]	Zone d'études	Area	Pas de Temps[2]	Références
Changement climatique (CC)	Analyse de données climatiques historiques pour l'évaluation des causes de sécheresse	R	Great South of Madagascar		M	(Harrington et al. 2022)
	Application de modèles climatiques CMIP6 pour la projection des caractéristiques de sécheresse	R	Great South of Madagascar		M	(Rabezanahary and Andrianarimanana 2024)
	Combinaison de réseaux de neurones et modèle SWAT pour la prédiction de changements hydrologiques	R	Mangoky	55 750 km²	M	(Rabezanahary et al. 2021)
	Modélisation des ressources en eau futures avec intégration de scénarios de changement	N	MRBM	320 373 km²	A	(Rakotoarimanana et al. 2024a)
Changement de couverture végétale (LUCC)	Utilisation d'un modèle hydrologique maillé pour l'évaluation de l'impact de la déforestation	L	Bassin versant de la Lokoho	1050 km²	30'	(Randriamaherisoa and Binard 1992)
	Quantification des incertitudes dans la modélisation des services écosystémiques	R	Corridor Ankeniheny-Zahamena (CAZ)	381 000 ha	M	(Soesbergen and Mulligan 2018)
	Intégration de SIG et télédétection dans un modèle hydrologique de bassin rural	R	Bassin versant de la Lokoho	1050 km²	30'	(Randriamaherisoa et al. 1993)
	La régénération forestière peut contribuer positivement aux services écosystémiques hydrologiques locaux : Implications pour la restauration des paysages forestiers	L	Corridor Ankeniheny-Zahamena (CAZ)			(van Meerveld et al. 2021)
Gestion de ressources en eau	Quand la gestion communautaire des ressources en eau va trop loin : Pauvreté et perte de pouvoir dans le sud de Madagascar	R	Great South of Madagascar			(Marcus 2007)
	Revue systématique de la littérature sur l'évaluation des ressources en eau	N	MRBM	320373 km²	_	(Rakotoarimanana et al. 2022)
	Analyse comparative des pratiques de gestion des bassins versants	N	Madagascar		_	(Rakotoarimanana and Hiroshi 2022)

[1] Echelle : N : Nationale ; R : Régionale ; L : Locale ; [2] Pas de temps : A : Annuel ; M : Mensuel ; J : Journalier : H : Horaire

2.7. Hypothèses et objectifs de la recherche

2.7.1. Hypothèses

Compte tenu des lacunes identifiées dans la modélisation hydrologique à Madagascar, particulièrement le manque d'études à échelle locale et le besoin d'analyses plus fines des dynamiques hydrologiques, et considérant la sous-représentation des recherches dans le Nord-Est malgache ainsi que les limitations en termes de données et d'instrumentation, les hypothèses suivantes ont été formulées pour guider cette recherche.

- Les données satellitaires à haute résolution spatiale constituent une alternative prometteuse aux mesures pluviométriques terrestres, lesquelles sont principalement limitées par la distribution spatiale hétérogène des stations de mesure au sol.
- Les comportements hydrologiques à l'échelle des méso-bassins dans la région peuvent être caractérisés et prédits efficacement à partir d'un nombre limité de facteurs clés, réduisant ainsi la nécessité d'une instrumentation extensive.
- Dans le bassin versant caractérisé par un climat tropical humide, les conditions hydrologiques, pédologiques et topographiques tendent à favoriser la prédominance des écoulements de subsurface (**SSF**) dans la génération des débits.
- Les données génériques et une intervention de terrain minimale permettent de maintenir un observatoire hydrologique fonctionnel et représentatif du bassin.
- Les modifications d'occupation des sols projetées pour un bassin versant malgache soumis à un climat tropical humide pourraient influencer la dynamique des crues, avec des effets potentiels sur l'amplitude et la fréquence des pics de débits à moyen terme (2050) et long terme (2090).

2.7.2. Objectifs

L'objectif global de cette thèse est de comprendre le fonctionnement hydrologique d'un bassin versant sous climat tropical humide dans le Nord-Est de Madagascar (le bassin d'Ankavia) et d'étudier ses altérations suite aux changements d'occupation des sols et au changement climatique, dans une perspective de gestion intégrée des ressources en eau.

Les objectifs spécifiques sont les suivants :

1. Evaluer et identifier les produits satellitaires de précipitation qui reproduisent au mieux les caractéristiques pluviométriques du bassin versant ;
2. Analyser les groupes de facteurs qui régissent les comportements hydrologiques à l'échelle des méso-bassins ;
3. Etudier les effets des différents types d'occupation du sol sur les réponses hydrologiques à l'échelle des micro-bassins ;
4. Identifier et paramétrer un modèle hydrologique adapté aux caractéristiques hydrologiques et aux variabilités du bassin versant, tout en veillant à un équilibre entre les coûts et les performances ;
5. En se basant sur les simulations de scénarios d'occupation de sols et climatiques pour les périodes 2040–2060 et 2080–2100, déterminer les répercussions de ces changements sur le régime hydrologique de la région étudiée.

3. Chapitre 3 : Zone d'études

Ce chapitre vise à présenter les sites d'études selon une échelle géographique croissante. Il commence par un aperçu général de l'île de Madagascar, puis se focalise sur la région SAVA, située dans le nord-est du pays. Ensuite, il propose une analyse détaillée du bassin versant d'Ankavia, en décrivant ses propriétés géomorphologiques, sa couverture végétale, son climat, sa géologie et ses caractéristiques pédologiques, ainsi que les spécificités de chaque sous-bassin. Le chapitre se termine par une présentation des dispositifs et stations de mesure utilisés pour collecter les différents paramètres exploités dans ce mémoire.

3.1. L'île de Madagascar

3.1.1. Localisation

Madagascar, située à environ 400 km des côtes du Mozambique, est la quatrième plus grande île du monde, couvrant une superficie de 587 041 km² et s'étendant sur 1 600 km de long et 570 km de large (Chaperon et al. 1993) (Figure 3.1). La capitale, Antananarivo, est située au centre du pays, à environ 2 000 km au sud de l'équateur.

3.1.2. Relief

La grande île est traversée asymétriquement par une chaîne de montagnes, le point culminant se situant à l'est, formant ainsi la région des « Hauts Plateaux ». Les reliefs sont plus prononcés sur la côte est que sur la côte ouest. On y trouve également trois massifs montagneux du nord au sud (Tsaratanana, Ankaratra, Andringitra). Le changement rapide de relief et la proximité de l'océan sont des facteurs déterminants qui influencent les conditions climatiques de l'île (Chaperon et al. 1993).

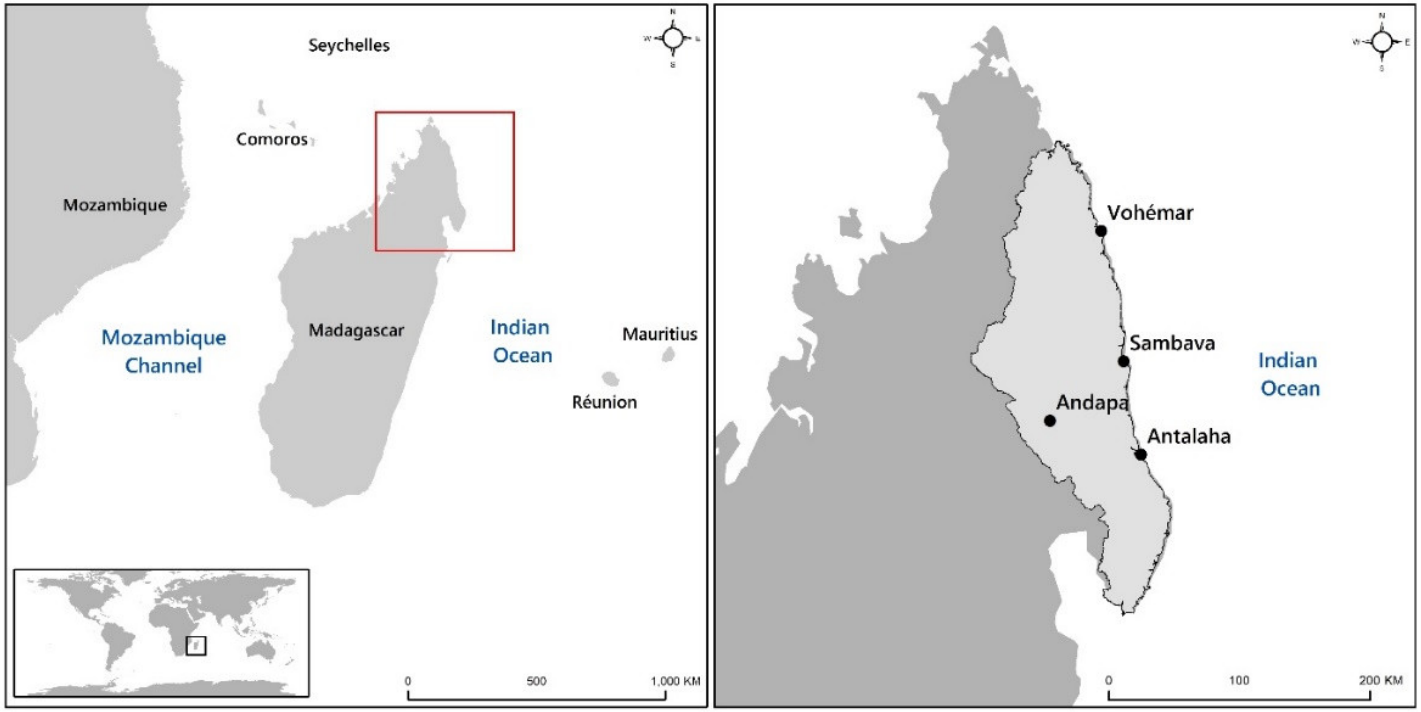

Figure 3. 1. Carte de localisation de Madagascar (à gauche) et de la région SAVA (à droite). Source : OpenStreetMap

3.1.3. Fonctionnement climatique

Le mouvement des masses d'air dans la troposphère près de Madagascar est régi par deux grands centres d'action : la Zone de Convergence Intertropicale (ZCIT) et la cellule anticyclonique océanique semi-permanente (Figure 3.2) (Tadross et al. 2008). La ZCIT, dont le déplacement méridien est lié au mouvement apparent du soleil, joue un rôle particulièrement important à la longitude de Madagascar, provoquant l'alternance des saisons chaudes et froides. Quant à la cellule anticyclonique semi-permanente, située au sud des Mascareignes, elle n'est pas continue dans le temps et dans l'espace. Elle est influencée par le courant de perturbation polaire, qui prend naissance du côté sud-est de la cellule anticyclonique de l'Atlantique (anticyclone de Sainte-Hélène) et qui est souvent suivi par des anticyclones mobiles. Ces deux systèmes atmosphériques régissent les alizés et les vents de nord-ouest qui affectent le climat de Madagascar (Chaperon et al. 1993; Joly 1941).

Les alizés, vents soufflant de l'est à l'est-sud-est, sont persistants toute l'année du côté équatorial de l'anticyclone de l'océan Indien. Ils proviennent de masses d'air polaire méridional qui se sont réchauffées en traversant des mers tropicales, entraînant une humidité relative élevée, des températures chaudes et une grande instabilité lorsqu'ils atteignent la grande île. Cela favorise la formation d'épais nuages et d'abondantes précipitations (Jury et al. 2003). Les vents de nord-ouest sont observés au nord de la ZCIT lorsqu'elle se trouve sur Madagascar pendant l'été austral. Instables, chauds et humides en raison de leur long parcours au-dessus des mers chaudes, ces vents connus sous le nom de "mousson du nord-ouest" alternent avec les alizés durant la saison chaude, selon la position de la ZCIT. De plus, des vents d'ouest intermittents soufflent dans le sud de l'île, causés par le passage de dépressions provenant des perturbations du front polaire. Bien que non persistants, ces vents apportent un air plus frais dans le sud de Madagascar. Occasionnellement, des incursions d'air froid en provenance des latitudes polaires peuvent provoquer des baisses de température importantes (Chaperon et al. 1993).

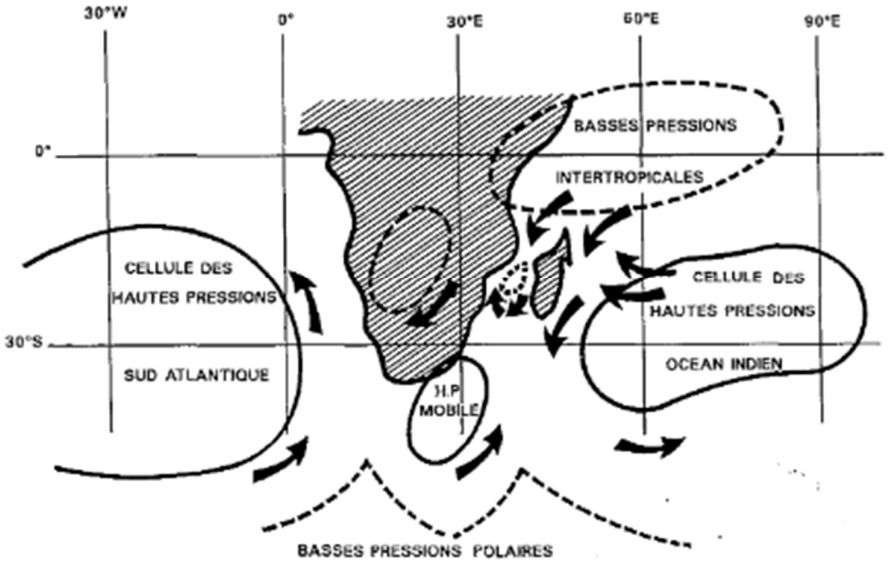

Figure 3. 2. Schématisation des principaux centres d'action réglant le climat à Madagascar. Source : Chaperon et al. (1993)

La situation géographique de Madagascar l'expose à divers aléas climatiques, notamment les cyclones tropicaux (Jury et al. 2003). La saison cyclonique s'étend généralement de décembre à mars, l'île se trouvant dans une zone propice à la formation de ces puissantes tempêtes qui se nourrissent de l'air chaud et humide des mers environnantes. Bien que la ZCIT joue un rôle crucial dans la saison des pluies, elle n'est pas l'unique facteur déclencheur des cyclones. Plusieurs conditions doivent être réunies pour leur formation : (i) la présence de la ZCIT créant une zone de convergence des masses d'air chaudes et humides, (ii) une perturbation atmosphérique initiale dans les basses couches pour amorcer la cyclogenèse, et (iii) le renforcement de l'un des anticyclones (de l'océan Indien ou un anticyclone mobile issu du courant de perturbation polaire) pour maintenir le mouvement tourbillonnaire du cyclone (Jury et al. 2003).

Le climat de Madagascar se caractérise par deux saisons distinctes : une saison des pluies de novembre à avril, et une saison sèche et plus fraîche de mai à octobre (Chaperon et al. 1993; Joly 1941). Le relief contrasté de l'île crée un gradient de précipitations marqué entre l'Est et l'Ouest. Les hauts plateaux à l'Est induisent un effet orographique, forçant l'humidité provenant de l'océan Indien à se déverser avant d'atteindre la côte Ouest, ce qui engendre des conditions plus sèches dans cette région. Les précipitations varient considérablement : la côte Est peut enregistrer jusqu'à 3 700 mm de pluie par an, tandis que l'Ouest ne reçoit qu'environ 400 mm. Un gradient pluviométrique Nord-Sud existe également, le Sud étant nettement plus sec en raison de la variation de latitude (Figure 3.3) (Joly 1941). Ces disparités climatiques (Figure 3.4) influencent la distribution des biomes : la côte Est est recouverte d'une forêt tropicale humide, alors que la côte Ouest est caractérisée par une végétation adaptée à des conditions plus arides (Ganzhorn et al. 2001).

3.1.4. Tendance climatique

Les projections climatiques pour Madagascar indiquent une augmentation significative des températures d'ici 2050, avec une hausse des températures minimales de +1,4°C à +2,0°C et des températures maximales de +1,5°C à +2,3°C (Figure 3.5) (Hannah et al. 2008). Ces tendances s'accélèrent dans la seconde moitié du siècle : à l'horizon 2100, selon le scénario RCP 8.5, ces augmentations pourraient atteindre +3,5°C à +5,0°C, avec des impacts particulièrement marqués dans les régions côtières et les zones de basse altitude. En termes de précipitations, les modèles projettent une modification profonde du régime pluviométrique avec une augmentation de l'intensité des pluies durant la saison humide (+5% à +15% d'ici 2050) et une diminution pendant la saison sèche (-10% à -20%), accentuant ainsi la saisonnalité déjà marquée (Figure 3.6) (Tadross et al. 2008). Cette évolution devrait s'accompagner d'une augmentation de la fréquence des événements climatiques extrêmes, notamment des cyclones plus intenses et des périodes de sécheresse prolongées, particulièrement dans le sud de l'île (Tadross et al. 2008).

3.1.5. Hydrographie

Les rivières de Madagascar sont principalement alimentées par l'écoulement de surface, l'écoulement hypodermique, et le drainage des couches d'altération, tandis que les nappes souterraines y contribuent très peu (Aldegheri 1972). Le régime des cours d'eau est largement influencé par le relief, lui-même déterminé par la géologie de la région. De plus, la nature des roches, façonnée par les mouvements tectoniques, influe sur la configuration actuelle du relief (Chaperon et al., 1993).

Ainsi, cette île-continent, à la topographie et au climat variés, peut être subdivisée en neuf régions hydrologiques distinctes (Figure 3.7), chacune présentant des régimes hydrologiques propres, influencés par ses caractéristiques géomorphologiques, géologiques et de couverture végétale.

- **Extrême Nord et la montagne d'Ambre** : Les bassins versants sont allongés avec des pentes fortes, des précipitations abondantes et des débits d'étiage relativement soutenus. Souvent de petite taille (maximum 100 km²), ils reposent sur des sols basaltiques fissurés, favorisant la perméabilité et réduisant l'intensité des crues.
- **Nord-Est** : Cette région partage des caractéristiques similaires à l'Extrême Nord, mais avec un relief moins accentué. Les cours d'eau s'organisent de manière complexe autour des formations cristallines altérées du massif, entraînant des pentes fortes et une rupture brutale au niveau des sédiments côtiers.
- **Tsaratanana** : Le relief très accidenté engendre des rivières avec un profil en long particulier et des cours supérieurs à forte pente. Les vallées s'ouvrent en fonds plats dans les plaines littorales, et les crues brutales sont courantes en raison des fortes pentes et des précipitations intenses.
- **Versant Est :** Caractérisée par un relief escarpé et une forêt dense, cette région reçoit les précipitations les plus élevées de l'île. Les cours d'eau, courts et au profil accentué, connaissent des crues violentes, souvent causées par des cyclones, et des débits d'étiage soutenus grâce à une évapotranspiration potentielle presque toujours satisfaite.

- **Nord-Ouest et de l'Ouest** : Les fleuves sont abondants avec des crues importantes et des débits d'étiage soutenus. Le réseau hydrographique est complexe, incluant les fleuves des Hauts-Plateaux et les rivières côtières marécageuses. Les crues brutales sont fréquentes en raison des pentes.
- **Hautes Terres Centrales** : Cette région présente un relief moins accidenté avec une couverture végétale de savane. Les précipitations sont modérées, les débits de crue moins prononcés, et les débits d'étiage plus faibles. Les bassins à pentes relativement faibles et les rizières marécageuses contribuent à l'écrêtement des crues.
- **Centre Hautes Terres Méridionales (Centre-Sud)** : Avec un climat semi-aride et un relief accidenté, cette région reçoit des précipitations moins abondantes. Les débits de crue sont rapides et les débits d'étiage très faibles. Le régime hydrologique est similaire à celui des Hauts-Plateaux, mais avec une altitude plus variable et des vallées très étroites et profondes.
- **Sud-Ouest** : Les terrains très perméables font que le lit des cours d'eau est généralement sec une grande partie de l'année. Les crues sont brutales lors de la saison des pluies, causées par des précipitations soudaines et intenses.
- **Sud** : Cette région aride reçoit des précipitations très faibles. Les crues sont brutales et concentrées, avec des débits d'étiage extrêmement faibles. Les rivières sont rares et les eaux souvent perdues dans les sables et calcaires fissurés. Les cours d'eau traversent des seuils rocheux et sont enfoncés dans les alluvions, entraînant des crues à débits de pointe important.

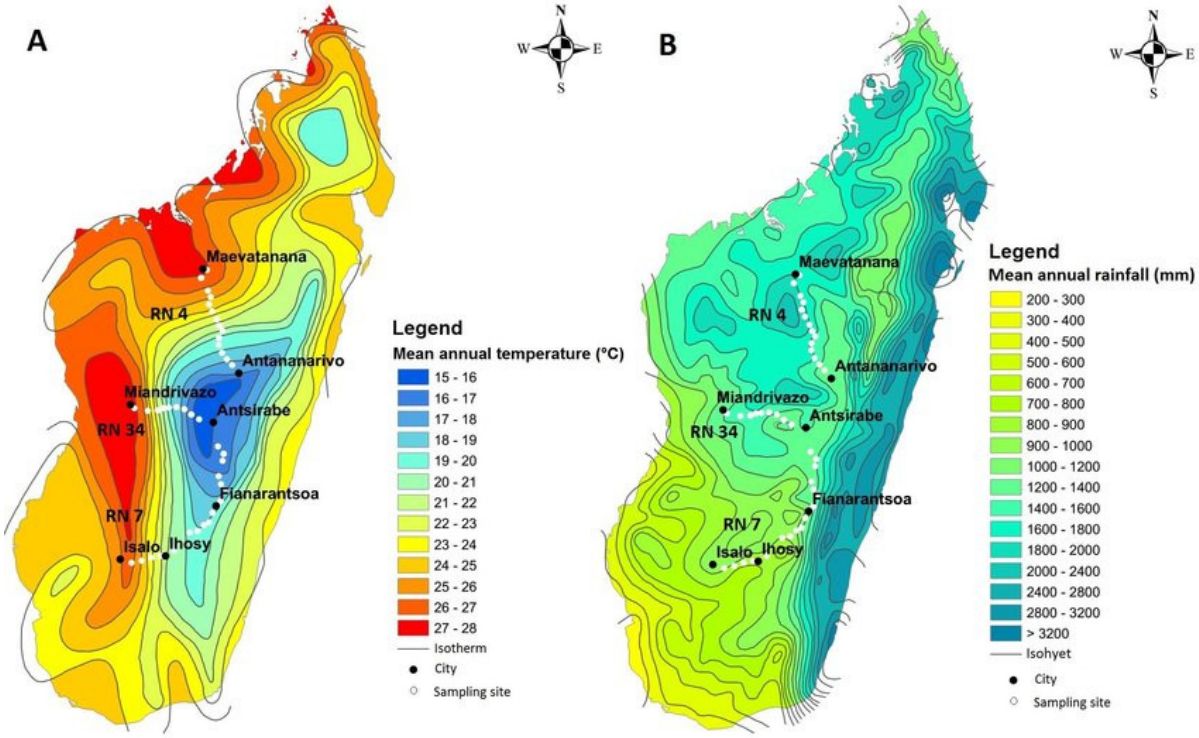

Figure 3. 3. Carte de Madagascar avec isohyètes (A : Température moyenne annuelle ; B : Précipitations moyennes annuelles). Les données ont été obtenues à partir de la base de données WORLDCLIM (Hijmans et al. 2005).

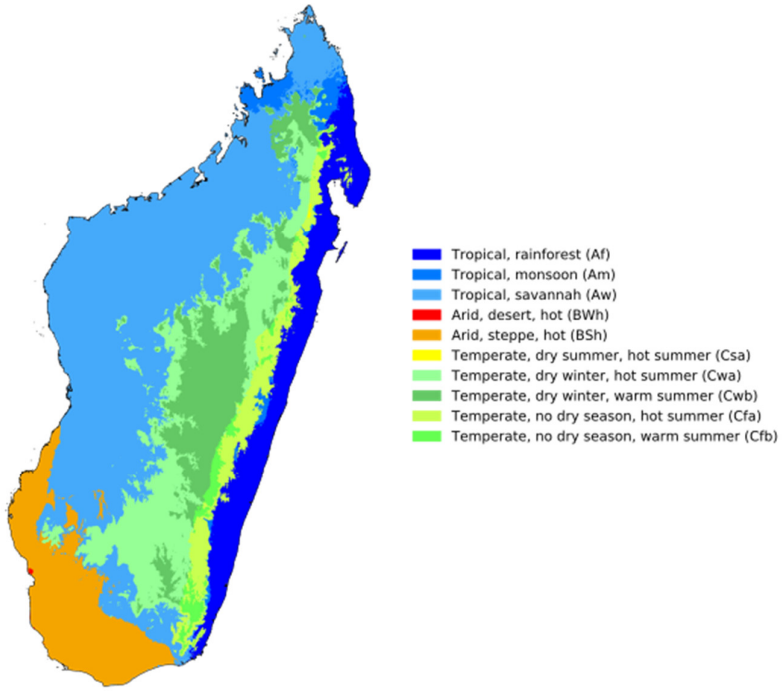

Figure 3. 4. Carte de classification climatique de Köppen-Geiger pour Madagascar (1980 - 2016). Source : Beck et al. 2018.

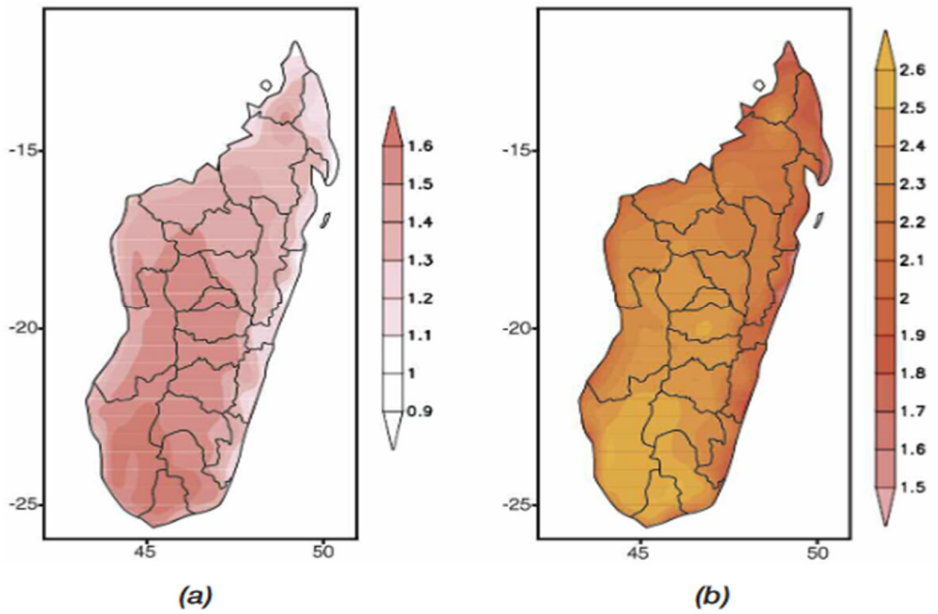

Figure 3. 5. Valeurs minimales (a) et maximales (b) des projections de l'augmentation de la température moyenne annuelle (°C) obtenues à partir de 13 modèles climatiques globaux et pour la période centrée en 2055 (Source : DGM, 2008).

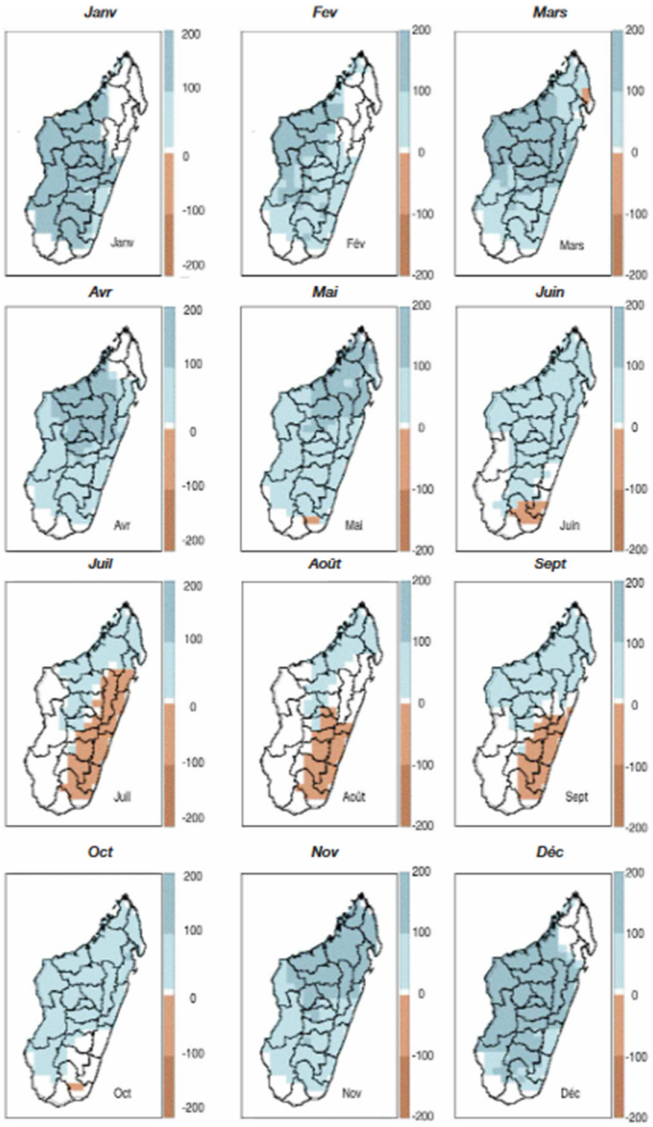

Figure 3. 6. Changements (Médiane) des précipitations mensuelles (mm/mois) obtenus à partir de la mise à l'échelle de 6 modèles globaux (période centrée en 2055). Les régions où 3 modèles ont donné des augmentations des précipitations et les 3 autres des diminutions sont laissées en blanc. Il en est de même pour les régions où les augmentations sont <10 mm/mois (Source : DGM, 2008).

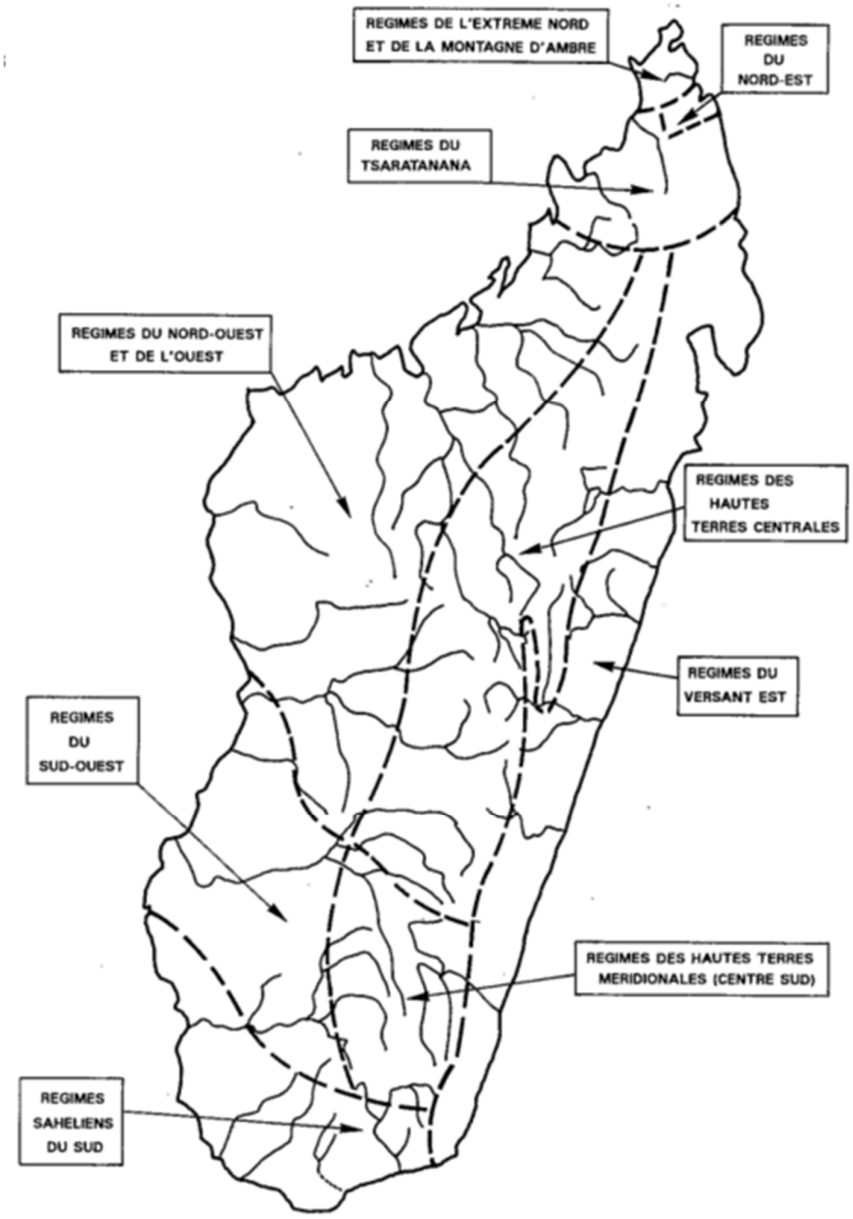

Figure 3. 7. Principaux régimes hydrologiques de Madagascar. (Source : Chaperon, 1993).

3.2. Cadre de l'étude : Région SAVA

3.2.1. Géographie

La région SAVA se situe au Nord-Est de Madagascar entre les longitudes 49°00' et 50°30' Est; et entre les latitudes 13°00' et 16° 00' Sud (Figure 3.1). L'acronyme SAVA est composé des initiales des quatre districts qui la constituent, à savoir Sambava (chef-lieu), Antalaha, Vohémar (ou Iharana) et Andapa. Elle est localisée dans la province d'Antsiranana et ne représente que 4 % de la superficie totale du pays. En 2018, la population était d'environ 1,1 million d'habitants, faisant de SAVA la 10ème région la plus peuplée de Madagascar (INSTAT 2020).

3.2.2. Relief et occupation de sol

Le relief de la région SAVA se caractérise par trois zones distinctes d'ouest en est, chacune présentant des couvertures de sol spécifiques. La zone montagneuse occidentale, s'élevant de 250 à plus de 2 000 m d'altitude, affiche un relief accidenté et est principalement couverte de forêts denses humides sempervirentes (Clark 2012). La zone intermédiaire, entre 60 et 250 m d'altitude, abrite des périmètres irrigués et des plantations de café et de vanille. Enfin, la zone littorale s'étend sur 8 à 15 km depuis la côte, avec une altitude de 0 à 60 m, et est dédiée aux cultures vivrières, notamment le riz.

La végétation de la région est diverse, avec environ 50% de prairies côtières, de pseudo-steppes et/ou de savanes, tandis que les terres cultivées ne représentent que 9% de la superficie totale (CPGU 2012). La région SAVA abrite également trois réserves naturelles importantes : Masoala, Marojejy et Anjanaharibe-Sud, contribuant à la richesse écologique de cette région aux paysages variés.

3.2.3. Fonctionnement climatique

La station climatique d'Antalaha fournissait des données mensuelles sur les précipitations et d'autres paramètres climatiques pour la période de 1960 à 2016. La

région SAVA, et par extension, le nord-est de Madagascar se caractérise par un climat tropical chaud et humide avec deux saisons distinctes. La saison chaude et pluvieuse, de novembre à avril, présente une moyenne annuelle de précipitations dépassant 2200 mm, tandis que la saison de mai à octobre est plus fraîche et moins pluvieuse. Les précipitations proviennent principalement des courants d'est de l'océan Indien, amplifiées par l'effet orographique (Tadross et al. 2008). La saison des pluies est marquée par de fortes averses, des vents violents et un risque accru de tempêtes tropicales et de cyclones. Les tempêtes tropicales (vents de 60 à 110 km h^{-1}) surviennent en moyenne tous les deux ans, tandis que les cyclones de catégorie 1 (vents de 110 à 160 km h^{-1}) ont une période de retour de 7 ans (CPGU 2012). Ces phénomènes ont des impacts plus importants dans le sud de la région, notamment dans le district d'Antalaha. De plus, la région est également sujette à des périodes de sécheresse de durée variable, particulièrement dans les districts d'Antalaha et de Vohémar, avec des sécheresses modérées ayant une période de retour moyenne de 5 ans (CPGU 2012). Cependant, la région ne connaît pas de saison extrêmement sèche.

3.2.4. Géologie

Dans la région SAVA, on distingue deux grandes catégories de terrains : les terrains sédimentaires et les terrains cristallins. Les terrains sédimentaires se sont principalement formés par des dépôts fluviaux et éoliens. Ces terrains relativement récents se sont superposés à des couches plus anciennes et constituent la majeure partie d'une étroite plaine côtière (Figure 3.8). Cette plaine, reposant en grande partie sur un socle précambrien, est caractérisée par ces terrains sédimentaires. Quant aux terrains cristallins, ils sont constitués de différents types de roches (granites, gabbros, migmatites) qui se sont formées en profondeur ou à la surface de la Terre, certaines étant d'origine magmatique.

Le nord-est de Madagascar est composé de plusieurs domaines de socle précambrien, dont la plupart ont subi un métamorphisme de haut grade, ainsi que de roches ignées (Figure 3.8). Ces domaines sont localement recouverts par des

roches sédimentaires non métamorphiques, ainsi que des métasédiments de bas grade. Dans la région d'Antalaha, deux séquences de couverture différentes reposent sur des roches métamorphiques et ignées de haut grade issues de la ceinture néoprotérozoïque de *Bemarivo* et du craton archéen d'*Antongil*. Le groupe d'*Andrarona*, la plus ancienne de ces deux séquences de couverture, est constitué de roches métasédimentaires de faible grade. Quant à la formation d'*Ampohafana*, la plus récente, elle est formée de roches sédimentaires non métamorphiques (Bauer et al. 2011).

3.2.5. Pédologie

La région SAVA est principalement constituée de sols de type ferralitique qui présentent plusieurs variations : sols ferralitiques sous forêts (*ati-ala* en malgache), sous jachère (*savoka*) et sous prairie (Figure 3.9). Ces sols altérés sont de couleur rouge ou jaune et sont couramment retrouvés dans les régions tropicales humides (Martinez et Souza 2020). Ils sont considérés comme des vestiges du passé, présents aujourd'hui dans des zones au climat chaud et humide. Les sols ferralitiques sont caractérisés par un bon drainage et une bonne perméabilité (CREAM 2013).

3.2.6. Hydrologie

La région Nord-Est de Madagascar possède un réseau hydrographique dense avec des cours d'eau souvent ramifiés. Les régimes hydrologiques des rivières de la région SAVA s'inscrivent dans la catégorie des cours d'eau du versant Est (Figure 3.7). En raison de la topographie accidentée, les cours d'eau présentent des pentes abruptes en sortie de massif, créant ainsi des chutes d'eau et des gorges impressionnantes (Aldegheri 1972). Cependant, en approchant la côte, les pentes s'adoucissent, permettant la formation de méandres. Les rivières qui traversent la région partagent trois caractéristiques communes : (i) elles s'étendent sur des distances relativement courtes ; (ii) elles drainent des périmètres allongés et étroits ; (iii) elles se jettent toutes dans l'océan Indien.

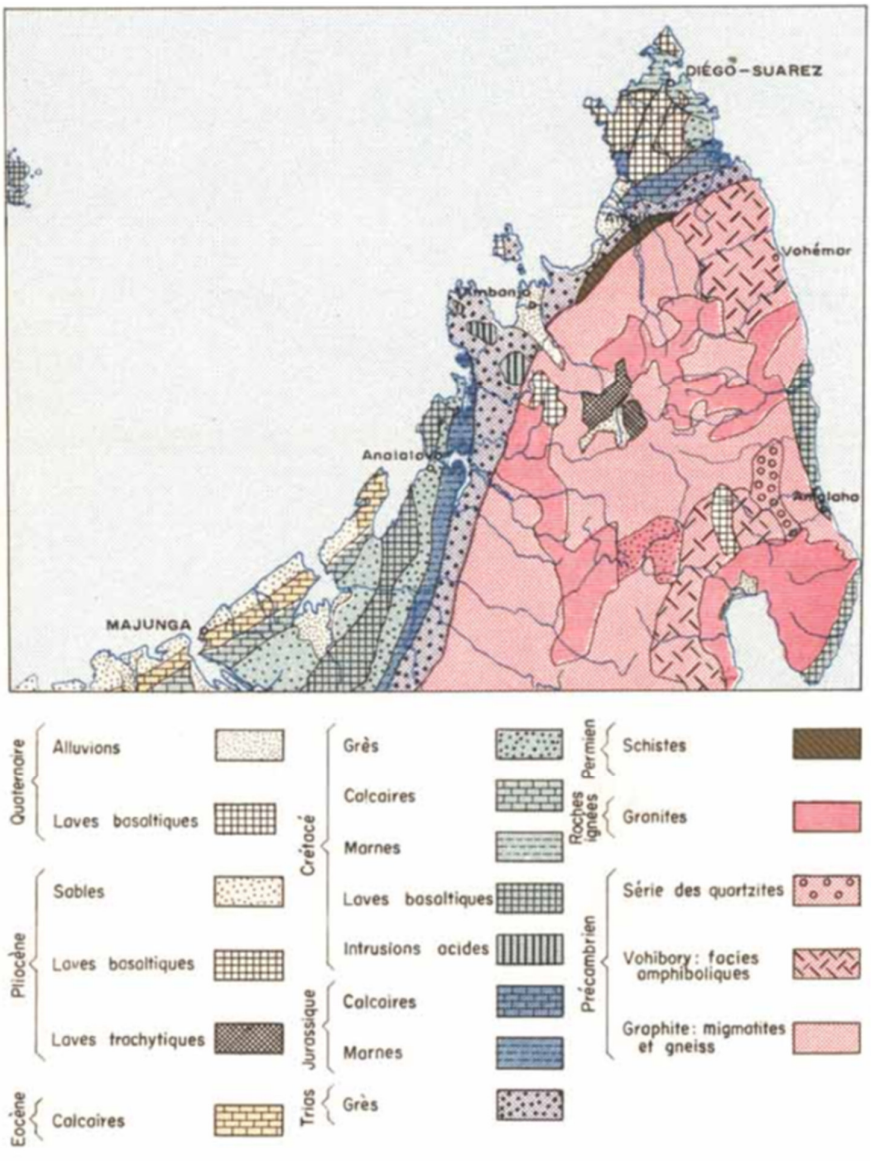

Figure 3. 8. Géologie et lithologie – Partie Nord de Madagascar, Source : cartothèque IRD (http://sphaera.cartographie.ird.fr/, mai 2024)

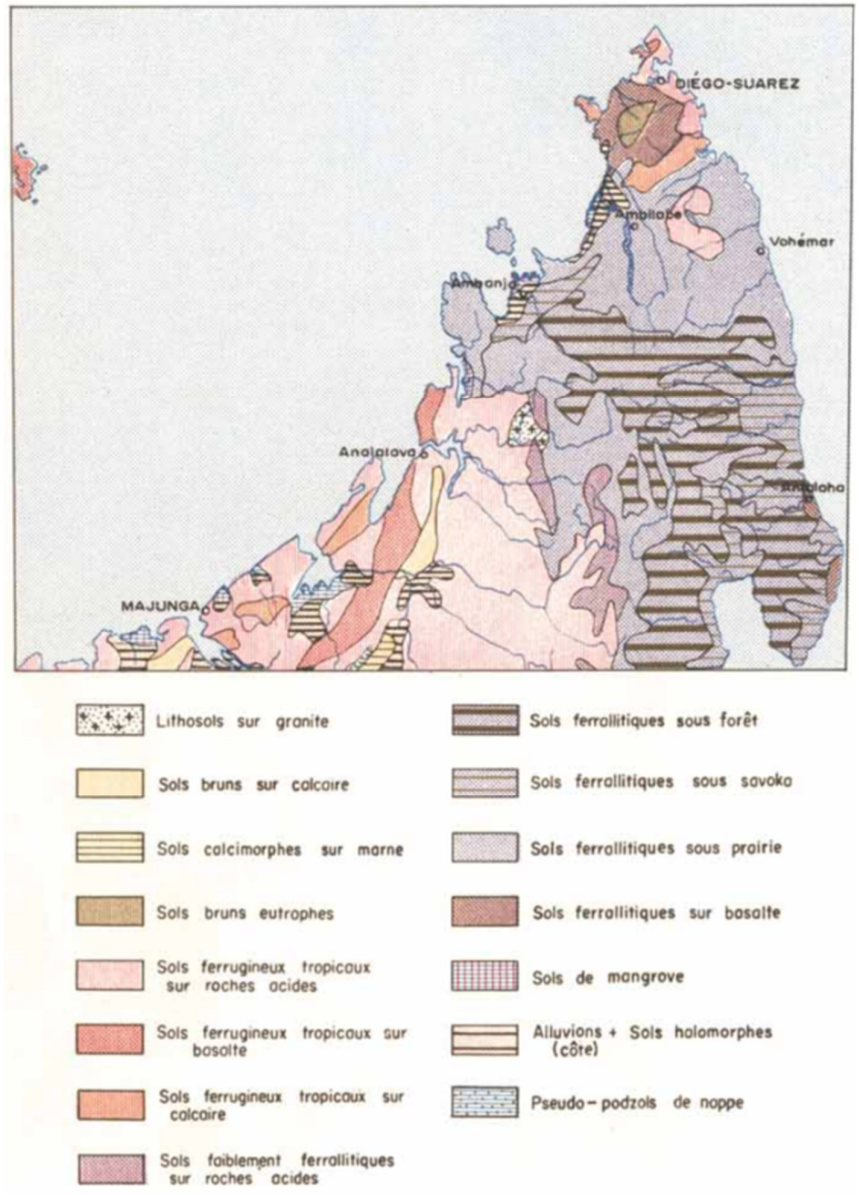

Figure 3. 9. Pédologie – Partie Nord de Madagascar, Source : cartothèque IRD (http://sphaera.cartographie.ird.fr/, mai 2024)

3.3. Bassin versant d'Ankavia

3.3.1. Localisation

Le bassin d'Ankavia, situé dans la région SAVA, s'étend entre les longitudes 49°50' – 50°20' Est et les latitudes 15°00' – 15°20' Sud (Figure 3.10). Le bassin couvre une superficie de 1 116 km² en prenant comme exutoire la station de captage de la JIRAMA (Jiro sy Rano Malagasy, Eau et Électricité de Madagascar) située à Antsahamanenona. Il est composé de quatre communes administratives : une urbaine (Antalaha) et trois rurales (Antombana, Marofinaritra, Manakambahiny). La rivière d'Ankavia prend sa source dans les hautes montagnes de Makira et de Masoala, et suit la direction Sud-Ouest/Nord-Est, pour rejoindre la rivière Ankavanana, avant de se jeter dans l'océan Indien. En amont du bassin, trois affluents, Ankaviabe, Sahafihitry et Antsahovy, forment les trois principaux sous-bassins du bassin d'Ankavia.

Il est important de souligner que l'analyse complète du bassin est présentée dans le **chapitre 5**, tandis que les **chapitres 7** et **8** se concentrent spécifiquement sur le sous-bassin de Sahafihitry.

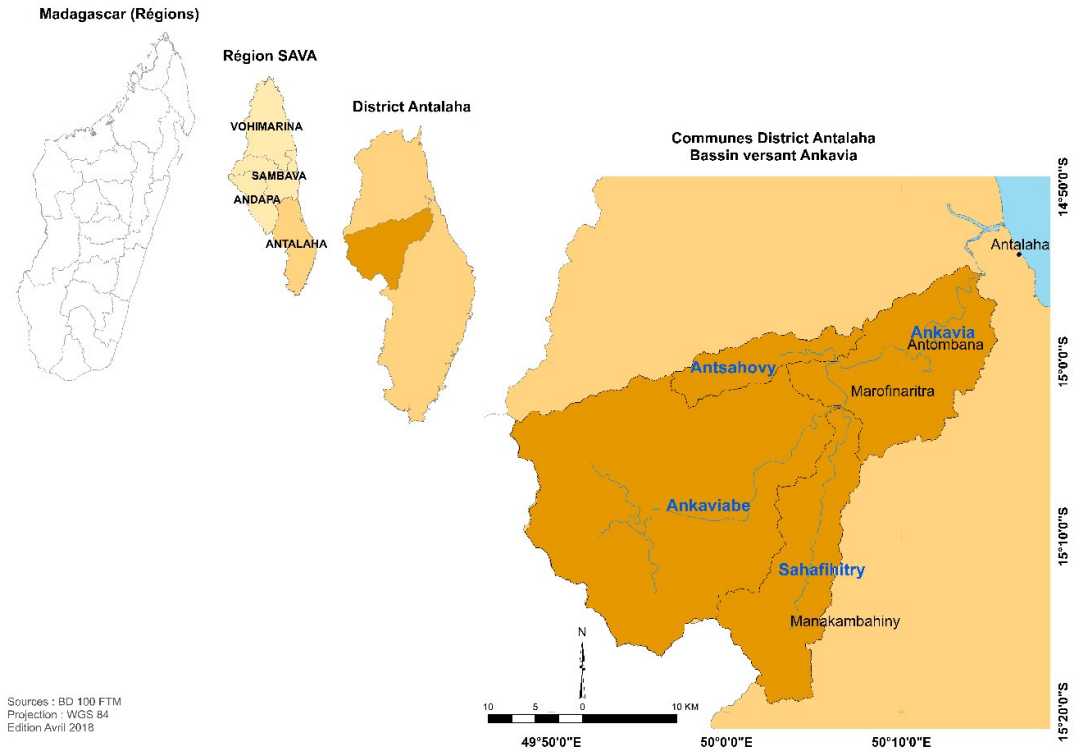

Figure 3. 10. Localisation du bassin versant d'Ankavia. Source : BD 100 FTM

3.3.2. Relief

Le bassin est caractérisé par une topographie contrastée, présentant des reliefs accidentés en amont et des terrains à faibles pentes en aval. La partie supérieure du bassin est dominée par de hautes montagnes et des collines escarpées, tandis que la partie inférieure s'aplanit progressivement vers la côte. L'altitude du bassin varie considérablement, allant de 14 m à l'exutoire jusqu'à 1 469 m dans les parties montagneuses les plus élevées (Figure 3.11).

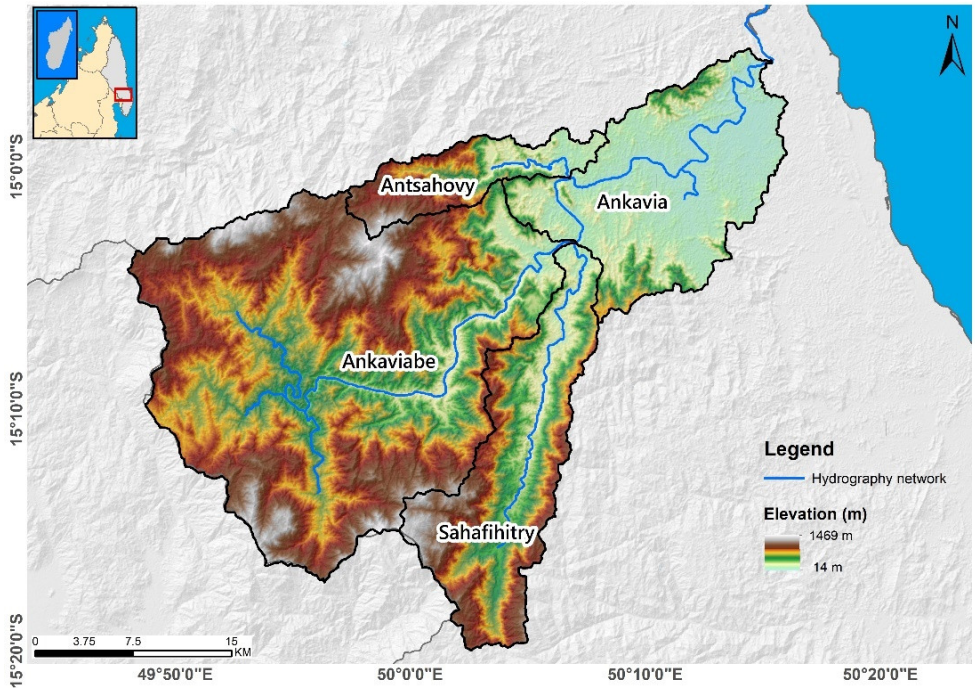

Figure 3. 11. Topographie du bassin versant d'Ankavia et le réseau hydrographique. Source : Digital Elévation Model (Earth Resources Observation And Science (EROS) Center 2017)

3.3.3. Climat

À l'échelle du bassin, le climat s'aligne sur la tendance générale observée dans la région SAVA (Figure 3.12). Sur la période de 2018 à 2020, la pluviométrie moyenne annuelle s'établit à 2 541 mm, dont 75% se concentrent pendant la saison pluvieuse, qui s'étend de novembre à avril. Le mois de mars se distingue comme le plus pluvieux de l'année. La température varie de 22,3°C à 27,7°C avec une moyenne de 25,4°C tout au long de l'année.

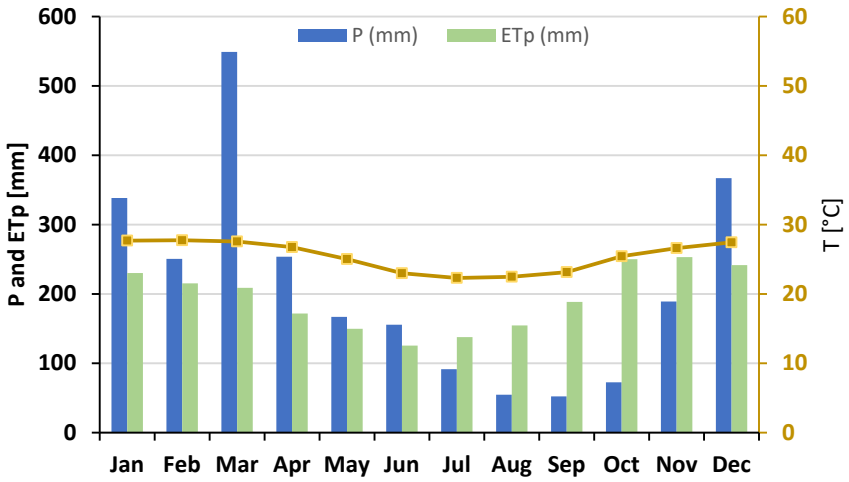

Figure 3. 12. Moyenne mensuelle des paramètres climatiques dans le bassin versant d'Ankavia, à partir des données recueillies au niveau de la station climatique de Marofinaritra pendant la période 2018-2020. Source : GIRE SAVA

3.3.4. Géologie

La géologie du bassin est complexe et caractérisée principalement par des roches sédimentaires et granitiques (Figure 3.13). Elle est constituée d'une mosaïque de roches précambriennes, principalement des domaines de socle métamorphiques de haut grade recouverts par des roches sédimentaires non métamorphiques et des métasédiments de faible grade peu altérés (Bauer et al. 2011). La partie sud du

bassin versant est constituée principalement de monzogranite, une roche magmatique intrusive, souvent associée à de la granodiorite. La partie nord, quant à elle, est formée de leucogranodiorite, une variété de granite à texture claire. Il est intéressant de noter que les gneiss (roches métamorphiques) s'associent fréquemment aux monzogranites dans cette partie.

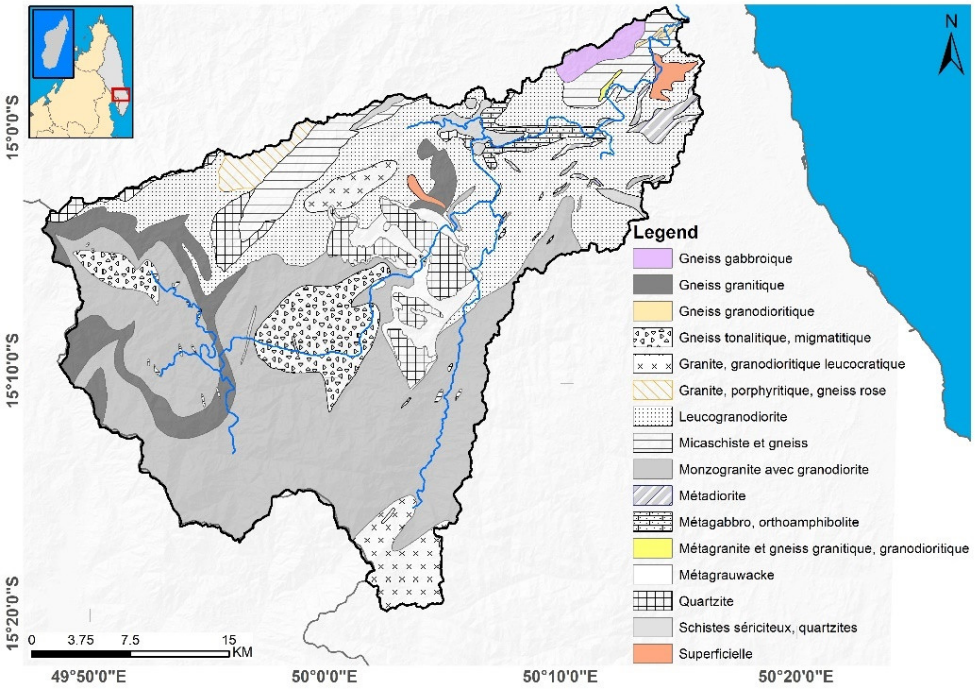

Figure 3. 13. Géologie du bassin versant d'Ankavia. Source : PGRM, 2018 (https://www.brgm.fr/fr/reference-projet-acheve/synthese-geologique-miniere-madagascar)

3.3.5. Pédologie

En termes de pédologie, le bassin d'Ankavia est dominé par des ferrasols avec des traces de lixisols en amont, et par des acrisols en aval (Figure 3.14) (Hengl et al. 2017). Les ferrasols présentent généralement des profils uniformes avec des teneurs

élevées en argile (kaolinite) et en oxydes de fer. Cela confère à ces sols une structure pseudo-sableuse qui explique leur forte perméabilité malgré une teneur importante en argile (Martinez et Souza 2020). En revanche, les acrisols présentent des profils plus hétérogènes avec un horizon argileux à faible perméabilité résultant de l'accumulation d'argile. Ces sols ont généralement une teneur en argile plus faible et sont particulièrement sensibles à l'érosion (Hengl et al. 2017).

Les principales textures de sols dans le bassin d'Ankavia sont argilo-limoneuse, sablo-argilo-limoneuse et sablo-argileuse. En majorité, ces sols contiennent moins de 50 % d'argile et sont riches à modérément riches en sable, avec une proportion significative de limon (Roose et al. 2012).

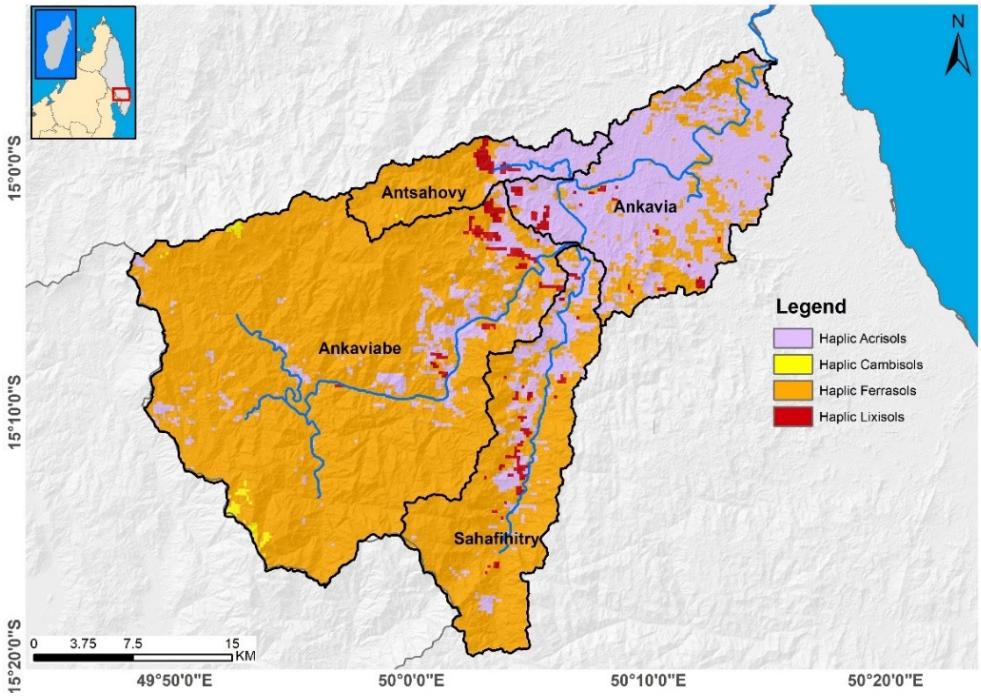

Figure 3. 14. Pédologie du bassin versant d'Ankavia. Source : SoilGRID, (Hengl et al. 2017)

3.3.6. Couvertures végétales et activités de conservation

La végétation est principalement naturelle, avec une distribution spatiale variée. Dans la partie aval, le paysage est caractérisé par des zones d'arbustes et de prairies, parsemées de quelques parcelles cultivées, représentant 35,6% de la superficie totale. En amont, la végétation est dominée par des mosaïques arborées (9,6%) et des forêts tropicales primaires (54,7%) (Figure 3.15). Dans le bassin versant d'Ankavia, les aires protégées s'étendent sur 32 200 ha, soit environ 28% de la superficie totale du bassin. Cette zone se répartit entre le Parc national de Masoala (5 420 ha) et le Parc naturel de Makira (26 780 ha) (Figure 3.14).

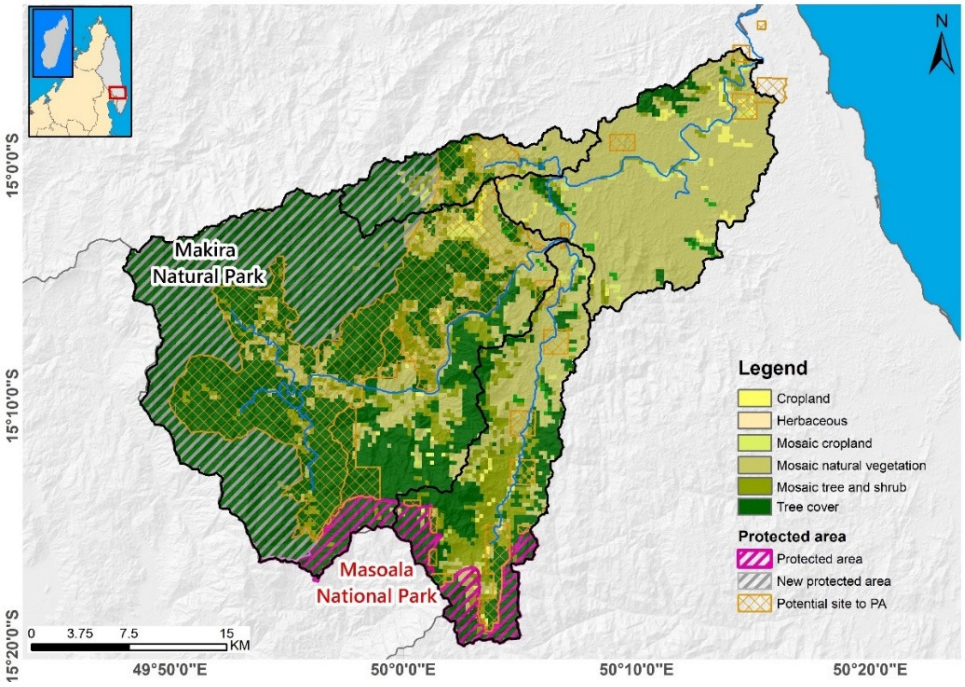

Figure 3. 15. Couvertures végétales en 2020 avec les aires protégées dans le bassin d'Ankavia. Source : Globcover 2020, (Bontemps et al. 2009)

3.3.7. Les sous-bassins versants de l'Ankavia

Le bassin d'Ankavia est composé de trois principaux sous-bassins, formés par ses affluents en amont : l'Ankaviabe, le Sahafihitry et l'Antsahovy. Le tableau 3.2 présente les caractéristiques de chacun des sous-bassins.

Table 3. 1. Caractéristiques des sous-bassins versants de l'Ankavia

Attributs (Références)	Caractéristiques	Ankavia*	Ankaviabe	Sahafihitry	Antsahovy
Topographie / Morphometrie (Earth Resources Observation And Science (EROS) Center 2017)	Supercifie, km²	1116.0	623.9	197.1	69.9
	Perimetre, km	198.0	131.8	93.2	56.8
	Longueur du bassin, km	54.6	35.1	32.1	17.1
	Pente moyenne, °	16.3	18.4	18.9	18.2
	Altitude (Min, Max), m	14, 1469	56, 1469	56, 1309	45, 1271
Couverture du sol (%) (Bontemps et al. 2009)	Prairies, terres cultivées	35.6	15	36.3	40.8
	Mosaïques arborées	9.6	7.6	23.1	10.7
	Forêts	54.7	77.4	40.6	48.4
Pédologie (%) (Hengl et al. 2017)	Acrisols	24.7	7.9	18.9	30.5
	Ferrasols	73.1	90.1	78.8	64.7
	Lixisols	2.1	1.9	2.3	4.9
	Cambisols	0.4	0.7	0.0	0.2
Géologie (%)** (PGRM, 2007)	Gneiss	14.3	22.6	0.0	0.9
	Granites	70.7	64.0	88.9	55.5
	Schistes	6.4	1.8	0.0	43.6
	Quartzites	8.6	11.6	11.1	0.0

* Ankavia représente le bassin entier, englobant les trois sous-bassins en amont (Figure 3.11).

**La représentation géologique a été simplifiée en regroupant les couches dominantes. Le tableau détaillé se trouve à l'Annexe B.

3.4. Stations de mesure

Dans le cadre du projet GIRE SAVA[2] (Gestion Intégrée des Ressources en Eau dans la SAVA), un réseau de surveillance hydrométéorologique a été déployé dans le bassin versant de l'Ankavia. Ce réseau comprend principalement des pluviomètres, des stations hydrométriques et une station climatique [Annexes C, D, E].

3.4.1. Mesure des précipitations et paramètres climatiques

Un réseau de 14 pluviomètres a été installé dans le bassin versant. La station climatique de Marofinaritra est équipée d'un pluviomètre Campbell Scientific® ARG100, tandis que les 13 autres, répartis dans le bassin, sont des modèles HOBO® RG3-M (fabriqués par Onset Computer Corporation, basée à Bourne, Massachusetts, États-Unis) (Figure 3.16). Toutes les stations sont positionnées à 1,5 m du sol et se situent entre 25 et 663 m d'altitude (Figure 3.17). La majorité d'entre elles est implantée le long des cours d'eau à basse et moyenne altitude, en dessous de 300 m. La station climatique de Marofinaritra, située à 87 m d'altitude, mesure plusieurs paramètres météorologiques : rayonnement solaire, vitesse et direction du vent, humidité relative, températures maximale et minimale, et pression atmosphérique. La pression atmosphérique est spécifiquement mesurée par un Solinst® 3001 LT Barologger Edge (Solinst Canada Ltd., Georgetown, Canada), avec une précision de ±0,05 kPa. Les autres paramètres sont collectés par un enregistreur Campbell Scientific® série CR300 (fabriqué par Campbell Scientific Inc., Logan, Utah, États-Unis). Tous les instruments sont programmés pour enregistrer les données à un pas de temps horaire.

Les données pluviométriques et climatiques ont été collectées sur une période de trois ans, de septembre 2018 à août 2021. Cette collecte a été assurée par des maintenances et des relevés mensuels réguliers.

[2] https://sites.google.com/view/giresava, consulté en août 2024.

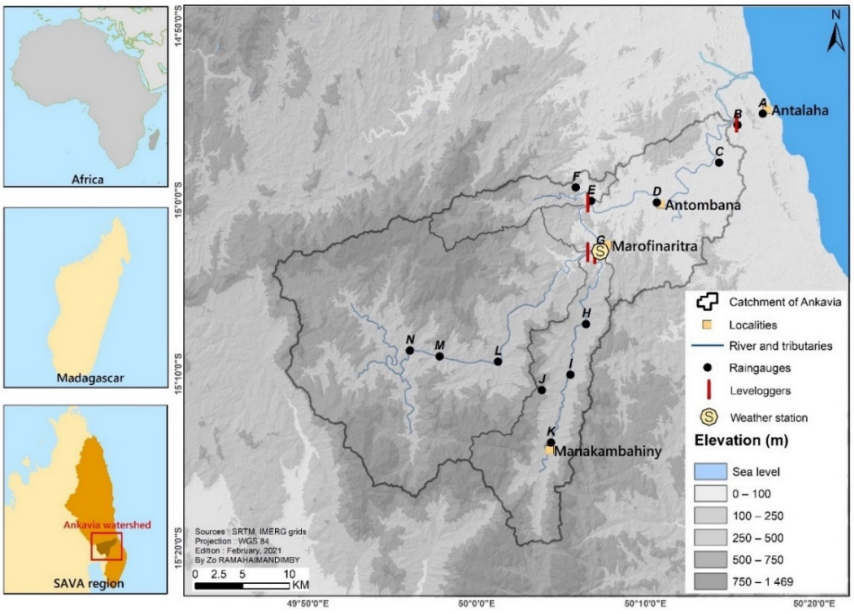

Figure 3. 16. Localisation des stations de mesures hydrométéorologiques dans le bassin versant d'Ankavia. Source : SRTM (Earth Resources Observation And Science (EROS) Center 2017), GIRE SAVA.



(a) (b)

Figure 3. 17. Equipements météorologiques : (a) Pluviomètre et (b) station climatique de Marofinaritra.

3.4.2. Mesure du niveau d'eau

Le niveau d'eau est mesuré à l'aide de capteurs de pression Solinst® LTC Levelogger Edge M5 C80 (conçu par Solinst Canada Ltd., Georgetown, Canada) d'une précision de ± 3 mm. En complément de ces capteurs automatisés, des échelles limnimétriques ont été installées pour permettre aux agents du bassin d'effectuer des relevés visuels directs (Figure 3.18).

Le calcul des hauteurs d'eau requiert au préalable un ajustement de la pression atmosphérique en fonction de l'altitude de chaque exutoire. Cette correction est réalisée à l'aide de la formule du nivellement barométrique (Equation 3.1).

$$p(h_i) = p(h_0).e^{\frac{-\Delta h}{hs}} \text{ , avec } hs = \frac{R.T}{M.g} \quad (3.1)$$

où $p(h_1)$ = pression atmosphérique mesurée à l'altitude h_i [Pa]

$p(h_0)$ = pression effective à l'altitude h_0 mesurée à Marofinaritra [Pa]

Δh = différence de hauteur entre h_1 et h_0 [m]

R = constante universelle des gaz parfaits [= 8.134 $J.K^{-1}$ mol^{-1}]

T = température absolue de l'air [K]

M = masse molaire des gaz de l'atmosphère [= 0.02896 kg mol^{-1}}

g = accélération due à la pesanteur [= 9.81 m s^{-2}]



Figure 3. 18. Capteurs de pression et échelles limnimétriques installés à l'exutoire de chaque sous-bassin : (a) Sahafihitry, (b) Ankaviabe, (c) Antsahovy, (d) Ankavia.

Une fois la correction barométrique effectuée, les données de pression enregistrées par les capteurs immergés sont converties en hauteurs d'eau. Cette conversion s'appuie sur la relation entre la pression hydrostatique (différence entre la pression mesurée au fond de l'eau et la pression atmosphérique corrigée) et la hauteur de la colonne d'eau. La hauteur d'eau est alors calculée selon l'équation 3.2.

$$Z = \frac{Pi - P(hi)}{\rho\, g} \qquad (3.2)$$

où Z = Hauteur d'eau [m]

P_i = Pression mesurée au fond de l'eau [Pa]

$P(h_i)$ = Pression atmosphérique au niveau de l'exutoire [Pa]

ρ = Masse volumique de l'eau [= 1000 kg m^{-3}]

g = Accélération due à la pésanteur [m^2 s^{-1}]

3.4.3. Mesure de débits faibles et moyens

En règle générale, le débit est calculé à partir de l'équation 3.3, qui exprime le produit de la vitesse d'écoulement par la section mouillée du cours d'eau. Cette dernière est déterminée à partir de la section en travers.

$$Q = C_s\, V \qquad (3.3)$$

Avec Q, le débit [m^3 s^{-1}] ; C_s, la surface de la section transversale du cours d'eau occupée par l'eau à l'instant de la mesure, aussi appelée section mouillée [m^2] ; V, la vitesse d'écoulement [m s^{-1}].

3.4.3.1. Section en travers

Les sections en travers, qui représentent le profil transversal d'un cours d'eau, sont choisies selon plusieurs critères importants. L'accessibilité facilite les mesures régulières et l'entretien des équipements. La stabilité du lit de la rivière, souvent composé majoritairement de roches, minimise les changements morphologiques (Figure 3.20). La représentativité hydraulique assure que la section est caractéristique du tronçon étudié. L'absence d'obstacles hydrauliques et l'emplacement approprié des limnimètres complètent ces critères de sélection. La détermination de ces sections consiste à mesurer la largeur et la profondeur de la rivière à un emplacement spécifique, permettant ainsi d'établir un profil vertical du lit à chaque exutoire.

3.4.3.2. Vitesse d'écoulement

Pour les mesures de jaugeage des débits faibles et moyens, la vitesse de l'eau a été mesurée à l'aide d'un courantomètre à induction électromagnétique OTT MF PRO (OTT HydroMet GmbH, Kempten, Allemagne) (Figure 3.19). Cet appareil de haute précision offre une plage de mesure de 0 à 6 m s^{-1}, avec une marge d'erreur de ±2% de la valeur mesurée pour des vitesses entre 0 et 3 m s^{-1}, et de ±4% pour des vitesses entre 3 et 5 m s^{-1}. Un minimum de 20 jaugeages a été réalisé à chaque exutoire afin d'établir la courbe de tarage avec précision. Cette courbe, généralement exprimée sous forme d'équation 3.5, permet de relier la hauteur d'eau au débit du cours d'eau.



Figure 3. 19. Photographie de la sonde du courantomètre électromagnétique (à gauche) et appareil d'affichage des résultats (à droite).

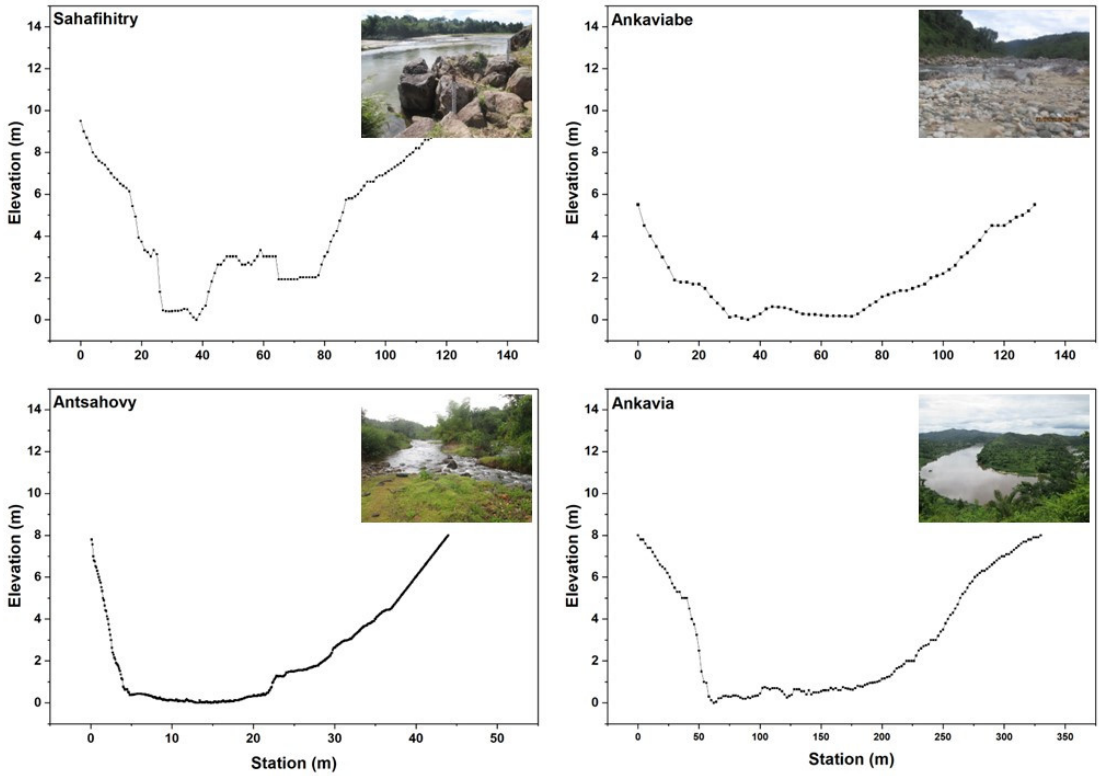

Figure 3. 20. Sections en travers représentatives des exutoires des sous-bassins versants, accompagnées des photographies correspondantes.

En pratique, pour mesurer le débit d'un cours d'eau, il est recommandé de diviser sa section transversale en plusieurs sous-sections verticales, en fonction des variations de profondeur observées. Le choix de la méthode de mesure de la vitesse le long de ces verticales dépend de la profondeur totale. Pour les faibles profondeurs (< 50 cm), la méthode en un point à 60% de la profondeur depuis la surface suffit généralement pour estimer la vitesse moyenne sur toute la verticale. En revanche, pour des profondeurs plus importantes, la méthode en deux points (à 20% et 80% de la profondeur) ou en trois points (à 20%, 60% et 80% de la profondeur, Figure 3.21) offre une estimation plus précise de la vitesse moyenne (Phillips et Tadayon 2006). Le débit total est ensuite calculé selon l'équation 3.4 suivante :

$$Q = \iint_S V \, dS = \int_0^Z \int_0^H vi \, dh \, dx \tag{3.4}$$

où Q est le débit du cours d'eau [$m^3 s^{-1}$], S est la surface de la section mouillée [m^2], v_i est la vitesse définie en chaque profondeur h_i de la section [$m s^{-1}$], et x, l'abscisse variant de 0 à H pour chaque verticale [m]. Z étant la hauteur d'eau [m].

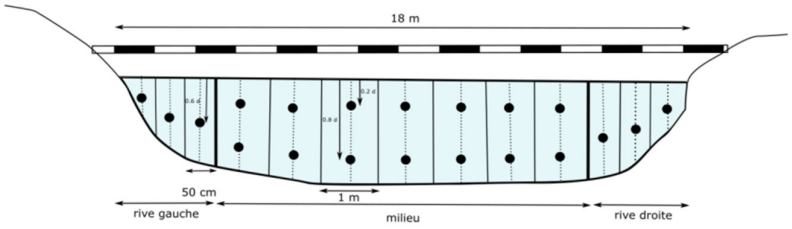

Figure 3. 21. Représentation de la section en travers avec intervalles et méthodes de mesure des vitesses ponctuelles d'écoulement (1 ou 2 points) au courantomètre électromagnétique. Source : modifiée à partir de Castermans (2019).

3.4.3.3. Courbe de tarage

La conversion des mesures de hauteur d'eau en débit s'effectue à l'aide d'une courbe de tarage (Figure 3.22). Cette courbe est établie à partir de multiples mesures de débit effectuées in situ, couvrant une large gamme de conditions d'écoulement. La relation entre la hauteur d'eau et le débit est généralement approximée par une équation, souvent de forme exponentielle ou polynomiale. Cette relation peut s'exprimer typiquement par l'Équation 3.5.

$$Q = a\,(Z - Z_0)^b \qquad (3.5)$$

où

Q	=	Débit [$m^3\,s^{-1}$]
Z	=	Hauteur d'eau [m]
Z_0	=	Hauteur d'eau où le débit vaut zéro [m]
a et b	=	Coefficients déterminés par la méthode des moindres carrées, en utilisant les données in situ.

Les sondes installées dans les trois sous-bassins (Ankaviabe, Antsahovy et Ankavia) ont rencontré des problèmes techniques, limitant la période d'acquisition des données à 10 mois, de septembre 2018 à juin 2019. En revanche, la sonde de pression située à l'exutoire de Sahafihitry est restée pleinement opérationnelle, fournissant une série de données continue sur au moins 3 ans, de juillet 2018 à août 2021. Par conséquent, en raison de leur exhaustivité et de leur continuité, les données du bassin versant de Sahafihitry ont été privilégiées et plus largement exploitées dans les **chapitres 7** et **8** de cette étude.

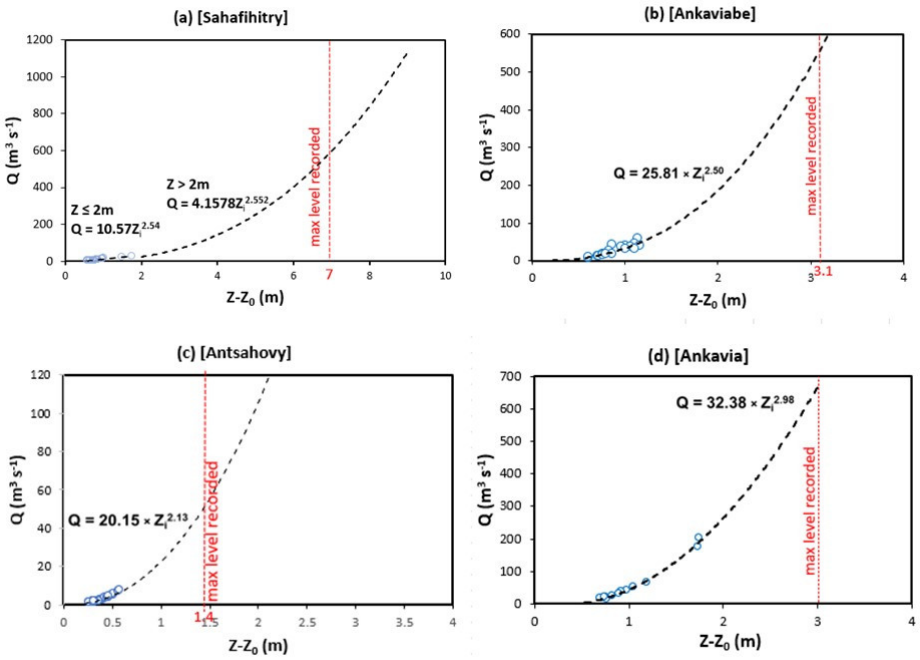

Figure 3. 22. Courbes de tarage de chaque cours d'eau du bassin versant, avec les hauteurs maximales enregistrées dépendant de la date d'acquisition des données. (a) Sahafihitry : 3 ans de données (08/2018 – 07/2021). (b) Ankaviabe, (c) Antsahovy et (d) Ankavia : 10 mois de données (09/2018 – 06/2019).

3.4.4. Mesure de hauts débits

En raison des contraintes pratiques rendant difficiles les mesures directes des débits élevés, ces derniers ont été estimés par extrapolation des courbes de tarage (Figure 3.18) à l'aide d'une méthode empirique basée sur l'équation de Manning (Equation 3.6).

$$Q = n^{-1} \, Cs \, Hr^{2/3} \, Sl^{1/2} \qquad (3.6)$$

avec
- n = coefficient de rugosité [$s \cdot m^{-1/3}$],
- Cs = aire de la section mouillée du cours d'eau [m^2],
- Hr = rayon hydraulique [m] (le rapport entre la section mouillée et le périmètre mouillé),
- Sl = la pente de la rivière [$m \, m^{-1}$] à la station de jaugeage, estimée à partir d'un MNT (Modèle Numérique de Terrain) à résolution de 30 m (source : SRTM).

L'estimation du coefficient de Manning (n) pour le lit mineur est réalisée en ajustant la courbe de débit calculée à l'aide de l'équation de Manning aux courbes de tarage dérivées des mesures de débit in situ. En revanche, pour le lit majeur, n est estimé en se basant sur les observations de terrain et en consultant des tables de référence qui fournissent des valeurs typiques de ce coefficient en fonction des caractéristiques du lit (Equation 3.7 et Table 3.3).

$$n = (n_0 + n_1 + n_2 + n_3 + n_4) \, m \qquad (3.7)$$

où
- n_0 = valeur de base de n pour un canal rectiligne, uniforme et lisse en matériaux naturels ;
- n_1 = facteur de correction pour l'effet des irrégularités de surface ;
- n_2 = valeur pour les variations de forme et de taille de la section transversale du canal ;
- n_3 = valeur pour les obstacles ;
- n_4 = valeur pour la végétation et les conditions d'écoulement ;
- m = facteur de correction pour le méandrement du canal.

Table 3. 2. Estimation des paramètres nécessaires au calcul du coefficient de rugosité de Manning.

Facteurs d'addition	
Matériel impliqué	**n_0 ($ft^{1/6}$)**
Terre	0.020
Matériel pierreux	0.025
Gravier fin	0.024
Gravier grossier	0.03
Galet	0.03 – 0.050
Rocher	0.040 – 0.070
Degré d'irrégularité	**n_1 ($ft^{1/6}$)**
Lisse	0
Mineur	0.005
Modéré	0.010
Sévère (rives érodées)	0.020
Variation de la section du canal (localisation du talweg)	**n_2 ($ft^{1/6}$)**
Graduelle	0
Alternant occasionnellement	0.005
Alternant fréquemment	0.010 – 0.015
Effet d'obstruction	**n_3 ($ft^{1/6}$)**
Négligeable	0
Mineur (15% de l'écoulement est turbulent)	
Appréciable (jusque 50% est turbulent)	
Sévère (>50% est turbulent)	
Végétation sur les rives	**n_4 ($ft^{1/6}$)**
Aucune	0
Petite (herbe)	0.005 – 0.010
Moyenne (buisson, pas de lit de rivière)	0.010 – 0.025
Haute (jeunes arbres)	0.025 – 0.050
Très haute (buissons dans la rivière, arbres matures)	0.050 – 0.100
Facteur de multiplication	
Degré des méandres	**m**
Mineur	1.00
Appréciable	1.15
Sévère	1.30

Pour le calcul des débits de hautes eaux sur le bassin de Sahafihitry, le coefficient de rugosité de Manning (n) du lit majeur (Z> 2m) a été fixé à 0,08 $s \cdot m^{-1/3}$ pour la rive gauche, correspondant à une végétation moins dense, et à 0,12 $s \cdot m^{-1/3}$ pour la rive droite, où la végétation est plus dense (Phillips et Tadayon 2006).

4. Chapitre 4 : Reliability of Gridded Precipitation Products for Water Management Studies : The Case of the Ankavia River Basin in Madagascar[3]

Abstract:

Hydrological modeling for water management in large watersheds requires accurate spatially-distributed rainfall time series. In case of low coverage density of ground-based measurements, gridded precipitation products (GPPs) from merged satellite-/gauge-/model-based rainfall products constitute an attractive alternative. The quality of which must, nevertheless, be verified. The objective of this study was to evaluate, at different time scales, the reliability of 6 GPPs against a 2-year record from a network of 14 rainfall gauges located in the Ankavia catchment (Madagascar). The GPPs considered in this study are the African Rainfall Estimate Climatology (ARC2), the Climate Hazards Group Infrared Precipitation with Station data (CHIRPS), the European Centre Medium-Range Weather Forecasts ECMWF Reanalysis on global land surface (ERA5-Land), the Integrated Multi-satellitE Retrievals for Global Precipitation Measurement V06 Final (IMERG), the Precipitation Estimation from Remotely Sensed Information using Artificial Neural Networks Cloud Classification System (PERSIANN-CCS), and the African Rainfall Estimation (RFEv2) products.

The results suggest that IMERG (R^2 = 0.63, slope of linear regression a = 0.96, root mean square error RMSE = 12 mm day^{-1}, mean absolute error MAE = 5.5 mm day^{-1}) outperforms other GPPs at the daily scale, followed by RFEv2 (R^2 = 0.41, a = 0.94, RMSE = 15 mm day^{-1}, MAE = 6 mm day^{-1}) and ARC2 (R^2 = 0.30, a = 0.88, RMSE = 16 mm day^{-1}, MAE = 6.7 mm day^{-1}). All GPPs, with the exception of the ERA5,

[3] Based on : Ramahaimandimby, Z., A. Randriamaherisoa, F. Jonard, M. Vanclooster, and C. L. Bielders. 2022. "Reliability of Gridded Precipitation Products for Water Management Studies: The Case of the Ankavia River Basin in Madagascar." *Remote Sensing*, 14 (16): 3940. Multidisciplinary Digital Publishing Institute. https://doi.org/10.3390/rs14163940.

overestimate the 'no rain' class (0–0.2 mm day^{-1}). ARC2, IMERG, PERSIANN, and RFEv2 all underestimate rainfall occurrence in the 0.2–150 mm day^{-1} rainfall range, whilst CHIRPS and ERA5 overestimate it. Only CHIRPS and PERSIANN could estimate extreme rainfall (>150 mm day^{-1}) satisfactorily. According to the Critical Success Index (CSI) categorical statistical measure, IMERG performs quite well in detecting rain events in the range of 2–100 mm day^{-1}, whereas PERSIANN outperforms IMERG for rain events larger than 150 mm day^{-1}. Because it performs best at daily scale, only IMERG was evaluated for time scales other than daily. At the yearly and monthly time scales, the performance is good with R^2 = 0.97 and 0.87, respectively. At the event time scale, the probability distribution function PDF of rain gauge values and IMERG data show good agreement. However, at an hourly time scale, the correlation between ground-based measurements and IMERG data becomes poor (R^2 = 0.20).

Overall, the IMERG products can be regarded as the most reliable gridded precipitation source at monthly, daily, and event time scales for hydrological applications in the study area, but the poor agreement at hourly time scale and the inability to detect extreme rainfall >100 mm day^{-1} may, nevertheless, restrict its use.

Keywords: Gridded precipitation products; IMERG; Ankavia catchment.

4.1. Introduction

Accurate precipitation data are essential for numerous theoretical and practical applications, be it for water balance calculations, flood warnings, drought monitoring, or water resource management (Sun et al. 2018; Burton 2003; WMO 1987). When properly installed and maintained, rain gauge observations provide accurate point-based precipitation measurements (Dai et al. 2017; Adhikary et al. 2015). However, in the case of low coverage density, they are poorly adapted to deal with the high spatiotemporal heterogeneity in precipitation. The latter can result in large errors when rain gauge data are interpolated to larger scales, particularly in mountainous areas with complex terrain (Huffman et al. 2007; Love et al. 2004). Furthermore, the spatial distribution of rain gauges is often highly uneven in

practice, with few gauges in remote areas, in less developed regions, in areas with complicated terrain, or in forested areas (Gosset et al. 2013). As a result, in situ rain gauge data seldom matches the needs of applications that require precipitation data with high spatiotemporal resolution (Beck et al. 2019a; Gosset et al. 2013). This is particularly true across vast swaths of the African continent (Bonsor 2010).

As opposed to rain gauges, gridded precipitation products (GPPs) from merged satellite-/gauge-/model-based rainfall products have the advantage of offering wide spatial coverage (Dahri et al. 2021; Sun et al. 2018). There are currently a number of GPPs available, including ARC2 (African Rainfall Estimate Climatology version 2), CHIRPS (Climate Hazards Group Infrared Precipitation with Station Data), ERA5 (European Centre Medium-Range Weather Forecasts Reanalysis), IMERG v06 Final (Integrated Multi-satellitE Retrievals for Global Precipitation Measurement), PERSIANN-CCS (Precipitation Estimation from Remotely Sensed Information using Artificial Neural Networks Cloud Classification System), and RFEv2 (African Rainfall Estimation version 2), among others (Sun et al. 2018). Recent GPPs also provide adequate spatial (≤0.1 × 0.1°) and temporal (daily to sub-hourly, depending on the product) resolution, allowing for credible precipitation estimates in data-scarce environments or at ungauged locations (Khan 2019; Sun et al. 2018; Funk et al. 2015). They have been used in a variety of applications, including hydrological modeling, extreme event analysis, infrastructure design (based on rainfall frequency analysis), and water resource management (Ombadi et al. 2021; Maggioni and Massari 2018; Gosset et al. 2013).

Since GPPs are based on indirect rainfall estimation methods, the results will be subject to uncertainty due to measurement errors, sampling, retrieval methods, and bias correction processes (Camberlin et al. 2019; Dinku et al. 2008). The errors depend on the number and type of sensors taking measurements across a certain location at a given time, as well as the strategies used to assimilate the available data into a coherent gridded dataset (van Genderen 2011; Hossain and Anagnostou 2006). Furthermore, the error characteristics differ based on the type of storm system, location, topography, and cloud properties (Hossain and Anagnostou 2006). Therefore, the accuracy of GPPs must be thoroughly explored both in time and space

(Dezfuli et al. 2017; Adeyewa and Nakamura 2003), and quantitative statistical evaluations are useful tools for assessing GPP precision (Dezfuli et al. 2017; Thiemig et al. 2012). Whereas some researchers assess GPPs based on the accuracy of streamflow rate predictions within hydrological modeling frameworks (Thiemig et al. 2012; Asadullah et al. 2008), most studies evaluate GPPs against gauge data or against estimates from ground-based weather radars (Beck et al. 2019a; Yeh et al. 2017).

Various studies have been undertaken to assess GPP performance at the global, continental, and regional levels during the last few decades. TRMM Multi-Satellite Precipitation Analysis (TMPA) products, for example, have been assessed in various parts of Africa, and the results revealed that TMPA products provide effective data in most regions (Ageet et al. 2021; Huffman et al. 2007). Camberlin et al. (2019) found that TMPA was the best product at a daily time scale over different parts of Central Africa. Following that success, Dezfuli et al. (2017) proved that the Integrated Multi-satellite Retrievals for GPM (Global Precipitation Measurement), which integrates observations from many satellites of the GPM satellite constellation, improves the quality and spatiotemporal resolution of precipitation data. Other investigations in eastern Africa (Zimbabwe) show that ARC2 and RFEv2 estimate the precipitation gauge data better than other GPPs (Dinku et al. 2008). In addition, an evaluation conducted by Ageet et al. (2021) in equatorial and eastern Africa showed that IMERG performed better for daily scales, while CHIRPS outperformed other products at monthly and annual scales. Overall, the reliability of GPPs appears to be governed by a number of factors, including the study scale, location, time scale, and, most significantly, the availability of ground-based data used for calibration (Dezfuli et al. 2017; Dinku et al. 2008).

Despite the significant efforts undertaken so far to evaluate GPPs, those products continue to require extensive validation against ground observations in order to assess their quality and quantify the appropriate level of confidence in their use for various hydrological applications (Sun et al. 2018). Furthermore, Van Soesbergen and Mulligan (2018) highlights that the choice of GPP has a significant impact on runoff estimation and underlines the need for rigorous assessment with in situ observations

to improve their confident application in water cycle research. As a result, temporal aspects and spatial distributions must be quantitatively analyzed. Nonetheless, the scale discrepancy problem persists when rain gauge data is used for validation. So far, the majority of existing GPP validation efforts in Africa have been conducted at large scales (country level or greater), with rain gauges separated by very large distances (Atiah et al. 2020; Gosset et al. 2013; Dinku et al. 2008), and they were often performed on public datasets or GPCP-1DD (Global Precipitation Climatology Project One-Degree Daily Precipitation) data (Dinku et al. 2018). Since numerous water management issues are dealt with at smaller scales, it is therefore of high interest to also evaluate the ability of GPPs to capture rainfall variations across short distances (5–10 km) for applications in medium to large watersheds (i.e., ~10^3 km^2) (Blöschl and Sivapalan 1995).

The aim of this study was, therefore, to evaluate, at different time scales (hourly to yearly), the reliability of six major GPPs (ARC2, CHIRPS, ERA5-Land (hereafter ERA5), IMERG v06 Final (hereafter IMERG), RFEv2, and PERSIANN-CCS (hereafter PERSIANN)) for water management applications in medium-size watersheds in Africa. More specifically, GPP data were evaluated against a network of rain gauges installed in the Ankavia watershed (1116 km^2) in northeastern Madagascar. Water-related issues abound in Madagascar, strongly impacting economic development and environmental conservation (Desbureaux and Damania 2018; Tadross et al. 2008). Indeed, northeastern Madagascar is characterized by heavy rainfall (1500 to 2500 mm/year), caused by southeasterly exchanges that start in the Indian Ocean anticyclone and reach the highlands of the east (Rabefitia 2008). This, along with deforestation from slash and burn, logging, and firewood harvesting, contributes to some of the world's greatest levels of erosion and catastrophic flooding (Gay-des-Combes et al. 2017; Styger et al. 2007). Furthermore, as a result of climate change, more powerful cyclones and increasing sea levels directly threaten coastal settlements and exacerbate floods and erosion in coastal areas (Otto et al. 2022). In contrast, during the dry season, some rivers in the north tend to dry up, and alternative groundwater sources are not always available (Rabefitia 2008). Previous research has shown that pressure on water resources in Madagascar is increasing

(Rasolofomanana 2016; AFD 2005). Hydrometeorological data are scarce and not always routinely collected, which impedes decision-making for integrated water resources management (IWRM), particularly at the basin scale (McNally et al. 2019; Macron et al. 2016). Hence the use of reliable GPP seems unavoidable for hydrological modeling, drought monitoring, and water resources management.

4.2. Materials and Methods

4.2.1. Study area

This study focuses on the Ankavia watershed, located between 14°50'–15°20'S and 49°50'–50°20'E in the SAVA region in northeast Madagascar (Figure 4.1). At a regional scale, the climate is governed by the southeasterly trade winds that originate from the Indian Ocean anticyclone, a zone of high atmospheric pressure that seasonally changes its position over the ocean (Macron et al. 2016). The northeastern coast of Madagascar is most directly exposed to the trade winds and has the highest rainfall in the country (Chaperon et al. 1974). Furthermore, the region is regularly affected by tropical storms and cyclones (Tadross et al. 2008). The area has a subequatorial climate with two main seasons; the hot, rainy season extends from November to April (approximately 70% of total annual precipitation), and the cooler, drier season from May to October. Temperatures range from 18 °C to 31 °C (CREAM 2013).

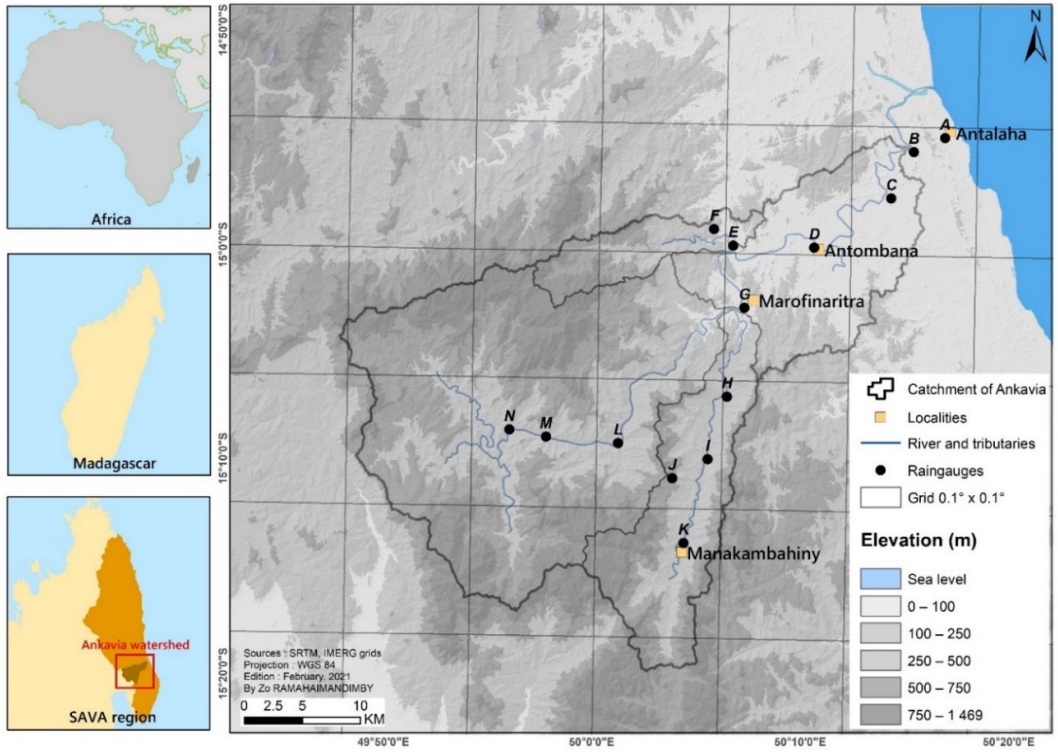

Figure 4. 1. Location of the Ankavia watershed in northeastern Madagascar with rain gauge network (rain gauges numbered A to N).

The hydrographic network in the SAVA region is dense and highly branched (Aldegheri 1972). The majority of the rivers originate in mountainous massifs and flow eastward into the Indian Ocean. These rivers are heavily fed throughout the year, with low flows in October and November. Floods are common during the rainy season and are often exacerbated in the coastal zone by sediment accumulation (UPDR 2003). For the last 60 years, the climatic data for the region have been provided solely by the Antalaha weather station located close to the coast (Figure 4.1).

The Ankavia watershed covers an area of 1116 km^2, i.e., roughly 5% of the total area of the SAVA region (Figure 4.1). It was chosen for this study due to its natural and social context, both exerting a strain on water resources. In particular, the Ankavia river provides water to the city of Antalaha (150,000 people in 2017). Altitude in the catchment varies from 14 m a.m.s.l. near the outlet in the east (hilly topography) to 1469 m a.m.s.l. in the southwest (mountainous topography). The western part of the Ankavia watershed is mainly occupied by primary forests, whereas the east is composed mostly of mosaic vegetation, including shrubs and herbaceous cover (CPGU 2012). The vast majority of inhabited and cultivated areas are clustered around the major rivers (CREAM 2013).

4.2.2. Ground-based precipitation data

Fourteen rain gauges and one meteorological station were established in the Ankavia catchment as part of the GIRE SAVA project (Gestion Integrée des Ressources en Eau in the SAVA region) (Figure 4.1). The rain gauge at the Marofinaritra climate station is a Campbell Scientific® ARG100, whereas the other 13 rain gauges scattered within the basin are HOBO® RG3-M instruments. These gauges are not part of the Global Telecommunications System (GTS) network. They are set with a recording interval of one hour. The stations are positioned 1.5 m above the ground, and their elevation ranges from 25 m to 663 m a.m.s.l., with the majority of the stations located along the rivers at low and mid altitudes and 90% of the rain gauges located below 300 m (Figure 4.1). Because of the remoteness, dense vegetation, and lack of roads, as well as the difficulty of ensuring routine

maintenance, no rain gauge could be installed in the high-elevation mountainous region (>1000 m a.m.s.l). The rainfall data used in the current study were collected for a two-year period, from September 2018 to August 2020, thanks to regular monthly maintenance and data collection.

4.2.3. Gridded precipitation products

Six GPPs were used in this study to compare with observed rain gauge data (Table 4.1). These products were chosen based on the availability of recent time series (from 2018 onwards), spatial (≤0.1°) and temporal (≤daily) resolutions that make them suitable for hydrological applications at the scale of the Ankavia watershed, near-real-time availability, public domain, and their coverage of Africa.

4.2.3.1. ARC2

ARC2 was developed by the National Oceanic and Atmospheric Administration (NOAA) Climate Prediction Center (CPC), which offers daily rainfall data for Africa (Sun et al. 2018). It uses inputs from two sources: (i) 3-hourly geostationary infrared (IR) data centered over Africa from the European Organization for the Exploitation of Meteorological Satellites (EUMETSAT), and (ii) quality-controlled GTS gauge observations reporting 24 h rainfall accumulations across Africa (Novella and Thiaw 2013). ARC2 has a spatial resolution of 0.1° over Africa (40°N–40°S, 20°W–55°E) with daily temporal resolution and can be downloaded at: https://iridl.ldeo.columbia.edu/SOURCES/.NOAA/.NCEP/.CPC/.FEWS/.Africa/.DAILY/.ARC2/.daily/ (accessed on 3 June 2021).

4.2.3.2. CHIRPS

Since 1981, the CHIRPS product has provided daily precipitation data with a spatial resolution of 0.05° for a quasi-global coverage of 50°N–50°S (Funk et al. 2015). The most recent product is Version 2.0, which was released in February 2015. The CHIRPS product and associated data can be found at: https://climateserv.servirglobal.net (accessed on 3 June 2021). The main datasets used for the construction of the CHIRPS product are the monthly precipitation climatology (CHPclim) information based on thermal infrared data archived from CPC and NOAA National Climate Data Center (NCDC), the Version 7 TRMM 3B42 data, the Version 2 atmospheric model rainfall

field from the NOAA Climate Forecast System (CFS), and rain gauge stations (Peterson et al. 2013). First, the cold cloud duration (CCD) data are calibrated with TRMM 3B42 to generate 5-day CCD-based precipitation estimates, which are then converted to fractions of long-term mean precipitation estimates (Funk et al. 2015; Peterson et al. 2013). The fractions are then multiplied by CHPclim data to remove systematic bias, and the resulting product is known as the CHIRP product (Dinku et al. 2018). Finally, the CHIRP product is combined with data from rain gauge stations using a modified inverse distance weighting algorithm to generate the CHIRPS (Peterson et al. 2013). All of the preceding processing is carried out on a 5-daily basis. Using a simple redistribution method, the CCD and CFS data are finally used to disaggregate the 5-daily products to daily precipitation estimates (Dinku et al. 2018).

4.2.3.3. ERA5

ERA5 is the most recent edition of the global atmospheric reanalysis of the ECMWF from 1979 (Emmanouil et al. 2021). ERA5-Land was created by rerunning the land component of the ERA5 climate reanalysis and spans the same time period as ERA5, from January 1950 to near real-time (NRT) (Xu et al. 2022). ERA5-Land is generated in a single simulation that is not coupled to the atmospheric module of the ECMWF's Integrated Forecast System. Observations have an indirect effect on the simulation due to the atmospheric forcing of ERA5 (Emmanouil et al. 2021; Muñoz-Sabater et al. 2021). This forcing is used to drive the single ERA5-Land simulation and was obtained by integrating observations using a 4D-Var data assimilation system and a Simplified Extended Kalman Filter (Sabater 2019). The fields are overlain for all oceans and have an hourly resolution. The Climate Data Store (CDS) Climate Copernicus website was used to download hourly total precipitation for the study period with a spatial resolution of approximately 0.1 × 0.1° (available at https://cds.climate.copernicus.eu/cdsapp#!/dataset/reanalysis-era5-land?tab=overview) (accessed on 3 June 2021).

4.2.3.4. IMERG

IMERG is available at https://giovanni.gsfc.nasa.gov/giovanni/ (accessed on 3 June 2021). The GPM project, a collaboration between the National Aeronautics and Space Administration (NASA) of the United States and the Japan Aerospace

Exploration Agency (JAXA), began in 2014 to provide half-hourly global precipitation data with a spatial resolution of 0.1° (Huffman et al. 2020). The GPM satellite is equipped with two major sensors: the GPM Microwave Imager (GMI), which measures precipitation intensity, depth, and duration, and the Dual-frequency Precipitation Radar (DPR), which observes storm internal structure within and beneath clouds (Huffman et al. 2020). The GPM Constellation provides three levels of data processing (IMERG products), but the most commonly used are the gridded products that combine GMI and DPR rainfall averages or rainfall estimates combined from data of all active and passive microwave instruments in the GPM Constellation (Huffman et al. 2020; Sungmin et al. 2017). There are three daily IMERG products: IMERG Early Run (near real-time with a latency of 4 h), IMERG Late Run (reprocessed near real-time with a latency of 14 h), and IMERG Final Run (gauged-adjusted with a 4-month latency) (Sungmin et al. 2017). In this study, we selected the IMERG-v06 Final Run half-hourly products (Huffman et al. 2020).

4.2.3.5. PERSIANN

The PERSIANN provides hourly precipitation estimates at the spatial resolution of 0.04° for the quasi-global coverage of 60°N–60°S from 2003 to the present (Hong et al. 2004). PERSIANN, developed at the University of Arizona and now operated by the Center for Hydrometeorology and Remote Sensing (CHRS) at the University of California Irvine, is based on an adaptive Artificial Neural Network (ANN) model that estimates fine-scale precipitation distribution using IR information (10.7 μm) from geostationary satellites in analyzing local and regional cloud properties (Nguyen et al. 2018). The PERSIANN-CCS algorithm converts rain rates from satellite cloud images in several steps, which consist of: (i) separating cloud images into recognizable cloud patches, (ii) extracting cloud properties based on their shape, texture, and coldness, (iii) clustering cloud patches into orderly subgroups, and (iv) calibrating cloud-top temperature and rainfall (Tb-R) correlations for the various cloud categories using gauge-corrected radar hourly rainfall data (Hong et al. 2004). The product is available at: http://chrsdata.eng.uci.edu/ (accessed on 3 June 2021).

4.2.3.6. RFEv2

Finally, RFEv2 is produced by the NOAA-CPC. It is primarily designed for the Famine Early Warning Systems Network to aid in disaster monitoring across Africa (Love et al. 2004). The product estimates daily precipitation for Africa with a spatial resolution of 0.1°. RFEv2 receives data from four operational sources: (1) daily GTS rain-gauge data, (2) Advanced Microwave Sounding Unit-based rainfall estimates, (3) Special Sensor Microwave Imager/Sounder-based estimates, and (4) the Geostationary Operational Environmental Satellite (GOES) precipitation index (GPI) calculated from cloud-top IR temperatures on a half-hourly basis (Herman et al. 1997). It is available at https://iridl.ldeo.columbia.edu/SOURCES/.NOAA/.NCEP/.CPC/.FEWS/.Africa/.DAILY/.RFEv2// (accessed on 9 June 2021). However, the use of polar-orbiting Passive Microwave (PM) and geostationary IR data differs between ARC and RFE. ARC uses 3-hourly IR data rather than 30-min data and does not include PM estimates, whereas RFE does (Novella and Thiaw 2013; Herman et al. 1997).

4.2.4. Data comparison methodology

4.2.4.1. Data quality control

Initially, the gridded product data were downloaded in files with half-hourly, hourly, or daily time steps (depending on availability; Table 4.1) based on the GMT 0:00 time zone. Negative values were removed from the gridded datasets. When necessary, daily totals were generated by summing the half-hourly or hourly files. For the study area (Madagascar +03H00 GMT), the observed rain gauge time series data were adjusted to the GMT and aggregated at an hourly or daily scale to be compared with the GPPs.

Table 4. 1. Selected gridded precipitation products.

Dataset	Full Name	Spatial Resolution	Timescale (Highest Resolution)	Period of Availability	Reference
ARC2	African Rainfall Climatology version 2	0.10°	Daily	1983–Present	(Novella and Thiaw 2013)
CHIRPS	Climate Hazards Group Infrared Precipitation with station data	0.05°	Daily	1981–Present	(Funk et al. 2015)
ERA5	ECMWF Reanalysis version 5 on global land surface	0.10°	Hourly	1979–Present	(Muñoz-Sabater et al. 2021)
IMERG	Integrated Multi-satellitE Retrievals for Global Precipitation Measurement	0.10°	Half-hourly	2000–Present	(Huffman et al. 2020)
PERSIANN	Precipitation Estimation from Remotely Sensed Information using Artificial Neural Networks—Cloud Classification System	0.04°	Hourly	2003–Present	(Hong et al. 2004)
RFEv2	Climate Prediction Center (CPC) African Rainfall Estimates version 2	0.10°	Daily	2001–Present	(Herman et al. 1997)

4.2.4.2. Data processing

Because of the scale discrepancy between GPPs and rain gauge data (Figure 4.2), two approaches were used to assess the performance of GPPs: (i) point-to-grid, (ii) point-gridded approach. Point-to-grid compares the precipitation recorded at each rain gauge with the precipitation from the GPP grid (0.04°, 0.05°, and 0.1°, respectively) that encompasses the rain gauge (Figure 4.2a). Because the location of rain gauges most often does not coincide with GPP grid centroids (Figure 4.2a), a second strategy was implemented: the point-gridded approach. In practice, a cell is delineated around each rain gauge (cell size of 0.04, 0.05, or 0.1° depending on the GPP; Table 4.1). Then, the rainfall value in those new cells was estimated as the area-weighted mean (max. 4) of the GPP grid cells overlapping with the new cell (Figure 4.2b). A third approach could have been to define an 'area of influence' (Thiessen polygon, section 2.1.2 Précipitations in Chapter 2) around each rain gauge and calculate area-weighted averages for each grid to be compared with the gridded data ('grid-to-grid' approach, Annexe F). However, such an approach leads to very different situations from one grid cell to another, some grids being in the area of influence of a single rain gauge while other grids are in the area of influence of up to five rain gauges. In addition, because the spatial resolution varies across GPPs, such an approach may introduce bias in the comparison.

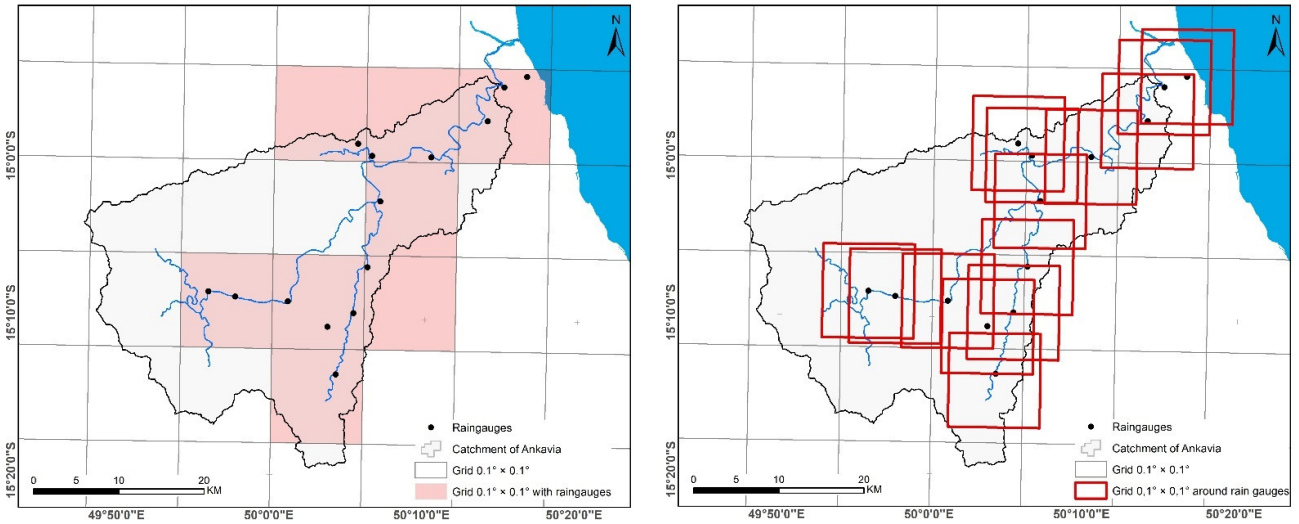

(**a**) (**b**)

Figure 4. 2. Data processing with two different approaches: (a) point-to-grid, (b) point-gridded.

4.2.4.3. Rainfall event definition and properties

In addition to evaluation at daily and hourly time scales, the most performing GPP was evaluated at the event time scale. There are numerous methods for identifying individual rainfall events (Molina-Sanchis et al. 2016). In this study, based on a study conducted by (Freitas et al. 2020) over a tropical area (Brazil), a minimum inter-event time interval of 6 h and a minimum rainfall depth threshold of 2.5 mm were chosen for the evaluation. In other words, a cumulative rainfall depth >2.5 mm is required to be considered as a rainfall event. The temporal resolution used to define rainfall events is one hour for both rain gauge and GPP data.

4.2.4.4. Metrics for accuracy assessment

Several widely used statistical indices (Table 4.2) were adopted to quantify the performance of the six GPPs against rain gauge observations: Coefficient of determination (R^2), Slope of the linear regression (a), Root Mean Square Error (RMSE), and Mean Absolute Error (MAE).

In addition, we also evaluated the capability of the GPPs in reproducing the distribution of observed precipitation intensities using the Probability Distribution Function (PDF) of daily rainfall intensities. For this purpose, we categorized precipitation into 12 different classes: 0–0.2 mm day^{-1}, 0.2–0.5 mm day^{-1}, 0.5–1 mm day^{-1}, 1–2 mm day^{-1}, 2–5 mm day^{-1}, 5–10 mm day^{-1}, 10–20 mm day^{-1}, 20–50 mm day^{-1}, 50–100 mm day^{-1}, 100–150 mm day^{-1}, 150–200 mm day^{-1}, and >200 mm day^{-1}.

Finally, the probability of detection (POD), false alarm ratio (FAR), and critical success index (CSI) were calculated to evaluate the precipitation detection ability of the six GPPs (Table 4.2). These indices aim at evaluating whether the estimated daily precipitation coincides with the precipitation observed on the ground. Specifically, POD represents the fraction of observed precipitation occurrences correctly detected by a given GPP. FAR corresponds to the fraction of detected precipitation occurrences that are incorrectly detected by a given GPP, while CSI measures the overall fraction of (detected and observed) precipitation occurrences correctly detected by a given GPP. The POD, FAR, and CSI values all range between 0 and 1. POD and CSI have perfect scores of 1, while FAR has a perfect score of 0. These indices are calculated for the different daily rainfall classes defined above.

Table 4. 2. Statistical metrics used to quantify GPP performance.

Name/Symbol	Formula	Optimal Value
Coefficient of determination/R^2	$R^2 = (CC)^2 = \left(\frac{\sum_{i=1}^{n}(0i - \bar{0})(Pi - \bar{P})}{\sqrt{\sum_{i=1}^{n}(Oi - \bar{O})2 \sum_{i=1}^{n}(Pi - \bar{P})2}} \right) 2$	1
Slope of linear regression/a	Y = aX + b	1
Root Mean Square Error/RMSE	$RMSE = \sqrt{\frac{\sum_{i=1}^{n}(Pi - Oi)2}{n}}$	0
Mean Absolute Error/MAE	$MAE = \frac{1}{n} * \sum_{i=1}^{n} \lvert Oi - Pi \rvert$	0
Categorical statistical metrics		
Probability of Detection/POD	$POD = \frac{Hits}{Hits\ +\ Misses}$	1
False Alarm Ratio/FAR	$FAR = \frac{FalseAlarm}{Hits + FalseAlarm}$	0
Critical Success Index/CSI	$CSI = \frac{Hits}{Hits + FalseAlarm + Misses}$	1

P = Gridded Products value, O = Observed (rain gauge) value, $\overline{P}$ = average value of P, $\bar{0}$ = average value of O, n = number of samples, X is the explanatory variable (O), Y is the dependent variable (P). The coefficient of determination R2 was computed using linear fit. Hits denotes the number of observed precipitation occurrences correctly detected by the gridded products. Misses represents the number of precipitation occurrences observed by the rain gauges but not detected by the gridded products. False Alarm indicates the number of precipitation occurrences not observed by the rain gauges but detected by the gridded products.

4.3. Results

4.3.1. Overall GPP performance at daily time scale

The comparison between rain gauge measurements and gridded rainfall product estimates reveals large differences between the six GPPs (Figure 4.3). However, all statistical metrics follow a similar pattern. Overall, IMERG data correlate best with the rain gauge data: highest R^2, the slope of the regression closest to 1, lowest RMSE and MAE. ARC2, PERSIANN, and RFEv2 perform rather similarly, though RFEv2 tends to have a better slope and MAE and PERSIANN a better R^2 than the two other products. ERA5 and, especially, CHIRPS perform worst.

Overall, the statistical indices are generally similar or slightly better using the point-gridded approach compared to the point-to-grid approach (Figure 4.3). As a result, the point-gridded approach was used for the remainder of the analyses.

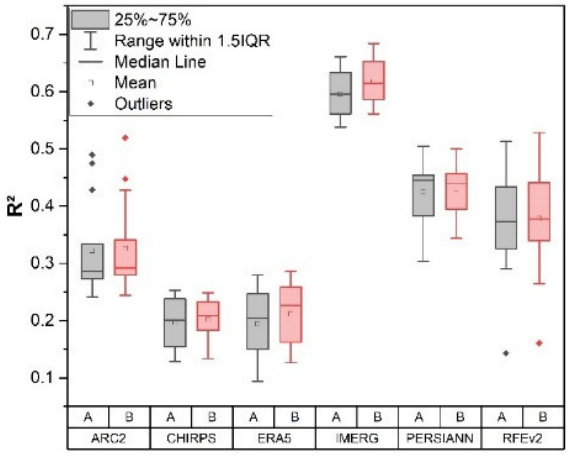

(**a**)

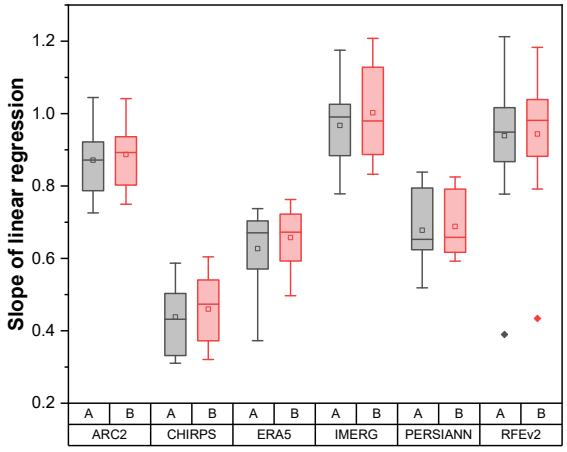
Slope of linear regression
1.2
1.0
0.8
0.6
0.4
0.2
A
B
ARC2
CHIRPS
ERA5
IMERG
PERSIANN
RFEv2

(b)

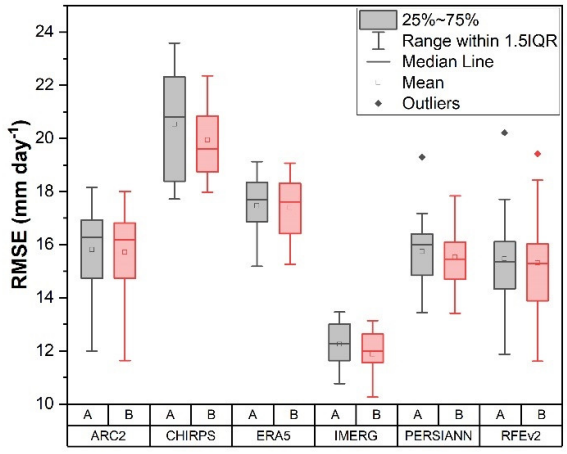
25%~75%
Range within 1.5IQR
Median Line
Mean
Outliers
RMSE (mm day-1)
24
22
20
18
16
14
12
10
A
B
ARC2
CHIRPS
ERA5
IMERG
PERSIANN
RFEv2

(c)

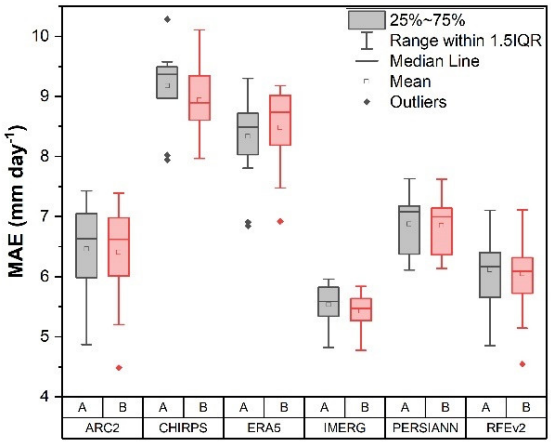

(**d**)

Figure 4. 3. Comparison of ground-based precipitation data with 6 GPPs at a daily time scale from September 2018 to August 2020 based on 4 indicators: (a) Coefficient of determination, (b) Slope of linear regression, (c) Root Mean Square Error, (d) Mean Absolute Error. Each box plot is based on 2 years of data from 14 rain gauges in the Ankavia watershed. 'A' refers to the point-to-grid approach (grey boxes and whiskers) and 'B' to the point-gridded approach (red boxes and whiskers) (see Figure 2). Box edges correspond to the 25th (Q1) and 75th (Q3) percentiles. Whiskers extend to Q1-1.5IQR (lower bound) and Q3+1.5IQR (upper bound), with IQR = Q3-Q1 (Inter-Quartile Range). Points outside the box are outliers.

4.3.2. GPP performance at daily time scale across the watershed

Figure 4.4 displays the R^2, slope, RMSE, and MAE for each rainfall gauge at a daily time scale across the Ankavia watershed. The greener the circle is, the closer the indicator is to its optimum value. In contrast, the color red indicates poor performance. Overall, IMERG shows good and fairly uniform levels of agreement across the entire watershed for all four indices. The performance of PERSIANN, RFEv2, and ARC2 varies widely from one location to another. CHIRPS and ERA5 show the poorest performance across the entire watershed.

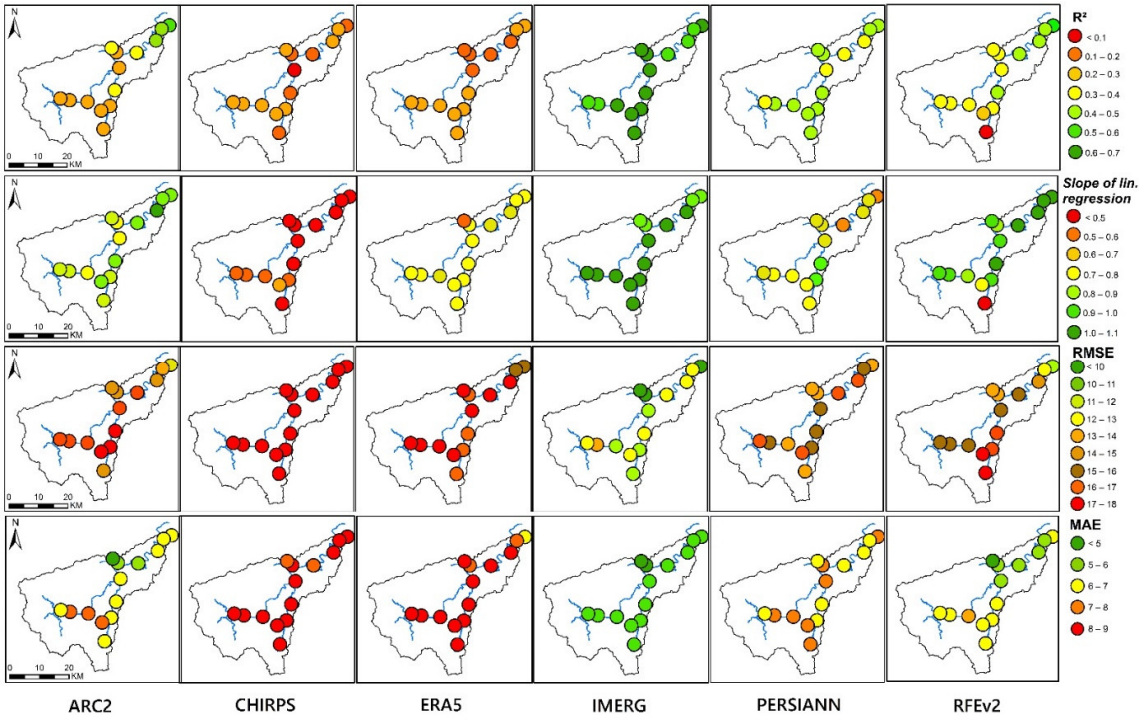

Figure 4. 4. Spatial distribution of the statistical evaluation metrics across the Ankavia watershed based on the point-gridded approach at a daily time scale from September 2018 to August 2020.

4.3.3. Daily rainfall probability distribution function

PDFs computed from the six GPPs and the rain gauge data over the Ankavia catchment are shown in Figure 4.5. Overall, all GPPs' PDFs follow the same general trend as the rain gauge PDF, except for ERA5 and CHIRPS for specific ranges. ARC2, CHIRPS, IMERG, PERSIANN, and RFEv2 tend to overestimate the precipitation class between 0–0.2 mm day^{-1}. Most GPPs tend to underestimate the precipitation class between 0.5 to 10 mm day^{-1}, while ERA5 overestimates frequency in that precipitation range. Furthermore, most GPPs tend to underestimate the frequencies in precipitation classes > 150 mm day^{-1}. More specifically, ARC2 cannot retrieve precipitation events > 150 mm day^{-1}. IMERG cannot retrieve precipitation events > 200 mm day^{-1}, while ERA5 and RFEv2 can retrieve it but strongly underestimate this class. Only CHIRPS and PERSIANN perform well for rainfall > 200 mm day^{-1}, although they underestimate this rainfall range.

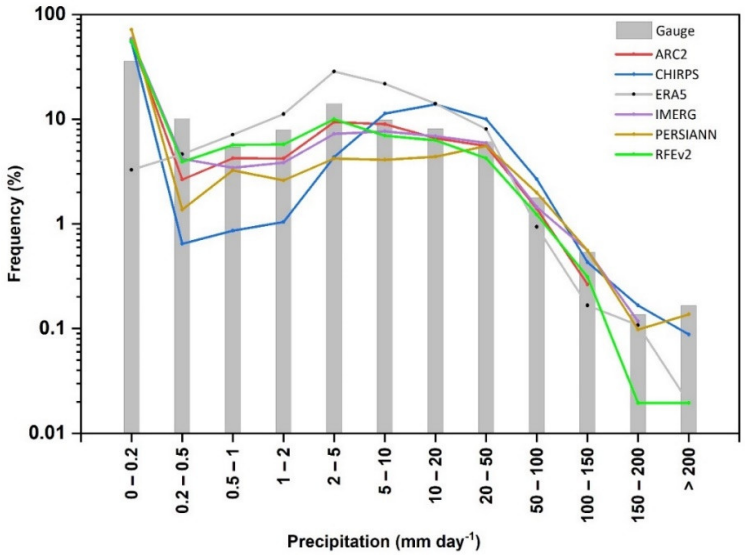

Figure 4. 5. Probability distribution function (PDF) of daily rainfall intensities based on GPP and rain gauge data from September 2018 to August 2020. Note logarithmic (Log10) scale for Y axis.

4.3.4. Precipitation detection ability

Figure 4.6 depicts the rainfall detection ability (POD, FAR, CSI) of the various GPPs. The results show that the POD values of ERA5 are highest among all products for the precipitation classes between 0 and 5 mm day^{-1} but are among the lowest for rainfall classes > 20 mm. As a matter of fact, the POD of ERA5 decreases steadily with increasing daily rainfall amount. The POD of ARC2, IMERG, RFEv2, and CHIRPS are similar (approximately 0.5 to 0.6) for the precipitation classes < 1 mm day^{-1}. However, the POD of IMERG remains rather constant in the range of 0.2–100 mm day^{-1}, whereas the PODs of ARC2 and RFEv2 decrease steadily.

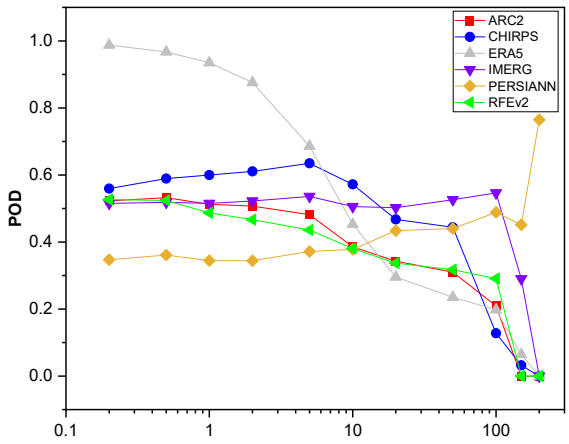

(**a**)

Figure 4. 6. Precipitation detection ability of the six GPPs based on daily rainfall: (a) Probability of detection (POD), (b) False alarm ratio (FAR), (c) Critical success index (CSI). Ground-based rain gauge data from September 2018 to August 2020 are used as reference. Note logarithmic (Log10) scale for X axis.

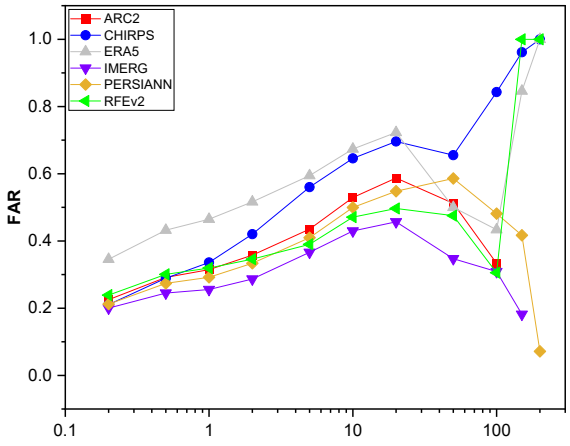

(b)

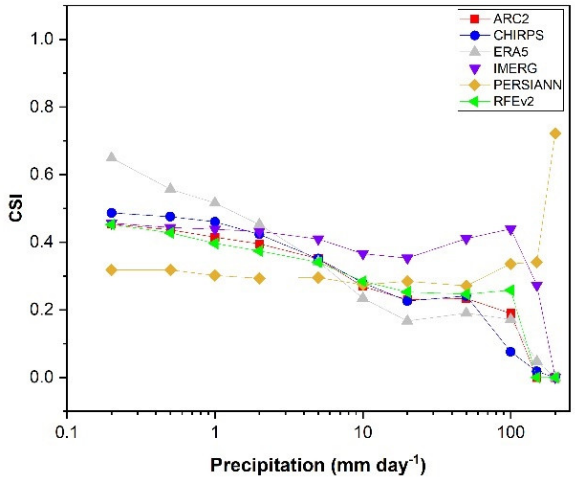

(c)

Figure 4. 6. (Cont.) Precipitation detection ability of the six GPPs based on daily rainfall: (a) Probability of detection (POD), (b) False alarm ratio (FAR), (c) Critical success index (CSI). Ground-based rain gauge data from September 2018 to August 2020 are used as reference. Note logarithmic (Log10) scale for X axis.

The POD of CHIRPS first increases slightly up to 5 mm day^{-1} and then decreases thereafter. PERSIANN performs worst of all GPPs for the lowest precipitation classes, but the POD tends to increase with increasing rainfall. For precipitation classes > 100 mm day^{-1}, only the PERSIANN product has a high POD value, while the PODs for all other GPPs tend towards 0.

The FARs of all GPPs increase steadily between 0.2 and 20 mm day^{-1}. For rainfall classes ≤ 100 mm day^{-1}, IMERG shows similar or better performance than all other products. For daily rainfall > 150 mm, only PERSIANN has a low FAR.

Based on the CSI value, the ERA5 product performs best in detecting precipitation in the 0.2–2 mm day^{-1} precipitation range. IMERG performs best in detecting rainfall in the range of 2–100 mm day^{-1}. Only PERSIANN performs well for rainfall >150 mm day^{-1}. Both IMERG and PERSIANN show rather constant performance in terms of CSI in the range of 0.2–100 mm, but IMERG outperforms PERSIANN in this range.

4.3.5. Different time scales assessment (hourly to yearly)

For the different time scales, only the IMERG product was evaluated, using the point-gridded approach, given that this product appeared to perform best at the daily time scale (§ 4.3.1). Figure 4.7 depicts the evaluation of IMERG at different time scales (hourly to yearly) against the gauge data over the Ankavia catchment. The coefficient of determination increases with increasing aggregation time scales from hourly to yearly. Specifically, IMERG exhibits good correlation at the yearly time scale (R^2 = 0.97; Figure 4.7a) and at monthly time scale (R^2 = 0.87; Figure 4.7b), and reasonable correlation at the daily assessment (R^2 = 0.65; Figure 4.7c). The correlation is poor at the hourly time scale (R^2 = 0.20; Figure 4.7d). Especially at the daily time scale, there is a tendency to underestimate the events > 150 mm (Figure 4.7c). IMERG also tends to underestimate yearly and, to a lesser extent, monthly rainfall. Additionally, it is apparent that the variability in yearly (Figure 4.7a) and monthly (Figure 4.7e) rainfall across the watershed is greater than the variability in IMERG rainfall data, especially for the high-rainfall months.

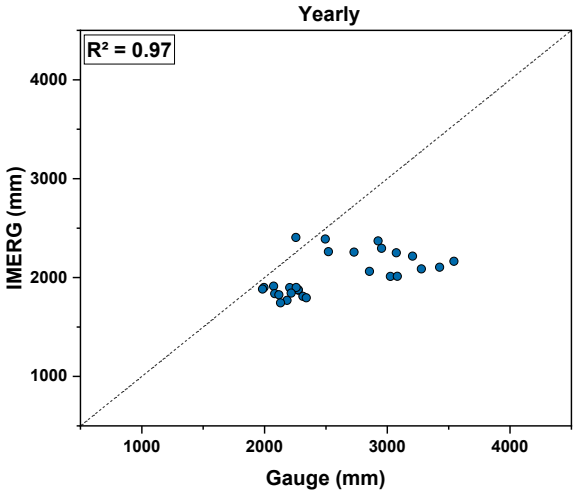

(a)

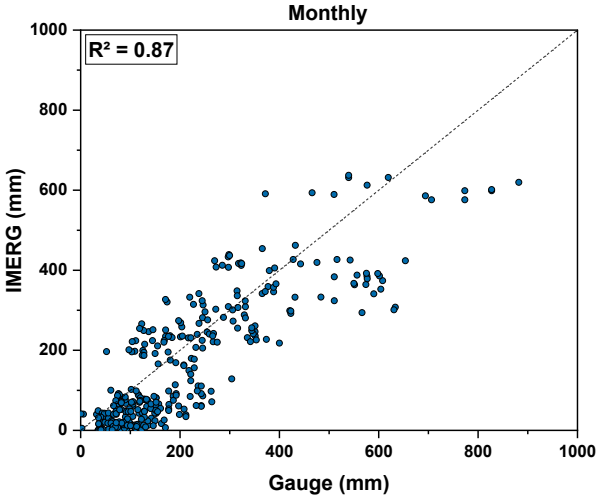

(b)

*Figure 4. 7. Comparison of ground-based precipitation data with IMERG at different time scales: (**a**) yearly, (**b**) monthly, (**c**) daily, (**d**) hourly, (**e**) barplot of monthly rainfall with standard deviation. R^2 value is determined for regression passing through (0,0).*

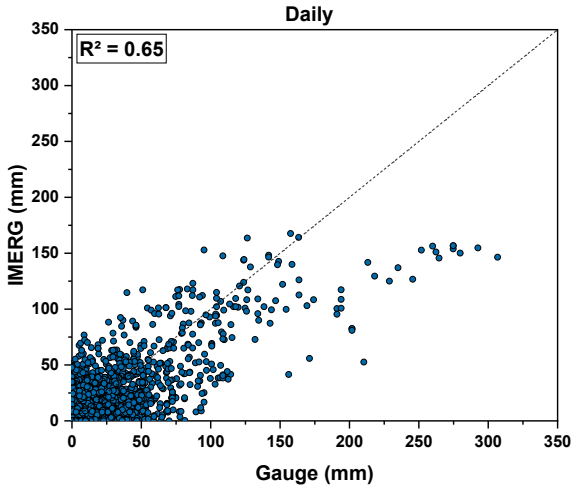

(**c**)

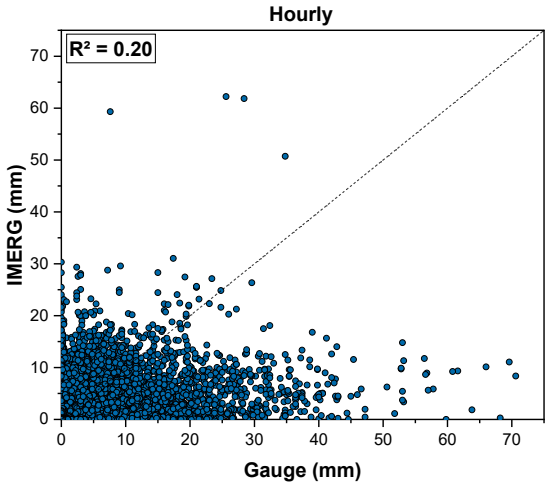

(**d**)

*Figure 4.7. (Cont.) Comparison of ground-based precipitation data with IMERG at different time scales: (**a**) yearly, (**b**) monthly, (**c**) daily, (**d**) hourly, (**e**) barplot of monthly rainfall with standard deviation. R^2 value is determined for regression passing through (0,0).*

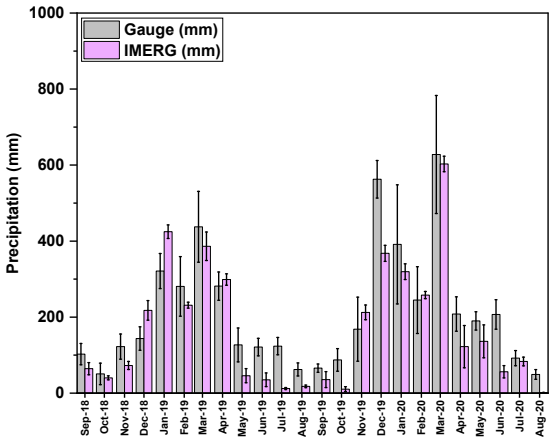

(**e**)

*Figure 4.7. (Cont.) Comparison of ground-based precipitation data with IMERG at different time scales: (**a**) yearly, (**b**) monthly, (**c**) daily, (**d**) hourly, (**e**) barplot of monthly rainfall with standard deviation. R^2 value is determined for regression passing through (0,0).*

4.3.6. Event scale assessment

Figure 4.8 shows the PDF plots for the rainfall event depths, durations, and intensities over the 2-year period. Overall, the IMERG precipitation product presents a good agreement with rain gauge data in terms of duration (Figure 4.8a) and depth (Figure 4.8b). However, the rainfall intensities between 0–5 mm h^{-1} are underestimated, while the 5–10 mm h^{-1} rainfall intensity class is largely overestimated (Figure 4.8c)

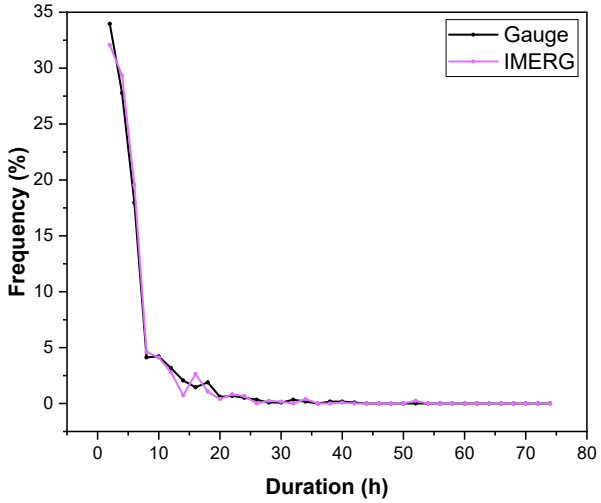

(**a**)

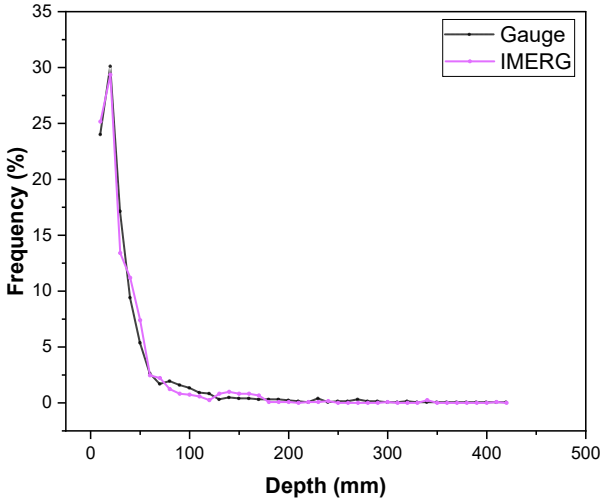

(**b**)

Figure 4. 8. Probability distribution function of (a) rainfall duration, (b) rainfall depth, and (c) rainfall intensity at event time scale for ground-based rain gauges and IMERG data from September 2018 to August 2020.

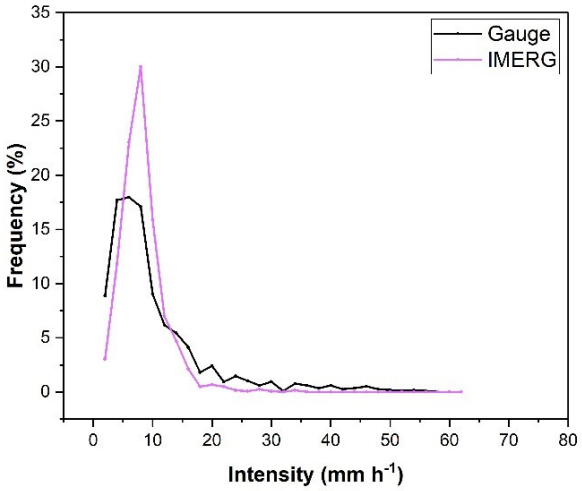

(c)

Figure 4. 8. (Cont.) Probability distribution function of (a) rainfall duration, (b) rainfall depth, and (c) rainfall intensity at event time scale for ground-based rain gauges and IMERG data from September 2018 to August 2020.

4.4. Discussion

For the validation of the GPP data using ground-based rain gauges, the point-gridded approach performs similarly or better than the point-to-grid approach (Figure 4.3). Since the grid cell centroids rarely coincide with the rain gauge position, the point-to-grid method is subject to greater inaccuracy (Rozante et al. 2020; Gebere et al. 2015). This inaccuracy grows in proportion to the spatial resolution of the GPP (Mayor et al. 2017). In contrast, the point-gridded approach reduces this mismatch problem between gauge data and GPP data while preserving the resolution of the gridded data. Nevertheless, the point-gridded technique is rarely studied (Mayor et al. 2017).

At the daily time scale, among the six GPPs, IMERG performed best at our study location (Figure 4.3). Its overall performance is reasonably good despite the small number of available rain gauges used for the Global Precipitation Climatology Centre

(GPCC) in Africa, especially in Madagascar (Huffman et al. 2020), resulting in biased precipitation data at rain gauge and catchment scale. Several previous studies have also underlined that IMERG outperforms other GPPs in tropical areas (Veloria et al. 2021; Liu et al. 2020; Dezfuli et al. 2017). This has been attributed to the GMI and the ability of the Ku/Ka-DPR to capture precipitation more effectively than the IR sensors and/or direct PM technologies used by other GPPs (Huffman et al. 2020). Specifically, the GMI instrument is a conically scanning, multi-channel microwave radiometer with 13 channels ranging in frequency from 10 GHz to 183 GHz (Huffman et al. 2020). The GMI employs a set of frequencies that have been refined over the last two decades to recover most ranges of precipitation, with the polarization difference of each channel serving as an indicator of optical thickness, water content, and precipitation systems (Huffman et al. 2020). Additionally, RFEv2, ARC2, and PERSIANN all show satisfactory performance (Figure 4.3). In contrast, CHIRPS and ERA5 perform poorly in the daily assessments. Some factors, such as gauge calibration and the sources of products play significant roles in the performance of GPPs (Mayor et al. 2017). In general, satellite-based precipitation products are currently more appropriate for meteorological applications than model-based products (e.g., ERA5) in tropical areas, especially over regions with extreme precipitation events. Nevertheless, reanalysis products such as ERA5 could have significant advantages in temperate regions or for research focusing on occurrence detectability at finer resolutions over high-latitude areas (Xu et al. 2022). Therefore, the fact that some products (ARC2, IMERG, PERSIANN, RFEv2) are gauge calibrated and satellite-based likely explains their better performance compared to CHIRPS and ERA5.

Table 4.3 summarizes the results from various studies that evaluated the performance of IMERG at a daily time scale in broadly similar climatic environments to the present study (humid tropical environment). Note that almost all of those studies used a point-to-grid or grid-to-grid approach; hence, the performance assessments are largely influenced by the density of the gauge network taken as a reference (Veloria et al. 2021; Tian et al. 2018; Sahlu et al. 2016). In terms of correlation (r), the results from our study are among the highest reported so far,

similar to Veloria et al. (2021). RMSE and MAE values in the present study are within the range of those reported previously. FAR values are also within the range of previously reported values, whereas POD and CSI are somewhat lower in the present study compared to previous studies. Nevertheless, IMERG's fairly high POD, CSI, and low FAR suggest a good detection capability for daily rainfall, particularly in the range of 0–100 mm day^{-1} (Figure 4.6), even though some rainy days are still being missed. Precipitation events estimated by the GPP may not be detected by the gauges as it might rain at other locations within the grid-cell area. Furthermore, given their spatial resolution, GPPs will be less sensitive to short-range variations in rainfall, which may explain the somewhat poorer performance of IMERG in the present study, given that many gauges are separated from each other by less than 10 km (i.e., roughly 0.1°, the spatial resolution of an IMERG grid box). Additionally, many factors could influence this variation of performance across studies, including the density of the rain gauge network and especially the validation technique (Ageet et al. 2021; Mahmoud et al. 2021; Veloria et al. 2021).

According to our results, the performance of IMERG is rather uniform across the watershed, i.e., there is no evidence of a spatial trend of the statistical metrics (Figure 4.4). Therefore, the negative effect of the topography, which often alters the performance of the precipitation satellites, is not apparent in our study area. Nevertheless, our results are consistent with previous findings for stations located in mid- and low-altitude, with relatively mild and wet climates (Li et al. 2021; Mahmoud et al. 2021; Tang et al. 2016a). Indeed, 13 of the 14 rain gauge stations in the Ankavia catchment are located between 14 and 300 m a.m.s.l.

The PDF analyses underline that most of the GPPs show the same distribution as the gauges except for the ERA5 data and, to a lesser extent, the CHIRPS data. Overall, the results reveal an overestimation for the 0–0.2 mm day^{-1} precipitation class and an underestimation of the >0.2 mm day^{-1} classes (Figure 4.5). Other studies have, however, reported that IMERG slightly overestimated the frequency of rainfall events between 1 and 50 mm day^{-1} (Liu et al. 2020; Tan and Santo 2018; Tan and Duan 2017). In addition, the findings also indicate that some GPPs underestimate the precipitation classes >150 mm day^{-1}.

Table 4. 3. Summary of IMERG assessment studies in tropical environments at a daily time scale.

References/ Study Area	Study Period/ Number of Rain Gauges for Validation	Validation Approach	r or $\sqrt{R^2}$	RMSE mm/day	MAE mm/day	POD	FAR	CSI
(Ageet et al. 2021)/ East Africa	2000–2018/36	grid-to-grid	0.41	12.4	7.6	0.88		
(Sahlu et al. 2016)/ East Africa	2014/37	grid-to-grid	0.53			0.87	0.04	
(Tan and Duan 2017)/ Singapore	2014–2016/48	grid-to-grid	0.53	11.83		0.78	0.28	0.60
(Veloria et al. 2021)/ Philippines	2014–2017/55	grid-to-grid	0.81	5.66	3.74			
(Liu et al. 2020)/ Bali	2015–2017/27	point-to-grid	0.32	17.19		0.84	0.54	0.44
(Wang et al. 2017a)/ Vietnam	2014–2016 53	grid-to-grid	0.58			0.73	0.22	0.61
(Tan and Santo 2018)/ Malaysia	2014–2016/31	point-to-grid	0.54	14.93		0.89	0.20	0.73
(Mayor et al. 2017)/ Mexico	2014–2015/99	point-gridded	0.54	7.93		0.2–0.6	0.2–0.6	0.2–0.8
Ankavia	2018–2020/14	point-gridded	0.80	12	5.5	0.5–0.6	0.2–0.4	0.4–0.5

The poor performance of GPPs at detecting extreme events was also reported in other assessment studies in tropical river basins (Asadullah et al. 2008; Tan and Duan 2017). Specifically, since gridded products contain spatially-averaged rainfall values, larger grid size (0.1 × 0.1°) products are more likely to smooth out the extreme rainfall values (>150 mm day^{-1}), which are especially associated with short-duration events with limited spatial extent (Zorzetto and Marani 2019; Wang et al. 2017a). In contrast, CHIRPS and PERSIANN outperform all other GPPs in this range (>150 mm day^{-1}). Their capacities to better represent very high-intensity rainfall could be due not only to their smaller grid size (0.05° and 0.04°, respectively) but also to their ability to categorize cloud-patch features based on height, areal extent, and variability of texture estimated from satellite imagery (Peterson et al. 2013; Hong et al. 2004). These classifications aid in the assignment of rainfall values to pixels within each cloud based on a predefined curve that describes the link between rain rate and brightness temperature (Hong et al. 2004).

With respect to the time scale of integration, the correlation between ground-based data and IMERG data improves with increasing summing time scales from hourly to yearly, which is in line with others' findings (Ageet et al. 2021; Liu et al. 2020; Tan and Santo 2018; Tan and Duan 2017). However, the strength of the correlation at a yearly timescale is constrained by the short duration of the study period (2 years). In addition, IMERG data have difficulty reproducing the spatial variability of rainfall within the catchment (Figure 4.7 a,b,e). This may at least partly result from the spatial smoothing inherent to GPPs, daily extreme events not identified by the satellite (Figure 4.5), as well as the small number of rain gauges used as the bias correction for IMERG (Huffman et al. 2020). At the event time scale, there is good agreement in terms of PDF of duration and depth (Figure 4.8), which is consistent with the results of Freitas et al. (2020) in Brazil. Finally, the poor performance of IMERG on an hourly scale has also been reported by other studies (Tan and Santo 2018; Khodadoust Siuki et al. 2017). This is particularly due to the inferior performance at locations where the estimate is derived by morphing, which occurs when no overpasses by any of the passive microwave instruments in the GPM constellation are available at a specific half-hour (Huffman et al. 2020). This is also

due to the temporal resolution of inputs (>1 h), cited above (Section 4.3.2 IMERG), used to calculate the IMERG product (Moazami and Najafi 2021; Huffman et al. 2020).

In this paper, we only focused on IMERG for the assessment at different time scales due to its better performance at a daily scale. However, it is important to note that the poor performance of some products at a finer scale does not necessarily suggest that they will be bad at longer time scales. As a matter of fact, the accuracy of gridded precipitation products increases as the time of accumulation increases (Ageet et al. 2021; Liu et al. 2020; Rahmawati and Lubczynski 2018).

4.5. Conclusion

In this study, we performed the first assessment of six gridded precipitation products (ARC2, CHIRPS, ERA5, IMERG, PERSIANN, RFEv2) over the Ankavia watershed in Madagascar, for a common period from September 2018 to August 2020, with 14 rainfall gauges taken as reference. The main findings of the study can be summarized as follows:

- The point gridded approach is better suited than the point-to-grid approach in terms of continuous statistical metrics to evaluate gridded precipitation products against rain gauge data;
- At a daily scale, IMERG outperforms all other tested gridded precipitation products, followed by RFEv2 and ARC2;
- GPPs tend to overestimate the 0–0.2 mm day^{-1} rainfall class but underestimate the >0.2 mm day^{-1} ranges. Only GPPs with smaller grid sizes (0.04°, 0.05°) accurately estimate the >150 mm day^{-1} precipitation class;
- IMERG is shown to perform well in detecting rain events up to 100 mm day^{-1} but is surpassed by PERSIANN in detecting rain events larger than 150 mm day^{-1}. Nevertheless, a substantial proportion of rainy days are not correctly estimated by IMERG;

- IMERG shows good performance at monthly, daily, and event time scales in our case study; nevertheless, its capacity to reproduce spatial variability of rainfall remains limited at the catchment scale.

Overall, this GPP assessment study in northeastern Madagascar provides evidence that the IMERG v06 final precipitation datasets perform satisfactorily when compared to rain gauge time series using the point-gridded technique at a daily time scale. In addition, the level of performance is fairly constant across a broad range of daily rainfall values, except for extreme events. Therefore, IMERG is the most reliable for estimating rainfall characteristics in this region. However, the product should be used with caution for hazard and flood assessment, given its limitations for extreme rainfall events.

5. Chapitre 5 : Driving Factors of the Hydrological Response of a Tropical Watershed : The Ankavia River Basin in Madagascar[4]

Abstract:

Understanding the hydrological behavior of watersheds (WS) and their driving factors is crucial for sustainable water resources management. However, at large scales, this task remains challenging due to the spatial heterogeneity in landscapes, topography and morphology (T), land cover (LC), geology (G), and soil properties (S). In this context, the aim of this study was to identify the key factors that influence the hydrological signatures of four watersheds: Ankavia (WS1: 55% forest cover), Ankaviabe (WS2: 77% forest cover), Sahafihitry (WS3: 41% forest cover), and Antsahovy (WS4: 48% forest cover), over a 10-month study period. These catchments are located within the SAVA region of northeastern Madagascar and have a humid tropical climate. We investigated the relationship between selected catchment descriptors and hydrological signatures by using a Pearson coefficient-based correlation matrix. More specifically, catchment descriptors (extracted from T, LC, G, and S) were correlated with the following hydrological signatures: base flow index (BFI), mean runoff coefficient (rc), mean peak flow (Qp), mean runoff event time scales (ts), high flows (Q5), low flows (Q95), and mean discharge (q_mean).

The analysis revealed that land cover, soil properties, and geology seem to be the best predictors for BFI and Q95, while soil properties mainly govern rc, Qp, Q5, ts, and q_mean. These findings provide valuable insights into the key drivers of hydrological behavior that can inform water resource management strategies. In particular, WS2 exhibits better flood buffering capacity but also experiences lower base flows in the dry season, potentially due to higher evapotranspiration.

[4] Based on : Ramahaimandimby, Z., A. Randriamaherisoa, M. Vanclooster, and C. L. Bielders. 2023. “Driving Factors of the Hydrological Response of a Tropical Watershed: The Ankavia River Basin in Madagascar.” *Water*, 15 (12): 2237. Multidisciplinary Digital Publishing Institute. https://doi.org/10.3390/w15122237.

Conversely, WS3 and WS4 (and to a lesser extent WS1) have lower flood buffering capacity, but these watersheds encounter less pronounced low flows in the dry season due to higher BFIs, possibly attributable to lower evapotranspiration rates.

The results underscore the importance of responsible land use practices and conservation efforts, which are essential for the sustainable development of the region. By incorporating these practices into water management strategies, we can help ensure a more stable and reliable water supply for communities and ecosystems within the region.

Keywords: catchment descriptors; hydrological signatures; driving factors; Ankavia catchment.

5.1. Introduction

Global changes, such as population growth, industrial development, agricultural expansion, and climate change, are exerting strong pressures on natural resources in general, and on water resources in particular (Wu et al. 2023; Papa et al. 2023; Group et al. 2001). In turn, the resulting stresses on water resources are having a significant impact on production, economic growth, health, livelihoods, and national security (Godinez-Madrigal et al. 2019). As a result, achieving sustainable management of water resources is a pressing issue, and it will be even more so in the future.

In order to support the sustainable use of water in the face of socio-economic and environmental constraints, understanding the impact of global changes on hydrology is essential (Bezerra et al. 2023; Kong et al. 2023). This includes an in-depth understanding of the physical drivers of the hydrological response over time and space within the regions to be managed (Blöschl and Sivapalan 1995). As water management is often operated across large areas, this represents a significant challenge considering the complex interactions of natural and human processes that may operate concurrently and affect the spatial and temporal variability of the water system (Blöschl et al. 2013; Merz et al. 2006). This is particularly true in large tropical

watersheds because of the rapid pace at which these processes change in response to the growing population pressure, economic development, and climate change. Furthermore, local economies and livelihoods across much of the tropics heavily rely on water availability (Soesbergen and Mulligan 2018), while the limited economic and development capabilities enhance water-related risks (limitations in water supply, floods, and droughts), making countries from the Global South among the most vulnerable to climate change impacts (Eckstein et al. 2021).

Most of our current understandings of hydrological responses are derived from small-scale catchment studies (Qazi 2020; Fritsch 1995). However, in tropical areas, the study of watershed behavior at a small- and meso-scale remains problematic due to a lack of monitoring infrastructure (Wu et al. 2021; Choubin et al. 2019; Ochoa-Tocachi et al. 2016). As a result, in recent decades, most efforts in tropical areas have been invested in studies of large watersheds rather than small-scale or meso-scale catchments (Gay-des-Combes et al. 2017; Baumann 2011). However, large tropical watersheds may be composed of a wide variety of soil types, geological formations, and land covers, making the scaling of hydrological behavior problematic and resulting sometimes in conflicting results (Bruijnzeel 2004). Indeed, whereas some studies conducted in tropical areas have reported considerable hydrological alterations in response to land cover changes in large watersheds (Hou et al. 2018; D'Almeida et al. 2007; Cui et al. 2007), others have shown that the influence of changing forest cover on river hydrology was insignificant (Arias et al. 2018b; Thanapakpawin et al. 2007; Wilk et al. 2001). These inconsistencies may be related to the specificities of the study sites, but also to the large scale of the study of the watersheds and the resulting complexity (Cui et al. 2007). More studies at the small- and meso-scale are thus needed to help better understand the hydrological behavior of tropical watersheds. Besides, the challenge to understand catchment response at smaller scales to changing environmental conditions in tropical regions is still very much a topical issue since many climate mitigation strategies are implemented at these smaller scales (Sivapalan et al. 2003; Blöschl and Sivapalan 1995).

Madagascar—a tropical island state in southern Africa—is faced with various water-related management issues (WMO 2022; Rabefitia 2008; AFD 2005). About 80% of

the active population's livelihoods, including agriculture, livestock farming, fishing, and fluvial transportation, are water dependent (WMO 2022). The impacts of global changes on hydrology have already been observed, particularly due to the location of the country in the Indian Ocean and its 5000 km coastline, which makes the island extremely vulnerable to climate change and extreme events (Ralaingita et al. 2022; Tadross et al. 2008). Floods often occur in northern and central areas, while droughts are recurrent in certain southern regions (Rabefitia 2008; Tadross et al. 2008). Over the past decades, to cater to the growing population needs, a significant amount of rainforest cover has been converted into a mosaic of land uses representing various stages of the swidden farming cycle, including severely degraded grasslands (Gay-des-Combes et al. 2017; Aubert et al. 2003). Such changes can potentially affect the soil infiltration capacity, leading to increased surface runoff and peak discharge of rivers (Pereira et al. 2014; Gade 1996). Unfortunately, the country has very few monitored watersheds, which is a prerequisite to better understanding the hydrological functioning at different scales and designing sustainable water and land use management strategies. Also, creating a credible database for hydrological studies is jeopardized by the highly incomplete and dispersed data from the national weather service stations (Tadross et al. 2008; CPGU 2012).

As a contribution to filling this current knowledge gap, this study aimed to identify the key factors governing hydrological response at the meso-scale using the humid tropical Ankavia catchment in Madagascar as a case study. The data collected will be used in a recently installed rainfall and discharge monitoring network. To reach this overall objective, we address the following specific objectives: (i) to document the Ankavia catchment characteristics; (ii) to analyze the hydrological responses in the catchment; and (iii) to identify the groups of factors (topographic, morphometric, pedo-geological, and land cover properties) that are the most informative to understand these hydrological responses. The study should serve as a basis for the future implementation of an Integrated Water Resources Management (IWRM) system in the SAVA region (northeastern Madagascar).

5.2. Materials and Methods

5.2.1. Study area

The Ankavia watershed (WS1) is situated in the district of Antalaha, a city in the SAVA (Sambava–Andapa–Vohémar–Antalaha) region of northeastern Madagascar (Figure 5.1). It covers an area of 1116 km² and 55% of the basin is occupied by forest. The watershed lies between 14°90′ and 15°20′ South Latitude and between 49°45′ and 50°15′ East Longitude. The Ankavia river is formed by three tributaries before flowing into the Ankavanana river, which reaches the Indian Ocean. The three upstream sub-catchments are Ankaviabe (WS2; 624 km^2; 77% forest cover), Sahafihitry (WS3; 197 km^2; 41% forest cover), and Antsahovy (WS4; 70 km^2; 48% forest cover). The basin has a total length of 54.6 km, and its elevation varies from 14 m a.m.s.l. at the outlet to 1469 m a.m.s.l. at the highest point on the escarpment (Figure 5.1). For the purpose of this study, the outlet of the Ankavia was located at the Antsahamanenona Drinking Water Supply Station of Antalaha, which provides drinking water for the city's 280,000 inhabitants (INSTAT 2020). Additionally, the water-related stresses experienced in the Ankavia basin are similar to those experienced in other basins in the region (Randriamaherisoa and Binard 1992).

According to the meteorological station in Antalaha, the average annual rainfall in the area is 2200 mm (1960–2016). There is a wet rainy season between November and April, while a dry (but still rainy) season occurs from May to October. The daily maximum temperature of 31.4 °C is observed in January, while the minimum temperature of 18.9 °C is observed in August (CREAM 2013). The western part of the Ankavia watershed is dominated by primary forests, while the eastern part is occupied by a mosaic of natural vegetation composed of shrubs and herbaceous cover (CREAM 2013).

The geology of Madagascar consists of a patchwork of Precambrian rocks, mainly high-grade metamorphic basement domains overlain by unmetamorphosed sedimentary rocks and poorly weathered low-grade metasediments (Bauer et al. 2011). In the Antalaha area, two different cover sequences lay on high-grade metamorphic and igneous foundation rocks of the Archaean 'Antongil' craton and the Neoproterozoic 'Bemarivo' belt.

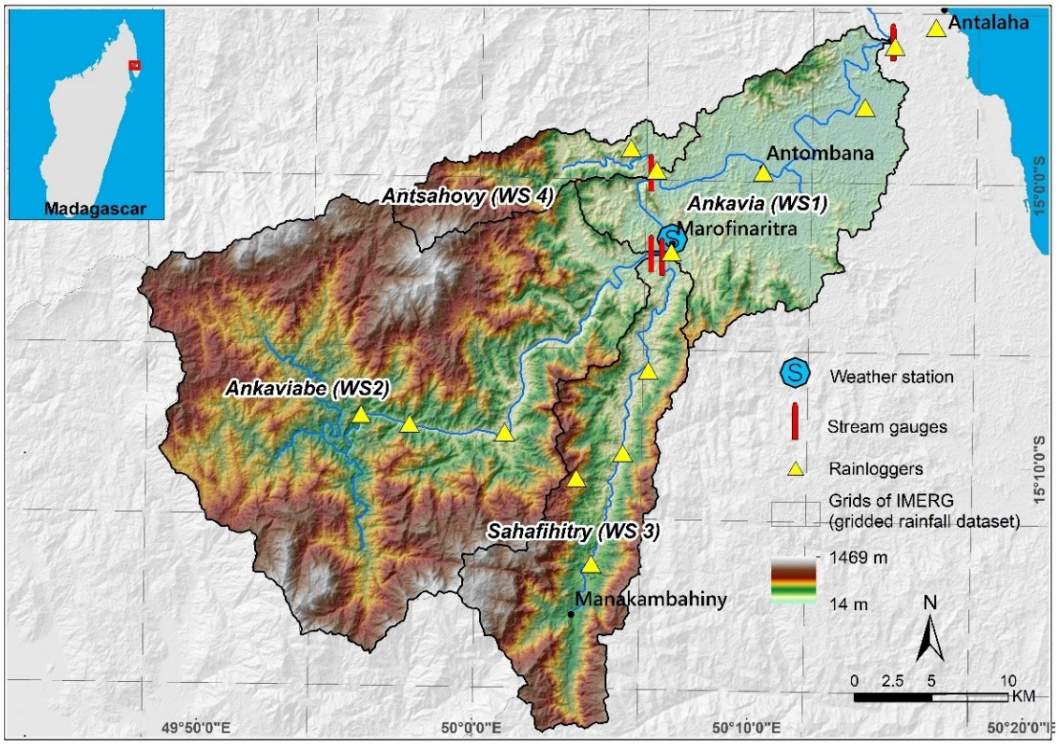

Figure 5. 1. Location of the Ankavia catchment (WS1) and its sub-catchments (WS2, WS3, and WS4). The map includes the location of the weather station, rain gauges, and stream gauges, as well as the grids of IMERG (a gridded rainfall dataset).

The elder of these two cover sequences, the 'Andrarona' Group, is composed of low-grade metasedimentary rocks, while the younger sequence, the 'Ampohafana' formation, is made up of unmetamorphosed sedimentary rocks (Bauer et al. 2011). The pedology of the basin is dominated by ferrasols upstream and acrisols downstream (Palm et al. 1996).

5.2.2. Watershed attributes

Several satellite products and thematic maps (Table 5.1) were used to determine the characteristics of the Ankavia catchment and sub-catchments in terms of topography/morphometry, land cover, soil, and geology (Figure 5.2). The 30-m digital elevation model (DEM) of the Shuttle Radar Topography Mission (SRTM; (Earth Resources Observation And Science (EROS) Center 2017)) was used to derive the topographic and morphometric attributes (Figure 5.1). The 2019 land cover of the Ankavia catchment was extracted from GlobCover v2 (Bontemps et al. 2009), which has a spatial resolution of 300 m (Figure 5.2a). The 250 m SoilGRIDs (global gridded soil information) was used to retrieve the soil attributes (Figure 5.2b), including the organic carbon data at three depths (0–5, 5–15, 15–30 cm), and the dominant soil order based on the World Reference Base (WRB) (Figure 5.2c) (Hengl et al. 2017). Hydrologic soil groups were extracted using HYSOGs250m (Figure 5.2d) (Ross et al. 2018), which were created to assist with USDA-based (United States Department of Agriculture) curve number runoff modeling at regional and continental scales. The four standard hydrological soil groups (HSG-A, HSG-B, HSG-C, and HSG-D) correspond to soils with increasing levels of runoff potential (low, moderately low, moderately high, and high, respectively). Lastly, the modified geological map (1/100,000 scale) was provided by the Ministry of Energy and Mines through the Mineral Resources Governance Program (PGRM) (Figure 5.2e).

Table 5. 1. Summary of the gridded products and maps used to characterize the Ankavia catchment.

Attributes	Data	Spatial Resolution/ Map Scale	Sources (Accessed on January 2022)	References
Topography	DEM (Digital Elevation Model)	30 m	https://earthexplorer.usgs.gov/	(EROS 2017)
Land Cover	GlobCover v2	300 m	https://maps.elie.ucl.ac.be/CCI/viewer/	(Bontemps et al. 2009)
Soil Texture	SoilGRIDs	250 m	https://soilgrids.org/	(Hengl et al. 2017)
Dominant Orders Soil	Soil World Reference Base (WRB)	250 m	https://soilgrids.org/	(Hengl et al. 2017)
Hydrological Group Soil	HYSOGs	250 m	https://daac.ornl.gov/SOILS/guides/Global_Hydrologic_Soil_Group.html	(Ross et al. 2018)
Geology	PRGM	1/100,000	https://www.brgm.fr/fr/reference-projet-acheve/synthese-geologique-miniere-madagascar	

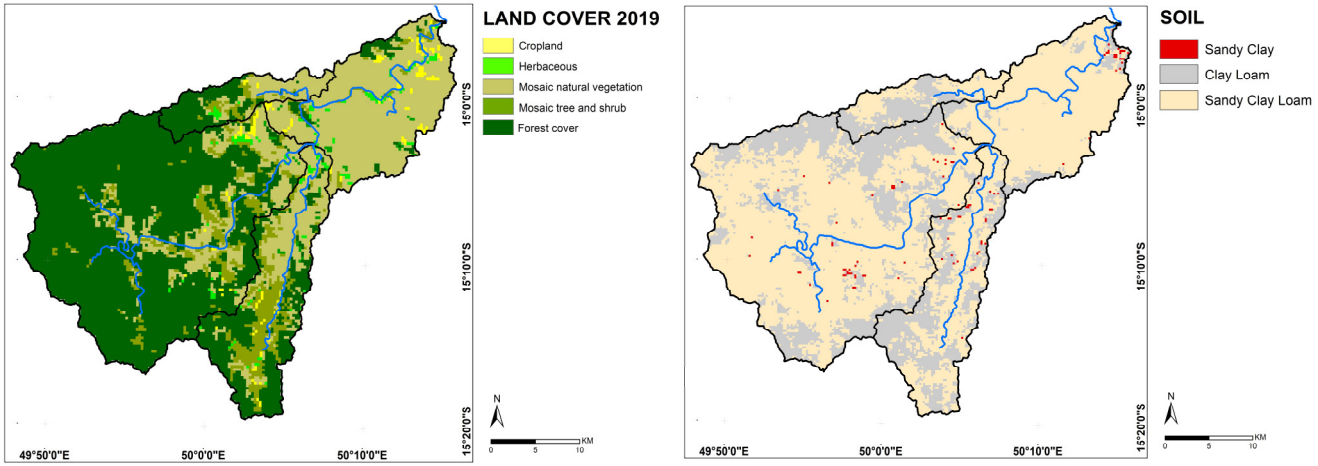

(**a**) (**b**)

*Figure 5. 2. (**a**) 2019 land cover of Ankavia catchment, (**b**) soil texture, (**c**) dominant soil orders, (**d**) hydrological soil group, (**e**) modified geological map. Data sources are listed in Table 5.1.*

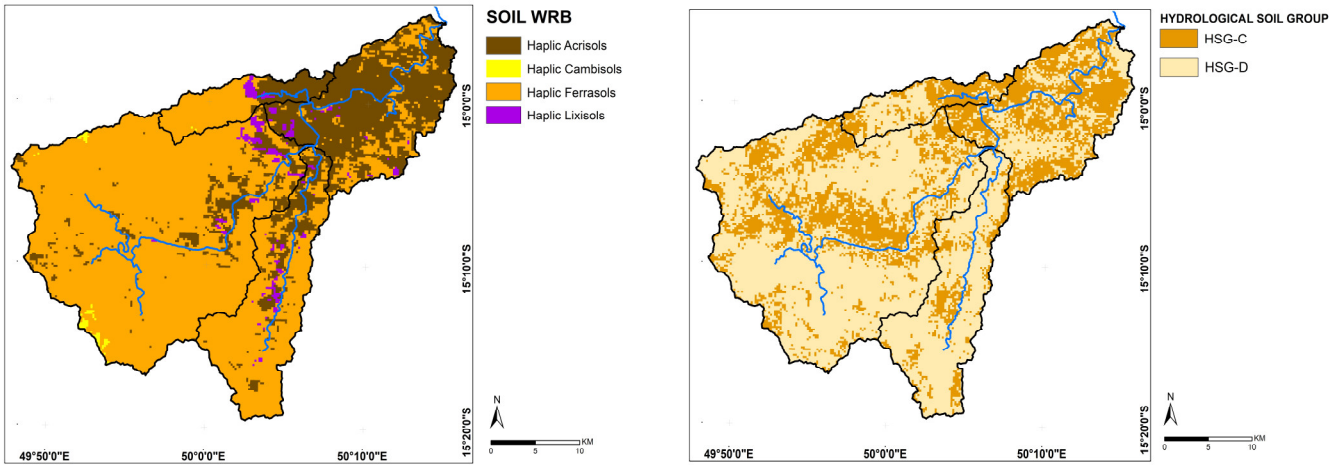

(**c**) (**d**)

*Figure 5.2. (Cont.) (**a**) 2019 land cover of Ankavia catchment, (**b**) soil texture, (**c**) dominant soil orders, (**d**) hydrological soil group, (**e**) modified geological map. Data sources are listed in Table 5.1.*

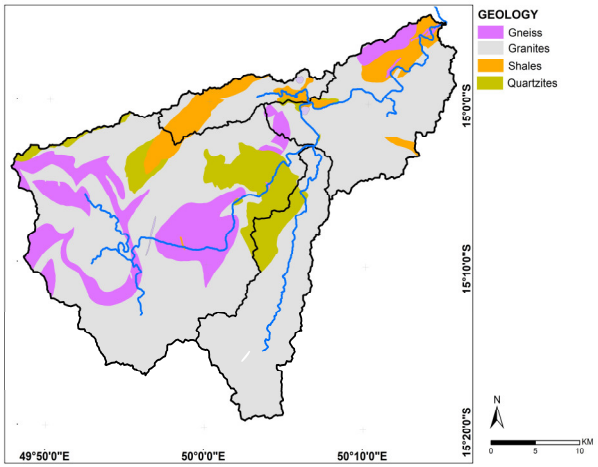

(e)

*Figure 5. 2. (Cont.) (**a**) 2019 land cover of Ankavia catchment, (**b**) soil texture, (**c**) dominant soil orders, (**d**) hydrological soil group, (**e**) modified geological map. Data sources are listed in Table 5.1.*

5.2.3. Hydrometeorological datasets

Even though rain gauges were installed as part of the project (Ramahaimandimby et al. 2022), their spatial coverage was uneven across the watershed, with no gauges in the western part and at the higher altitudes due to accessibility issues (Figure 5.1). Consequently, the gridded precipitation product IMERG V06 Final was used in the present study (Huffman et al. 2020) (Figure 5.1). Ramahaimandimby et al. (2022) demonstrated that the IMERG v06 Final data is a reliable alternative to ground-based measurements for event and daily time scales or greater. We used the IMERG product at the event time scale for the time period covered by the discharge measurements, as described below.

To measure the discharge, we installed four gauging stations at the outlet of each catchment (Figure 5.1). These locations were chosen for their accessibility and the stability of the riverbed sections (predominantly composed of rocks) (Chapter 3, section 3.5.3). Starting on September 2018, all four stations were operational. Water levels were monitored using Solinst® LTC Levelogger Edge M5 C80 pressure sensors (Level measurement device, Solinst Canada Ltd., Georgetown, Canada) with an accuracy of ±0.3 cm. The atmospheric pressure was recorded using a Solinst® sensor 3001 LT Barologger Edge, M1.5/F5, with a precision of ±0.05 kPa located at the climatic station of Marofinaritra (Figure 5.1).

The data were collected with a 1 h timestep (GMT+ 0). The equipment was checked monthly, and data were regularly checked for consistency and completeness. In this study, we used the hydrometric data collected from September 2018 to June 2019, which is the period during which all 4 gauging stations were operational concurrently. After this period, one or more stations were not operational due to damage by extreme floods or technical issues with the probes.

5.2.4. Catchment descriptors (CD) analysis

A wide range (37 in total) of catchment descriptors representing topography/morphometry (T), land cover (LC), soil properties (S), and geology (G) of the Ankavia catchment were acquired and calculated. Table 5.2 and Annexe B list the metadata of catchment descriptors.

Table 5. 2. Descriptors and calculation of catchment descriptors.

Groups	Variables	Label (Units)	Calculation/Description	Reference
Topography-morphometry (**T**)	Drainage area	A (km²)	GIS calculation [1]: area calculation	(Horton 1932)
	Perimeter	P (km)	GIS calculation: perimeter calculation	(Horton 1932)
	Basin length	L_b (km)	GIS calculation: spatial analyst tool/hydrology	
	Mean slope	S_I (°)	GIS calculation: spatial analyst tool/surface	
	Elevation range	H_{min}, H_{max} (m)	H_{min} is the minimum elevation; H_{max} is the maximum elevation.	
	Hypsometric curve		The shape of a hypsometric curve is an indicator of dominant geomorphic processes at work in a watershed area. A convex curve indicates that a greater part of the watershed's area is held relatively high in the watershed. A concave curve indicates that the bulk of the watershed's area resides at a relatively low elevation.	(Strahler 1952)
	Gravelius coefficient	K_g (-)	$K_g = P/(2(\pi A)^{1/2})$ $1 < K_g < 1.5$: circular shape $1.5 < K_g < 1.9$: elongated shape	

Table 5.2. (Cont.) Descriptors and calculation of catchment descriptors.

Groups	Variables	Label (Units)	Calculation/Description	Reference
Topography-morphometry (**T**) (continued)	Effective basin width	R_b (km)	$R_b = A/L_b$ where A is the watershed area and L_b is the watershed length	
	Elongation ratio	R_e	$R_e = 2(A/\pi)^{0.5}/L_b$ R_e is the ratio of the diameter of a circle having the same area as the watershed to the maximum watershed length. $R_e < 0.7$: more elongated $0.8 < R_e < 0.9$: oval $R_e > 0.9$: circular	(Schumm 1956)
	Unit shape factor	R_u	$R_u = L_b/A^{½}$ R_u is the ratio of the length of the watershed to the square root of the area.	
	Total relief	R_r (km)	$R_r = H_{max} - H_{min}$ R_r is the maximum vertical distance between the lowest (outlet) and the highest (divide) points on the valley floor of a watershed.	

Table 5.2. (Cont.) Descriptors and calculation of catchment descriptors.

Groups	Variables	Label (Units)	Calculation/Description	Reference
Topography-morphometry (**T**) (continued)	Relief ratio	R_h	$R_h = R_r/L_b$ where R_r is the total relief and L_b is the watershed length R_h indicates the overall steepness of the drainage watershed and the intensity of erosional processes operating on the slope of the watershed.	(Schumm 1956)
	Total stream length	L_t (km)	GIS calculation: spatial analyst tool/hydrology	(Strahler 1957)
	Length of main stream	L_c (km)	GIS calculation: spatial analyst tool/hydrology	(Strahler 1957)
	Total number of stream segments	N_u	GIS calculation: spatial analyst tool/hydrology	

Table 5.2. (Cont.) Descriptors and calculation of catchment descriptors.

Groups	Variables	Label (Units)	Calculation/Description	Reference
Topography-morphometry (**T**) (continued)	Drainage density	D_d (km km^{-2})	$D_d = L_t/A$ D_d is the stream length per unit area in the watershed. $D_d < 2$: very coarse density $2 < D_d < 4$: coarse density $4 < D_d < 6$: moderate density $6 < D_d < 8$: fine density $D_d > 8$: very fine density	(Horton 1932)
	Constant of channel maintenance	C_m (km² km^{-1})	$C_m = 1/D_d$ C_m expresses the watershed surface required to encompass a 1 km long stretch of stream.	(Schumm 1956)

Table 5.2. (Cont.) Descriptors and calculation of catchment descriptors.

Groups	Variables	Label (Units)	Calculation/Description	Reference
Topography-morphometry (**T**) (continued)	Ruggedness number	R_n	$R_n = R_r \times D_d$ R_n indicates the structural complexity of the terrain in association with relief and drainage density.	(Strahler 1957)
Land cover variables (**LC**)	Land cover		% of catchment area covered by the following land cover types: mosaic crop (cropland, herbaceous cover) and mosaic natural vegetation (M_**Crop**)/mosaic tree and shrub (**Mos**)/tree cover (**Tree**).	
	Estimated Curve Number (CN)	CN_est	**CN_est** = Σ (%land_cover(i)×CN(i))/100) where CN_i is the respective CN to land cover, which is based on USDA Curve Number. CN_Crop = 77, CN_Mos = 60, CN_Tree = 55.	(Mishra and Singh 2013)
Soil variables (**S**)	Soil texture		% of catchment area covered by soils having the following soil textures: sandy clay (**S-C**), clay loam (**C-L**), sandy clay loam (**S-C-L**).	
	Soil types		% of catchment area covered by the following soil types: Acrisols (**Acri**), Ferrasols (**Ferra**), Lixisols (**Lixi**), Cambisols (**Cambi**).	

Table 5.2. (Cont.) Descriptors and calculation of catchment descriptors.

Groups	Variables	Label (Units)	Calculation/Description	Reference
Soil variables (**S**) (continued)	Soil hydrological group		% of catchment area covered by the following hydrological soil group: HSG-C (**H-C**), HSG-D (**H-D**).	
	Organic Carbon density	OC (g kg^{-1})	$OC = OC_{0–5cm}. \times 1/6 + OC_{5–15cm} \times 2/6 + OC_{15–30cm} \times 1/2$	
	Grain diameter	Dg (µm)	$Dg = \%Sand \times øsa + \%Clay \times øsi + \%Silt \times øc$ where øsa, øsi, øc are the median particle diameter of sand, silt, clay, which are 900 µm, 25 µm, 1 µm, respectively.	
Geological variables (**G**)	Geological characteristics		% of catchment area covered by the following geological classes: Gneiss (**gneiss**), Granites (**gran**.), Shales (**shales**), Quartzites (**quartz**.).	

5.2.5. Streamflow analysis

Discharge data calculations are described in Chapter 3, section 3.4.2 and 3.4.3.

5.2.6. Hydrological signatures (HS) Analysis

Hydrological signatures (HS) are quantitative metrics or indices that define statistical or dynamical properties of hydrologic data series (Addor et al. 2018). These signatures can be computed using various data sources but, in practice, they are most often calculated using rainfall-runoff time series. In this study, the HS indicators were derived from rainfall-runoff datasets for the 10-month study period.

5.2.6.1. Event identification

Rainfall events were defined as periods of non-zero basin-average rainfall interspersed with periods of zero rainfall, considering a minimum cumulative rainfall amount of 2.5 mm and a minimum inter-event time of 6 h (Ramahaimandimby et al. 2022).

A runoff event is characterized by a runoff start, peak(s), and end. The start of a direct runoff event was defined as the moment in time closest to the (first) peak when total streamflow equals baseflow (Figure 5.3). The end is reached as soon as total streamflow falls back to the baseflow level (see further). Rainfall and runoff events were then matched, resulting in three cases: (i) rainfall event without runoff event, (ii) rainfall with runoff event, and (iii) runoff without (measured) rain event. In the study, we took into account only the two first cases.

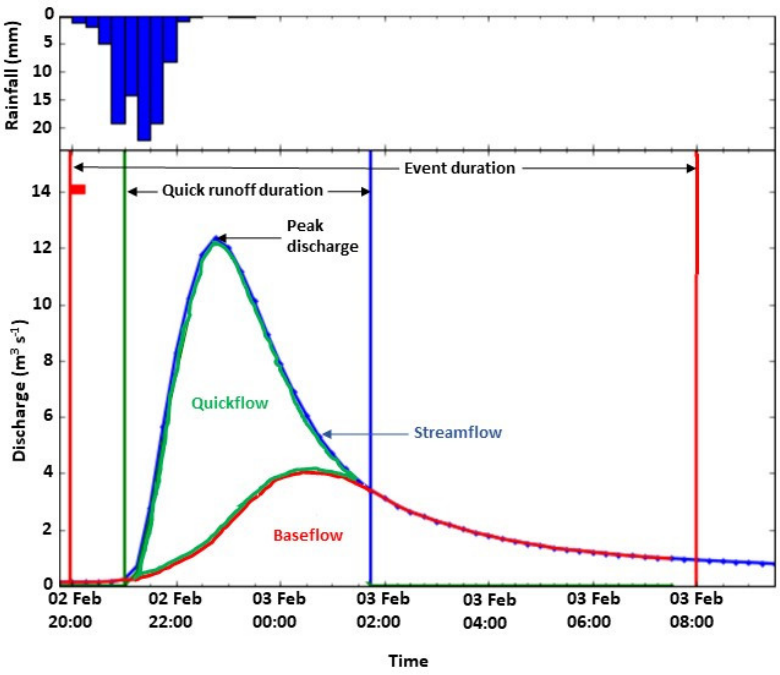

Figure 5. 3. Event identification and hydrograph separation.

5.2.6.2. Hydrograph separation

The Eckhardt method (Equation 5.1; Eckhardt (2005)) was used to separate the discharge data into quickflow (Qf; the direct flow in response to a rainfall event) and baseflow (Qbf: the delayed flow from storage) [Annexe G). This method relies on two parameters: the filter parameter (k) and the maximum baseflow index (BFI_{max}). The filter parameter, which describes the rate at which the streamflow decreases with time following a recharge event, is estimated through recession analysis, while the BFImax is the maximum value of the baseflow index that can be modeled through the recursive digital filter algorithm (Eckhardt 2005).

$$Q_{b,t} = \frac{(1-BFI_{max})\times k\times Q_{b,t-1} + (1-k)\times BFI_{max}\times Q_{s,t}}{1-k\times BFI_{max}} \quad (5.1)$$

where $Q_{b,t}$ and $Q_{b,t-1}$ are the baseflow at time steps t and t − 1, respectively; $Q_{s,t}$ is the total streamflow at time step t; BFI_{max} refers to maximum baseflow index (ratio of baseflow to the total flow), and k is the filter parameter.

In the present study, we employed the Web-based Hydrograph Analysis Tool (WHAT) (Lim et al. 2005) to separate baseflow from total streamflow. In Equation (5.1), baseflow for the first time step, $Q_{b,t-1}$, was assumed to be 50% of the total streamflow. Eckhardt (2008) proposed different BFI_{max} values for various aquifer types. Based on the hydrological and geological characteristics of the studied watersheds, we considered the catchments to have porous aquifers and perennial streams. Therefore, the default BFI_{max} was set to 0.80 while the filter parameter 'k' was optimized through recession analysis of selected events (Eckhardt 2012).

5.2.7. Hydrological signatures analysis

A large number of hydrological signatures (HS) have been proposed in the literature but there are some general selection criteria. According to McMillan et al. (2017), HS should meet the following requirements: (i) they can be related to hydrological processes to better understand catchment behavior; (ii) they are sensitive to events occurring over different time periods; and (iii) they are not redundant. Based on these criteria, this study used the following HSs: baseflow index (BFI); runoff coefficient (rc); peak discharge (Qp); runoff event time scale (ts); high flows (Q5); low flows (Q95); and mean discharge (q_mean) (Table 5.3).

BFI is the ratio of total baseflow to total discharge during the observation period. Runoff coefficient rc is the ratio of the quickflow volume of a specific runoff event to the corresponding rainfall. The peak discharge, Qp, represents the maximum rate of discharge during the period of runoff resulting from a rainfall event. The time scale ts is the ratio between quickflow volume and the peak discharge of a specific runoff event. It is an indicator of catchment flashiness and a measure of the importance of

fast runoff generation processes, such as overland flow or fast subsurface storm flow. Fast-reacting catchments will have small ts, while catchments with slower runoff generation processes tend to have larger ts. In this study, ts is normalized by the length of the main river. Rc, Qp, and ts were determined for each individual event. Q5 and Q95 were derived from the flow duration curves (FDC), which are cumulative frequency curves that show the percentage of the time that a specified discharge is equaled or exceeded during a given period (Castellarin et al. 2013). The FDC combines the flow characteristics of a stream throughout the range of observed discharges, without regard to the sequence of occurrence. Q5 (the 5th percentile of flow) and Q95 (the 95th percentile) correspond to the discharge that equaled or exceeded 5% (high flows) or 95% (low flows) of the time, respectively. Finally, q_mean is the mean daily discharge during the 10-month study period.

Table 5. 3. Hydrological signatures of runoff events used in the present study.

HS (Unit)	Descriptions	Calculation	References
BFI (-)	Ratio of total baseflow (Q_{bf}) to total discharge (Q) during the observation period; hydrograph separation performed according to (Lim et al. 2005).	BFI = $\frac{\sum Q_{bf}}{\sum Q}$	(Lim et al. 2005)
rc (mm mm^{-1})	The ratio of the quickflow volume (Q_f) of a specific runoff event [mm] to the corresponding rainfall (R_i). Mean of all events [mm].	rc = $\frac{Q_f}{R_i}$	(Sawicz et al. 2011)
Qp (mm h^{-1})	Highest value of the discharge during an event (mean value).		(Hu and Shrestha 2020)
ts (h km^{-1})	Ratio between quickflow volume (Q_f) [mm] and the peak discharge (Q_p) [mm h^{-1}] multiplied by the length of the main river (L_c) [km] (mean of all events).	ts = $\frac{Q_f}{Q_p \times L_c}$	
Q5 (mm day^{-1})	5th percentile of the flow duration curve (high flows).		
Q95 (mm day^{-1})	95th percentile of the flow duration curve (low flows).		
q_mean (mm day^{-1})	Mean daily discharge		

5.2.8. Linking hydrological signature and catchment descriptors

A correlation matrix was used to select the most significant CDs. When two or more CDs within the same group of variables (T, LC, S, or G) were strongly correlated ($r > |0.7|$), only the one showing the highest correlation with the principal component was retained. The links between event characteristics and selected landscape features were then analyzed to provide insights into the physical drivers of the event runoff response.

Pairwise correlations between individual HSs and selected CDs were determined using the Pearson correlation coefficient and summarized in a matrix. It was displayed as a heat map to ease the examination of these interactions. Additionally, to assess the robustness of the correlation between CD and HS, we checked for the presence of any influential data points (high leverage), which can unduly influence any part of the regression analysis, such as the predicted responses or the estimated slope coefficients. To identify these points, we used the "Difference in Fits" measure, denoted DFFITS in OriginPro ® (Equation 5.2).

$$DFFITS_i = \frac{\widehat{yi} - \widehat{y(i)}}{\sqrt{MSE(i).l_{ii}}} \quad (5.2)$$

The numerator of Equation (5.6) measures the difference in the predicted responses obtained when the ith data point is included and excluded from the analysis. The denominator is the estimated standard deviation of the difference in the predicted responses, where MSE is the mean square error, and the leverage lii is a measure of the distance between the y value for the ith data point and the mean of the y values for all d data points. Therefore, the difference in fits quantifies the number of standard deviations that the fitted value changes when the ith data is omitted. An observation is deemed influential if the absolute value of its DFFITS value is greater than: $2\sqrt{\frac{k+2}{d-k-2}}$, where d is the number of observations and k is the number of predictor terms.

If there are no particular influential data points, a second approach is to delete one observation at a time and refit the regression model on the remaining n−1 observations. We then compare the results obtained using all n-observations with the results obtained by deleting the ith observation to see how much influence that observation has on the analysis. If the predicted responses and estimated slope coefficients are roughly the same, it suggests the absence of influential data points (high leverage), indicating a robust correlation. Otherwise, if the results are significantly different, it implies that the correlation is not robust.

5.3. Results

5.3.1. Catchment descriptors characteristics

5.3.1.1. Hypsometric curves

The hypsometric slope–area curves for the catchments are quite similar, with 80% of the catchment areas having slopes between 5 and 25 degrees, and 20% of the catchment areas with slopes above 25 degrees (Figure 5.4). The elevation–area hypsometric curves for each catchment are more diverse. WS1 and WS4 have two inflection points, one at 20–30% of the cumulative area, and another at 70–80% of the cumulative area. WS3's curve is initially fairly linear but becomes concave at higher elevations. WS2's curve shows a marked S-shape, which seems to indicate that WS2 is in a younger geomorphic stage compared to the other three catchments, which are approaching the mature/old stage (Strahler 1952).

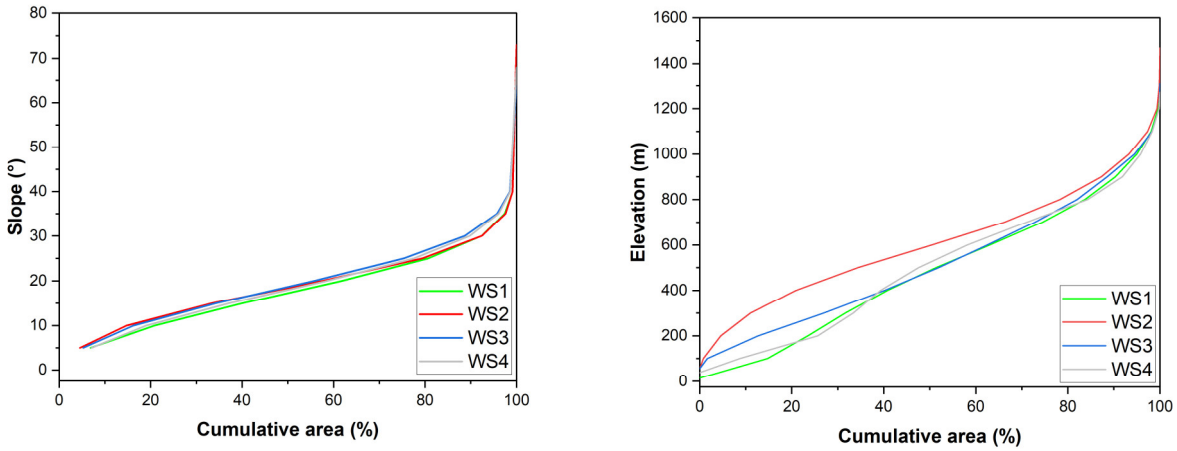

(a) (b)

*Figure 5. 4. Hypsometric curves: (**a**) slope–area (**b**) elevation–area.*

5.3.1.2. Correlation between CDs

In the first step, the least correlated variables within each attribute were selected based on Figure 5.5a. As a result, only Slope, Kg, and Dd were retained out of the 14 topographic (T) attributes. Among the four-land cover (LC) attributes, only the CN_est was selected. Ferra, S-C, S-C-L, and OC were chosen from the 11 soil attributes. Finally, Gran and Gneiss were kept among the geology (G) attributes.

Figure 5.5b was used to assess the between-group correlations, i.e., correlations between CDs from different groups. Kg (T) was found to be positively correlated with CN_est (LC) and negatively correlated with Ferra (S), S-C-L (S), and Gneiss (G). Additionally, there was a strong correlation between Slope (T) and OC (S), as well as between Dd (T) and S-C (S) and between Dd and Gran (G). CN_est (LC) is correlated negatively with both Ferra (S) and Gneiss (G). Finally, S-C (S) shows a positive correlation with Gran (G), and S-C-L (S) is positively correlated with Gneiss (G).

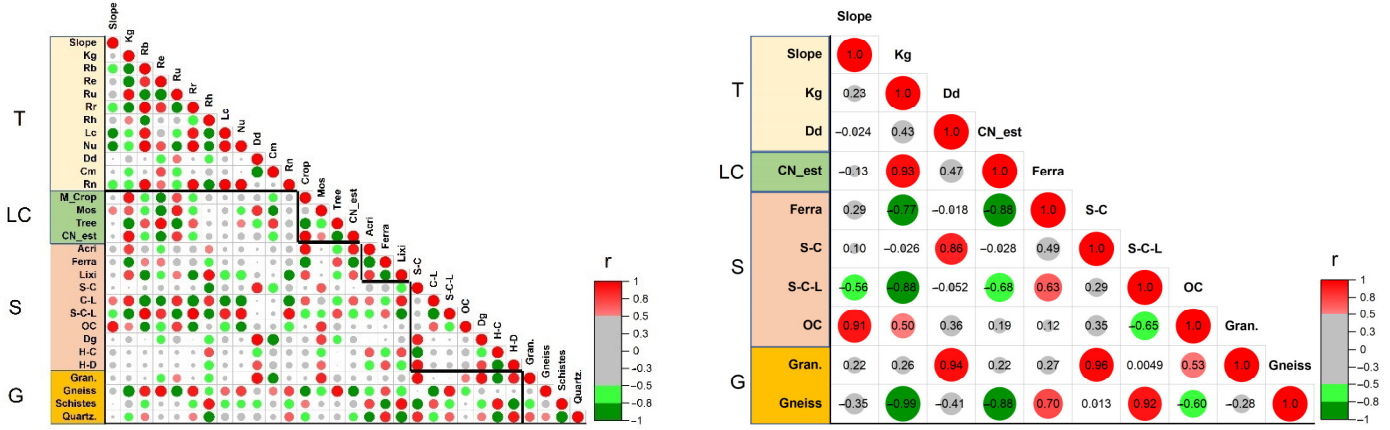

*Figure 5. 5. Correlation plot between (**a**) all catchment descriptors, and (**b**) selected catchment descriptors, based on Pearson's coefficient r. The catchment descriptors are color-coded according to their generic group: topographic (T), land cover (LC), soil (S), and geology (G). The size of the circles indicates the strength of the correlation, with red corresponding to positive and green to negative correlations. Gray circles mean poor correlation (r < |0.5|).*

5.3.2. Hydrological signatures and their spatial patterns

5.3.2.1. Rainfall characteristics

Most rainfall fell between mid-December and mid-April (wet rainy season, Figure 5.6). The cumulative rainfall amount varied across the catchments during the study period. Specifically, WS4 in the western part received the highest amount of rainfall (~1800 mm), whereas WS3 in the eastern part received the lowest amount of rainfall (~1670 mm).

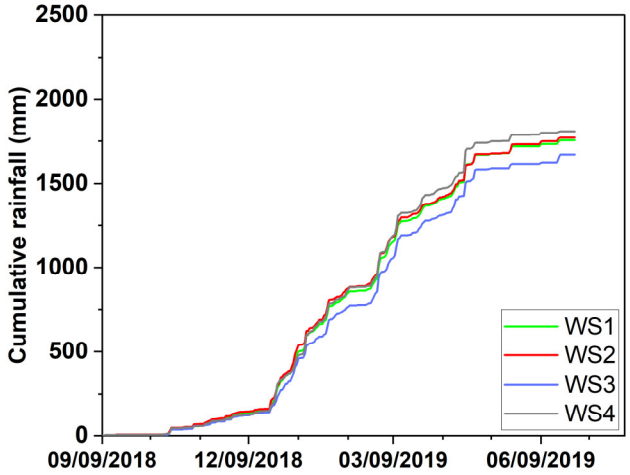

Figure 5. 6. Cumulative rainfall (IMERG) over the 10-month study period (September 2018–June 2019). Date on X-axis in MM/DD/YYYY format.

5.3.2.2. Streamflow characteristics

In terms of flow distribution (Figure 5.7a), WS1 had the highest cumulative flow during the study period, accounting for 66% of total rainfall, while WS2 had the lowest (46%). When considering cumulative quickflow (Figure 5.7b), WS1 had the highest value (20% of total rainfall), whereas WS2, WS3, and WS4 had fairly similar values (12–15%). In terms of cumulative baseflow (Figure 5.7c), WS1, WS4, and WS3 had similar values (42–46% of total rainfall), while WS2 had noticeably lower values (31%).

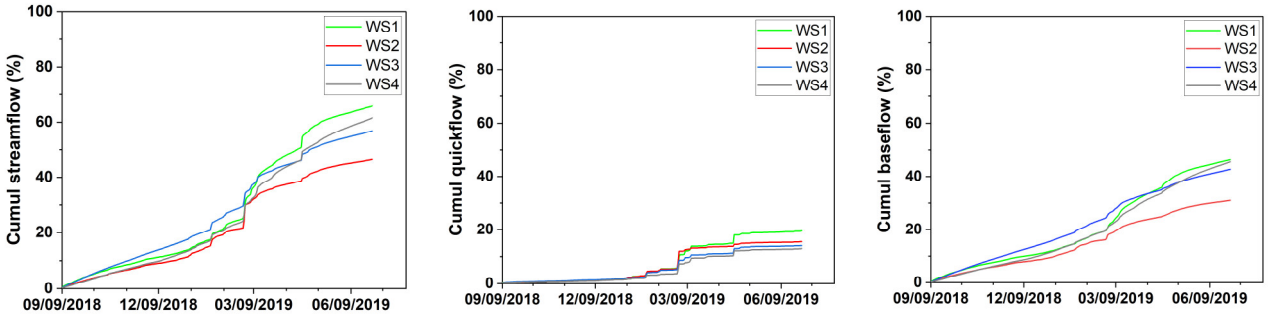

*Figure 5. 7. Streamflow characteristics of sub-catchments (%): (**a**) cumulative streamflow, (**b**) cumulative runoff (quickflow), (**c**) cumulative baseflow from September 2018 to June 2019. All values are expressed relative to the total rainfall of each sub-catchment (Figure 6). Date in X-axis in MM/DD/YYYY format.*

5.3.2.3. Flow duration curve

The flow duration curve (Figure 5.8) reveals that the 'high flows' (0–5% exceedance probability) for all the watersheds are relatively similar. The curves differ more strongly in the medium flow range (20–80 percent), with WS1, WS3, and WS4 displaying the highest values and WS2 having the lowest. In terms of low flows (95–100% exceedance probability), the WS2 and WS1, in that order, exhibit the lowest, while the WS3 and WS4 have the highest.

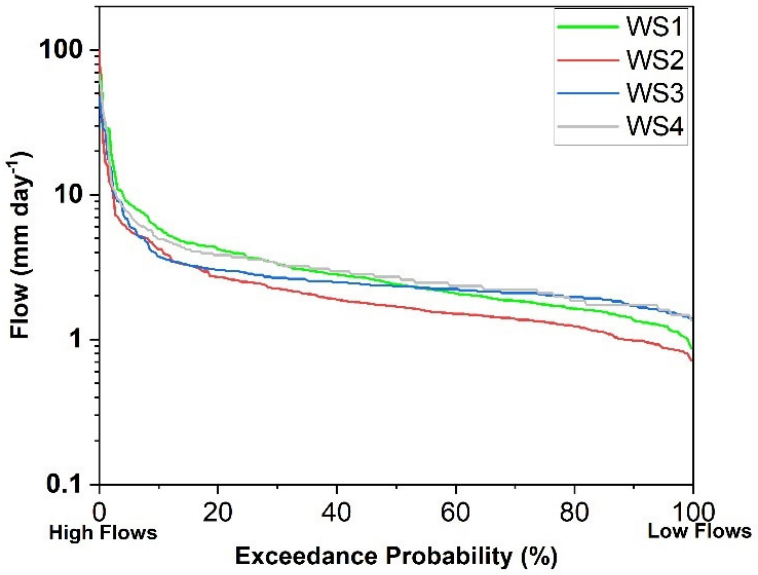

Figure 5. 8. Flow duration curve of the four sub-catchment rivers. Note logarithmic (Log10) scale for Y axis.

5.3.2.4. Hydrological signatures

The BFI values range from 0.60 to 0.68, with the watersheds ranked in ascending order, as follows: WS2, WS1, WS3, and WS4 (Figure 5.9a). Values of rc, Qp, and ts are highly variable across events in all four watersheds (Figure 5.9b–d). Considering the mean values, we can observe that the runoff coefficient range between 0.09 and 0.34, with WS2 displaying the lowest value, followed by WS3, WS4, and WS1. Mean peak discharge Qp ranges from 0.34 to 1.38 mm h^{-1}, with WS2 having the lowest value, followed by WS1 and WS3, while WS4 shows the highest value. Regarding the runoff event time scales, they range between 0.11 and 0.22 h/km, with WS4 having the highest value, followed by WS1, WS3, and WS2 in descending order. Additionally, the low flows Q95 follow a similar trend to the BFI. Finally, the high flows Q5 and mean discharge generated by WS1 are the highest, followed by WS4 and WS3, while the lowest value pertains to WS2 (Figure 5.9e).

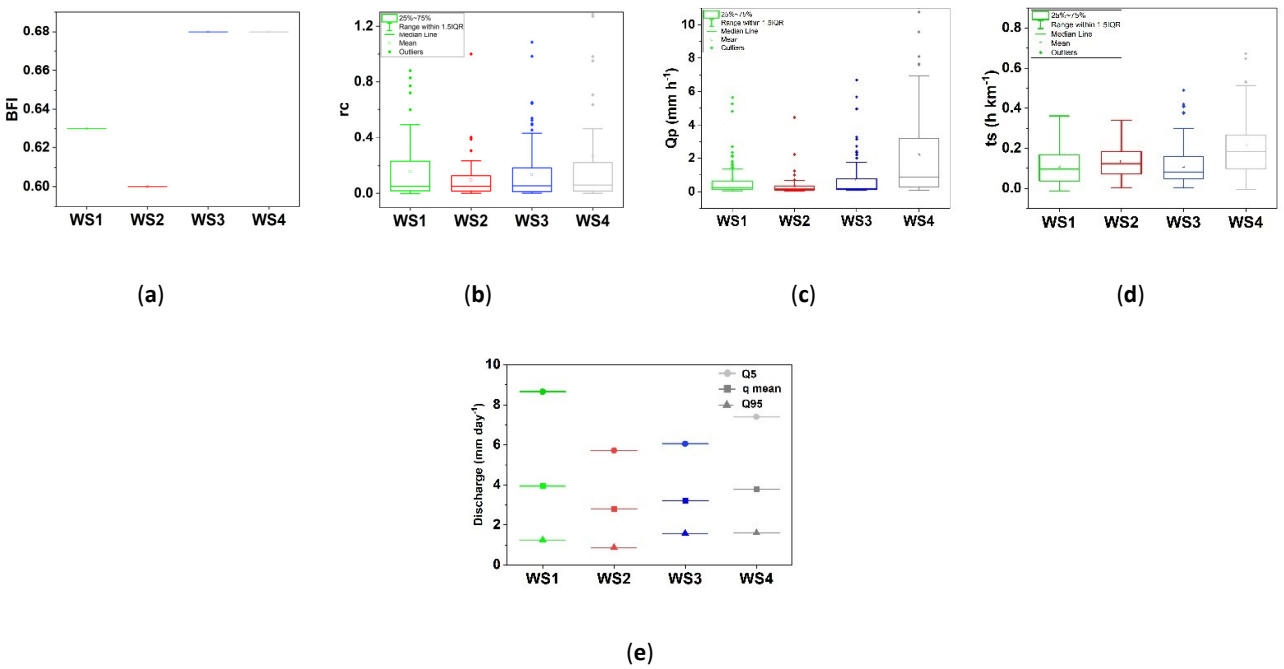

Figure 5. 9. Boxplots of hydrological signatures of the Ankavia catchment sub-watersheds over the 10-month study period. (a) Baseflow index (-), (b) runoff coefficient (-), (c) peak discharge (mm h^{-1}), (d) runoff event time scale (h km^{-1}), (e) high flows Q5, mean discharge and low flows Q95 (mm day^{-1}). Box lower and upper edges correspond to the 25th (Q1) and 75th (Q3) percentiles. Whiskers extend to Q1 − 1.5IQR (lower bound) and Q3 + 1.5IQR (upper bound), with IQR = Q3 − Q1 (inter-quartile range). Points outside the box are outliers.

5.3.2.5. Correlation between hydrological signatures

According to Figure 5.10, there are strong correlations between the hydrological variables. Specifically, BFI exhibits a strong positive correlation with Q95 (low flows). rc is positively correlated with Q5 and q_mean, while Qp is related to ts. Furthermore, there is a strong correlation between Q5 and q_mean.

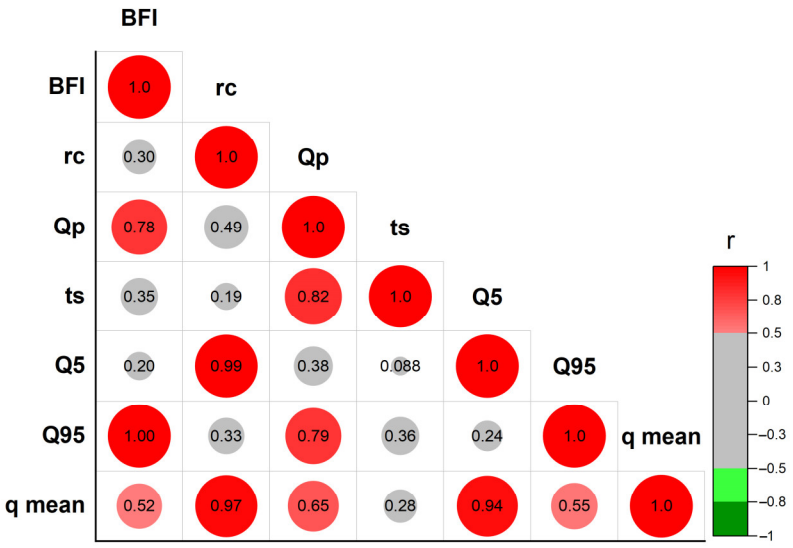

Figure 5. 10. Correlation plot between hydrological signatures using Pearson's coefficient r. The size of the circles indicates the strength of the correlation, with red corresponding to positive and green to negative correlations. Gray circles mean poor correlation (r < |0.5|).

5.3.3. Correlation between selected CDs and HSs

The correlation plot shows links between the selected catchment descriptors (CDs) and the hydrological signatures (HSs, Annexe H). However, not all the strong correlations (indicated by red and green circles) are reliable due to the strong dependence on a single 'high leverage' point. Accordingly, we added an '*' to

indicate a robust correlation. As a result, each HS was found to be correlated with at least two or more CDs (Figure 5.11, Annexe I).

Specifically, BFI and Q95 both exhibit a positive correlation with Kg (T) and CN_est (LC), and a negative correlation with Ferra (S), S-C-L (S), and Gneiss (G). rc is negatively correlated with Slope (T) and Ferra (S), while Qp is positively correlated with Kg (T) and negatively with Ferra (S) and Gneiss (G). ts is negatively correlated with S-C (S) and Gran (G). Q5 is negatively related to Slope (T) and OC (S), while q_mean is negatively correlated with Ferra (S).

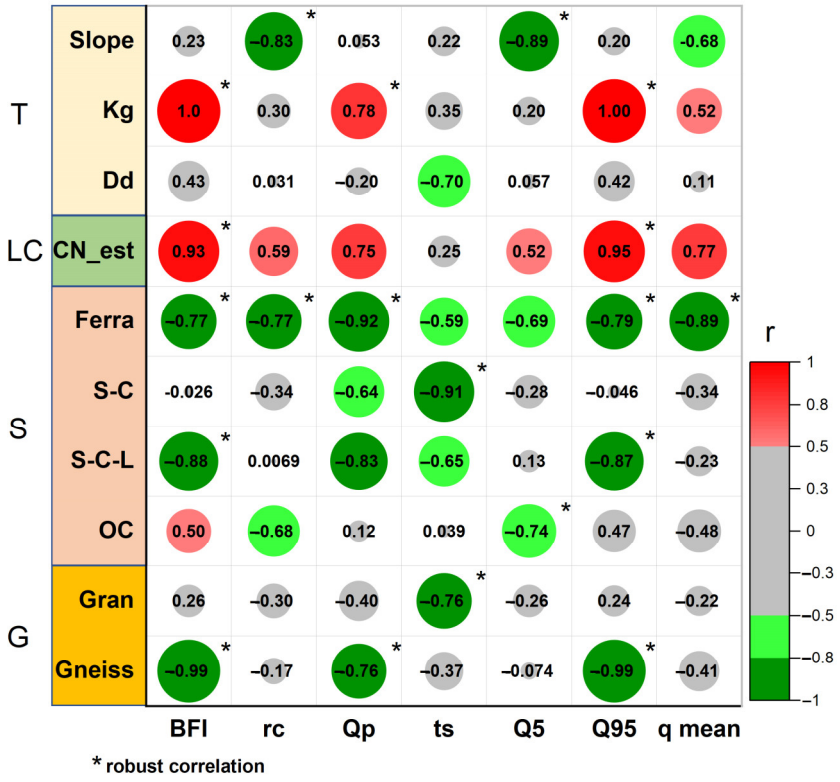

Figure 5. 11. Correlation plot between HSs and CDs using Pearson's coefficient r. The catchment descriptors are color-coded according to their generic group: topography (T), land cover (LC), soil (S), and geology (G). The size of the circles indicates the strength of the correlation, with red corresponding to positive and green to negative correlations. Gray circles mean poor correlation (r < |0.5|). '' indicates a robust correlation.*

5.4. Discussion

5.4.1. General hydrological characteristics

The study period (September 2018–June 2019) can be qualified as a normal year. The cumulative rainfall curves clearly show a distinct wet rainy and dry (but still rainy) season. The hot and wet rainy season occurs from November to April, while the cool and dry season occurs from May to October. During the rainy season, the region receives a large amount of precipitation, but this does not immediately translate into increased river discharge. Indeed, although rainfall increases sharply as of December, notable changes in the cumulative streamflow happen only as of February, which is likely due to a slow response time of the groundwater table. Conversely, during the dry season, the region receives little precipitation, resulting in a period of low flows in the rivers. This strong seasonality of rainfall and river discharge in the northeastern region of Madagascar is the result of a complex interplay between several atmospheric and oceanic processes, such as convective precipitation and trade winds, as well as the movement of the intertropical convergence zone (ITCZ) (Macron et al. 2016). Specifically, the position of the ITCZ shifts northward from March to August and southward between September and December, resulting in distinct rainy and dry seasons in tropical regions (Nassor and Jury 1998; Chaperon et al. 1993).

The proportion of precipitation that turns into streamflow within the Ankavia basin is somewhat variable, ranging from 40% to 60% depending on the watershed. Generally, in humid regions with well-drained soils and gentle topography, such as parts of the eastern United States, Europe, and Southeast Asia, the proportion of rainfall that becomes streamflow is lower, ranging from about 10% to 40% (Ghimire et al. 2020; Lee and Kim 2017). On the other hand, in arid and semi-arid regions characterized by limited vegetation cover and poorly drained soil, the streamflow proportion ranges from approximately 20% to 60% (Kazemzadeh and Malekian 2018). In tropical regions with highly drained soils and rugged topography, such as those in Asia and Brazil, the proportion of precipitation that flows as streamflow ranges from 30% to 60%, and sometimes can exceed 90% during extreme events (Abreu et al. 2022; Jayapadma et al. 2022). Finally, in mountainous areas with high

precipitation and steep topography, such as the Andes, the Alps, and the Himalayas, this rate can reach up to 80% or more (Cassalho et al. 2017). Therefore, the discharge-to-rainfall ratio observed in the Ankavia basin appears consistent with observations from tropical regions with highly drained soils and rugged topography. The calculated BFI values in this study range from 0.60 to 0.68, which is consistent with studies conducted in Brazil (Guzha et al. 2015) and Indonesia (Tarigan et al. 2018) in similar environments. However, other regions in Indonesia have shown smaller BFI values (ranging from 0.49 to 0.56) compared to Ankavia (Taufik 2022). In contrast, higher BFI values were reported for watersheds in Thailand (Ditthakit et al. 2021) and Malaysia (Khomsiati et al. 2021).

The study findings show that the mean runoff coefficient values range from 0.09 to 0.34, which is consistent with similar research conducted on meso-scale watersheds in Brazil (Guzha et al. 2015) and in West Africa (Giertz et al. 2005). However, the observed rc values are slightly higher than the value reported in other parts of Brazil (Machado et al. 2022), ranging from approximately 0.008 to 0.12, and lower than the value estimated in Malaysia (Katimon and Wahab 2003), ranging from 0.32 to 0.92. Additionally, some runoff coefficient values greater than 1 were observed in this study, especially during some extreme events, which is theoretically impossible since the amount of rainfall should always be greater than the volume of runoff. This could be due to several factors. Firstly, the rainfall data used in the study were obtained from IMERG and are known to underestimate some classes of rainfall, in particular, extreme rainfall events (>100 mm day^{-1}) (Ramahaimandimby et al. 2022). Additionally, the method used to separate the hydrographs could also contribute to uncertainty in the estimation of runoff. Moreover, since the rating curve was extrapolated for high water, the runoff during extreme events may be biased (possibly overestimated).

The mean peak discharge and runoff event time scales in the Ankavia watershed range from 0.34 to 1.38 mm h^{-1} and 0.11 to 0.22 h km^{-1}, respectively. It is important to note that a wide range of values for these two hydrological signatures are found in the literature, which means that there are more dependent on basin

characteristics, rather than the specific tropical regions themselves (Abdulkareem et al. 2018, 2019; Shamsuddin et al. 2014).

When compared to other tropical regions, the Ankavia River in Madagascar has a slightly higher range of flow rate values (Q5, q_mean, Q95) (8.65, 9.93, 1.25). For instance, the Sapucaí River in Brazil (Abreu et al. 2022), the Mae Klong River in Thailand (Guo et al. 2017), and the Mekong River in Vietnam (Adamson et al. 2009) have flow rates of (5.48, 2.45, 1.33), (5.6, 2.19, 1.11), and (2.50, 1.74, 1.06) [mm day^{-1}], respectively. The region where the Ankavia River is located receives high levels of precipitation, which contributes to its relatively high flow rate even in normal years such as 2019 (~1800 mm). Overall, the Ankavia River exhibits similar discharge values when compared to other basins studied in the SAVA region. For instance, the Lokoho River, which is located to the north of the Ankavia basin, has (Q5, q_mean, Q95) of (7.83, 4.5, 1.94), as reported by Randriamaherisoa and Binard (1992). Similarly, the Sambirano River, situated further north, has a Q95 flow of 1.29 mm day^{-1} and an average flow of 4.06 mm day^{-1} (Chaperon et al. 1993). Hence, the observed range of values in this study falls within the 'normal' range for rivers in the SAVA region, Madagascar (Chaperon et al. 1993).

5.4.2. Catchment Descriptors

We examined all the catchment attributes using the correlation matrix based on Pearson's coefficient (Figure 5.5a). A critical analysis of these correlations is crucial before deriving any linkages; otherwise, potentially misleading relationships may be inferred (Tarasova et al. 2018). In addition, strong correlations between two or more attributes belonging to the same group may arise because these parameters roughly evaluate the same characteristics. This is for instance the case with the attributes related to catchment area and perimeter (Kg, Cc, Re, etc.) which all determine the watershed morphometry.

The strong relationships that have been found between CDs of different groups in the present study can be explained by the spatial distribution of these CDs in the Ankavia watershed (Figure 5.2 and Annexe B). For instance, WS2 has a more compact

and rougher landscape, lower CN (i.e., higher forest cover), more ferrasols, more SCL soils, and more Gneiss than the other WSs. In contrast, WS3 and WS4 are more elongated, less rough, have higher CN (i.e., lower forest cover), and more acrisols and CL soils than WS2. The differences in land cover characteristics are likely due to the absence of secondary roads and navigable rivers in WS2, making it less accessible and, therefore, less prone to human activity. Moreover, the presence of natural parks and protected areas in WS2 also probably contributes to its higher forest cover. The distribution of soils in the watershed depends on various factors such as topography, climate, and geology. In our case study, acrisols dominate in the downstream (northeast) part, while ferrasols dominate in the upstream (southwest) part of the watershed. Typically, acrisols are found on erosive slopes of low hills while ferrasols are found on adjacent stable pediments or high hills (Hengl et al. 2017).

5.4.3. Which catchment descriptors are the best predictors for each hydrological signature?

The BFI calculated in this study ranges from 0.60 (WS2) to 0.68 (WS4) and is positively correlated with CN_est, the latter being negatively correlated with the forest cover. Land cover attributes thus appear to be an important predictor of baseflow (BFI). Indeed, forest cover has a higher evapotranspiration rate than cropland, degraded land, and tree fallow cover, which may explain why BFI declines as forests cover increases (van Meerveld et al. 2021; Rodriguez-Martínez and Santiago 2017). This is consistent with other studies conducted in Brazil (Guzha et al. 2015) and Indonesia (Tarigan et al. 2018). However, some studies contradict this finding, such as a study conducted in the southern Amazon (Guzha et al. 2015), which reported a higher BFI in forested areas than in grazing areas, supporting the “sponge effect theory” (Bruijnzeel 2004) that forested watersheds produce more baseflow during the dry season than watersheds with disturbed vegetation (Ogden et al. 2013).

BFI also appears to be correlated with Kg and the relative area occupied by Ferralsols (and sandy clay soils). The positive correlation with Kg is likely the result of a confounding effect since Kg is highly correlated with CN_est (the most forested watershed is also the most compact). The negative correlation with Ferralsols may

also be spurious, as Ferralsols are negatively correlated with CN_est. Indeed, Ferralsols are known to have favorable physical properties, especially high infiltration capabilities (Ramaroson et al. 2018). A higher BFI would, therefore, be expected in Ferralsol-dominated watersheds, which is not observed here. Similarly, the negative correlation with gneiss may also be spurious, especially since fractured hard rocks such as quartzites and gneisses more generally lead to aquifers reservoirs with high capacities (Eckhardt 2008).

The mean runoff coefficient values in our study range from 0.09 to 0.34, depending on the watershed. The WS2 watershed, which has a higher proportion of Ferralsols and forest compared to the other basins (Figure 5.2c), has the lowest runoff coefficient. Ferralsols are known for their excellent physical properties, including high permeability due to their well-developed microaggregate structure, sometimes referred to as "pseudo-sands" (Martinez and Souza 2020). Conversely, acrisols, present mainly downstream of the basin, have a poorer structure and horizons with clay accumulation, which may explain higher runoff, particularly if the soil is cultivated. While the correlation is not strong, we observe that the runoff coefficient is lower in WS2 (Figure 5.9b), which has the most forested cover, and higher in the other less forested WSs. This observation is consistent with the well-known role of forest cover in intercepting rainwater (litter and canopy) and protecting and improving the hydrological conditions of the soil thanks to the litter layer that accumulates on the surface. The average slope is negatively correlated with the runoff coefficient, but this relationship is most likely spurious since the range of average slopes across the watersheds is small (~2°) and topographic parameters may not significantly affect the runoff coefficient (Blöschl et al. 2013). Other studies have also demonstrated a strong correlation between runoff coefficient, soil properties, and land cover characteristics, such as those conducted by Guzha et al. (2015) in Brazil and by Giertz et al. (2005) in West Africa.

The mean peak discharge in the Ankavia catchment ranges from 0.34 mm h^{-1} to 1.38 mm h^{-1}. The peak discharge of WS2 is found to be the lowest compared to the other three WSs. In this case study, there appears to be a positive correlation between Qp and Kg (T); however, this relationship may be spurious. Indeed, more compact

watersheds are expected to lead to shorter response times and higher peak discharges. Instead, the relationship between Qp and runoff/quickflow (rc) seems more relevant. Indeed, the positive relationship between these two parameters is well-established in the literature, indicating that if runoff increases (rc), Qp also increases (Horton 1932). Therefore, predictors of runoff coefficients, such as soil type, are also predictors for peak discharge.

The WS1, WS2, and WS3 catchments exhibit faster hydrologic responses (lower runoff event time scale ts) compared to WS4, which is located towards the west. Our correlation analysis suggests a strong positive relationship between Qp and ts (Figure 5.10). Meanwhile, soil attributes, which are critical factors for runoff, also appear to contribute to the hydrologic responsiveness of the catchments (Figure 5.11). Additionally, we observed that WS4 has the lowest proportion of granite and the highest proportion of shale.

The correlation analysis reveals that Q5 and q_mean are positively correlated with rc and that Q95 is positively correlated with BFI (Figure 5.10). Q5 (high flows) is the result of runoff, and factors that are good predictors of rc, such as soil attributes, are therefore also good at predicting Q5. It is worthing that the mean discharge values are heavily influenced by extreme values. Hence, soil attributes that are predictors of rc and Q5 also serve as good predictors for q_mean. Q95 (low flows) originate from soil releases, groundwater, or channel storage; hence, catchment descriptors for predicting the BFI and Q95 are expected to be roughly the same (Figure 5.11).

In summary, the more forested WS2 watershed has a better flood buffering capacity (lower Q5 and Qp values), but lower BFI (potentially due to higher ET). Consequently, this watershed experiences more pronounced low flows during the dry season (lower Q95 values). In contrast, the less forested WS3 and WS4 watersheds (and to a lesser extent WS1) have higher Q5 and Qp values, which indicates a lower flood buffering capacity than WS2. Nevertheless, they have higher BFI than WS2, resulting in less pronounced low flows (higher Q95) during the dry season.

5.5. Conclusion

In this study, we aimed at gaining a better understanding of the factors driving the hydrological response of the Ankavia watershed by investigating the linkages between watershed descriptors and hydrological signatures using a fairly unique dataset for northeastern Madagascar. Our findings indicate that all watershed attributes play a role in governing hydrological responses to a greater or lesser extent. Land cover, soil properties, and geology are the best predictors of baseflow and low flows (Q95). In contrast, soil properties mainly govern the runoff coefficient (rc), mean discharge (q_mean), peak flow (Qp), and runoff event time scales (ts).

The findings indicate that the WS2 watershed, primarily covered by forests, has the lowest runoff coefficients and peak flows. This emphasizes the importance of protecting the forest cover in this area, not just to protect biodiversity but also to mitigate downstream flooding risks. However, this watershed is also characterized by the lowest low flows (Q95), reflecting a limited capacity for maintaining sufficient discharge during the dry season. Furthermore, the notably higher peak discharges in WS3 and WS4 vs. WS2 highlight the impact of land cover on the hydrological characteristics of the river basin, which suggest that human activities, such as deforestation, shifting cultivation, as well as agriculture, can have a considerable impact on the hydrological behavior, and must be considered in water resource management in the SAVA region.

This study highlights the complexity of the interactions between the factors governing hydrological systems in a large tropical watershed. Nevertheless, the findings can serve as a basis for interpreting hydrological responses in other basins within the SAVA region but also more generally in the northeastern part of Madagascar that are under similar hydrological conditions. Ultimately, the study provides valuable information on the hydrological characteristics of the Ankavia watershed's sub-basins, particularly on the roles of forests, and encourages the adoption of sustainable land use practices and strengthening of conservation efforts for effective watershed management.

6. Chapitre 6 : How Tropical Land Cover Shapes Streamflow: Insights from the Ankavia River Basin, Madagascar

Abstract:

Land cover, which plays a crucial role in stream flow production processes, faces increasing pressures, particularly in tropical regions. These changes disrupt hydrological processes and impact significantly water availability. In order to better understand these impacts, this study aims at quantifying the effects of various land cover types on streamflow generation in three headwaters in the Ankavia river basin, northeastern Madagascar: 1) a fully forested catchment (FOR), 2) a mixed catchment (MIX) composed of 38% forest, 45% fallow, and 17% cropland, and 3) a predominantly fallow catchment (FAL) with 87% fallow, 9% pasture (formerly irrigated rice fields), and 4% cropland. We analyzed soil and hydrological properties for each land cover type as well as the runoff coefficients (rc) in the micro-catchments (MC).

Despite similarities in soil textures (sandy clay loam) across the MC, results revealed significant differences in soil structure. Soil bulk density was highest under pasture and lowest under forest. These structural differences were reflected in the measured infiltration rates, which decreased in the following order: forest (3192 mm h^{-1}) > cropland (715 mm h^{-1}) > fallow (562 mm h^{-1}) > pasture (146 mm h^{-1}). Given that rainfall intensity is generally lower than the infiltration capacities in the MC, subsurface flow (SSF) appears to be predominant for all land cover types. However, surface runoff, in the form of Hortonian overland flow (HOF) or saturation overland flow (SOF), may occur in the pastures during high-intensity rainfall events.

The analysis of rc between the MC revealed distinct hydrological dynamics. The FOR exhibited a lower rc compared to MIX, indicating that deforestation tends to increase streamflow, likely due to reduced rainfall interception and evapotranspiration.

Moreover, FAL demonstrated a lower rc than MIX, suggesting that an increase in the proportion of cultivated surfaces increases runoff.

These findings underscore the significant influence of vegetation cover and landscape heterogeneity on streamflow regulation. The complex interplay between land cover characteristics and hydrological responses emphasizes the need for integrated approaches in watershed management to maintain hydrological balance and ecosystem services.

Keywords: land cover types; streamflow generation; subsurface flow; micro-catchments.

6.1. Introduction

Vegetation cover plays a central role in regulating hydrological processes in general, and streamflow in particular (Bernard et al. 2018; Musy 2004). Through their canopy structure, plants significantly contribute to rainfall interception, thus limiting the amount of water directly reaching the ground. Their impact on soil structure through their root systems and organic matter inputs as well as on the level of soil cover then influence the fate of water at the soil surface, promoting either infiltration or surface runoff (Barasa et al. 2018; Modeste et al. 2018; Nunes et al. 2011). Depending on soil conditions, infiltrated water can follow several pathways: subsurface stormflow (**SSF**), which moves laterally at shallow depths; return flow from shallow aquifers (**RF**), which directly feeds watercourses; and deep groundwater flow, largely controlling the base flow and potentially sustaining continuous stream flow during dry periods (Bonell 2005; Dunne and Black 1970). Conversely, water that fails to infiltrate produces surface runoff. Runoff generation can result from two main processes: 1) when rainfall intensity exceeds the soil's infiltration capacity, referred to as Hortonian overland flow (**HOF**), or 2) when the soil reaches its maximum water holding capacity, preventing further infiltration, which is referred to as saturation excess overland flow (**SOF**) (Elsenbeer 2001). These various components of

subsurface and overland flow are then drained by the hydrographic network to the basin outlet (Musy 2004).

Quantitative characterization of streamflow processes is crucial for managing water resources, designing resilient civil infrastructure, evaluating best management practices, and addressing numerous environmental issues including soil conservation and erosion control (Abe et al. 2018b; Modeste et al. 2018). However, measuring the intricate interplay between vegetation, water, and soil presents unique challenges, especially in tropical regions. The distinctive soil properties and climatic conditions of the tropics, characterized by high variability in precipitation, temperature, and humidity, restrict the direct transfer of knowledge and methodologies developed in temperate regions (Blöschl et al. 2013; Bruijnzeel 2004). Furthermore, rugged terrain, dense vegetation, and logistical barriers often complicate the installation and maintenance of monitoring stations, hindering data collection efforts (Brandon 2014; Baumann 2011; WMO 1987). These difficulties have led to the widespread use of dominant process concepts and single-process models in interdisciplinary studies (Grayson and Blöschl, 2001; Sivapalan, 2018). However, the simplifying assumptions of these models, such as steady-state approximations, reduced dimensionality, and indirect coupling of surface-groundwater interactions, often underestimate complex processes like flow convergence, transient response dynamics, and runoff generation (Fatichi et al. 2016; McDonnell et al. 2007). Consequently, there is a pressing need for tailored research approaches suited to the complexities of tropical hydrological systems (Levia et al. 2020).

Despite the crucial role of tropical ecosystems in global hydrological cycles, hydrological research in these regions suffers from chronic underfunding, leading to persistent knowledge gaps (Burt and McDonnell 2015; Wohl et al. 2012). This deficiency is particularly evident in the understanding of complex environments, where inconsistencies are observed between in-situ hydraulic conductivity measurements and outflow rates at watershed outlets (Zimmermann et al. 2006). For instance, tropical forests, traditionally viewed as effective hydrological

regulators (Andréassian 2004; Bruijnzeel 1989), can paradoxically increase the risk of major floods according to some studies (Calder and Aylward 2006). Fallow and cultivated lands show ambivalent effects: sometimes mimicking the ecosystem functions of secondary forests (Zwartendijk et al. 2017), sometimes negatively altering hydrological processes (Rodriguez et al. 2010). These divergences are explained by the multiplicity of factors at play, including subsurface flows (**SSF**) even on soils reputed to be highly permeable such as ferralsols, spatial variability of soil properties, and differences in temporal scales between point measurements and watershed-scale processes (McDonnell et al. 2007; Zimmermann et al. 2006; Elsenbeer 2001). Moreover, the presence of temporary saturation zones can generate significant surface runoff (**HOF** and/or **SOF**) despite high surface hydraulic conductivity (Bruijnzeel 2004). This intricate interplay underscores the need for a holistic approach, integrating measurements at different scales and field observations to better understand the interactions between land cover, soil properties, topography, and rainfall patterns in determining hydrological responses (Blöschl and Sivapalan 1995).

In hydrological research, much of the focus has been on large catchment areas characterized by diverse land uses, geology, soil types, and topography (Cui et al. 2007; D'Almeida et al. 2007; Wilk et al. 2001). While these studies have yielded valuable insights into broader hydrological patterns, the inherent heterogeneity within these vast river watersheds poses challenges in isolating and quantifying the specific influence of land cover on hydrological processes (Ramahaimandimby et al. 2023; Qazi 2020). In contrast, headwater catchments are better suited for unraveling the impacts of land cover on streamflow dynamics. With their relatively small contributing areas, they exhibit heightened responsiveness to variations in energy and water inputs (Birkel et al. 2020; Ochoa-Tocachi et al. 2018). However, despite their pivotal role in water regulation and provision of ecological services, research attention directed towards these smaller catchments remains notably limited in tropical environments (Birkel et al. 2020; Guzha et al. 2015).

Considering the crucial role of headwater regions in hydrological processes, this study aims to quantify the impacts of contrasting land cover types (including primary forest, fallow land, cropland and pasture) on stream flow generation mechanisms in a humid tropical environment. For this purpose, we employ a paired catchment approach based on three neighboring tropical headwater micro-catchments located in the Ankavia river basin of northeastern Madagascar. These small catchments facilitate intensive monitoring and data collection efforts, allowing to better isolate and quantify the specific effects of different land cover types on hydrological response. Such knowledge is essential for developing improved water resources and land management strategies at the watershed scale, thus minimizing environmental harm and fulfilling the needs of local communities.

6.2. Materials and Methods

6.2.1. Study area

The study focuses on three neighboring headwater micro-catchments (MC) located in the Ankavia catchment, which itself is located in the SAVA region of north-eastern Madagascar (Figure 6.1, Table 6.1). The Ankavia river is the main source of water supply for the city of Antalaha, which had a population of 280,000 inhabitants in 2020 (INSTAT 2020). Mean annual rainfall is 2300 mm (2018-2021), with the majority (76 %) occurring between December and May. Maximum annual temperature, 32°C, is typically observed in January, while minimum annual temperature, 18°C, is observed in August. Additionally, based on the geological map, the MCs are all located on a granitic formation (Collins and Windley 2002).

The MCs were selected for their contrasting land covers, close proximity to each other, and convenient location near the village of Ambarabaha, which facilitates data collection and equipment maintenance. All three MCs are drained by first-order streams and have similar, south-east-facing aspects. Average steepness ranges from 12° to 24° (Table 6.1). The first MC, hereafter referred to as 'FOR', spans 1.6 ha and is entirely covered by primary forest (**frst**) (Figure 6.1). Adjacent to FOR, the second

MC, termed 'MIX', encompasses 3.8 ha. It comprises 17% cropland or swidden cultivation (**crop**), 38% of primary forest, and 45% of fallowed land (**fall**). The upstream part (1.4 ha) of MIX, which is occupied by primary forest, will be referred to as 'MIX-frst', while the downstream part (2.4 ha) covered by cropland and fallowed areas is named 'MIX-crop-fall'. Approximately 150 m away from MIX, the third MC, 'FAL', covers an area of 6.4 ha (Figure 6.1). It is covered by 87% of fallowed land, 9% of pasture, and 4% of cropland. The land cover information was obtained from a supervised classification of 10-m resolution Sentinel-2 images taken in September 2019. The FAL stream flows into the Antsahovy river, while the MIX and FOR streams flow into the Ankavia river (Figure 6.1).

The primary forests ('*atiala*' in Malagasy) are composed of an assemblage of tree species typical of the SAVA region, such as *Canarium madagascariense* ('*ramy'*), *Dalbergia baronii* (palissandre), *Diospyros sp.* ('*ebony*'), *Uapaca thouarsii*, *Ocotea cymosa*, and *Cryptocarya sp.,* along with a diverse understory of shrubs, grasses, and other plants (CREAM 2013; Figure 6.2a). Fallow areas ('*savoka'*) consist of plant communities primarily composed of regrowing forest, bamboo, ferns, and other invasive plant species (Styger et al. 2007; Figure 6.2b). The cropland area comprises mainly rainfed rice, cultivated using shifting cultivation techniques on steeply sloping plots (Fox et al. 2000; Figure 6.2c). These plots have low soil cover and are typically cultivated for one or two years without tillage of any kind. After this period, farmers leave the land fallow and allow natural vegetation to regrow for a period of 5 to 7 years. The pasture in the FAL watershed corresponds to a former terraced rice field (Figure 6.2d) that was irrigated by a small-scale irrigation canal, which drew water from the nearby mountainous region. The last rice cultivation in this area dates back to 2012. Traditionally, the soil in irrigated rice fields is tilled by oxen while saturated (puddling).

Table 6. 1. Morphometric characteristics of the three headwater micro-catchments (FOR, MIX and FAL) and the upstream forested sub-catchment of MIX (MIX-frst).

Parameters (Symbol), units	**FOR**	**MIX**	**MIX-frst**	**FAL**
Area, ha	1.6	3.8	1.4	6.4
Elevation range (min, max), m	131 ; 203	53 ; 173	107 ; 173	59 ; 127
Basin length, m	191.0	471.4	180.1	371.5
Stream bed length(*), m	116.3	370.7	107.6	353.5
Mean slope, degrees	23.8	15.5	22.0	12.3

(*) Permanent and intermittent flow (see Figure 6.1)

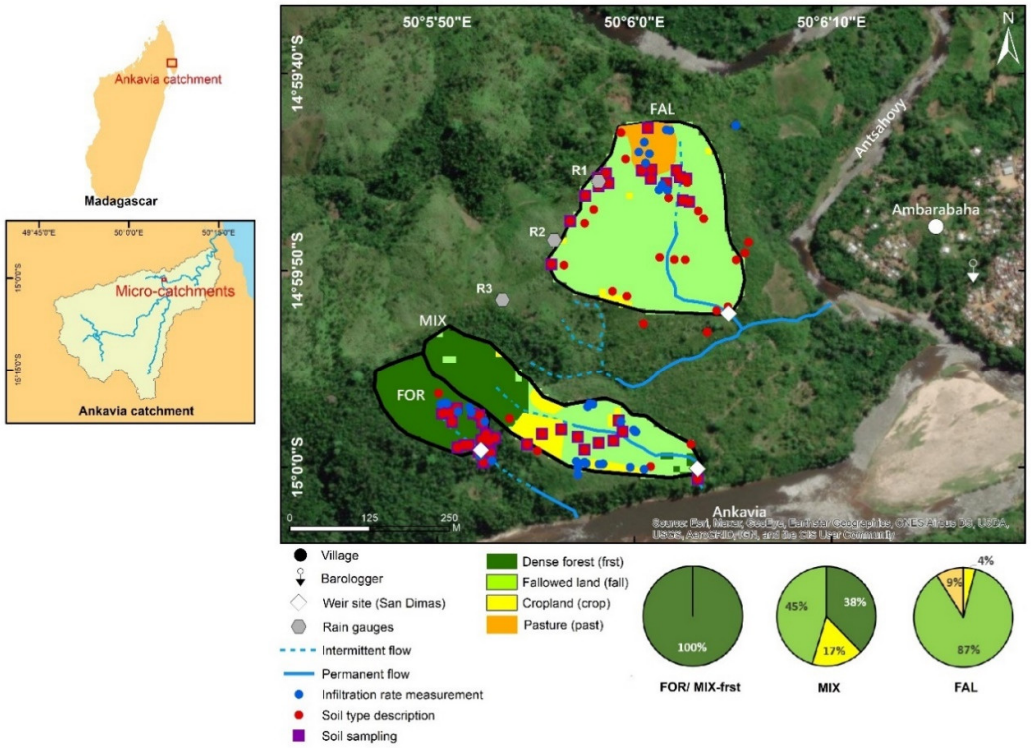

Figure 6. 1. Location of the three micro-catchments and their respective land cover distribution, stream networks, instrumentation (section 6.2.2), and soil sampling sites.

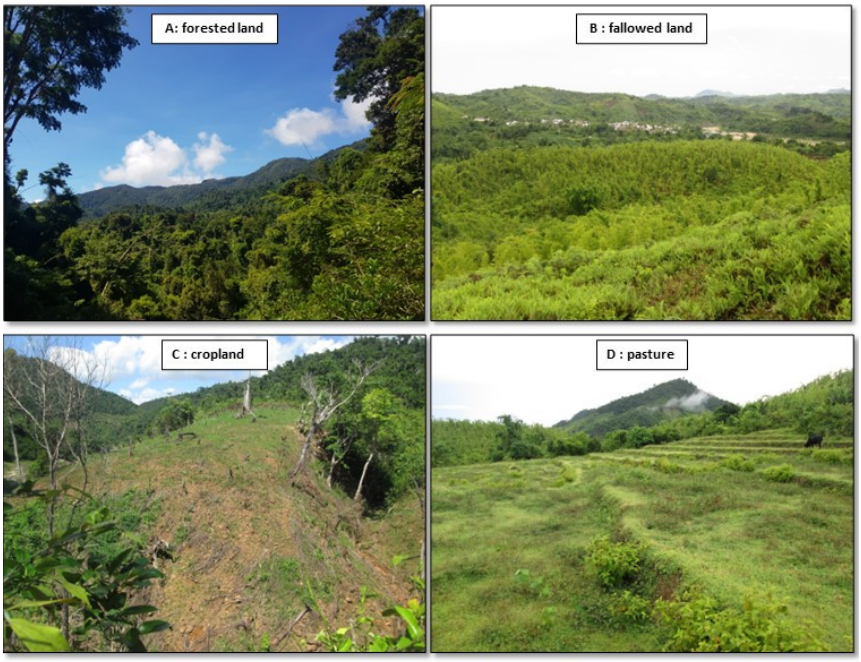

Figure 6. 2. Illustration of dominant land cover types: A) forested land, B) fallowed land, C) cropland, D) pasture (former irrigated rice field).

6.2.2. Methodology

6.2.2.1. Rainfall measurements

Three HOBOware RG3-M® tipping bucket rain gauges with dataloggers were installed to capture rainfall variability within the micro-catchments (Figure 6.1). The instruments were positioned 1.5 m above the ground and have a resolution of 0.2 mm. The rainfall data were collected from July 2019 to December 2021, using a recording interval of 5 minutes. Unfortunately, after this period, all the rain gauges were vandalized.

6.2.2.2. Discharge measurements

Streamflow was measured for two years using modified San Dimas flumes (30 cm wide and 60 cm high) at each micro-catchment outlet (Figure 6.1 and 6.3; Kilpatrick and Schneider 1983). Although a fourth flume should ideally have been placed at the MIX-frst outlet, accessibility did not allow for it. Each system was equipped with a Solinst® LTC Levelogger Edge M5 C80® sensor, with ±3 mm accuracy, which recorded water levels every 5 minutes. The water levels, corrected for fluctuations in atmospheric pressure measured using a Solinst Barologger®, were then converted to streamflow using a published stage-discharge relationship for San Dimas flumes (Equation 6.1; Kilpatrick and Schneider 1983).

$$Q = 6.35\ W^{1.04}\ Z^{1.5-n} \qquad (6.1)$$

where Q is the flow (cubic feet per second or cfs), W is the width of the outlet of the channel (0.948 ft), Z is the water level (ft), and $n = 0.179\ W^{0,32}$ ($n = 0.175967$).

Flow data were collected from December 2020 to November 2021 for FOR, from July 2019 to November 2021 for MIX, and from February 2020 to June 2020 for FAL, respectively. A complete discharge dataset (July 2019 to November 2021) was thus only available for MIX, because the probes and flumes of the other micro-catchments (FOR, FAL) experienced technical problems. Hence, given that there is no single period during which all three datasets overlap, we compared pairs of catchments: MIX/FOR from December 2020 to April 2021, and MIX/FAL from February 2020 to June 2020. Both sampling periods occurred during the rainy season.

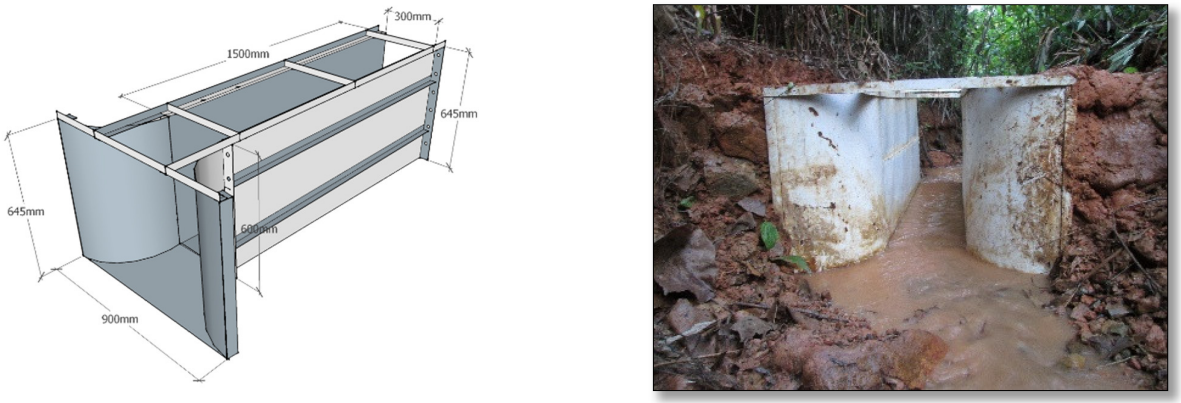

(a) (b)

Figure 6. 3. View of the type of modified San Dimas weir used to gauge streamflow at the micro-catchment outlets: (a) dimensions of San Dimas flume, (b) San Dimas flume installed at the outlet of the FAL micro-catchment.

6.2.2.3. Soil sampling and analyses

To assess possible differences in soil type within the MCs, approximately sixty soil profiles were investigated to a depth of 1.5 m using an auger. The sampling was carried out by initially following transects transversal to the stream bed, and then random transects at a second stage (Figure 6.1). However, dense vegetation prevented access to parts of the micro-catchments.

To determine soil color, hue, and soil properties (texture, pH-water, organic carbon), thirty-nine disturbed soil samples were collected across the different land cover types from specified depths of 0 - 20 cm (A horizon), 20 - 45 cm (B1/B horizon), and > 45 cm (B2 horizon). Several 300 g composite samples were constituted to obtain representative samples for each combination of depth and land cover type. Soil samples in the crop and pastureland cover were collected in February 2019, while those from the fallow and forest land cover were sampled in March 2021. The soil color and hue were evaluated by using Munsell's color chart [Annexe J]. The evaluation of soil texture (clay: <2 µm; silt: 2-50 µm, sand: 50-2000 µm), pH-water (1:5 soil: water volumetric fraction), and organic carbon content (dry combustion) were performed at the accredited laboratory of the Centre Provincial de l'Agriculture et de la Ruralité (La Hulpe, Belgium).

To estimate the bulk density and the water retention curve, twenty-four undisturbed 100-cm³ soil samples were also taken from the top two horizons (when possible) in February 2019. The retention curves were determined using a sand box apparatus for pF 1, 1.5 and 1.85 (van der Harst and Stakman 1961), and a pressure plate apparatus for pF 2, 2.4, 3, 3.5 and 4.2 (pF = Log10 (|h|), where h is the matric head in cm) (Cresswell et al. 2008). The analytical relation proposed by Van Genuchten et al. (1991) was fitted to the measured data (Equation 6.2 for unimodal pore size distribution & Equation 6.3 for bimodal pore size distribution):

$$\theta = \theta r + \left[(\theta S - \theta r)\left(\frac{1}{\left((1+(\alpha\, h))^{n}\right)^{m}}\right)\right] \qquad (6.2)$$

$$\theta = \theta r + (\theta s - \theta r)\begin{bmatrix} \omega 1\left(1+\left(1+(\alpha 1\, h)\right)^{n1}\right)^{-m1} \\ +(1-\omega 1)\left(\left(1+(\alpha 2\, h)\right)^{n2}\right)^{-m2} \end{bmatrix} \quad (6.3)$$

where θs is the saturated volumetric water content [-]; θr is the residual volumetric water content [-], h is defined as soil matric head [cm]; α_i is related to the inverse of the air entry suction [cm^{-1}], and n_i is a measure of the pore size distribution [-]. m_i = 1 – ($1/n_i$), i = {1,2} ; θs, θr, α_i , and n_i were determined by means of non-linear least-squares optimization.

To assess the infiltration rate, thirty-five infiltration tests were conducted in February 2019 and March 2021 using double ring infiltrometers (Burgy and Luthin 1956). The infiltrometer consisted of an inner ring with a diameter of 20 cm and an outer ring with a diameter of 50 cm, both with a height of 30 cm. The tests were conducted at least five times on each combination of land cover type and soil type. During the test, the water was maintained at a height of 15 cm.

6.2.2.4. Rainfall – runoff analysis

Hydrological signatures

The hydrological analysis was based on rainfall-runoff events. To enable comparisons between the micro-catchments, the stream discharge data was normalized based on their respective areas (Table 6.1). Then, the resulting normalized discharge data time series was separated into quickflow (runoff) and baseflow components (for MIX and FAL; no baseflow observed in FOR), using the graphical linear hydrograph separation approach developed by Rocha (2014) and implemented in the Visuhydro tool (Annexe K).

Rainfall events were defined as periods of non-zero basin-average rainfall interspersed with periods of zero rainfall, with a minimum cumulative rainfall of 2.5 mm and a minimum inter-event time of 1 hour. A runoff event is defined by its start, peak(s), and end. The direct runoff event begins at the point in time closest to the first peak when total streamflow equals baseflow. The event is concluded as soon as the total streamflow reaches the baseflow level. Subsequently, rainfall and runoff

events were matched. For this study, only events with discharge data corresponding to water levels ≤ 60 cm (= max. height of flumes) were taken into account.

Two important hydrological signatures, namely the runoff coefficient (rc) and the lag time were used in this study to characterize the rainfall-runoff events. The event runoff coefficient rc [mm mm^{-1}] is defined as the ratio between the runoff volume [mm] and the corresponding rainfall volume [mm]. Lag time (t_lag) [min 100 m^{-1}] refers to the time it takes for water to travel from the center of mass of total rainfall to the peak flow of a direct runoff hydrograph. In this study, we normalized lag time by the stream bed length (Table 6.1) to facilitate comparison between the three micro-catchments.

Curve-Number (CN) analysis

Based on the rainfall-runoff data, a Curve Number (CN) value was determined for each land cover type. The CN (30 ≤ CN ≤ 100) is an empirical parameter used in hydrology to estimate the amount of rainfall that is likely to become direct runoff (Mishra and Singh 2013). In this study, we used the U.S. Soil Conservation Service Curve Number approach. This method assumes that the initial abstraction (*Ia*), which is the amount of precipitation that is retained or stored on the land surface before runoff starts to occur, is proportional to the maximum potential retention (*S*, mm), which is expressed as $Ia = \lambda S$. Simulated runoff is then estimated from Equation (6.4):

$$R = \frac{(P-Ia)^2}{P-Ia+S} \quad (6.4)$$

where R is the estimated runoff (mm), P is the rainfall amount (mm), Ia represents the initial abstraction, and S refers to the maximum potential retention.

This equation is valid for $P \geq \lambda S$, otherwise R = 0. Here, we used λ = 0.05 as recommended by Tan et al. (2018). The potential retention (S) is derived from CN using Equation 6.5:

$$S = \frac{25400}{CN} - 254 \quad (6.5)$$

CN values were first determined for each micro-catchment. For this purpose, we fitted Equation 6.4 to the observations using the least-squares (LS) method, which involves minimizing the root mean square error (RMSE) between the observed and estimated runoff (Miller 2006). Given that MIX and FAL have mixed land uses, in order to obtain CN_i values for each land cover type, we minimized the root mean square error (RMSE) between the CN derived from observed data (Equation 6.4 and 6.5) and the CN derived from the area-weighted method (Equation 6.6) by selecting the CN_i values as variables.

$$CN = \frac{\sum Ai\ CNi}{\sum Ai} \tag{6.6}$$

where CN is the area-weighted curve number for the entire micro-catchment, A_i is the area of the land cover type i (section 6.2.1), and CN_i the curve number value assigned to land cover type i.

6.3. Results

6.3.1. Rainfall characteristics

The rainfall amounts measured with the three gauges were very similar (Fig. 6.4a). Consequently, the mean rainfall from the three rain gauges was used for subsequent analysis (in Figure 6.4b; Figure 6.4c; Section 6.3.3; 6.3.4). The cumulative rainfall amounts recorded during the five-month MIX/FAL period (from February 2020 to June 2020) and MIX/FOR period (from December 2020 to April 2021) were 1350 and 1270 mm, respectively (Figure 6.4b).

The distribution of rainfall intensity followed a similar pattern for both periods, with MIX/FOR exhibiting higher frequencies than MIX/FAL across all intensity classes (Figure 6.4c). During the MIX/FAL period, rainfall events did not exceed 96 mm h^{-1} (8 mm $5min^{-1}$), while during the MIX/FOR period, several events exceeded this range, reaching up to 120 mm h^{-1} (10 mm $5min^{-1}$) in some cases.

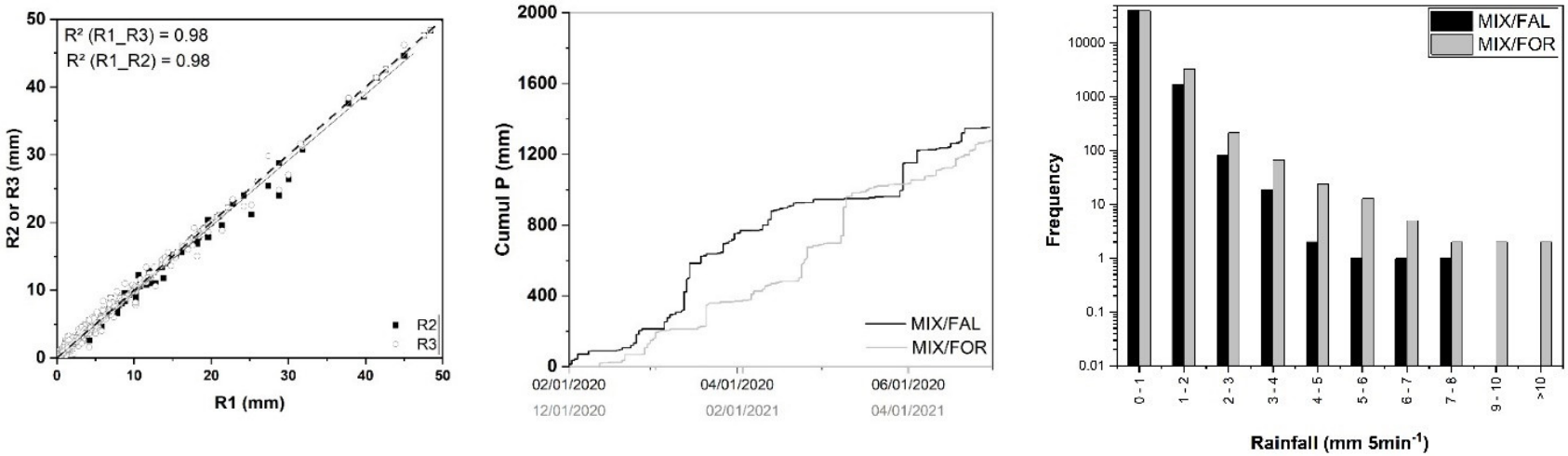

(a) (b) (c)

Figure 6. 4. (a) Correlations between hourly rainfall from the R1 and the R2 or R3 rain gauges (see Figure 6.1 for location of gauges). (b) average cumulative rainfall for each discharge monitoring period: in black, cumulative rainfall during the rainy period when both the MIX and FAL discharge flumes were operational (upper X axis, Feb-June 2020); in grey, cumulative rainfall during the rainy period when both the MIX and FOR discharge flumes were operational (lower X axis, Dec 2020 – April 2021). Period in X-axis is in MM/DD/YYYY format (c) distribution of rainfall intensity.

6.3.2. Soil characteristics

Two different soil types were identified in the micro-catchments (Table 6.3). "SOIL 1" (Figure 6.5a) was located under the forest, cropland and fallow land covers, while "SOIL 2" (Figure 6.5b) was exclusively located under the pastureland cover.

Table 6. 2. Properties of the two identified soil types.

SOIL 1 (Figure 6.5a)
The **A horizon (0 – 20 cm)** has color ranges from Y to YR, typically appearing dark brown.
The **B1 horizon (20 – 45 cm).** Its color is lighter than the A horizon, typically yellow orange (between 5YR and 10YR on the color chart). Some profiles may exhibit gray patches of hydromorphy, indicating previous episodes of waterlogging.
The **B2 horizon (>45 cm)** is drier than the B1 horizon and contains red-colored coarse elements that disintegrate easily. It is darker in color, typically tending towards red. In some locations, large stones may be present at depths ranging from 70 cm to 150 cm, which could suggest fragmented bedrock.
SOIL 2 (Figure 6.5b)
The **A horizon (0 – 20 cm)** has a dark brown color ranging from 7.5 to 10 YR. It generally feels slightly wetter than the A horizon in SOIL 1. Gray patches of hydromorphy are present as from a depth of 20 cm, and up to more than one meter deep, in greater quantity than in SOIL 1.
The **B horizon (>20 cm)**. Its color is similar to that of the B1 horizon of SOIL 1, between yellow orange (5YR and 10YR), but slightly darker. The transition from the A horizon is gradual, extending over about 15 cm, which is less pronounced than the transitions between the SOIL 1 horizons. As for SOIL 1, large stones and pebbles appear around 70 cm in some profiles, possibly indicating fragmented bedrock.



(a) (b)

Figure 6. 5. (a) Profile description of SOIL 1 found under forest, fallow and cropland covers; (b) Profile description of SOIL 2 found under the pasture cover. The rulers in the photo measure 30 cm.

SOIL 1 and SOIL 2 exhibit mostly Sandy Clay Loam and Sandy Loam texture in the A horizon and the B/B1 horizons, although some samples are characterized by Clay Loam and Loam textures (Figure 6.6). Meanwhile, the B2 horizon (SOIL 1) predominantly shows a Sandy Loam texture. Although SOIL 1 samples cover a broader range of textural classes, the samples from SOIL 2 do not differ markedly from those of SOIL 1.

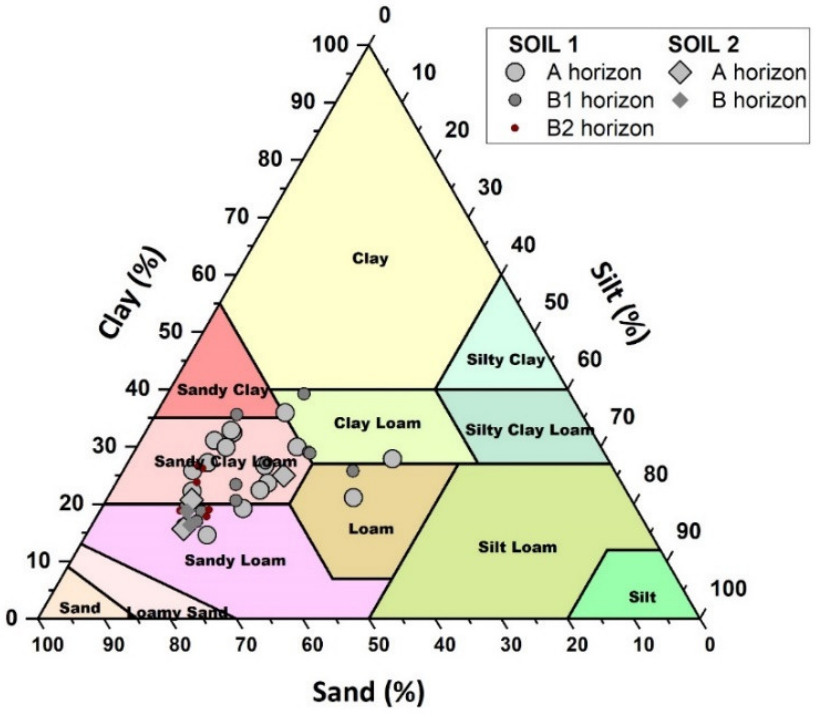

Figure 6. 6. Texture of the soil samples for the two soil types identified in the micro-catchments and different horizons, according to the National Resources Conservation Service (NRCS) textural diagram.

The sand and clay content remained generally constant with depth. However, SOIL 1 had a lower proportion of sand and a higher proportion of clay compared to SOIL 2 across all soil horizons (Figure 6.7a, 6.7b). Soil pH-water ranged from 4.8 to 5.3, indicating an acidic soil environment [Annexe L]. These values remained fairly constant across different soil depths. The organic carbon content decreased with depth, with the A horizon containing 12 to 17 g C kg^{-1} and the B horizon containing 5 to 7 g C kg^{-1}. There was no statistically significant difference in organic carbon content between the different land cover types (*p*-value > 0.05) but a tendency for fallow and forest to have higher organic carbon content than cropland and pasture.

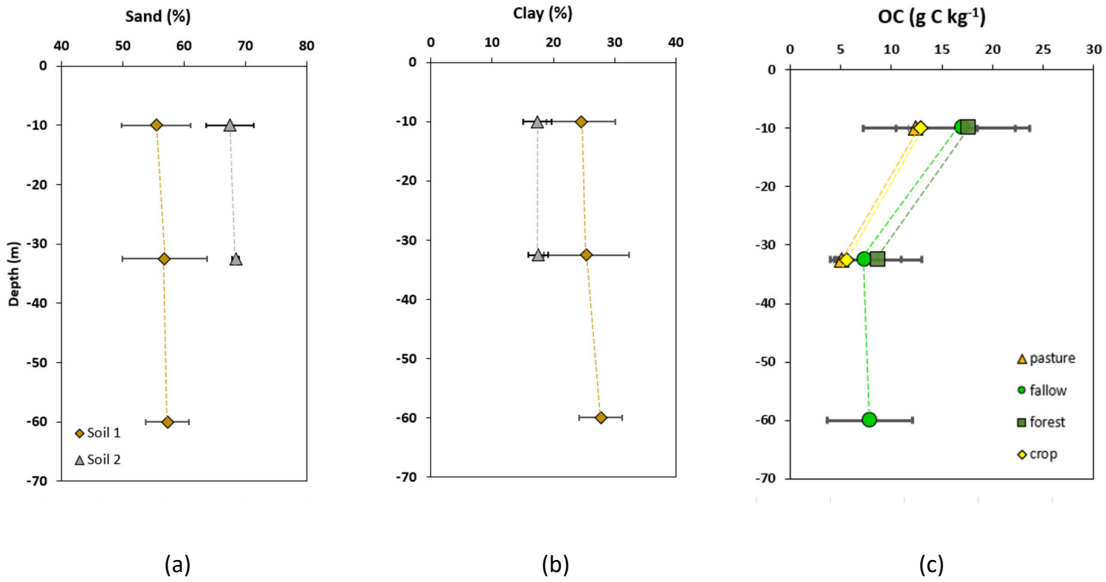

Figure 6. 7. Soil characteristics: (a) proportion of sand (%); (b) proportion of clay (%); (c) Organic carbon content; sand and clay content are differentiated by soil type, while pH and OC are differentiated by land use.

The soil bulk density varied significantly, ranging from 1.25 to 1.58 g cm^{-3} depending on the land cover type and the soil depth (Figure 6.8). Specifically, within the A horizon, the soil under forest cover exhibited the lowest bulk density, followed by soils under fallow and crop, while the soil under pasture (former irrigated rice field) had the highest bulk density (*p*-value < 0.05). The bulk density of soil in the B horizon is higher than in the A horizon.

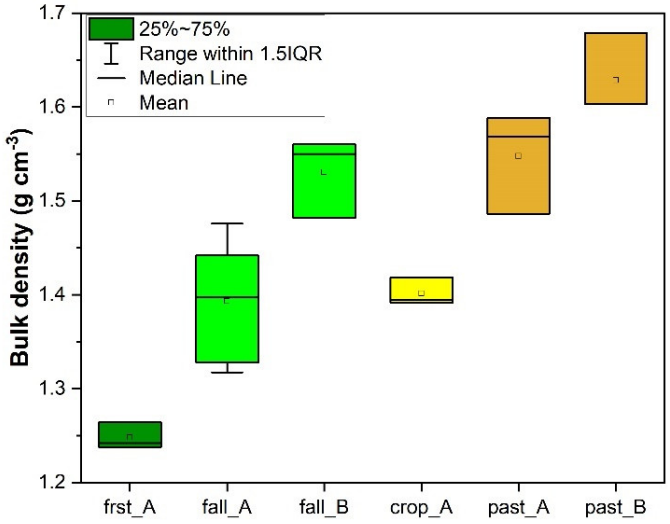

Figure 6. 8. Soil bulk density under each respective soil and land cover type (Soil 1: forest (frst), fallow land (fall), cropland (crop); Soil 2: pasture (past)). A indicates A horizon; B indicates B or B1 horizon. Box edge corresponds to the 25th (Q1) and 75th (Q3) percentiles. Whiskers extend to Q1-1.5QR (lower bound) and Q3+1.5QR (upper bound), with IQR = Q3 – Q1 (Inter-Quantile Range).

As illustrated in Figure 6.9 and 6.10, a clear hierarchy of soil hydraulic properties was observed. Based on the soil water retention curve, the soil under pasture exhibited a unimodal pore size distribution, whereas a clear bimodal pore size distribution was observed in the soils under forest and cropland and, to a lesser extent, fallow land covers. The soil water content under forest cover was the highest across most of the matric head range. In the wet range (|h| < 10 cm), water content was highest under forest, followed by cropland, fallow, and finally pasture. In the intermediate range (30 < |h| < 1000 cm), little difference is observed between crop, fallow and pasture. For suction heads > 5000 cm, soil from the pasture releases significantly less water than the three other land uses.

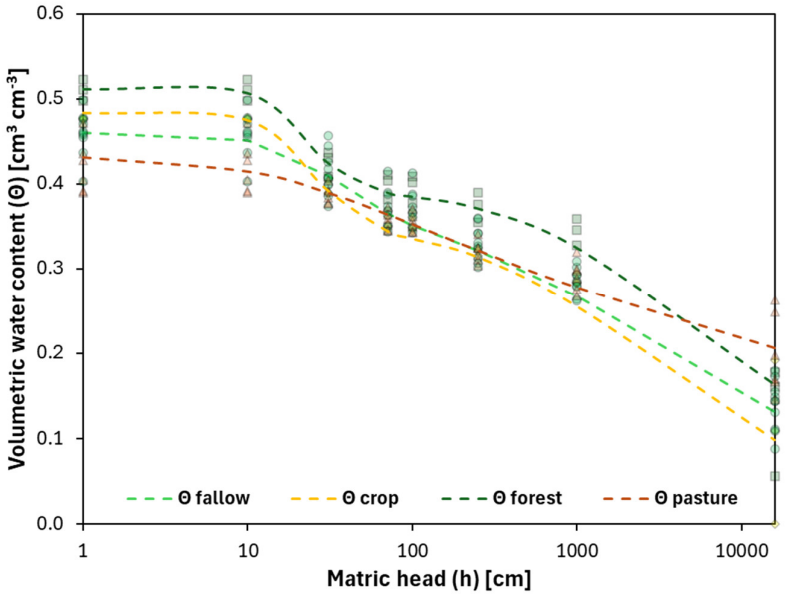

Figure 6. 9. Soil water retention curve for each land cover type. Note logarithmic (Log10) scale for X axis. Matric head values should be understood as being negative.

The infiltration rate varied significantly among different vegetation covers. Pastureland exhibited the lowest infiltration rate. Fallow and cultivated areas had similar infiltration rates, approx. 4 to 5 times higher than under pasture (Figure 6.10). The infiltration rate in forested areas was even higher, approximately five times higher than in fallow and cultivated areas, and about twenty times higher than in the pastures.

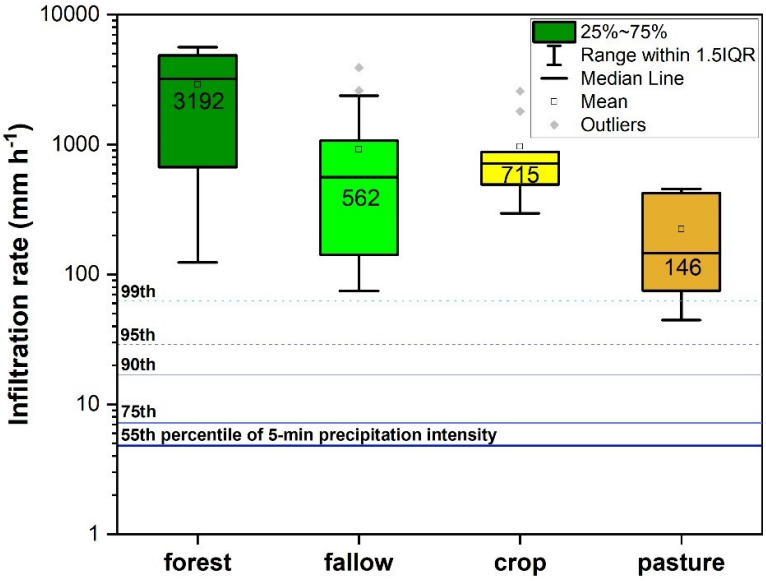

Figure 6. 10. Infiltration rate as measured by double ring infiltrometer under each land cover type. Box edges correspond to the 25th (Q1) and 75th (Q3) percentiles. Whiskers extend to Q1-1.5QR (lower bound) and Q3+1.5QR (upper bound), with IQR = Q3 – Q1 (Inter-Quantile Range). Points outside the box are outliers. Note logarithmic (Log10) scale for Y axis. The blue lines represent the percentiles of the 5-min rainfall intensity recorded at rain gauge R2: 55th (4.8 mm h^{-1}, bold solid line), 75th (7.2 mm h^{-1}, medium bold solid line), 90th (16.8 mm h^{-1}, thin solid line), 95th (28.8 mm h^{-1}, dashed line), 99th (62.4 mm h^{-1}, dotted line).

6.3.3. Event-based hydrological characteristics of micro-catchments

Both the mean and median runoff coefficient (rc) followed a similar trend across the micro-catchments, with MIX exhibiting the highest values (0.15 and 0.11, respectively), followed by FAL (0.11; 0.06) and then FOR (0.05; 0.01) (Figure 6.11a).

The mean values of the lag time (t_lag) for FAL and MIX were similar, both averaging around 10 min per 100 m. t_lag was the highest for FOR, at 25 min per 100 m. The median t_lag follows the same trend, with FAL and MIX having the lowest values, and FOR having the highest (Figure 6.11b).

6.3.4. Curve Number for each land cover

Given the known curve number (CN) values for forest and fallow land (deduced from MC_FOR and MC_FAL), the CN value of cropland could be derived from the CN of the MIX watershed based on Equation 5 (Table 6.4). Based on the CN values derived by the LS fitting approach, the modeled CN values followed an ascending order: forest exhibited the lowest CN, followed by fallow land and then cropland. The CN for pasture could not be determined.

Table 6. 3. Curve Number of each land cover type. (LS = Least Square method).

Land cover	Curve Number LS fit
Forest (frst)	52
Fallow (fall)	59
Cropland (crop)	69

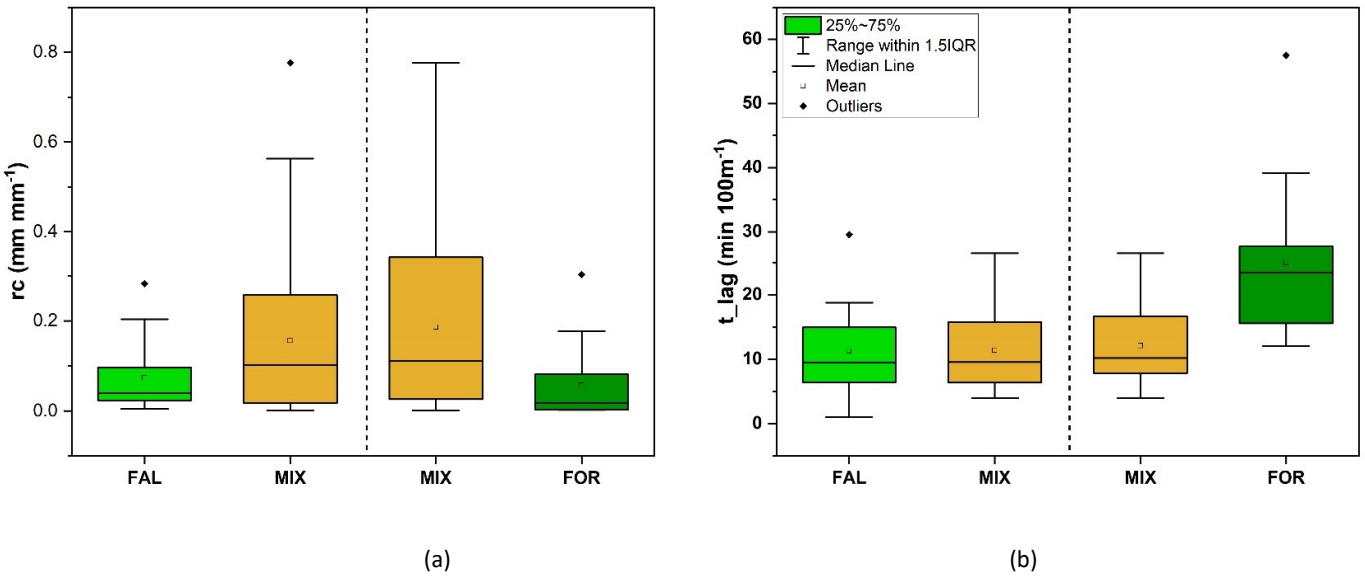

Figure 6. 11. Hydrological signatures of the three micro-catchments: (a) Runoff coefficient (rc) and (b) normalized lag time (t_lag). Box edge corresponds to the 25th (Q1) and 75th (Q3) percentiles. Whiskers extend to Q1-1.5QR (lower bound) and Q3+1.5QR (upper bound), with IQR = Q3 – Q1 (Inter-Quantile Range). Points outside the box are outliers. Each pair of signatures corresponds to a specific rainy period: the MIX/FAL comparison extends over the period from February 2020 to June 2020, while the MIX/FOR comparison relates to the period from December 2020 to April 2021 (see materials and methods section for further details).

6.4. Discussion

6.4.1. Spatial variation in soil physical characteristics across land cover types

The soils in the micro-catchments are classified predominantly as sandy clay loams and sandy loams, though the soil under pasture is, on average, sandier than the under the other land uses (Figure 6.6). However, they differ significantly in terms of acidity, organic carbon content, bulk density, water retention capacity, and infiltration properties depending on land use (Figure 6.7c, Figure 6.8, Figure 6.9, Figure 6.10). Furthermore, soils under forests, fallows, and croplands exhibit similar profile characteristics (SOIL 1, Table 6.3, Figure 6.7a, 6.7b), which differ markedly from the soil under pasture.

Soils under primary forest cover are characterized by higher organic matter content and have a less compact, more porous structure compared to other land cover types. As an undisturbed ecosystem, the primary forest benefits from continuous, long-term input of organic matter from decomposing litter and woody debris, producing substances such as fulvic and humic acids (Bonell 2005). These substances promote clay particle aggregation by forming complexes with metal ions (e.g., iron and aluminum), stabilizing these particles into micro and macro-aggregates and increasing soil porosity (Bruijnzeel 2004; Bonell 1993). This leads to very high permeability, enhanced by biopores created by soil fauna and root systems, increasing water retention and infiltration. The high infiltration rate recorded in the primary forest (3192 mm h^{-1}) is notably higher than values reported in other studies in tropical environments. For comparison, Zimmermann et al. (2006) reported infiltration rates of up to 2000 mm h^{-1} in Amazonian tropical forests. Similarly, Godsey and Elsenbeer (2002) measured infiltration rates exceeding 700 mm h^{-1} in humid tropical forests in Panama, highlighting the exceptional capacity of primary forest soils to absorb water.

Soils under croplands and fallows have a denser, less porous soil structure than under forests, resulting from processes related to deforestation and cultivation (Paré et al. 2010). Indeed, vegetation removal for cultivation decreases organic matter input, reducing soil organic carbon content and affecting the formation of clay-humic complexes crucial for soil structure (Figure 6.7c) (Zwartendijk et al. 2017). Moreover, direct soil exposure to these elements accelerates organic matter oxidation and can cause soil acidification through leaching of basic cations (Ca^{++}, Mg^{++}, K^{+}; Auvet et al. 2015). These chemical changes, documented by Zwartendijk et al. (2017) and Styger et al. (2007), alter the colloidal properties, reducing its ability to form stable aggregates. In addition, land clearing for cultivation may affect the intensity of biological activity. The result is a more compact structure with reduced porosity, decreasing cation exchange capacity and limiting water infiltration.

The pasture soil (SOIL 2, formerly used for irrigated rice cultivation), exhibits a significantly sandier and denser profile than SOIL 1, particularly in the upper layer (Figure 6.7 and 6.8). This difference is primarily attributable to historical land use and current management practices. Frequent ploughing and puddling operations in irrigated rice fields have disrupted soil aggregate stability, leading to structural degradation and preferential removal of finer clay particles, resulting in a sandier texture (Ghimire et al. 2014; Stockfisch et al. 1999). Paradoxically, despite this sandier composition, soil permeability remains limited. This can be explained by two main factors. Firstly, the remaining fine clay and silt particles tend to lodge in the pore spaces between sand grains, reducing the infiltration capacity. Secondly, in tropical soils such as ferralsols, nitisols, and acrisols, iron oxides play a crucial role in micro-aggregation (Song et al. 2022). Under reducing irrigated conditions, iron changes from the Fe^{3+} to the Fe^{2+} oxidation state, becoming more mobile. This reduction of iron (Fe^{2+}) likely leads to aggregate destruction under saturated conditions, resulting in pore clogging, increased bulk density, and significantly reduced permeability (Barral et al. 1998). Additionally, the constant passage of livestock on these lands, now converted to pasture, likely contributes to soil structure densification. The resulting compaction reduces interstitial space and,

consequently, further decreases soil infiltrability. Overall, these chemical and physical processes interact to create a denser, less permeable soil, despite its apparently sandier texture.

6.4.2. Effect of land cover on runoff processes

In simulating hydrological properties, the calculation of Curve Number (CN) values revealed differences between the two adjustment methods employed. The Least-Square (LS) adjustment method, which minimizes the RMSE between observed and simulated runoff, generated a ranking of CN values as follows: CN_frst < CN_fall < CN_crop. This order corresponds to the infiltration rate measurements observed for each land use type. Although the CN values obtained here are slightly lower than those reported by Mishra and Singh (2013) (52 vs 75 for forest, 59 vs 82 for fallow, and 69 vs 87 for cultivated lands), the relative ranking aligns with their findings.

In forested areas (CN = 52), typically located in the upstream portions of watersheds, the hydrological dynamics differ markedly from other landscapes. Beyond the absence of baseflow, the exceptionally high infiltration rates in the topsoil, which almost invariably exceed the typical rainfall intensities observed in the study area, render the occurrence of Hortonian overland flow (**HOF**) practically impossible in these environments (Figure 6.4c, Figure 6.10). Subsurface flow (**SSF**) emerges as the sole contributor to streamflow at the watershed outlet. However, numerous studies conducted in tropical environments have revealed significant variability in hydrological processes. In Amazonian forests on Ultisols, Zimmermann et al. (2006) found that **SSF** was the dominant mechanism, corroborating our results. However, Bonell (2005), in a comprehensive review of humid tropical forest hydrology (often on Oxisols and Ultisols), indicated that saturation overland flow (**SOF**) was a predominant mechanism, coexisting with substantial **SSF**. Moreover, Germer et al. (2010) observed that **SOF** could be significant in certain tropical forests on Alfisols, particularly during high-intensity rainfall events. This variability in hydrological

processes can be attributed to multiple factors, including soil characteristics, topographic conditions, and precipitation regimes. Overall, while **SSF** often predominates in forested areas, the importance of **HOF** or **SOF** should not be disregarded, particularly in certain soil types and during high-intensity rainfall events.

The median runoff coefficient in forested environments remains remarkably low (1%), suggesting that water is primarily absorbed (through canopy interception and infiltration), stored (in the litter layer), or slowly transmitted through the soil rather than rapidly flowing over the surface (Figure 6.11a). A relatively long lag time is observed (Figure 6.11b), which is consistent with the low runoff coefficient. While water quickly infiltrates forest soils, it moves laterally at moderate velocities through macropores created by roots and soil fauna (Beven and Germann 2013). Furthermore, the presence of hydromorphic features in the B horizon may also indicate the possible existence of temporary perched water tables which, through the piston effect, can displace pre-event water in the soil at the watershed outlet (McDonnell 1990).

In fallow lands (CN = 59) and cultivated areas (CN = 69), generally located in the middle and lower parts of watersheds, infiltration rates are significantly lower than in forested areas (although they remain high, Figure 6.10). These soil characteristics favor probably **SSF** as the dominant runoff generation mechanism. However, under certain conditions, such as crust formation or soil compaction, **HOF** may occasionally occur. Moreover, the presence of hydromorphic features in the B horizon suggests the possible existence of temporary perched water tables. At the interface with **SSF**, these saturated zones can also induce **RF** through the piston effect (Giertz et al. 2005). Numerous studies conducted in agricultural environments have identified different types of flow. In West African croplands (intercropping systems) on Lixisols, Giertz and Diekkrüger (2003) found that surface runoff, encompassing both **HOF** and **SOF**, was more pronounced than in adjacent forests. Similarly, Janeau et al. (2014), studying fallow lands on Acrisols in Southeast Asia, reported significant contributions

from surface runoff (**HOF/SOF**) and subsurface flow (**SSF**). Generally, surface runoff plays a more significant role in cultivated and fallow lands than in forests. In these landscapes, surface runoff, subsurface flow, and groundwater flow can all contribute substantially to the total streamflow, their relative importance depending on soil conditions, agricultural practices, and precipitation intensity.

In pasture areas (CN value not provided, but likely the highest), the hydrological dynamics differ considerably from those of forests, fallows, and cultivated lands. The dense soil texture and reduced (but still high) infiltration rates in the topsoil facilitate the generation of **SSF**. However, during heavy rainfall events, **HOF** can occur (Figure 6.10). Furthermore, the presence of hydromorphic features in the A horizon indicates persistent saturation near the surface. This condition is likely to induce **SOF** during prolonged periods of precipitation or low-intensity rainfall episodes. In former rice paddies of Southeast Asia, Matsuno et al. (2006) found that surface runoff was dominant. Janeau et al. (2014), examining pasture hydrology on compacted soils, reported that **HOF** and **SOF** were the predominant mechanisms, with minimal **SSF**. Corroborating these findings, Ziegler (2004) observed significant **HOF** in tropical pastures (formerly rice paddies), particularly during moderate to intense rainfall events. This difference in hydrological behavior can be attributed to several factors, including soil compaction, altered topographic conditions, and the legacy of prior land use. **HOF** often contributes substantially to total runoff, but the importance of **SOF** should not be overlooked, particularly during prolonged rainfall events and in areas where the water table is consistently high.

6.4.3. Effect of spatial configuration of land cover on hydrological responses

The comparative study of the FOR, FAL, and MIX micro-watersheds reveals the significant impact of deforestation and land use heterogeneity on local hydrology. Observations show a clear hierarchy in runoff coefficients: the forest basin (FOR)

exhibits the lowest runoff, followed by the fallow-dominated basin (FAL), while the mixed basin has the highest (MIX).

The comparison between FOR and MIX land covers reveals that a 62% reduction in forest cover, replaced by 45% fallow land and 17% cultivated land (Figure 6.1), results in a significant increase in the median runoff coefficient from 0.01 to 0.11 (Figure 6.11). This tenfold increase can be attributed to reduced rainfall interception by vegetation cover, decreased soil infiltration capacity due to loss of soil organic matter, and degradation of soil structure. These alterations collectively increase the likelihood of runoff formation, particularly in areas where soil quality has deteriorated. Similar trends have been observed in other tropical watersheds. In Ecuador, Molina et al. (2007) found that converting 30% of forests to pastures increased the annual runoff coefficient from 0.05 to 0.09. In an Amazonian watershed, Germer et al. (2010) observed that forest-to-pasture conversion increased the average runoff coefficient from 0.17 to 0.45, with surface runoff in grazed areas reaching up to 70% of precipitation during intense rainfall events, compared to only 17% in adjacent forested areas. These studies underscore the significant impact of deforestation on local hydrology. Indeed, forested areas maintain a complex interaction between interception and infiltration, thus creating an efficient system for modulating streamflow. In contrast, deforestation can lead to increased flood responses and alter the overall hydrological balance of the ecosystem (Zimmermann et al. 2006).

The comparison of median runoff coefficients between the FAL micro-watershed (primarily composed of fallow land, median rc: 0.06) and the MIX micro-watershed (a mosaic of land covers with 38% primary forest, 17% cultivated land, and 45% fallow land, median rc: 0.11) suggests that a more homogeneous landscape (fallow in this study) generates less runoff than a heterogeneous landscape. This observation could be explained by several factors. The primary factor is the increase in cultivated surfaces, which have a higher CN and therefore generate more runoff (Beven et al. 1988). Secondly, heterogeneous watersheds probably present flow

convergence zones or spatial variations in soil properties that promote streamflow formation (Grayson et al. 1997). Finally, edge effects between different land cover types in heterogeneous watersheds can create localized saturation zones and increase overall stream flow (Van De Giesen et al. 2000). These results corroborate observations by Iroumé et al. (2005) who found that watersheds under the same rainfall regime with more homogeneous secondary forest cover exhibited lower runoff rates than those with mixed coverage. Similarly, Zhang et al. (2017) in China demonstrated that landscape heterogeneity can increase runoff by creating preferential flow paths.

The relationship between landscape homogeneity and runoff is complex and can vary depending on local conditions and soil characteristics. Nippgen et al. (2011) observed that the impact of landscape heterogeneity on runoff can be counterintuitive. In watersheds with high soil infiltration capacity, a homogeneous landscape may generate less streamflow compared to a heterogeneous one. Conversely, in areas with poorly permeable soils, the opposite effect might occur. Furthermore, landscape heterogeneity can sometimes reduce runoff by creating water storage zones. These observations, while relevant to this study, are not universally applicable and may differ based on the specific characteristics of the site under investigation.

6.5. Conclusion

The influence of vegetation cover on streamflow generation is a crucial issue for water and land management, particularly in tropical regions where shifting agriculture and deforestation are rapidly transforming landscapes. In a granitic geological context with the presence of ferralsols, our study, conducted in micro-catchments of northeastern Madagascar, reveals a gradient of hydrological properties based on land use.

Tropical primary forests exhibit optimal hydrological characteristics, with exceptionally high infiltration rates. Cultivated lands and fallows, despite a denser soil structure, maintain high infiltration rates, albeit lower than those of forests. Pastures, which were formerly irrigated rice fields, present the least favorable hydrological properties, with reduced permeability and lower infiltration rates, though these remain relatively high.

Subsurface flow likely predominates in forest areas, underscoring the rarity of surface runoff in this region. However, surface runoff can occur, particularly in fallowed land, cropland and pastures during significant or prolonged rainfall events. The streamflow rate also varies significantly depending on land use types and their distribution in the landscape.

Our findings underscore the critical importance of considering not only vegetation cover, but also soil properties and the land use composition in both modeling and managing hydrological responses. Furthermore, this research highlights the pivotal role of primary forests in hydrological regulation and emphasizes the imperative for their preservation. It also elucidates the intricate interplay between vegetation, soil, and water in these tropical ecosystems. This complexity manifests particularly in the variability of hydrological responses contingent upon local conditions, thereby accentuating the necessity for a holistic approach in watershed management.

7. Chapitre 7 : Raingauge vs IMERG precipitation data : Balancing Accuracy and Cost for a Reliable Hydrological Observatory in a Tropical River Basin[5]

Abstract:

Reliable hydrological monitoring is crucial for effective water resource management, but establishing observatories in remote areas with extreme weather presents significant challenges. This study aimed at identifying cost-effective methods for streamflow estimation in such environments. We evaluated the performance of the Soil and Water Assessment Tool (SWAT) model using various precipitation data sources: ground-based rain gauge networks with different densities (one-gauge 1RG, two-gauge 2RG, and five-gauge 5RG configurations) and satellite-derived Integrated Multi-satellite Retrievals for GPM (IMERG) data. The study focused on the Sahafihitry catchment, a ~200 km² area in northeastern Madagascar.

The results demonstrated that denser rain gauge networks (5RG and 2RG) captured the spatial variability of rainfall more effectively than single gauges or IMERG data. This translated into superior SWAT model performance. Denser networks achieved higher statistical metrics (R^2, slope of regression a, Nash-Sutcliffe efficiency NSE, root mean square error RMSE, Kling-Gupta efficiency KGE) indicating a better fit between simulated and observed streamflow. Specifically, 5RG: $R^2 = 0.84$, a = 0.92, NSE = 0.83, RMSE = 3.33, KGE = 0.82; 2RG: $R^2 = 0.85$, a = 0.95, NSE = 0.83, RMSE = 3.36, KGE = 0.88; 1RG: $R^2 = 0.73$, a = 0.80, NSE = 0.72, RMSE = 4.28, KGE = 0.88; IMERG: $R^2 = 0.48$, a = 0.63, NSE = 0.37, RMSE = 6.46, KGE = 0.66. Furthermore, rain gauge configurations outperformed IMERG in simulating both flood events and low-flow periods.

While IMERG offers low cost, readily available data, its lower performance introduces significant uncertainty into hydrological modeling, particularly during extreme events. In contrast, the two-gauge network (2RG) achieved satisfactory

[5] Submitted to *Hydrological Sciences Journal* in September 2024.

streamflow simulations and represents the most cost-effective option for establishing reliable observatories within the specific characteristics of this study area.

Keywords: Hydrological monitoring; streamflow estimation; SWAT model; rain gauge network, IMERG.

7.1. Introduction

The establishment of a reliable hydrological monitoring system is crucial for many applications, such as drought monitoring, flood prevention, water balance calculations and water resources management (Di Baldassarre et al. 2010). When properly installed and maintained, such monitoring systems can provide precise real-time data on hydrological variables, including precipitation, river discharge, and ground water levels (Carrière et al. 2021). However, given the high costs of maintaining accurate measurement networks, the implementation of such an observatory remains challenging, particularly in remote and hard-to-access sub-tropical regions that experience extreme weather conditions (WMO 2022, 1987 ; Sivakumar 2017; Sivapalan et al. 2003). These challenges are further exacerbated by the risk of infrastructure damage as well as insufficient public involvement in water resources monitoring, resulting in limited, fragmented, and discontinuous hydrological monitoring networks that impede a comprehensive understanding of the hydrological processes and hinder proper water resources management. Therefore, it is increasingly urgent to design easy-to-maintain and cost-effective observation systems that minimize field interventions while ensuring reliable operation of hydrological observatories.

Recent advances in remote sensing techniques have led to the emergence of satellite-based, data reanalysis-based, model-based products as a potential solution to meet the needs of hydrological observatories (Sun et al. 2018; Tapiador et al. 2012). They offer an attractive alternative, especially to ground-based rain gauges (WMO 2022). Among recent satellite-based gridded precipitation products, the

Global Precipitation Measurement Integrated Multi-satellitE Retrievals GPM IMERG v06 Final has garnered much attention due to its 20-year availability of precipitation data, fine spatial resolution (0.1° x 0.1° or ~11 x ~11 km²), and high temporal resolution (30 min) compared to other products (Huffman et al. 2020). Given their characteristics, IMERG products appear to be suitable data sources for forcing rainfall-runoff models used in a variety of hydrological applications, such as extreme event analysis and water resources management (Ombadi et al. 2018; Maggioni and Massari 2018; Gosset et al. 2013).

Despite their high potential, IMERG products are subject to errors arising from various factors, such as the nature of the precipitation measurement (Villarini et al. 2009), sampling uncertainties (Khan 2019), retrieval algorithms, and variations in land surface properties (Kummerow et al. 1998). Furthermore, since IMERG incorporates ground-based rainfall measurements from the Global Precipitation Climatology Center (GPCC) through its multi-satellite algorithms, the product may be affected by greater uncertainties in tropical areas where there is a limited availability of rain gauges for calibration or validation (Huffman et al. 2020). In addition, several researchers have highlighted the limitations of IMERG, which include low accuracy representation of the spatial variability of rainfall, as well as both overestimation and underestimation of certain rainfall classes depending on the study area (Ramahaimandimby et al. 2022; Tan and Duan 2017). Despite these limitations, the research community continues to explore the applications of IMERG in the hydrological domain, especially in countries with poor rainfall monitoring networks.

While a significant amount of research has been conducted to quantify errors in IMERG products (e.g., Derin et al. 2021; Dezfuli et al. 2017), limited attention has been paid to understanding the implications of these errors on rainfall-runoff model forecasts. As hydrological models exhibit strong nonlinearity, errors in precipitation measurements can greatly affect the accuracy of flood simulations. The extent of this impact is contingent on the quality of input data and the interplay between different components of the model (Sellami et al. 2013). For instance, some studies indicate that, conditional upon recalibrating the hydrological model, IMERG can produce

satisfactory flow simulations (Derin et al. 2021; Maggioni and Massari 2018). Some research even suggests that IMERG can be as effective as using ground-based rainfall data (Jiang et al. 2021; Li et al. 2017; Tang et al. 2016b). However, in other cases, hydrological models relying on IMERG products as input data exhibited inadequate performance despite repeated model calibration (Jiang et al. 2018; Wang et al. 2017b). The main reasons for the lower performance of IMERG-data driven models have been attributed to significant biases between IMERG and ground-based observations. Hence, there is a need to recalibrate the hydrological model when using IMERG products to better account for IMERG rainfall-runoff model interactions. Furthermore, the inherently lower accuracy of IMERG rainfall data compared to those derived from ground-based networks exacerbates these challenges (Su et al. 2021).

Since numerous factors influence the performance of numerical simulations in hydrological processes, no single rainfall product used as input can guarantee excellent results across all scenarios. These factors include the scale of the study, spatial coverage of rainfall data, location, time scale, basin characteristics, choice of hydrological model, process representation, and model calibration algorithms (Jiang and Bauer-Gottwein 2019; Yuan et al. 2018). For instance, although satellite- and gauged-based products such as IMERG have demonstrated their efficacy in estimating rainfall patterns compared to ground-based measurements in remote areas (Mahmoud et al. 2021), knowledge gaps remain regarding their reliability in hydrological applications, particularly in tropical areas with complex terrain and frequent extreme rainfall events. Moreover, most evaluations of the suitability of IMERG products for hydrological applications have focused on China, where extensive hydrometeorological monitoring equipment is available for conducting validation studies (Jiang and Bauer-Gottwein 2019; Jiang et al. 2018; Yuan et al. 2018; Wang et al. 2017b). For the vast African continent, however, reliable data are scarce, and evaluations have often been conducted at large spatial (e.g., country level or larger) or temporal (e.g., annual or longer) scales, and on large river basins. Hence, given that many water management issues are addressed at smaller scales, it is

crucial to also evaluate the effectiveness of rainfall products from different sources for hydrological observatory applications for small or meso-scale watersheds.

The overall aim of this study was to evaluate the usefulness of ground-based rain gauge data (RG) and remote sensing IMERG products for streamflow estimation. More specifically, the study assesses the performance of the semi-distributed SWAT (Soil and Water Assessment Tool) model at predicting streamflow using either different configurations of a ground-based rain gauge network or the IMERG product. The study was conducted in the Sahafihitry watershed (ca. 200 km^2) located in northeastern Madagascar. This tropical watershed experiences high seasonality in rainfall frequency, intensity and duration (Ramahaimandimby et al. 2022). Heavy precipitation, including those accompanying large cyclone events which tend to occur every other year on average, threatens human activity and causes natural disasters such as floods and landslides (CREAM 2013; Tadross et al. 2008). Data collection and measurement in this region are particularly challenging due to rugged terrain and impassable roads during the rainy season. Furthermore, a lack of awareness among the local population can make equipment vulnerable to vandalism. These factors complicate establishing and maintaining long-term hydrological observatories. By assessing different sources of rainfall data and considering the trade-offs between data cost and quality, this study can help decision-makers select the most appropriate data sources and hydrological observatory designs for their specific needs, ultimately contributing to the sustainable management of water resources in Madagascar and other regions facing similar challenges.

7.2. Materials and Methods

7.2.1. Study area

The Sahafihitry river basin covers an area of 197 km² in the District of Antalaha, SAVA region, N-E of Madagascar (Figure 7.1). It lies between 15°00' and 15°20' South latitude and between 50°00' and 50°10' East longitude, with elevations ranging from 56 m to 1309 m a.m.s.l. The outlet is located at the confluence with the Ankaviabe river. The climate is humid-tropical with annual mean temperatures ranging from 22.3 to 27.7°C (CREAM 2013; CPGU 2012). Annual precipitation is around 2200 mm (1960 – 2016), with high spatial variability (Jury et al. 1995). Precipitation is unevenly distributed throughout the year, with a warm and rainy season from November to April and a cooler (less rainy) season from May to October (Chaperon et al. 1993). Moreover, the region is often affected by storms and tropical cyclones, which frequently cause significant damage (CPGU 2012).

The upstream portion of the watershed is dominated by tropical rainforests and a mosaic of trees and shrubs, while the downstream section exhibits a mosaic of diverse natural vegetation types. The Masoala National Park, managed by Madagascar National Park, encompasses 18% of the total watershed area (Figure 7.1; CREAM 2013; Ormsby and Mannle 2006).

According to the World Reference Base, the dominant soils in the watershed are ferralsols in the southern highlands and acrisols in the downstream part of the watershed (Hengl et al. 2017). Ferralsols typically exhibit uniform profiles with high clay (kaolinite) and iron oxide contents, leading to a pseudo-sand structure that explains their high permeability in spite of the high clay content (Martinez and Souza 2020). In contrast, acrisols display more heterogeneous profiles with a lower permeability argillic horizon resulting from clay accumulation. These soils generally have lower clay content and are particularly susceptible to erosion (Rossi 1979).

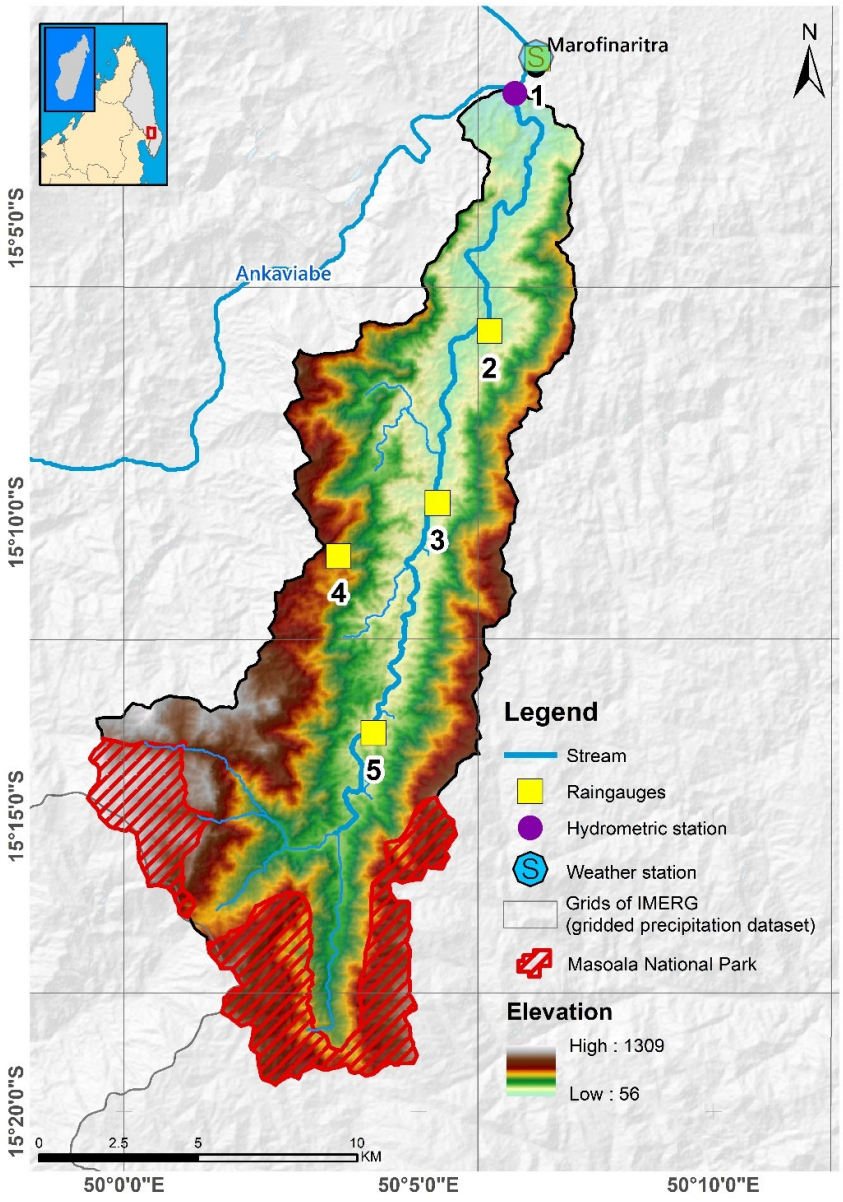

Figure 7. 1. Geographical context of the Sahafihitry catchment in Northeastern Madagascar: topography and location of weather station, additional rain gauges and river discharge monitoring station within the watershed. Rain gauge No. 1 is located at the weather station in Marofinaritra. Grids correspond to the grid of the IMERG gridded precipitation dataset.

7.2.2. Data collection

A comprehensive hydrometeorological network was established, comprising a meteorological station, five rain gauges, and a water level measurement station. This network became fully operational in August 2018. The dataset utilized in this study spans from August 2018 to July 2021, representing three complete years of observations.

7.2.2.1. Weather data

A meteorological station was installed at Marofinaritra (Figure 7.1) to record solar radiation, wind speed, relative humidity, and maximum and minimum temperatures. Data were collected hourly using a Campbell Scientific® CR300 series data logger. Concurrently, precipitation was measured using a network of five HOBO® RG3M rain gauges (accuracy of ±1%), deployed within the study area (Figure 7.1). These rain gauges, situated 5 to 10 km apart from one another, also recorded data on an hourly basis.

7.2.2.2. Discharge data

Discharge data calculations are described in Chapter 3, section 3.4.2 and 3.4.3.

7.2.2.3. Gridded precipitation data: IMERG

Given its good performance in estimating daily precipitation across the Sahafihitry watershed (Ramahaimandimby et al. 2022), IMERG precipitation data were used for forcing the hydrological model. GPM-IMERG, short for Integrated Multi-satellitE Retrievals for Global Precipitation Measurement, is a satellite-based precipitation product developed by the National Aeronautics and Space Administration Global Precipitation Measurement (GPM) mission. The IMERG product uses an algorithm that blends measurements from passive microwave sensors and infrared sensors to estimate precipitation. It incorporates data from ground-based rain gauges (GPCC) to calibrate and validate the satellite-derived estimates. The product is available with a spatial resolution of 0.1° x 0.1° and a temporal resolution of 30 minutes (Huffman et al. 2020).

7.2.2.4. Spatial data

The 2020 land cover map was generated based on the 300-m resolution GlobCover v.2 product (Bontemps et al. 2009; Figure.7.2a), while soil attributes were obtained from the 250-m resolution SoilGRID classification (Deckers et al. 2010; Figure.7.2b). The delineation of Sahafihitry catchment boundaries, hydrological structures, and slope information relied on a 30-m resolution DEM sourced from Shuttle Radar Topographic Mission (SRTM) (Earth Resources Observation And Science (EROS) Center 2017; Figure.7.2c).

7.2.3. Rainfall spatial variability

An exploration of rainfall spatial variability in the Sahafihitry catchment was undertaken. Using the coefficient of variation as a key measure (Equation 7.1 and 7.2), the analysis aims to quantify the degree of variation in daily rainfall across the five rain gauges or the IMERG product grids for each of the three years of measurement. A high coefficient of variation (>70%) in rainfall indicates that the daily precipitation values within the dataset exhibit a substantial degree of spatial variability compared to the mean (Jalilibal et al. 2021). The coefficient of variation (CV_i) was first calculated on a daily basis and subsequently averaged per year (CV; Equation 7.5 and 7.6):

$$CV = \frac{\sum_{i=1}^{k} CVi}{k} \quad (7.1)$$

$$\text{where } CV_i = (\sigma_i/\mu_i) \times 100 \quad (7.2)$$

and where k represents the number of days in a given year, and CV_i is the coefficient of variation for day i. μ_i and σ_i are the average precipitation for day i and the corresponding standard deviation. The calculations of daily CV (CV_i) were performed by using either the five rain gauges or the eight IMERG grid cells comprising the catchment area (Figure 7.1).

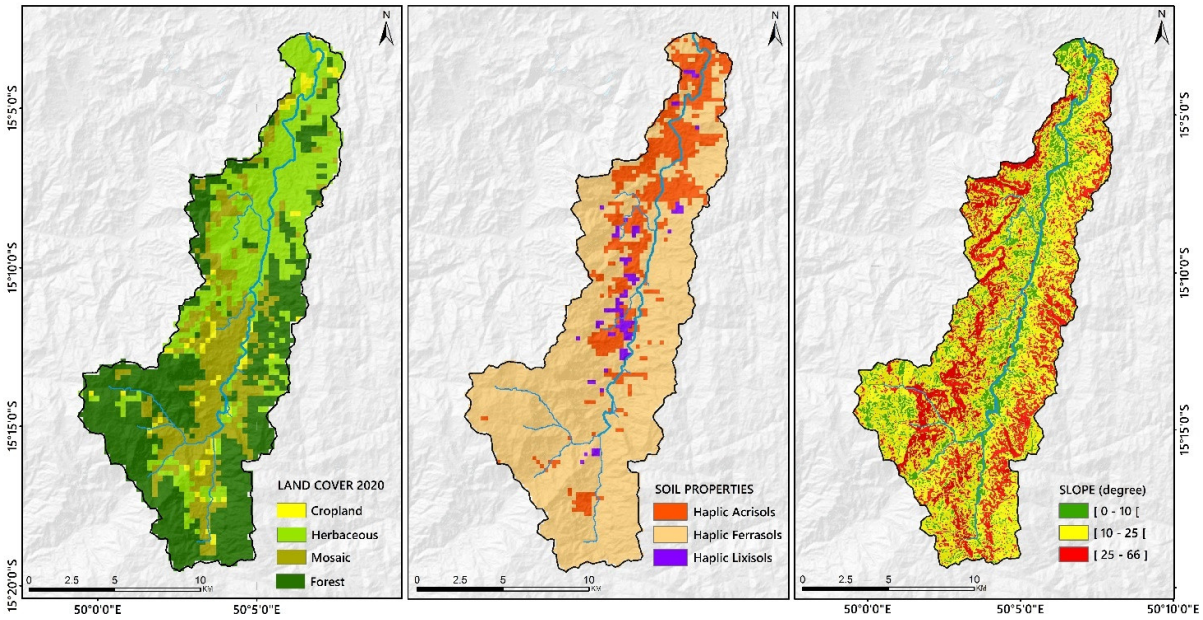

(a) (b) (c)

Figure 7. 2. Characteristics of the Sahafihitry catchment: (a) 2020 Land cover, (b) Soil properties, (c) Slope.

7.2.4. Hydrological modelling: SWAT semi-distributed model

7.2.4.1. Model description

The SWAT model is used in this study. This hydrological model is a widely used hydrological model that operates on a continuous daily time scale or greater (Arnold et al. 2012). It is a semi-distributed model that is coupled with a Geographic Information System interface. Besides daily weather and hydrological data (see section 7.2.2.), SWAT uses data on land cover, soil, and slope properties (Figure 7.2). The watershed is then divided into Hydrologic Response Units (HRUs), which are composed of areas with homogeneous land cover, soil, and slope characteristics. The hydrological components of the SWAT model are linked through the water balance equation (Chapter 2, section 2.5, Equation 2.7).

7.2.4.2. Sensitivity Analysis, Calibration and Validation

The Sequential Uncertainty Fitting version 2 (SUFI-2; Nkonge et al., 2014; Wu and Chen, 2015) available in the SWAT-Calibration and Uncertainty Programs (SWAT-CUP; Abbaspour, 2015) was used to calibrate the model for the diverse scenarios (see section Scenarios below). The Nash-Sutcliffe efficiency (NSE) index was adopted as an objective function during the auto-calibration process (See Table 7.2. below).

Model parameters were calibrated using observed streamflow data from August 2018 to July 2020, and the calibrated models were validated using streamflow data from August 2020 to July 2021. Since only three years of discharge data were available, the August 2020 – July 2021 data served as both the validation and warm-up period, although they were not used for calibration.

For each scenario, a set of 10 key parameters governing hydrological processes was selected for model calibration and validation. CN2 is associated with the runoff generation process, while SOL_AWC regulates soil water content. The parameter set related to groundwater flow includes GW_DELAY, GWQMN, SHALLST, DEEPST, GW_REVAP, RCHRG_DP, GWHT, and GW_SPYLD (Table 7.1). The initial parameter ranges and the selection of these parameters were determined through a comprehensive literature review and prior knowledge.

Table 7. 1. Description of the parameters used in the calibration process, their possible range, the initial value as well as the optimum values after calibration using the 1RG, 2RG, 5RG and IMERG rainfall scenarios (see section Scenarios below).

Parameters	Description	Range		Initial value	1RG	2RG	5RG	IMERG
		Min	Max					
1: CN2	Multiplication factor for SCS runoff curve number	0	1	0.5	0.506	0.563	0.545	0.834
2: SOL_AWC	Multiplication factor for available water capacity of the soil layer	0	1	1	0.774	0.649	0.686	0.879
3: GW_DELAY	Groundwater delay (days)	0	450	31	367	58	72	70
4: GWQMN	Threshold depth of water in the shallow aquifer required for return flow to occur (mm)	0	5000	1000	1097	922	4982	1572
5: SHALLST	Initial depth of water in the shallow aquifer (mm)	0	5000	1000	802	2442	1002	2697
6: DEEPST	Initial depth of water in the deep aquifer (mm)	0	10000	2000	8115	7725	5275	9555
7: GW_REVAP	Groundwater "revap" coefficient	0.02	0.2	0.02	0.081	0.105	0.113	0.120
8: RCHRG_DP	Deep aquifer percolation fraction	0	1	0.05	0.3	0.4	0.9	0.8
9: GWHT	Initial groundwater height (m)	0	25	1	6.4	22.0	12.0	6.3
10: GW_SPYLD	Specific yield of the shallow aquifer ($m^3 m^{-3}$)	0	0.4	0.003	0.3	0.2	0.2	0.3

7.2.4.3. Scenarios

To assess the hydrological performance for different rainfall data sources, five rainfall scenarios were implemented in SWAT. The first three scenarios (1RG, 2RG, 5RG) utilize the ground-based rain gauges spatialized using the Thiessen method. Specifically, scenario 1RG relies on data from the catchment's central rain gauge (No. 3; Figure 7.1), while scenario 2RG uses data from rain gauges No. 2 and No. 5. Scenario 5RG, which serves as the reference scenario, uses data from all five rain gauges. The choice of these specific gauges was based on their spatial distribution. These scenarios seek to evaluate potential accuracy loss when reducing rain gauges from 5 to 2 and to 1. The fourth scenario relies on IMERG gridded precipitation products. For each of these four scenarios, all parameters are specifically calibrated. The final scenario, referred to as IMERG_in_5RG, involves the use of IMERG rainfall data using the optimized parameters derived from the 5RG scenario. This last scenario seeks to assess the possible loss in performance when using IMERG rainfall data in a model calibrated using ground-based data.

7.2.4.4. Hydrological model performance

The performance of the hydrological model was assessed using five continuous quantitative metrics: the coefficient of determination (R^2), the slope of regression (a), Nash-Sutcliffe efficiency (NSE), the Root-Mean-Square Error (RMSE), and the Kling-Gupta Efficiency (KGE) (Table 7.2). These metrics, especially NSE, RMSE and KGE, were also applied to evaluate the ability of the model to reproduce different discharge classes (>5, >10, >15, >20, and >50 $m^3 s^{-1}$).

Table 7. 2. Statistical metrics used for evaluating the SWAT model performance.

Name/Symbol	Formula	Optimal value
Coefficient of determination/ R^2	$R^2 = \left(\frac{\sum_{i=1}^{n}[(Qmi - \bar{Q}m)(Qsi - \bar{Q}s)]}{\sqrt{\sum_{i=1}^{n}(Qmi - \bar{Q}m)^2 \sum_{i=1}^{n}(Qsi - \bar{Q}s)^2}} \right)^2$	1
Slope of linear regression/ a	Qs=a(Qm) + b	1
Nash-Sutcliffe efficiency/ NSE	$NSE = 1 - \frac{\sum_{i=1}^{n}(Qmi - \bar{Q}si)^2}{\sum_{i=1}^{n}(Qmi - \bar{Q}m)^2}$	1
Root-Mean-Square Error/ RMSE	$\mathrm{RMSE} = \sqrt{\frac{\sum_{i=1}^{n}(\mathrm{Qm}i - \mathrm{Qs}i)^2}{n}}$	0
Kling-Gupta Efficiency/ KGE	KGE = 1 - $\sqrt{(CC-1)^2 + \left(\frac{\sigma s}{\sigma m} - 1\right)^2 + (\frac{\bar{Q}si}{\bar{Q}mi} - 1)^2}$	1

Qm is the measured discharge, Qs is the simulated discharge, $\overline{Q}$m is the average measured discharge, $\overline{Q}$s is the average simulated discharge, σm is standard deviation of measured discharge, σs is standard deviation of simulated discharge, and CC = R is the Pearson coefficient value.

7.3. Results

7.3.1. Rainfall characteristics

The coefficient of variation computed from 5RG data consistently exceeds that derived from IMERG for each of the three periods, indicating a greater degree of spatial variability in the 5RG data compared to the IMERG data (Table 7.3).

The cumulative rainfall curves for 1RG, 2RG, and 5RG scenarios are very similar, reaching up to 7200 mm over the three-year study period (Figure 7.3). The cumulative IMERG curve is notably lower, especially as from 04/01, and totaling only 5000 mm over the three years.

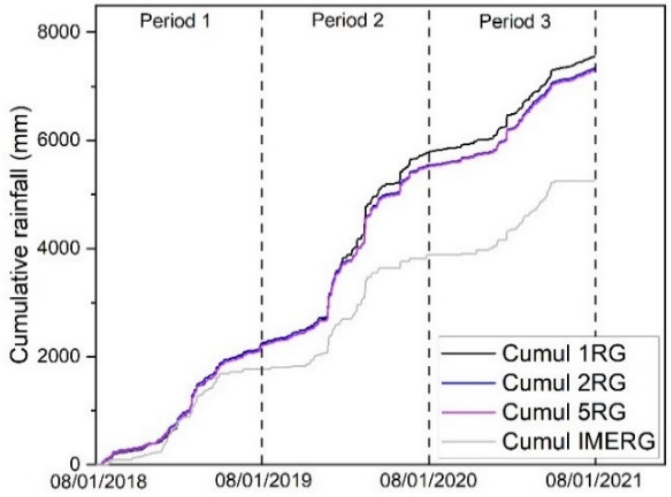

Figure 7.3. Mean cumulative rainfall for one rain gauge (1RG), two rain gauges (2RG), five rain gauges (5RG) and IMERG satellite-based precipitation data. The date on the X-axis is in MM/DD/YYYY format.

Table 7. 3. Cumulative rainfall and average coefficients of variation (CV) between the five ground-based rain gauges (5RG) and eight IMERG grids across the Sahafihitry watershed for three successive years.

Period (MM/DD/YYYY)	CV 5RG (%)	Cumulative rainfall 5RG	CV IMERG (%)	Cumulative rainfall IMERG
Period 1 (08/01/2018 – 07/31/2019)	71.9	2100	70.2	1721
Period 2 (08/01/2019 – 07/31/2020)	73.8	3350	62.9	2121
Period 3 (08/01/2020 – 07/03/2021)	63.4	1806	60.3	1370

Numerous events occurred in the region over the study period. The onset of extreme events is predominantly observed in January and extends until April. Less intense rainfall events are noted annually from April to November. When analyzing the cumulative curves seasonally, a consistent pattern emerges in the RG curves across all seasons (Figure 7.4). Throughout the 'wet' rainy season (November to April), the cumulative RG and IMERG rainfall curves are strikingly similar for the first and third rainy seasons. However, in the second 'wet' rainy season, the IMERG curve consistently underestimates rainfall by approximately 720 mm. Similarly, during the observed 'dry' rainy seasons throughout the study period, the IMERG data consistently underestimates rainfall, by around 440 mm on average.

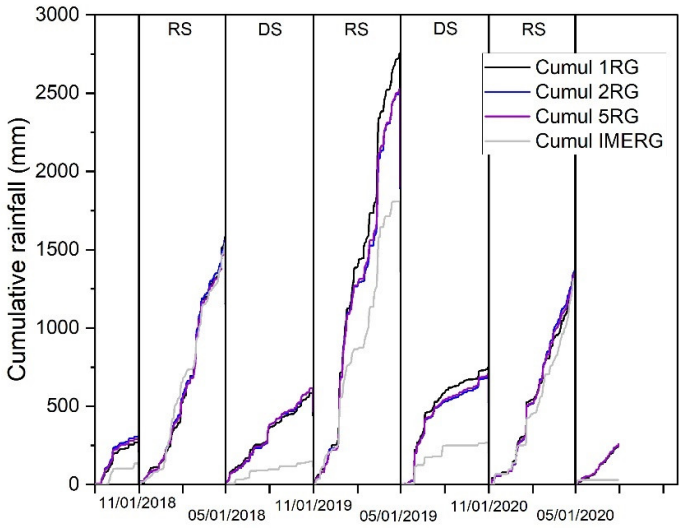

Figure 7.4. Cumulative rainfall for one rain gauge (1RG), two rain gauges (2RG), five rain gauges (5RG) and IMERG satellite-based precipitation data based on 'wet' rainy season (RS) and 'dry' rainy season (DS). The date on the X-axis is in MM/DD/YYYY format.

7.3.2. Streamflow characteristics

The cumulative discharge curve reached 4500 mm over the study period. The discharge curve rises in tandem with rainfall, except during period 1 when the rainfall escalates but the discharge exhibits a delayed ascent (Figure 7.5a). On a yearly basis, the difference between cumulative rainfall and cumulative discharge at the end of period 1 is 1320 mm, while for periods 2 and 3, it stands at 882 mm and 568 mm, respectively (Figure 7.5b).

7.3.3. Rainfall-runoff model performances

7.3.3.1. Overall performance

Optimal parameter values for the 1RG, 2RG, 5RG and IMERG scenarios are provided in Table 7.1 following calibration. Overall, the observed vs. measured discharge data cloud exhibits greater dispersion for the 1RG scenario than for the 2RG and 5RG scenarios (Figure 7.6). In particular, the model has great difficulty in reproducing the low flows (< 10 $m^3 s^{-1}$) based on the rain gauge located at the center of the watershed (1RG scenario). In addition, there is a slight overestimation in the flow classes from 10 $m^3 s^{-1}$ to 50 $m^3 s^{-1}$ for the 1RG, 2RG, and 5RG scenarios.

There is also a much greater dispersion in the data for the IMERG scenario compared to the RG scenarios (Figure 7.6). The 1RG, 2RG, and 5RG scenarios outperform the IMERG scenario, as evidenced by their higher R^2 values, regression slopes closer to 1, NSE and KGE values closer to 1, and RMSE values closer to 0. The observed flows in the <10 $m^3 s^{-1}$ flow class are underestimated when using 1RG and IMERG precipitation data.

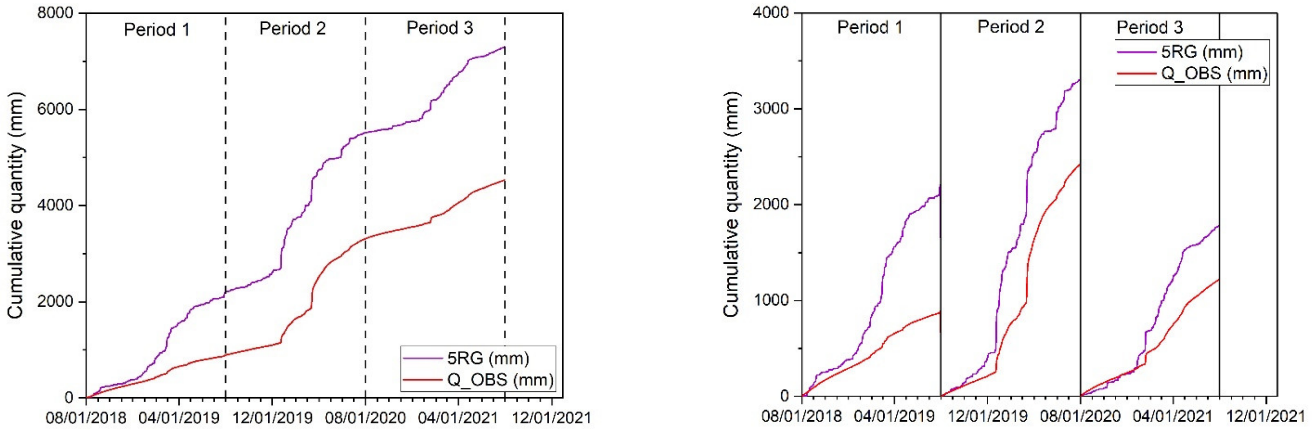

(a) (b)

Figure 7.5. Cumulative rainfall (5RG) and discharge (Q_OBS) curves of the Sahafihitry watershed over (a) the entire study period and (b) on an annual basis.

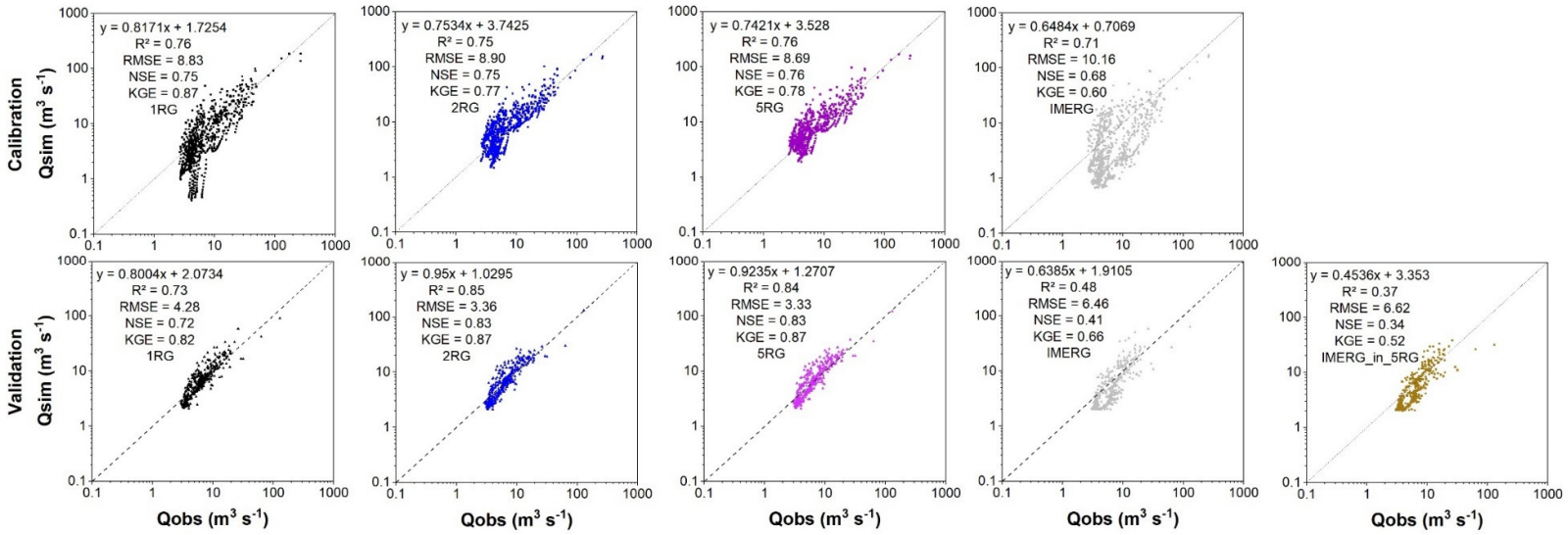

Figure 7.6. Plots of observed and simulated daily flows for the 5 rainfall-runoff scenarios (from the left to the right: 1RG, 2RG, 5RG, IMERG) for the calibration period (top, from 08/2018 to 07/2020) and validation period (bottom, 08/2020 – 07/2021). The last scenario (IMERG_in_5RG) corresponds to the model calibrated using 5 rain gauges but run with IMERG data for the validation period. Note logarithmic (Log10) scale for Y and X axis.

For the validation period, the dispersion of data is less pronounced than during calibration, yet the 1RG/2RG/5RG scenarios still exhibit less scatter than the IMERG scenario. Additionally, the value of the statistical parameters (correlation coefficient, R^2, NSE, KGE approaching 1, and RMSE nearing 0) indicate that the 2RG/5RG scenarios outperform the 1RG and IMERG scenarios (Figure 7.6 and 7.7). Running the model with IMERG data after calibration with 5RG data (IMERG_in_5RG) results in an overall degradation of the model performance compared to the 5RG and IMERG scenarios (Figure 7.6 and 7.7).

7.3.3.2. Performance across discharge classes

RMSE values tend to rise as the flow rate class increases for both calibration and validation periods (Figure 7.8a). NSE and KGE values remain fairly constant for most scenarios except for discharges > 50 $m^3 s^{-1}$ for which a sharp drop in these values is observed (Figure 7.8b and 7.8c). For the IMERG and IMERG_in_5RG scenarios, NSE and KGE values tend to decline steadily as the flow rate class increases. In the calibration phase, RMSE and NSE values are generally comparable across all scenarios, but notable distinctions emerge during the validation phase. Conversely, while KGE values for the 1RG scenario slightly outperform those for 5RG and 2RG, they marginally decrease in the IMERG scenario compared to RG scenarios. Based on RMSE and NSE values in the validation phase, the scenarios rank in decreasing order of performance as 5RG, 2RG, 1RG, IMERG, and IMERG_in_5RG. According to KGE values, the ranking is 2RG, 5RG, 1RG, IMERG, and IMERG_in_5RG.

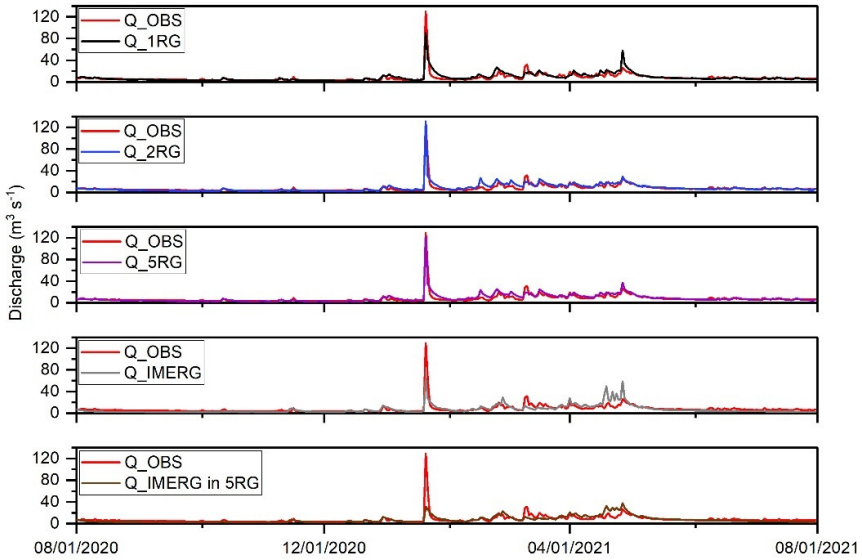

Figure 7.7. Comparison of observed (Q_OBS) and simulated hydrographs for the validation period (08/2020-07/2021) at the Sahafihitry station for the 5 rainfall-runoff scenarios. Model calibrated using one rain gauge (Q_1RG), 2 gauges (Q_2RG), 5 gauges (Q_5RG) or IMERG data (Q_IMERG). The last scenario corresponds to the model calibrated using 5 rain gauges but run with IMERG data for the validation period (IMERG_in_5RG).

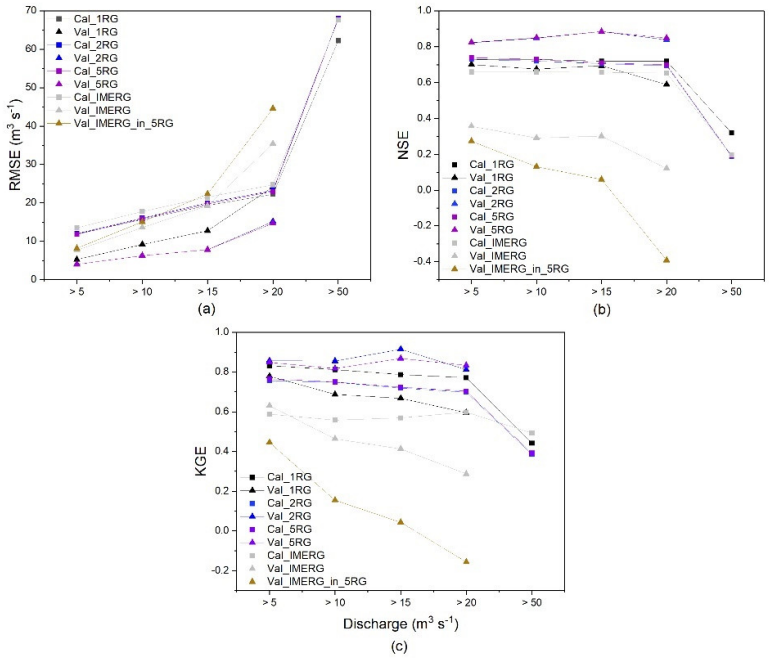

Figure 7.8. (a) Root Mean Square Error (RMSE), (b) Nash Sutcliffe Efficiency coefficient (NSE) and (c) Kling-Gupta efficiency (KGE) for various classes of discharge for the 5 rainfall-runoff scenarios. Model calibrated using one rain gauge (1RG), 2 gauges (2RG), 5 gauges (5RG) or IMERG data (IMERG). The last scenario corresponds to the model calibrated using 5 rain gauges but run with IMERG data for the validation period (IMERG_in_5RG). Square markers refer to the calibration period, triangular markers refer to the validation period.

7.4. Discussion

7.4.1. Rainfall characteristics

During the study period, average rainfall aligned with the expected annual average of 2240 mm (2018 – 2021), although it was slightly below average in periods 1 and 3, and significantly above average in period 2 (Table 7.3). The study area displays also notable spatial variability in rainfall, as evidenced by the coefficients of variation observed across the five rain gauges. The spatial variability was most pronounced during the peak of the rainy season (period 2). Such variability was also observed in other parts of the region, particularly in the northeast of Madagascar (CREAM 2013; Chaperon et al. 1974).

The coefficients of variation derived from the rain gauge dataset consistently exceed those obtained from the IMERG dataset. This can partly be attributed to the inherent difference in data nature, with 5RG representing point-based observations and IMERG relying on gridded data (Huffman et al. 2020, 2015). While IMERG accurately captures rainfall during typical rainy seasons, its performance diminishes during exceptionally wet seasons due to challenges in detecting rainfall events exceeding 100 mm day^{-1}, leading to a significant underestimation of rainfall amounts (Ramahaimandimby et al. 2022; Tan and Duan 2017). Additionally, during less rainy periods like the 'dry' season, a notable gap emerges between observed cumulative rainfall and IMERG-reported values, attributed to IMERG's tendency to underestimate the low-intensity rainfall events that prevail during that season (Randriatsara et al. 2022b; Ramahaimandimby et al. 2022; CREAM 2013).

7.4.2. Hydrological usefulness of precipitation data

In this study, we assessed the performance of four precipitation datasets in the SWAT model: data from 1, 2 or 5 RG, or IMERG precipitation data. These datasets differ in their measurement methods, detection accuracy, and spatial representation of precipitation, which resulted in substantially different discharge simulation results.

In hydrological analyses involving RG scenarios, utilizing 2RG or 5RG outweighs that of using a 1RG for discharge simulation. With a single rain gauge, there is a tendency to underestimate flow classes < $10m^3\ s^{-1}$, a phenomenon not observed when multiple rain gauges are utilized (Figure 7.6, calibration). Similarly, the use of a single rain gauge leads to a decline in indicators (R^2, RMSE, NSE, KGE), which is largely attributable to the underestimation of high flow classes >$100m^3\ s^{-1}$ (Figure 7.6, validation). Integrating multiple RGs enhances spatial coverage, facilitating a comprehensive capture of rainfall variability across the study area. This is particularly crucial in tropical regions characterized by significant rainfall variation over short distances, attributed to factors like topography, land cover, and local weather patterns (Leigh 1975; Chaperon et al. 1974) (section 7.4.1). Additionally, the use of multiple rain gauges offers a larger dataset, enabling the mitigation of errors or biases inherent in individual measurements, thereby providing more reliable estimates of rainfall inputs for hydrological models (Bayat et al. 2019; Gosset et al. 2013). Conversely, sole reliance on a single RG may result in inaccurate representation of this variability, introducing uncertainties into hydrological modeling outcomes. This observation is supported by existing literature, where the spatial variability of precipitation input significantly influences the performance of runoff simulations (Hohmann et al. 2020).

The results obtained from the study highlight the superiority of ground-based rain gauge data, particularly from multiple gauges, over satellite-derived IMERG data in hydrological modelling. Other studies have also highlighted the limited applicability of IMERG satellite-based rainfall estimates in flood and low-water forecasting (Getirana et al. 2020). This limitation mainly arises from the tendency of IMERG products to underestimate rainfall rates by 12 - 35% (mostly for very low and very high rainfall intensities) and their low spatial variability at the catchment scale (Ramahaimandimby et al. 2022; Huffman et al. 2020). IMERG products tend to smooth precipitation values due to their gridded nature and size, which averages precipitation values within each grid cell (Huffman et al. 2020).

The use of a potentially limited rating curve for high flows (section 7.2.2.), combined with uncertainties in IMERG data, may introduce significant biases in flood estimations, particularly during extreme events like the 2020 rainy season (Table 7.3). This can lead to a decline in performance metrics (such as NSE and KGE) and inaccurate flood simulations, especially during peak flows (Figure 7.7). Additionally, relying solely on Nash-Sutcliffe efficiency (NSE) during self-calibration might oversimplify model performance evaluation (section 7.2.4.). While NSE helps mitigate mean errors and variances, it may overlook deviations during floods and low flow periods, as highlighted by Krause et al. (2005). Consequently, the model could exhibit satisfactory statistical performance (acceptable NSE and KGE values) but fail to capture the intricacies of extreme events. This could lead to an underestimation of flood risks and inadequate preparedness measures for future events.

7.4.3. Implication of the selection of precipitations datasets in streamflow simulation

The study underscores the crucial importance of adjusting model parameters before integrating rainfall data into the hydrological model, especially considering the diminished reliability of the IMERG_in_5RG scenario compared to the IMERG scenario. While calibration based on IMERG rainfall data yields improved results compared to IMERG_in_5RG, this raises concerns about the physical significance of these parameters. Ideally, hydrological model characteristics should not be contingent on rainfall data sources, emphasizing the necessity of ensuring that model parameters maintain their physical interpretation despite variations in rainfall input data (Musy 2004). However, there may be instances where the calibrated parameter values exceed their reasonable ranges (Jiang et al. 2018; Yuan et al. 2018). Consequently, the recalibrated model may feature parameter values that do not accurately represent real-world features, potentially compromising the model's predictive capability in internal basins.

7.5. Conclusion

Motivated by the need for a cost-effective and efficient system observatory that can provide reliable hydrological data, we investigated the performance of four configurations of precipitation datasets: 1RG/2RG/5RG (see Scenarios in section 7.2.4) and IMERG, as inputs to the SWAT model for daily streamflow simulation. The study was conducted in the Sahafihitry watershed (~200 km²), a medium-sized tropical mountainous watershed in northeast Madagascar.

Our findings can be summarized as follows:

- The utilization of a network of multiple rain gauges offers a more accurate depiction of the spatial variability of precipitation in tropical mountainous regions, surpassing the representation provided by a single rain gauge or IMERG satellite-based precipitation data.
- The performance of the SWAT model, driven by four different precipitation datasets, decreased in the order 5RG > 2RG > 1RG > IMERG, indicating the effectiveness of a denser network for capturing rainfall variability in high-altitude watersheds.
- Rain gauge scenarios performed better for accurate flood and low-flow forecasting.
- Despite underestimating extreme precipitation and peak flow, IMERG achieved quite good performance based on statistical indicators. However, its application as input data for hydrological applications comes with several limitations, including the physical significance of the parameters.
- While IMERG data are readily available at low cost, its lower performance in hydrological modeling introduces significant uncertainty into the results. In comparison, the 2RG network configuration achieved satisfactory streamflow simulation and remains the most cost-effective option for establishing reliable hydrological observatories in this particular study area, considering its characteristics.

These results may only be applicable to watersheds with similar climatic conditions, soil properties, land cover, topography and scales as our study area. Therefore, caution should be exercised when applying these findings to other regions and it is recommended that further research be conducted in such areas to determine the most suitable configuration of rainfall networks for accurate streamflow modeling.

8. Chapitre 8 : Unraveling the impacts of land cover and climate changes on hydrological response of a tropical river basin: the case of the Sahafihitry catchment, Madagascar

Abstract:

Land-use change (LUCC) and climate change (CC) exert increasing pressure on hydrological systems, creating significant uncertainties for water resource managers and planners. While numerous studies address this issue, their findings are often context-specific and not readily generalizable, underscoring the need for research tailored to local conditions and ecosystems. Besides, very few studies have addressed this issue in the case of Madagascar. This study therefore aimed to quantify the hydrological alterations induced by expected LUCC and CC in the meso-scale Sahafihitry watershed (~200 km²), located in northeastern Madagascar. We analyzed the independent and combined impacts of future LUC and CC on hydrological responses (low flows Q95, mean daily discharge q mean, and high flows Q5) for the mid-term (2050) and long-term (2100) periods using the SWAT model calibrated on 3 years of daily discharge measurements. Future land use scenarios were simulated using the Cellular Automata-Markov chain approach, while climate data were generated from five Regional Climate Models under two Representative Concentration Pathway (RCP) scenarios: RCP 4.5 and RCP 8.5.

Results indicate a 47.9 km² (-24.5%) decline in forest area for the mid-term period and a 52.7 km² (-27%) decline for the long-term period compared to 1992 land cover, but a minor long-term increase in cropland area. Climate projections indicate increased precipitation during the rainy season, showing a trend toward more moderate rainfall and fewer extreme events. Concurrently, temperature projections suggest rises of 1-2°C for max temperatures and 1-3°C for min temperatures. While LUCC show limited effects on most flow indicators, displaying a slight decrease until 2010, their impacts remain stable over the subsequent period. Furthermore, the hydrological alterations observed under CC scenarios alone closely resemble those

under combined LUCC and CC scenarios. This similarity suggests a lack of significant interaction between LUCC and CC factors, with predicted CC effects largely overshadowing those of LUCC.

This research provides valuable insights for water resource management in the region, emphasizing the critical importance of integrating climate variability into future planning. The findings underscore the need to adapt hydraulic infrastructure and refine flood and drought management strategies in light of projected changes.

Keywords: hydrological alterations, land use changes, climate change, SWAT model.

8.1. Introduction

Natural resources, particularly water, face escalating pressures that have reached a critical juncture (Group et al., 2001). The rapid growth of the global population, projected to reach 9.7 billion by 2050 (Dorling 2021), coupled with the intensification of agricultural demand, primarily drive the current crisis (Ling, 2022; Jewitt, 2006; Group et al., 2001). The unprecedented demographic surge necessitates a significant expansion of habitable spaces and food production capacities, generating substantial anthropogenic pressures on the environment. Consequently, the world witnesses accelerated deforestation, severe soil degradation, and critical biodiversity loss (Di Marco et al. 2019; Clark 2012). Climate change further exacerbates environmental challenges, creating a feedback loop of increasing ecological stress (Mariotti et al. 2011; Change 2007). The combined pressures threaten the global water resources and the delicate balance of ecosystems worldwide, with far-reaching implications for food security, public health, and socioeconomic stability.

Resource managers and planners are facing significant uncertainty regarding future water availability due to the complex interplay between land use and land cover changes (LUCC) and climate change (CC) (Medina 2010; Group et al. 2001). LUCC

following deforestation can disrupt the natural water cycle, leading for instance to increased surface runoff, accelerated soil erosion, and enhanced sedimentation, while impeding groundwater recharge processes (Bruijnzeel 2004, 1988; Fritsch 1986). Concurrently, CC, characterized by rising temperatures and altered precipitation patterns, is projected to significantly modify surface and groundwater reserves, potentially amplifying the risk of hydrological hazards (Arnell and Lloyd-Hughes 2014; Tadross et al. 2008). The combined effects of LUCC and CC are particularly concerning, as they are likely to exacerbate extreme weather events, further straining already stressed water resources and ecosystems (Burgess et al. 2020).

Recent studies have shed light on the complex and diverse impacts of LUCC and/or CC on water resources. Systematic reviews by Kayitesi et al. 2022, Li et al. 2022, and Teuling et al. 2019 synthesized over 200 studies, revealing significant spatial and temporal heterogeneity in effects. These meta-analysis demonstrated that LUCC tends to exert more immediate and localized impacts on hydrology, while CC produces longer-term and larger-scale effects. For instance, deforestation in tropical watersheds has been associated with increased peak flows and decreased low flows in Southeast Asia (Bonell 2005). Regarding CC, a study by Gudmundsson et al. (2021) revealed a global trend of increasing mean flows in high latitudes and decreasing flows in dry subtropical regions. Moreover, Blöschl et al. (2019) identified changes in flood seasonality in Europe attributable to CC, with earlier floods in the northeast and later floods around the North Sea. The combined effects of LUCC and CC can be particularly pronounced in the Amazon basin, where deforestation coupled with rising temperatures has exacerbated drought periods, significantly reducing low flows (Hecht et al. 2021). On the other hand, Rogger et al. (2017) highlighted how agricultural intensification, combined with more intense precipitation due to CC, has amplified flood risks in certain regions of Central Europe, increasing the frequency and magnitude of flood discharges. This diversity of effects underscores the complex and non-additive interactions between stream flows, climate, and land use changes, making it challenging to generalize impacts across different regions and

necessitating an integrated, context-specific approach to water resource management.

Unraveling the intricate relationship between LUCC and CC impacts on water resources would be invaluable for developing robust water management strategies and adaptation plans (Milly et al. 2008; Poff et al. 2016). However, comprehensive assessments are hindered by the scarcity of studies that simultaneously evaluate both LUCC and CC effects on hydrological processes (Dey and Mishra 2017). Several key methodological challenges persist, among which disentangling climate change signals from land use impacts in observed hydrological changes (Montanari et al. 2013; Thompson et al. 2009), and reconciling scale mismatches between global climate models and local hydrological processes (Chen et al. 2011; Maraun et al. 2010). In tropical regions, these challenges are further compounded by significant data limitations, including insufficient long-term hydrometeorological records, sparse monitoring networks, and inadequate spatial coverage (Montanari et al. 2013; Wohl et al. 2012), which collectively hamper effective model calibration and validation. Moreover, many existing hydrological simulations operate at coarse temporal resolutions - typically annual or monthly time steps - which fail to capture the rapid hydrological responses characteristic of tropical watersheds and the fine-scale processes crucial for accurate assessments of water resource dynamics (Addor and Seibert 2014; Kayitesi et al. 2022).

Madagascar, a tropical island, exemplifies how environmental pressures affect diverse ecosystems and the associated ecosystem services. Current research examining these impacts has significant limitations in both methodology and scope, particularly regarding hydrological studies across its diverse watersheds. While Rabezanahary et al. (2021), Harrington et al. (2022); and Rabezanahary and Andrianarimanana (2024) conducted pioneering research on CC impacts on the Malagasy hydrological systems, their approach focused solely on CC effects without considering LUCC influences. Their analysis using annual time steps proves inadequate for small watersheds characterized by daily hydrological responses - the temporal scale at which water resource management typically operates.

Furthermore, Randriamaherisoa and Binard (1992) examined the specific hydrological responses to LUCC in the Lokoho watershed, demonstrating how forest conversion to agricultural lands led to increased surface runoff and reduced baseflow, though their analysis excluded CC considerations. Additionally, van Meerveld et al. (2021) quantified the impacts of LUCC on streamflow patterns in eastern Madagascar's rainforest regions, revealing significant alterations in seasonal flow regimes following forest clearance, but similarly to other studies, they did not account for potential CC effects in their assessment. These research gaps impair our understanding of the complex dynamics governing Madagascar's ecosystems and hydrological processes, particularly given the vulnerability of the island to these twin environmental challenges. Yet this quantification is crucial for developing sustainable water resource management strategies adapted to the Malagasy tropical context and, more generally, to tropical watersheds in similar environments, while effectively mitigating the effects of land use and climate change on hydrological processes.

Given the limited knowledge about the combined effects of LUCC and CC on tropical river hydrology and the site-specific nature of hydrological processes, the objective of this research was to assess the independent and combined impacts of future LUCC and CC scenarios on the hydrological responses of a tropical catchment. Our study focuses on the Sahafihitry catchment, a watershed situated in the humid tropical region of Madagascar (~200 km²) and confronted with challenges posed by deforestation, agricultural expansion, climate change, and a projected population growth of 260% by 2100 (Kaba 2020; Rasolofomanana 2016).

8.2. Materials and Methods

8.2.1. Study area

Study area is described in Chapter 7, section 7.2.1 (Figure 7.1).

8.2.2. Data collection

8.2.2.1. Spatial data

The land cover maps for the years 1992, 1995, 2000, 2005, 2010, 2015, and 2020 were derived from the 300-m resolution GlobCover v.2 dataset (Bontemps et al. 2009); Figure 8.1 & 7.2a), while soil attributes were obtained from the 250-m resolution SoilGRID global soil mapping (Deckers et al. 2010, Figure 7.2b). The catchment boundaries of Sahafihitry river basin, slope and hydrological structures were delineated using a 30-m resolution Digital Elevation Model (DEM) retrieved from the Shuttle Radar Topographic Mission (SRTM) (Earth Resources Observation And Science (EROS) Center 2017; Figure 7.1 & 7.2c).

8.2.2.2. Temporal data

Climate data

Although climate data (solar radiation, wind speed, relative humidity, maximum/minimum temperature, and atmospheric pressure) was collected at the Marofinaritra weather station (Figure 7.1), the records were restricted to the August 2018 - December 2021 period. Robust analysis of climate change effects requires at least 20 years of data. Accordingly, the on-site climate data record was not used in the present study. Similarly, although on-site raingauge data was available for the period encompassing the discharge measurements (2018 - 2021; see below), this data was not used in the present study for reasons explained in section 8.2.4.

Discharge data

Discharge data calculations are described in Chapter 3, section 3.4.2 and 3.4.3.

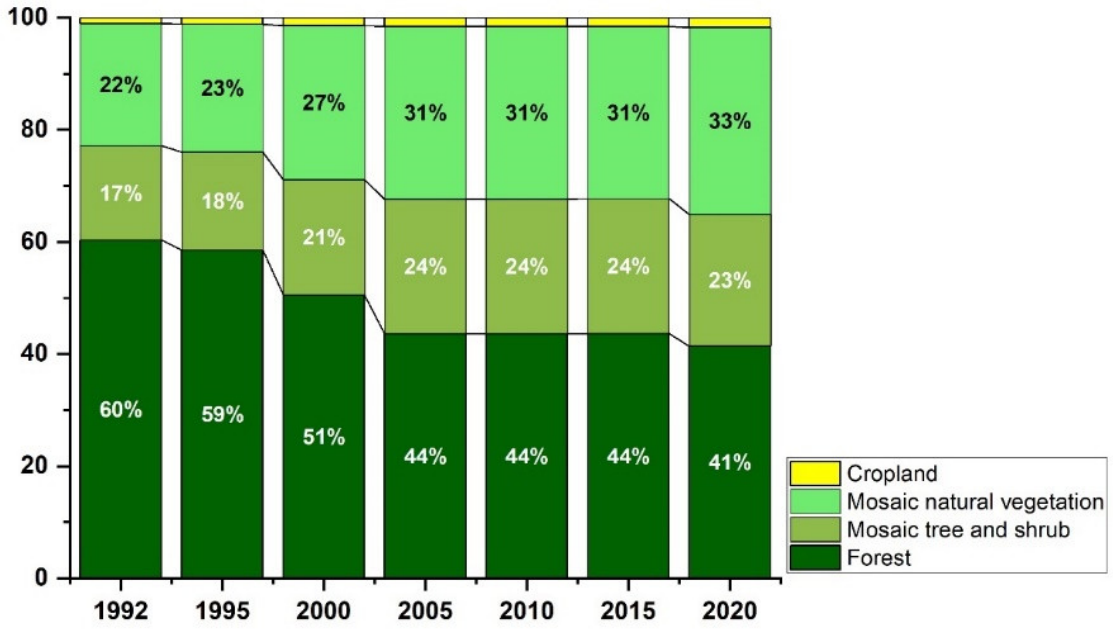

Figure 8. 1. Land use and land cover (LULC) alterations from 1992 to 2020 in the Sahafihitry catchment. Derived from GlobCover images (section 8.2.2.).

8.2.3. Scenarios analysis

8.2.3.1. Climate scenarios

Historical climate data and future climate projections

Future climate projections (2040-2060; 2080-2100) were compared against historical data (2001-2021). Historical daily climate data (solar radiation, wind speed, relative humidity, maximum/minimum temperature, and atmospheric pressure) for the 2001 – 2021 period were obtained from the NASA Earth Science Data Access System (https://power.larc.nasa.gov/data-access-viewer/, accessed on June 2023). For historical precipitation data, the Global Precipitation Measurement (GPM) mission's IMERG (Integrated Multi-satellitE Retrievals for GPM) datasets were utilized (Huffman et al. 2020; Table 8.1). These datasets provide high-resolution, multi-satellite precipitation estimates derived from a constellation of passive microwave sensors, supplemented by merged infrared fields from geostationary satellites. This approach ensures a consistent, long-term precipitation record spanning over 20 years. Furthermore, the reliability of IMERG data as a proxy for ground measurements across a wide spectrum of daily rainfall intensities has been demonstrated by Ramahaimandimby et al. (2022), thus substantiating the robustness of the historical dataset.

Future climate projections (2040-2060; 2080-2100) were based on data from the Coordinated Regional Climate Downscaling Experiment-Africa (CORDEX-Africa) framework (Hewitson et al. 2012). These projections are derived from dynamic downscaling of the ICHEC-EC-EARTH Global Climate Model (GCM), providing a refined spatial resolution of 0.44° x 0.44° (approximately 50 x 50 km). We selected five Regional Climate Models (RCMs) for their comprehensive precipitation data: the Rossby Center Regional Atmospheric model (RCA4), HIRHAM5, RACMO22T, REMO2009, and CCLM4 (Table 8.1). These RCMs were driven by two Representative Concentration Pathway (RCP) scenarios: RCP 4.5, a moderate stabilization scenario aiming to stabilize radiative forcing at approximately 4.5 W m^{-2} (roughly 650 ppm CO_2), and RCP 8.5, a high-emission scenario where radiative forcing increases to 8.5 W m^{-2} (roughly 1370 ppm CO_2). These data were obtained from the Earth System

Grid Federation (ESGF) Node at Lawrence Livermore National Laboratory (https://esgf-node.llnl.gov, accessed in June 2021). Besides the future climate projections data (2040-2060; 2080-2100), data for the historical 1980-2000 period was also downloaded. This data was used for bias correction, as explained below. Note that Cordex-Africa does not provide simulated historical rainfall and temperature data for the period 2001-2021.

Bias correction

Given the systematic deviations often observed between climate model outputs and observed data, we employed distribution mapping methods to correct simulated rainfall and temperature data. These methods seek to align the statistical distribution of the simulated historical rainfall and temperature data with that of observed data. This bias correction process, grounded in the methodology outlined by McGinnis et al. (2015), substantially improves the reliability of future precipitation projections. Unfortunately, as mentioned above, Cordex-Africa does not provide simulated historical rainfall and temperature data for the period 2001-2021 to be corrected against the corresponding 2001-2021 GPM-IMERG data. Likewise, the GPM-IMERG record does not cover the period 1980-2000 of the Cordex-Africa simulated historical rainfall data. Given this limitation, we corrected the Cordex-Africa data of the historical period 1980-2000 against the GPM-IMERG data of the historical period 2001-2021.

The correction is achieved using the Panofsky and Brier (1968) method, which involves creating a transfer function. This function transforms modeled values into probabilities using the cumulative distribution function (CDF) of the modeled values, and then converts these probabilities back into data values using the inverse CDF (or quantile function) of the distribution of observed data. This process can be expressed mathematically as equation (8.1).

$$x_{corrected} = tf(x_{raw}) = CDF^{-1}_{observed}\,(CDF_{model}(x_{raw})) \qquad (8.1)$$

where tf() is the transfer function and CDF is the cumulative distribution function.

Table 8. 1. Summary of spatial data and temporal data used to assess hydrological alterations in Sahafihitry catchment.

Data set	Resolution/ Scale (Date)	Source/ link (Accessed on June 2022)	Used parameters
Digital Elevation Model (DEM)	30 m	Shuttle Radar Topography Mission (SRTM) (https://earthexplorer.usgs.gov/)	Topographical, slope and physical properties
Land cover maps	300 m (1992, 1995, 2000, 2005, 2010, 2015, 2020)	GlobCover v.2 (http://due.esrin.esa.int/page_globcover.php)	Land cover classes
Soil map	250 m	SoilGRID (https://soilgrids.org/)	Soil classes
Discharge	Daily (2018 – 2021)	GIRE SAVA project	Discharge measured at the outlet of the Sahafihitry catchment
Climate	Daily (2001 – 2021)	(https://power.larc.nasa.gov/data-access-viewer/) (2001 – 2021)	Relative humidity, solar radiation, wind speed, temperature min and max, atmospheric pressure
IMERG Precipitation	0.1° x 0.1° Daily (2001 – 2021)	Integrated Multi-satellitE Retrievals for Global Precipitation Measurement (https://giovanni.gsfc.nasa.gov/giovanni/)	Daily precipitation
GCM-RCMs (RCA4, IRHAM5, CCLM4, RACMO22T, REMO2009)	0.44° Daily (1980 – 2000) (2040 – 2060) (2080 – 2100)	Downscaling Methods ICHEC-EC-EARTH (https://esgf-node.llnl.gov)	Projected daily precipitation, temperature

Climate change scenarios

The climate change simulations focused on two future periods: mid-term (2040-2060) and long-term (2080-2100), under both RCP 4.5 and RCP 8.5 scenarios. These were compared against a baseline period of 2001-2021. However, to isolate the effects of precipitation and temperature changes, other meteorological variables (solar radiation, relative humidity and wind speed) were held constant at their baseline values (McGinnis et al. 2015, Table 8.1).

8.2.3.2. Land use – land cover scenarios

Cellular Automata-Markov model

The Cellular Automata (CA)-Markov model is used to project future land-use/cover scenarios for both the mid-term (2050) and long-term (2090) timeframes. This model merges the strengths of spatial modeling with temporal forecasting capabilities. Cellular Automata excels in capturing spatial relationships, while the Markov Chain excels in predicting transitions between LULC states over time (Ghosh et al. 2017). To determine the likelihood of a LULC transition, the Markov Chain utilizes a transition probability matrix, which is calculated using Equation (8.2).

$$S_{(t+1)} = P \times S_{(t)} \tag{8.2}$$

where $S_{(t)}$ and $S_{(t+1)}$ are the land use/cover status at the time of t and t+1, respectively; P is the transition probability matrix in a state which is calculated as follows (Equation 8.3):

$$P = \|Pij\| = \begin{Vmatrix} P1,1 & P1,2 & \dots & P1,N \\ P2,1 & P2,2 & \dots & P2,N \\ \dots & \dots & \dots & \dots \\ PN,1 & PN,2 & \dots & PN,N \end{Vmatrix} \tag{8.3}$$

$$(0 \le P_{ij} \le 1)$$

P represents the transition probability matrix; P_{ij} stands for the probability of transitioning from current state i to state j in the next time step; where i = 1 to N and j = 1 to N, N is the total number of states.

The CA-Markov model predicts future LULC through a three-step process. First, using the Markov Chain model in TerrSet® software, a land cover transition matrix is developed, calculating the probability of each land cover class transitioning to another over a specified time period. Second, multi-criteria evaluation (MCE) is employed to create suitability maps for each land cover class. These maps incorporate various factors, including elevation, slope, proximity to urban areas and water bodies. Finally, the Cellular Automata model utilizes both the transition probability matrix and the suitability maps to predict the future land cover distribution for the desired timeframe (Ghosh et al. 2017).

Projected land cover/model performance

The model was initially calibrated by using the reference LULC maps from 1995 and 2010 to predict the LULC map for 2020. The simulated 2020 map was then validated against the actual 2020 LULC data to assess the model's accuracy using Kappa coefficients (Equation 8.4). After this validation, the derived transition probability matrix was utilized to project future LUCC scenarios for the mid-term (2050) and long-term (2090) timeframes.

$$Kappa = \frac{Po - Pc}{1 - Pc} \tag{8.4}$$

Where P_o represents the proportion of correctly simulated cells; P_c is the expected proportion correction by chance between the observed and simulated maps. A Kappa value of less than or equal to 0.5 indicates poor agreement; a value between 0.5 and 0.75 represents medium agreement; a value between 0.75 and 1 is considered as high level of agreement and a Kappa value of 1 indicates perfect agreement (Kraemer 2015).

8.2.4. Hydrological alterations analysis

8.2.4.1. Hydrological modelling

SWAT Model description

SWAT model is described in Chapter 7, section 7.2.4, 7.2.4.1.

Input rainfall data

This investigation employs IMERG products for direct calibration and validation of the hydrological model, rather than ground-based precipitation measurements. This approach is justified by several factors. Firstly, the projections in this study are corrected using IMERG as a reference, ensuring methodological consistency. Secondly, the scenario analysis requires a minimum of 20 hydrological years of data, while in situ measurements only span a 3-year period (2018-2021). IMERG provides a longer and more consistent time series to meet this requirement. Lastly, Ramahaimandimby et al. (under review) have shown that direct calibration with IMERG yields superior results compared to calibration with ground data and then implementing the model with IMERG data (Chapter 7).

Calibration and Validation, Sensitivity Analysis

This section is described in Chapter 7, section 7.2.4, 7.2.4.2 (Table 8.2).

Hydrological model performance

Five continuous quantitative metrics were employed to evaluate the performance of the hydrological model in simulating observed streamflow (Table 8.3). The evaluation was conducted on the complete discharge datasets, as well as on specific discharge classes of >2, >5, >10, >15, >20, and >50 $m^3 s^{-1}$.

Table 8. 2. Description of the parameters used in the calibration process, their possible range, the initial value as well as the optimum values after calibration using IMERG rainfall (see section 8.2.3).

Parameters	Description	Range		Initial value	Calibrated
		Min	Max		
1: CN2*	Multiplication factor for SCS runoff curve number	0	1	0.5	0.834
2: SOL_AWC	Multiplication factor for available water capacity of the soil layer	0	1	1	0.879
3: GW_DELAY	Groundwater delay [days]	0	450	31	70
4: GWQMN	Threshold depth of water in the shallow aquifer required for return flow to occur [mm]	0	5000	1000	1572
5: SHALLST	Initial depth of water in the shallow aquifer [mm]	0	5000	1000	2697
6: DEEPST	Initial depth of water in the deep aquifer [mm]	0	10000	2000	9555
7: GW_REVAP	Groundwater "revap" coefficient	0.02	0.2	0.02	0.12
8: RCHRG_DP	Deep aquifer percolation fraction	0	1	0.05	0.8
9: GWHT	Initial groundwater height [m]	0	25	1	6.3
10: GW_SPYLD	Specific yield of the shallow aquifer [$m^3 \cdot m^{-3}$]	0	0.4	0.003	0.3

*CN_cropland = 81; CN_Mosaic natural vegetation = 76; CN_Mosaic tree and shrub = 73; CN_forest = 70.

Table 8. 3. Statistical metrics to evaluate the hydrological model performance.

Name/Symbol	Formula	Optimal value
Coefficient of determination/ R^2	$R^2 = \left(\frac{\sum_{i=1}^{n}[(Qmi - \bar{Q}m)(Qsi - \bar{Q}s)]}{\sqrt{\sum_{i=1}^{n}(Qmi - \bar{Q}m)^2 \sum_{i=1}^{n}(Qsi - \bar{Q}s)^2}} \right)^2$	1
Slope of linear regression/a	*Qsi=a Qmi + b*	1
Nash-Sutcliffe efficiency/ NSE	$NSE = 1 - \frac{\sum_{i=1}^{n}(Qmi - \bar{Q}si)^2}{\sum_{i=1}^{n}(Qmi - \bar{Q}m)^2}$	1
Root-Mean-Square Error/ RMSE	$RMSE = \sqrt{\frac{\sum_{i=1}^{n}(Qmi - Qsi)^2}{n}}$	0
Kling-Gupta Efficiency/ KGE	$KGE = 1 - \sqrt{(CC - 1)^2 + \left(\frac{\sigma s}{\sigma m} - 1\right)^2 + (\frac{\bar{Q}si}{\bar{Q}mi} - 1)^2}$	1

Qm is the measured discharge, Qs is the simulated discharge, $\overline{Q}$m is the average measured discharge, and $\overline{Q}$s is the average simulated discharge, σm is standard deviation of measured discharge, σs is standard deviation of simulated discharge, and CC = R is the Pearson correlation coefficient value.

8.2.4.2. Simulations of the possible scenarios

Overall, twelve scenarios were simulated to evaluate the combined and separate impacts of LUCC and CC on the river basin in the mid-term (2038 - 2060) and long-term (2078 - 2100) timeframes (Table 8.4).

Table 8. 4. Separate or combined land cover and climate change scenarios considered in the present study.

		Land cover	Climate data	Scenario #
Separate effect	Land cover only	1992	2001 – 2021	1.1
		2010	2001 – 2021	1.2
		2050	2001 – 2021	1.3
		2090	2001 – 2021	1.4
	Climate change only	2010	2040 - 2060, RCP 4.5	2.1
		2010	2040 - 2060, RCP 8.5	2.2
		2010	2080 - 2100, RCP 4.5	2.3
		2010	2080 - 2100, RCP 8.5	2.4
Combined effect		2050	2040 - 2060, RCP 4.5	3.1
			2040 - 2060, RCP 8.5	3.2
		2090	2080 - 2100, RCP 4.5	3.3
			2080 - 2100, RCP 8.5	3.4

8.2.4.3. Indicator of hydrological alterations

Hydrological indicators were employed in this study to evaluate the extent of potential alterations. However, there is no universally agreed-upon set of hydrological indicators for studying the impacts of LUCC and CC at a watershed scale. Therefore, we assessed the extent of streamflow alterations by comparing three indicators: Q5 (the 5th percentile of flow, representing high flows), Q95 (the 95th percentile of flow, representing low flows), and q_mean (the mean daily discharge) for the 20-year simulated flows under each scenario.

8.3. Results

8.3.1. Climate model performance/ Projected climate change

Prior to bias correction (Figure 8.2a), the CCLM4, RACMO22T, and RCA4 models consistently overestimated GPM-IMERG precipitation throughout most of the annual cycle. In contrast, the REMO2009 and HIRHAM models exhibited a seasonal bias, underestimating precipitation during the wet season (November-April) and

overestimating it during the dry season (May-October). After applying bias correction techniques (Figure 8.2b), precipitation projections from all models, including their ensemble mean, show improved alignment with IMERG precipitation data, with the exception of January, for which rainfall is underestimated. For subsequent analyses, we utilize the ensemble mean.

Both in the medium and long term, precipitation classes ranging from 0 to 5 mm are projected to decrease, while classes between 5 and 100 mm are expected to increase. Precipitation classes exceeding 100 mm, however, exhibit a tendency towards a slight decline (Figure 8.3).

Analysis of projected precipitation patterns reveals significant seasonal variations in future climate scenarios compared to the IMERG baseline (Figure 8.4a). The wet season (December-April) generally exhibits pronounced precipitation increases, particularly in March and April, with some scenarios projecting a rise by >150 mm (Figure 8.4b). January and February show substantial decreases in precipitation across all future scenarios. Conversely, the (less rainy) “dry” season (May-November) maintains relatively stable precipitation levels, with slight decreases projected in some scenarios.

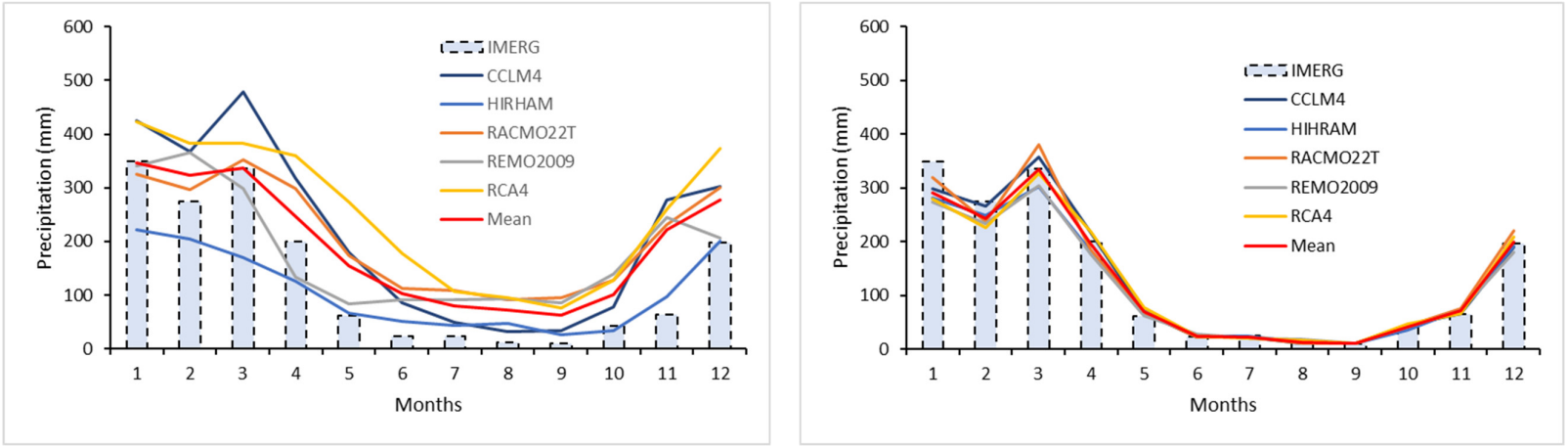

Figure 8. 2. Alignment of monthly simulated historical precipitation (CCLM4, HIRHAM, RACMOT22T, REMO2009, RCA4) and their ensemble mean over a twenty-year period (1980-2000) with monthly IMERG precipitation over a twenty-year period (2001-2021) (a) before and (b) after bias correction.

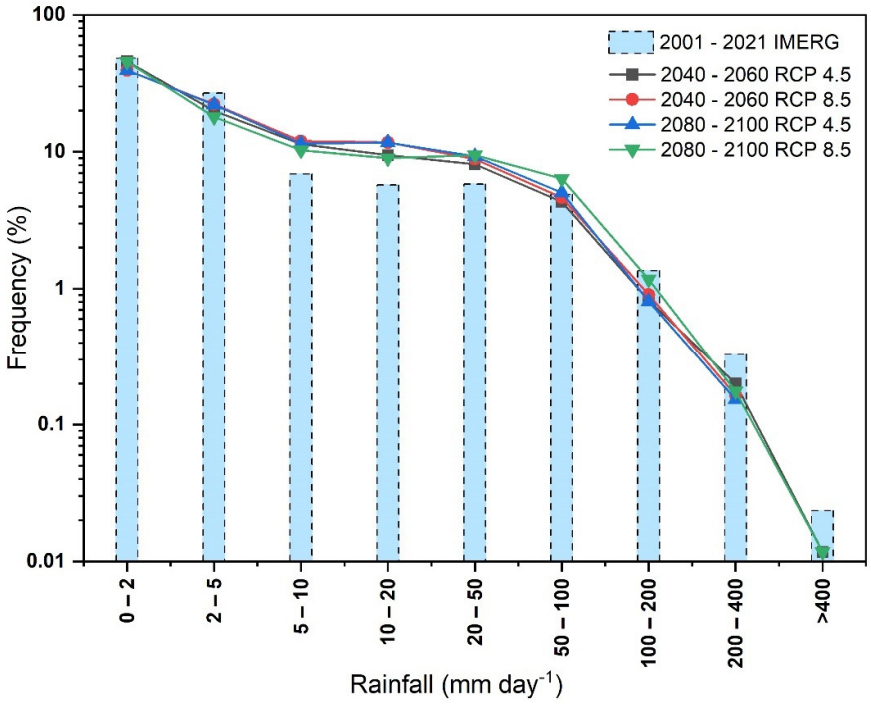

Figure 8. 3. Frequency distribution of daily precipitation intensities based on IMERG (2001-2021) and the ensemble mean of five regional climate model-generated precipitation for the mid-term (2040-2060) and long-term (2080-2100) periods under RCP 4.5 and RCP 8.5 scenarios. Note the logarithmic scale for the Y-axis.

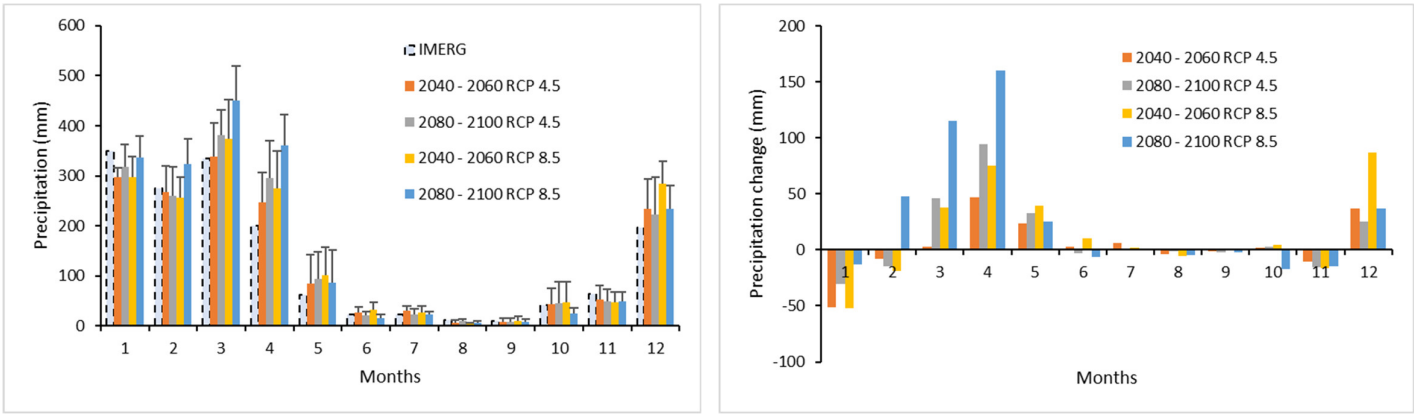

(a) (b)

Figure 8. 4. Projected precipitation patterns: (a) Monthly precipitation totals for IMERG baseline (2001-2021) and ensemble means of regional climate models for medium-term (2040-2060) and long-term (2080-2100) under RCP 4.5 and RCP 8.5; (b) Monthly mean (across climate models) precipitation changes (mm) relative to IMERG baseline for future scenarios. Error bars in (a) correspond to standard deviation across the five climate models.

Prior to bias correction (Figure 8.5a and 8.5b), all models exhibit trends similar to the observed maximum and minimum temperature data. With the exception of REMO2009 (and to some extent RCA4), all models underestimate the observed values. Upon application of bias correction techniques (Figure 8.5c), temperature projections from all models, including their ensemble mean, show excellent alignment with observed climate data.

Analysis of projected temperature changes reveals consistent increases across all months and scenarios compared to the 2001-2021 baseline, with variations in magnitude depending on the climate scenario and time period. Both maximum (Figure 8.6a) and minimum (Figure 8.6b) temperatures are expected to rise, with minimum temperatures showing more pronounced increases overall. The RCP 8.5 scenarios project larger temperature changes than RCP 4.5, particularly for the 2080-2100 period, where increases of 1-2°C for maximum temperatures and 1-3°C for minimum temperatures are common. The 2080-2100 period consistently shows greater warming than the 2040-2060 period across all scenarios. Maximum temperature increases are most significant in the later months of the year (October-December), while minimum temperature rises peak in the middle months (March-July).

8.3.2. CA Markov model performance and land use/land cover change projections

Land cover changes from 1992 to 2010 and projections for future scenarios in 2050 and 2090 are provided in Table 8.5 and illustrated in Figure 8.7. The CA-Markov model achieved a Kappa coefficient of 0.89 when comparing the simulated 2020 land cover map with observed data, indicating good agreement between predictions and reality. These projections suggest an increase in cropland, mosaic natural vegetation, and mosaic tree and shrub for both 2050 and 2090, while forest cover is expected to decrease.

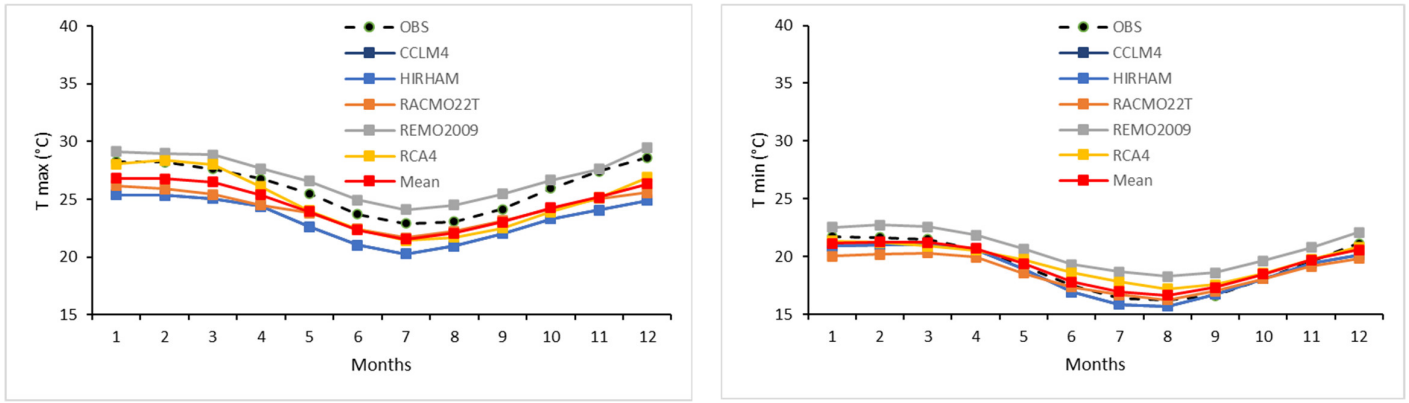

(a) (b)

Figure 8. 5. Alignment of monthly simulated historical temperature max and min (CCLM4, HIRHAM, RACMOT22T, REMO2009, RCA4) and their ensemble mean (1980-2000) with monthly observed temperature (2001-2021) (a,b) before and (c) after bias correction. See Table 8.1 for details.

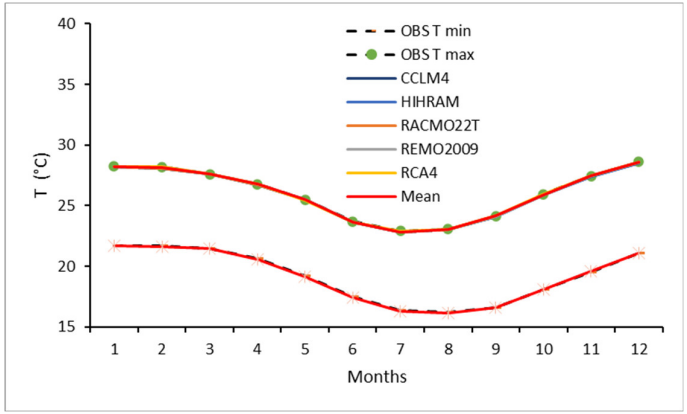

(c)

Figure 8. 5. (Cont.) Alignment of monthly simulated historical temperature max and min (CCLM4, HIRHAM, RACMOT22T, REMO2009, RCA4) and their ensemble mean (1980-2000) with monthly observed temperature (2001-2021) (a,b) before and (c) after bias correction.

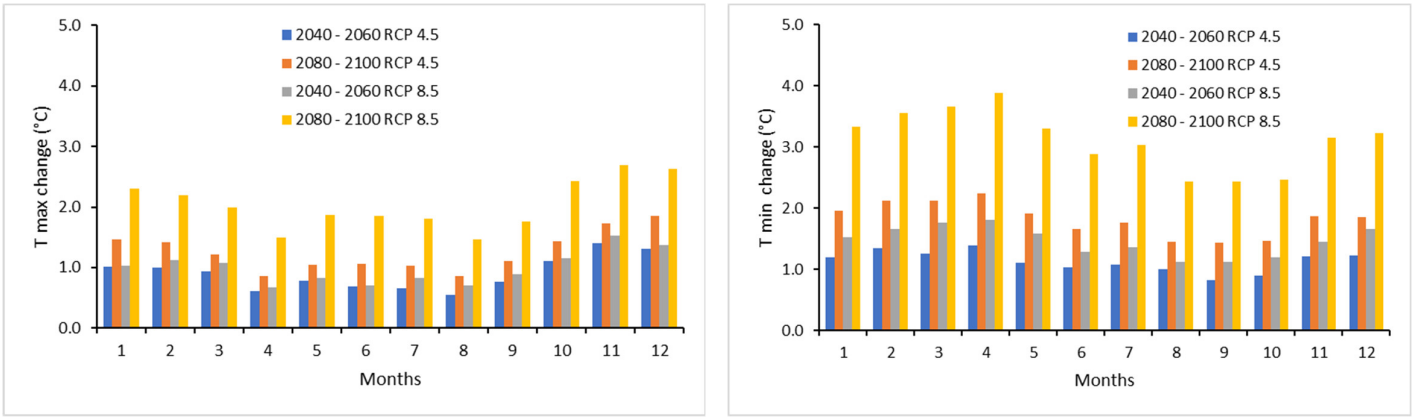

(a) (b)

Figure 8. 6. Projected monthly temperature changes (°C) relative to climate station baseline for future scenarios (a) maximum temperature, (b) minimum temperature. Error bars are not shown due to their negligible magnitude.

Table 8. 5. Land use and land cover in 1992, 2010, 2050 and 2090. Values between brackets express changes in LULC relative to 1992 (in %).

LULC Classes	**LULC 1992 km²**	**LULC 2010 km² (%)**	**LULC 2050 km² (%)**	**LULC 2090 km² (%)**
Cropland	4.4	6.1 (+0.9)	6.8 (+1.2)	6.8 (+1.2)
Mosaic natural vegetation	42.8	60.4 (+9.0)	68.4 (+13.1)	71.9 (+14.9)
Forest	118.1	82.0 (-18.5)	70.2 (-24.5)	65.4 (-27.0)
Mosaic tree and shrub	30.2	47.0 (+8.6)	50.1 (+10.1)	51.4 (+10.8)

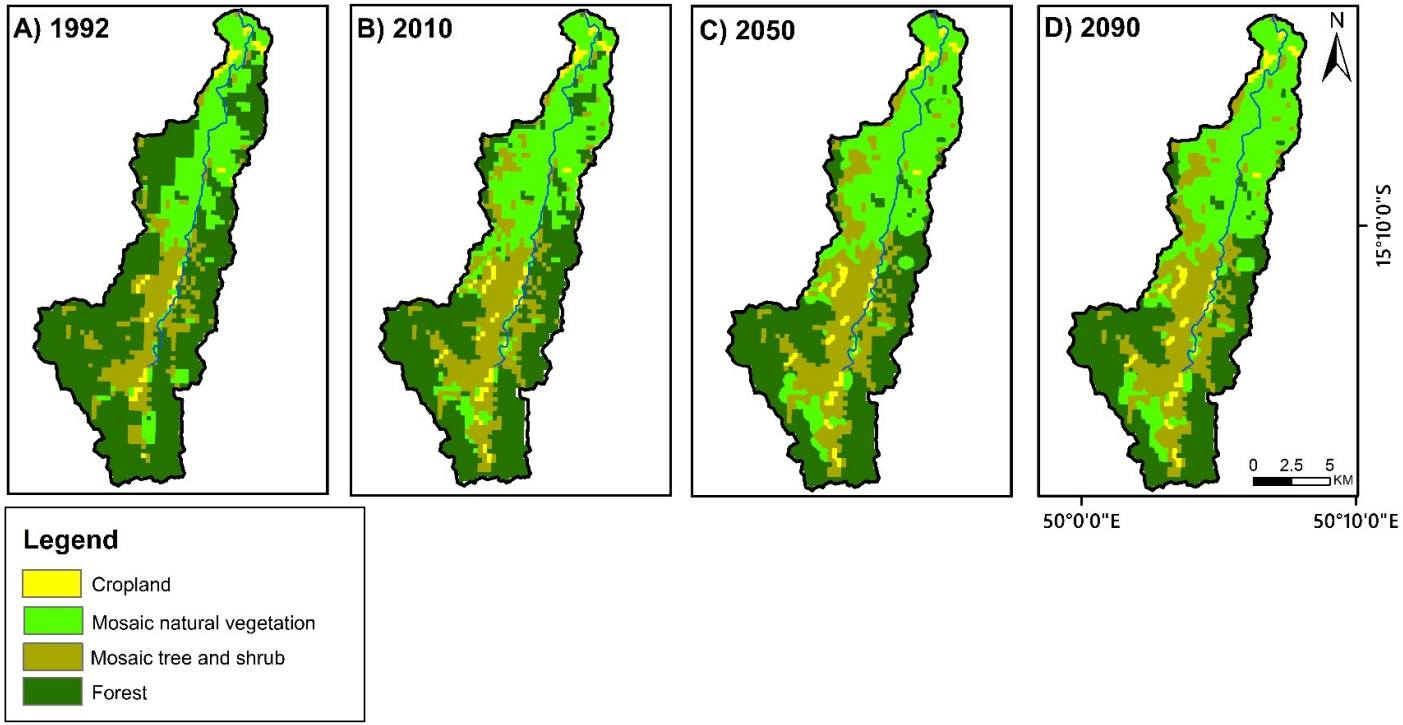

Figure 8. 7. Observed land use/land cover in the Sahafihitry catchment in 1992 and 2010; and predicted LULC for 2050 and 2090.

8.3.3. Hydrological model performance

In the first year of calibration (Figure 8.8a), flows were reasonably well simulated with a slight overestimation. The second year showed significant underestimation, especially during peak flows and recession periods. During validation (Figure 8.8b), the model generally reproduced well the observed flows but underestimated some peak flows while overestimating others.

The scatter plot of observed versus simulated flows shows greater dispersion during calibration (Figure 8.9a) than validation period (Figure 8.9b). The calibration period exhibits a slope and NSE closer to 1, while the validation period shows RMSE closer to 0 and KGE closer to 1.

For different flow classes (Figure 8.10), the RMSE is quite similar for flow classes <20 $m^3 s^{-1}$ in both the calibration and validation periods. It increases rapidly for flows >50 $m^3 s^{-1}$ during calibration period (Figure 8.10a). Metrics of model performance for flows <50$m^3.s^{-1}$ could not be calculated due to insufficient data in this range during validation. NSE values are consistently lower for validation than for calibration, with a sharp decline for flows >50 $m^3 s^{-1}$ during calibration (Figure 8.10b). KGE values remain relatively constant during calibration across all flow classes but progressively decrease during validation as flow magnitude increases (Figure 8.10c).

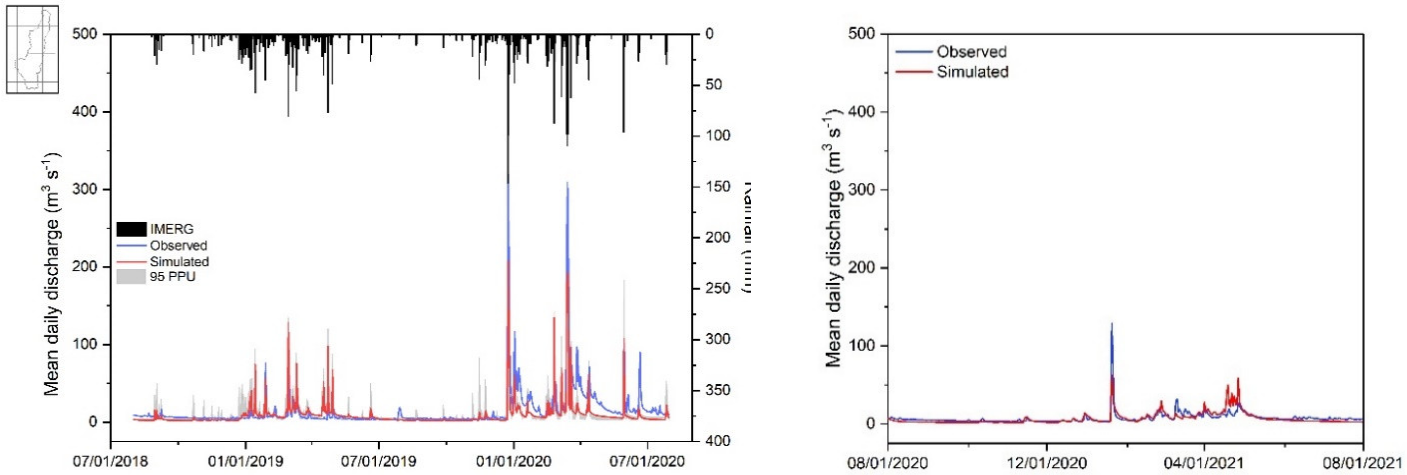

(a) (b)

Figure 8. 8. Comparison of observed and simulated mean daily discharge using SWAT model: (a) Calibration period (08/2018 – 07/2020) and (b) Validation period (08/2020 – 07/2021). 95 PPU indicates the 95th percentile prediction uncertainty.

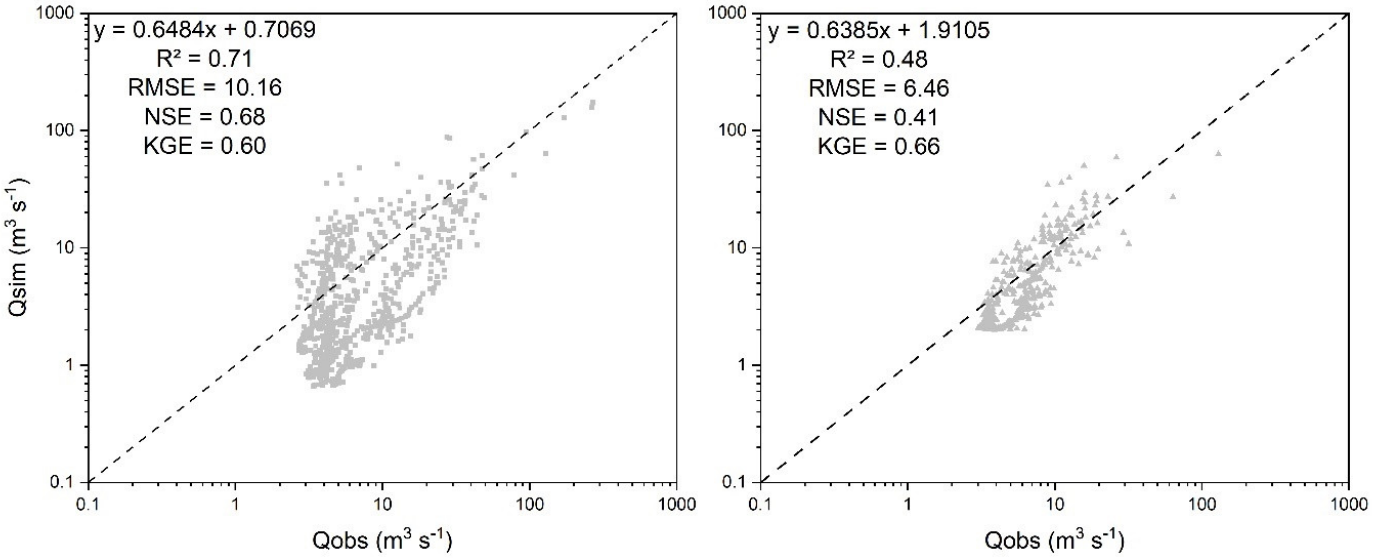

Figure 8. 9. Observed (Qobs) and simulated (Qsim) daily discharge obtained from the hydrological model for the (a) calibration period (08/2018 to 07/2020) and (b) the validation period (08/2020 – 07/2021). Note logarithmic (Log10) scale for X and Y axis. For metrics of model performance, see Table 8.3. Metrics are calculated on actual discharge values (not log-transformed).

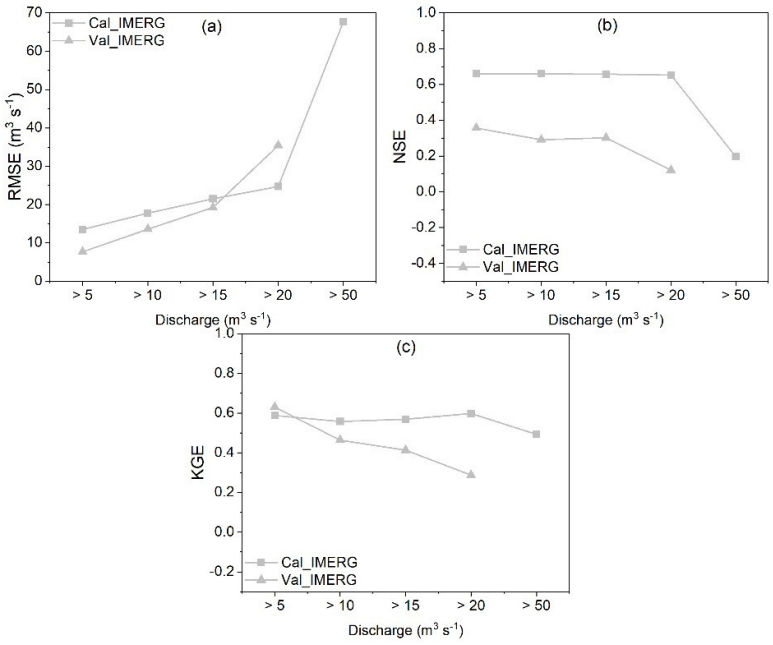

Figure 8. 10. (a) Root Mean Square Error (RMSE), (b) Nash Sutcliffe Efficiency coefficient (NSE) and (c) Kling-Gupta efficiency (KGE) for different classes of discharge for the SWAT model by IMERG rainfall data. Square markers refer to the calibration period (08/2018 to 07/2020), triangular markers refer to the validation period (08/2020 – 07/2021).

8.3.4. Hydrological alterations

Projected land use and land cover changes have little to no impact on average Q95, q_mean and Q5 compared to past land use (1992) under constant climatic conditions (2001-2020) (Figure 11; scenarios 1.1 to 1.4). However, for Q5, there is slight decrease in the upper bound (most extreme high flows) between scenarios 1.1 and 1.2, which remains stable thereafter (Figure 11c).

Projected climate changes, with (scenarios 3.1 to 3.4) or without (scenarios 2.1 to 2.4) land use and land cover changes, significantly impact average q mean and Q5 but not Q95. In the absence of LUCC, for RCP 4.5, there is a slight increase in average

q mean between the years 2010 and 2050, followed by a stronger increase thereafter (Figure 11b). For Q5, however, there is a slight decrease between the years 2010 and 2050, and a strong increase in 2090 (Figure 11c). For RCP 8.5, an increase in average q mean is observed between 2010 and 2050, with a slight increase thereafter. For average Q5, however, the increase is more pronounced between 2050 and 2090 than between 2010 and 2050.

When LUCC are combined with CC, the overall trends are essentially similar to those observed without LUCC alone, although some small differences can be observed, particularly a slight decrease in mean values for q mean and Q5.

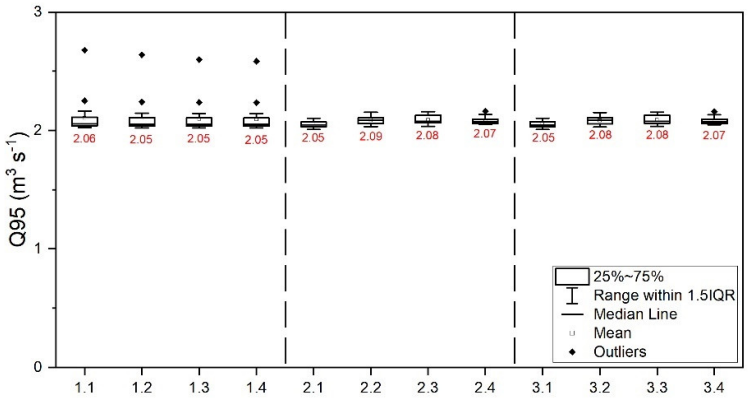

(a)

Figure 8. 11. Projected changes in streamflow characteristics based on simulations twenty hydrological years: (a) Q95 (95th percentile flow); (b) q_mean (mean daily discharge); (c) Q5 (5th percentile flow), under three scenarios: Scenario 1 : effect of land cover change only; Scenario 2 : effect of climate change only; Scenario 3 : combined effect of land cover and climate changes. Refer to Table 4 for details. Box edges correspond to the 25th (Q1) and 75th (Q3) percentiles. Whiskers extend to Q1-1.5QR (lower bound) and Q3+1.5IQR (upper bound), with IQR = Q3-Q1 (Inter-Quartile Range). Points outside the box are outliers.

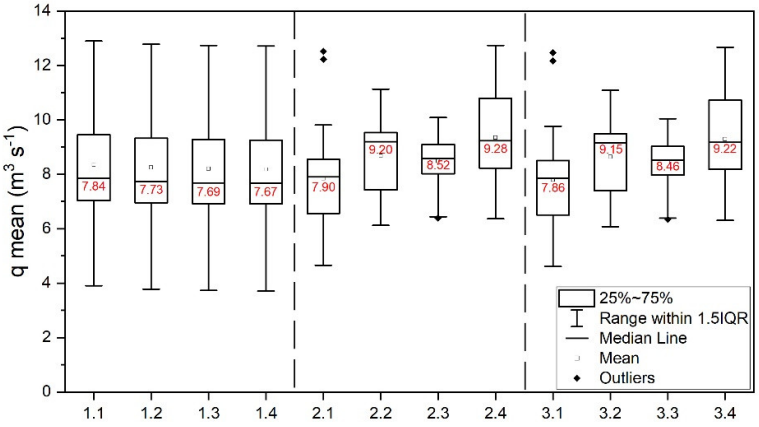

(b)

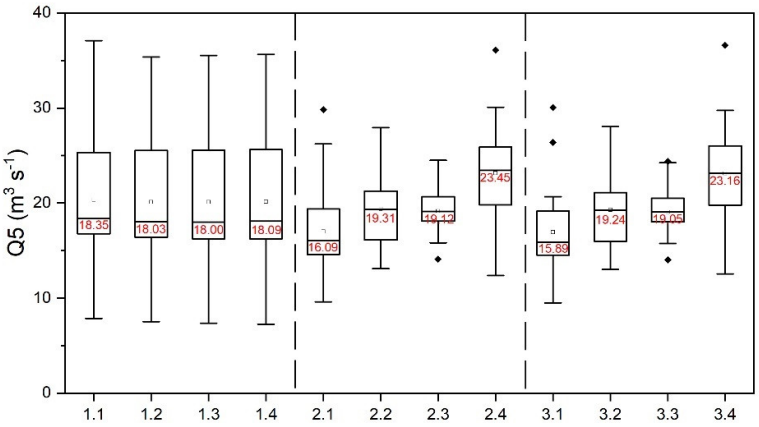

(c)

Figure 8.11. (Cont.) Projected changes in streamflow characteristics based on simulations twenty hydrological years: (a) Q95 (95th percentile flow); (b) q_mean (mean daily discharge); (c) Q5 (5th percentile flow), under three scenarios: Scenario 1 : effect of land cover change only; Scenario 2 : effect of climate change only; Scenario 3 : combined effect of land cover and climate changes. Refer to Table 4 for details. Box edges correspond to the 25th (Q1) and 75th (Q3) percentiles. Whiskers extend to Q1-1.5QR (lower bound) and Q3+1.5IQR (upper bound), with IQR = Q3-Q1 (Inter-Quartile Range). Points outside the box are outliers.

8.4. Discussion

8.4.1. Climate change modelling

Climate projections for northeastern Madagascar indicate increased precipitation during the rainy season while maintaining relatively stable precipitation levels during the dry season. Concurrently, temperature projections suggest rises of 1-2°C for maximum temperatures and 1-3°C for minimum temperatures. These patterns align with observed trends in other tropical regions. For instance, in Southeast Asia's Maritime Continent, mean monthly rainfall during the monsoon season is expected to increase by 150 mm while multi-model ensemble projections indicate an increase in annual mean temperature of 2-3°C, with greater warming expected over land areas compared to adjacent seas (Tangang et al. 2018). Similarly, in the Amazon basin, annual mean temperatures are projected to increase by 1-3°C by the end of the 21st century, with the dry season experiencing the most pronounced warming (Marengo and Espinoza 2016).

The studied region is projected to experience an increase in moderate precipitation events while showing a reduction in extreme events. However, this trend contrasts with observations in other tropical regions, where extreme events are generally expected to intensify (Chou et al. 2013). These divergent projections warrant careful interpretation. Several methodological factors may influence the results. First, the temporal mismatch between the climate data period (2001-2021) and the historical period used for bias correction (1980-2000) could affect the robustness of the projections. This discrepancy may introduce uncertainties in the bias correction process and limit our ability to capture recent climate trends. Additionally, this temporal gap could obscure important changes in interannual and decadal climate variability, particularly modifications in the El Niño-Southern Oscillation (ENSO), which significantly influences Madagascar's precipitation patterns (Jury et al. 2003).

8.4.2. Land cover modelling

The Sahafihitry watershed experienced significant deforestation between 1992 and 2010, a phenomenon primarily attributed to the intensification of slash-and-burn agriculture, locally known as '*tavy*' (Styger et al. 2007). '*Tavy*' is a traditional agricultural practice in Madagascar that involves clearing and burning a forest plot for temporary cultivation, typically for rain-fed rice production. After a few years of exploitation, when soil fertility declines, the plot is abandoned for a fallow period, and the process is repeated on a new forested area (Kull 2004). Although deeply rooted in local culture and adapted to the socio-economic conditions of farmers, this practice has considerable impacts on forest ecosystems and biodiversity (Harper et al. 2007), leading to progressive forest degradation and loss of essential ecosystem services, particularly in the SAVA region.

Predictive models suggest a continuous, albeit less pronounced, decrease in forest cover in the medium and long term, specifically for forested areas located outside the Masoala national park. This distinction is crucial, as it highlights the performance of the CA-Markov model in capturing spatial relationships and predicting transitions. The difference in dynamics between protected and non-protected areas not only reflects the relative effectiveness of conservation measures created since 1997, but also the potential concentration of subsistence activities (*tavy*) in the remaining forested areas outside protected zones (Grinand et al. 2013). However, the LULC model, used in this study, does not account for several key factors that could significantly influence deforestation dynamics in the future. These include socio-economic aspects such as fluctuations in cash crop prices (e.g., vanilla), which can have a substantial impact on agricultural practices and pressure on forests (Zhu 2018). Furthermore, demographic pressures from a growing population demanding more land for agriculture are not integrated (Scales 2014). The model also does not consider (as yet unknown) political factors, including possible changes in forestry or agricultural policies and variations in the effectiveness of environmental law enforcement (Rasolofoson et al. 2015). Lastly, broader economic dynamics, such as

the development of alternative livelihoods for local communities, can play a crucial role in forest preservation or degradation (Gardner et al. 2016).

Another aspect not accounted for in the CA-Markov approach is the impacts of climate change on LULC, that could significantly influence species composition and vegetation structure. Malhi et al. (2009) postulate the potential 'savanization' of tropical forests, while other scholars emphasize the adaptive capacity of plant species to rapid changes, thereby complicating long-term predictions of ecosystem composition (Urban et al. 2016). Furthermore, ecosystems may exhibit tipping points or threshold effects which, once breached, can trigger rapid and irreversible changes. These thresholds are challenging to anticipate and model with precision within our current methodological framework (Lenton et al. 2008).

8.4.3. Hydrological model performance

With promising statistical indicators (KGE ≈ 0.6), the model shows considerable potential. While there are areas for improvement, particularly in forecasting floods and low flows, the calibrated model successfully captures the general dynamics of the hydrological regime. This makes it a valuable tool for studying long-term hydrological changes and their potential impacts on the river ecosystem.

The evaluation of the SWAT model using IMERG data revealed a systematic underestimation of extreme flows (<10 $m^3 s^{-1}$ and >50 $m^3 s^{-1}$). This underestimation can be attributed to various factors. The coarse resolution of IMERG satellite data (0.1° x 0.1°) (Huffman et al. 2020) struggles to capture the high spatio-temporal variability of precipitation in northeastern Madagascar (Jury et al. 1995; Aldegheri 1972). Ramahaimandimby et al. (2021) confirmed also IMERG's tendency to underestimate extreme precipitation events, a phenomenon observed in other tropical regions (Liu et al. 2020; Rahmawati and Lubczynski 2018). Ramahaimandimby et al. (submitted) further demonstrated that model calibration with measured rainfall leads to better model performance compared to calibration

with IMERG data. This further highlights the limitations of the IMERG data for scenario analysis, even though IMERG was also shown to be the best performing rainfall dataset out of 6 different global precipitation products for the study region.

The use of a potentially biased rating curve for high flow conditions (section 8.2.2.) combined with uncertainties in the IMERG precipitation data may also lead to significant inaccuracies in the estimation of flood events, especially during extreme situations like the heavy rainfall observed during the 2020 rainy season (Figure 10a). Moreover, the exclusive use of Nash-Sutcliffe Efficiency (NSE) as the objective function in auto-calibration can lead to an oversimplification of model performance evaluation. As highlighted by Krause et al. (2005), this approach may neglect significant deviations during flood and low-flow periods, resulting in a statistically acceptable model that fails to adequately capture the dynamics of extreme events.

8.4.4. Hydrological alterations

Scenario 1, which evaluates the isolated impact of land use changes on the hydrological regime under constant precipitation conditions, reveals little effects of LUCC on the low, median, and high flows. This lack of trend can be explained by the nature of the predicted land use changes and the modeling of these changes in the SWAT model. Because of the predominance of the slash and burn practice, deforestation mostly leads to the conversion of forests into trees and shrubs mosaic and natural vegetation mosaic, with very limited impact on the actual extent of cropland (Table 8.5). The shift from forests to tree and shrub mosaics results in a marginal decrease in canopy interception and maximum canopy storage; substantial vegetation cover remains, effectively intercepting rainfall. For both types of mosaics, the surface roughness, though slightly reduced compared to dense forests, still provides significant resistance to overland flow. Evapotranspiration rates in tree and shrub mosaics, while somewhat lower than in forests, remain relatively high, helping to maintain the ecosystem's capacity to regulate water fluxes naturally (Arnold et al. 2012; Neitsch et al. 2011). Finally, in terms of runoff generation, the transition from forests (CN = 70) to natural vegetation mosaics (CN = 76) and trees and shrubs

mosaics (CN = 73) results in a limited increase in Curve Number (CN) values (Table 8.2) and hence a limited increase in surface runoff. Although the CN of cropland (CN = 81) is significantly higher than the CN of forested areas, this has minimal impact on runoff because the cropland acreage increases only marginally. Consequently, the observed and predicted land-use changes result in a more nuanced alteration of hydrological processes than initially anticipated. The transfer of precipitation to streams is moderated, leading to a slight decrease in discharge peaks between 1992 and 2010 during which the largest change in LULC occurred (Table 8.5). This unexpected outcome highlights the complex interplay between land cover characteristics and hydrological processes in this specific ecosystem.

Scenario 2 examined the isolated effects of climate change while maintaining land cover unchanged (based on the 2010 map), while scenario 3 explored the combined effects of both land use changes and climate change. Notably, scenarios 2 and 3 show very similar flow values and trends. This similarity suggests a lack of significant interaction between land use and land cover change (LUCC) and climate change (CC) factors, with climate change effects largely overshadowing those of land use changes. Overall, our models project a slight decrease for RCP 4.5 in the medium term followed by an increase in the long term, while for RCP 8.5, an increase in mean flow occurs already in the medium term with a marked acceleration by 2100, mainly due to the upward trend in precipitation predicted by climate models. Consequently, the future hydrological alteration of the studied watershed appears to be primarily driven by CC rather than by LUCC (Kayitesi et al. 2021; Rabezanahary et al. 2021).

Several studies in tropical humid areas corroborate these findings. For instance, in the Amazon basin, Sorribas et al. (2016) found that climate change impacts on river discharge were more pronounced than those of land use change. Similarly, in Southeast Asia, Aragaw et al. (2021) reported that climate change was the dominant factor influencing future water availability in the Johor River Basin, Malaysia. In the Congo Basin, Aloysius et Saiers (2017) projected increases in runoff primarily due to climate change, with land use change playing a secondary role. Likewise, in the humid tropics of Costa Rica, Birkel et al. (2011) demonstrated that climate variability

had a more significant impact on streamflow than land use change. These examples from diverse tropical humid regions reinforce the notion that while both land use change and climate change affect hydrological processes, climate change often emerges as the dominant driver of long-term hydrological alterations in these ecosystems (Veldkamp et al. 2017; Döll et Schmied 2012). However, these findings may not necessarily apply to arid or semi-arid regions, where the interplay between LUCC and CC can yield different outcomes. Studies by El Ghoul et al. (2024); Sellami et al. (2016) have shown that in water-scarce environments, LUCC can have a more pronounced effect on local hydrology, potentially rivaling or exceeding the impact of CC in some cases.

8.5. Conclusion

This study of the Sahafihitry tropical watershed in northeastern Madagascar provides significant insights into future hydrological alterations for both medium-term (2040-2060) and long-term (2080-2100) climate and LUC change scenarios. Climate change effects emerge as the predominant factor determining the watershed's future hydrological response. This preeminence of climatic impacts over land-use changes suggests that adaptation strategies should prioritize long-term climate projections. These findings emphasize the critical importance of incorporating climate variability into future water resource management, particularly for adapting hydraulic infrastructure and refining flood and drought management strategies. Should significant deviations from the future predicted land uses be observed as a result of socio-economic changes or policy changes, this may warrant reconsideration of the present conclusions, especially if the percentage of cropland increases significantly.

While this study underscores the significance of conservation efforts, it also exposes the potential limitations of these approaches in the face of large-scale climate change. In the future, the mere protection of forested areas may prove insufficient to preserve the ecological and hydrological integrity of tropical watersheds. This

realization necessitates a paradigm shift in our approach to environmental management. Ultimately, this study calls for a fundamental reconsideration of our relationship with tropical ecosystems, urging us to view them not as static entities to be preserved, but as dynamic systems that require adaptive management in the face of 21st-century environmental challenges.

9. Chapitre 9 : Discussion et conclusion générales

Cette étude avait pour objectif d'approfondir la compréhension du fonctionnement hydrologique et des altérations hydrologiques potentielles du bassin versant d'Ankavia, situé dans la région SAVA de Madagascar. Le but était de combler les lacunes en données hydrométéorologiques et en connaissances hydrologiques locales, afin de proposer des perspectives de gestion durable des ressources en eau face aux pressions croissantes liées aux changements d'occupation du sol et au changement climatique. L'approche, à la fois multiscalaire et interdisciplinaire, s'est articulée autour de cinq axes de recherches complémentaires, dont les principaux résultats sont présentés ci-après.

9.1. Synthèses des résultats

9.1.1. Fiabilité des produits satellitaires pour une étude de gestion des ressources en eau dans le milieu tropical

L'évaluation rigoureuse de sources alternatives de données pluviométriques constitue une étape cruciale pour toute analyse hydrologique fiable, en particulier dans les zones comme le bassin versant d'Ankavia où les pluviomètres au sol sont mal répartis et, par conséquent, non représentatifs. Ce premier axe cherchait à identifier les produits satellitaires de précipitations reproduisant au mieux les caractéristiques pluviométriques du bassin (Chapitre 4). Parmi les six produits évalués (ARC v2, CHIRPS, ERA5, IMERG v06 Final, PERSIANN-CSS, RFE v2), les produits IMERG se sont révélés être les sources de données pluviométriques les plus fiables aux échelles journalière (R^2 = 0,63 ; pente de régression linéaire = 0,96 ; RMSE = 12 mm j^{-1} ; MAE = 5,5 mm j^{-1}) et événementielle pour les applications hydrologiques dans la zone d'étude. Ces produits sont également performants dans la détection des événements pluvieux compris entre 2 et 100 mm j^{-1}. Cependant, leur utilisation peut être limitée par leur faible concordance à l'échelle horaire (R^2 = 0,2) et leur incapacité à détecter avec précision les précipitations extrêmes supérieures à 100 mm j^{-1}. Par contre, les produits à mailles plus fines (0,05° x 0,05°), tels que PERSIANN,

s'avèrent plus performants pour estimer les précipitations extrêmes, mais moins efficaces dans les autres classes de pluie. En conclusion, les produits IMERG, couvrant des données depuis 2001 et ayant une résolution de 0,1° x 0,1°, peuvent être considérés comme une source fiable de données pluviométriques pour le bassin d'Ankavia, avec les limitations mentionnées ci-dessus.

9.1.2. Facteurs déterminants les réponses hydrologiques à l'échelle des méso-bassins

Cet axe s'efforçait de comprendre le comportement du bassin d'Ankavia (Chapitre 5) en analysant ses réponses hydrologiques aux précipitations estimées par les produits satellitaires IMERG, récemment identifiés comme une source alternative fiable de données pluviométriques (Chapitre 4). L'occupation du sol, les propriétés pédologiques et géologiques semblent être les principaux facteurs influençant la dynamique hydrologique du bassin, en particulier les débits de base et les débits d'étiage (Q95). Les caractéristiques du sol jouent un rôle crucial dans la détermination du ruissellement, des pics de crue (Qp), des débits de crue (Q5), des temps de réponse (ts) et des débits moyens (q_mean). De plus, l'étude a mis en évidence des différences significatives entre les sous-bassins versants en fonction de leur couverture forestière. Le bassin le plus boisé (Ankaviabe) démontre une meilleure capacité d'atténuation des crues, mais présente des débits de base plus faibles pendant la saison sèche. À l'inverse, les bassins moins boisés (Ankavia, Antsahovy, Sahafihitry) ont une capacité de régulation des crues réduite, mais connaissent des étiages moins prononcés durant la saison sèche, grâce à des débits de base plus élevés. Ces observations révèlent le rôle complexe de la forêt dans la régulation des crues et des étiages.

9.1.3. Facteurs de contrôle hydrologiques à l'échelle des micro-bassins

Cette approche à l'échelle de micro-bassins (un bassin forestier, un bassin mixte et un bassin principalement en jachère, Chapitre 6) a permis de réduire les problèmes d'hétérogénéité rencontrés à l'échelle du méso-bassin (Chapitre 5) et d'offrir une compréhension plus fine des effets de l'occupation du sol sur l'hydrologie en milieu tropical humide. En effet, les caractéristiques hydrologiques diffèrent selon les quatre principaux types d'occupation du sol présents dans le bassin : forêts primaires tropicales, terres cultivées, jachères et pâturages (anciennes rizières irriguées). Les forêts primaires tropicales présentent des taux d'infiltration exceptionnellement élevés et un taux d'écoulement 'rapide' très faible. Les terres cultivées et les jachères, malgré une structure de sol plus dense, conservent des taux d'infiltration élevés, bien qu'inférieurs à ceux des forêts. Les pâturages, quant à eux, présentent les propriétés hydrologiques les moins favorables, avec une perméabilité réduite et des taux d'infiltration plus faibles, augmentant ainsi le potentiel de ruissellement de surface. L'écoulement de subsurface, ou écoulement hypodermique (SSF), prédomine probablement en milieu forestier, tandis que le ruissellement de surface (de type hortonien HOF ou par saturation SOF) peut survenir, particulièrement dans les zones de pâturage, les terres cultivées et les jachères lors d'épisodes pluvieux intenses ou prolongés. De plus, la présence de surfaces cultivées semble amplifier la production d'écoulement, comme l'indiquent les coefficients de ruissellement plus élevés observés dans les bassins versants à utilisation mixte des terres par rapport aux bassins plus homogènes (jachères). Ces résultats soulignent l'importance cruciale de l'occupation du sol dans la dynamique hydrologique du bassin d'Ankavia. Ils mettent notamment en évidence la nécessité de préserver les forêts pour maintenir des taux d'infiltration élevés et de gérer prudemment les anciennes rizières irriguées pour limiter le ruissellement de surface.

9.1.4. Importance des réseaux de mesure au sol

En se fondant sur les connaissances acquises concernant le fonctionnement hydrologique des bassins (Chapitres 4, 5 et 6), ce quatrième axe explorait l'approche de simulation numérique des processus hydrologiques. Le but était d'évaluer diverses sources de données pluviométriques (réseaux de pluviomètres au sol de densités variables et données satellitaires IMERG) pour leur fiabilité dans les observatoires hydrologiques, en utilisant le modèle SWAT (Soil and Water Assessment Tool). Les résultats révèlent que les réseaux de pluviomètres plus denses représentent mieux la variabilité spatiale des précipitations, conduisant à de meilleures simulations des débits. En particulier, le réseau à deux pluviomètres offre le meilleur compromis entre précision et coût (R^2 = 0,85 ; a = 0,95 ; NSE = 0,83 ; RMSE = 3,36 ; KGE = 0,88), surpassant largement les données IMERG (R^2 = 0,48 ; a = 0,63 ; NSE = 0,41 ; RMSE = 6,46 ; KGE = 0,66). Ces dernières (IMERG), malgré leur accessibilité aisée, introduisent une incertitude significative dans la modélisation, particulièrement pour les débits d'étiage et les pics de crue. Cette analyse met en lumière l'importance d'un réseau de pluviomètres bien conçu pour une surveillance hydrologique fiable et rentable dans des environnements difficiles, notamment pour la simulation précise des inondations et des périodes d'étiage. Elle souligne également la nécessité de maintenir et d'optimiser les réseaux de mesure au sol, même à l'ère des données satellitaires, pour garantir une représentation fidèle des processus hydrologiques dans des bassins versants complexes.

9.1.5. Impacts du changement climatique versus changements d'utilisation des terres.

Cette étude, reposant sur une solide compréhension des dynamiques hydrologiques et exploitant des séries de données pluviométriques fiables et étendues du bassin, aspirait à évaluer les impacts futurs des changements climatiques et de l'évolution de l'occupation des sols sur le régime hydrologique du bassin versant d'Ankavia (Chapitre 8). L'objectif principal était d'examiner les effets séparés et combinés des

futurs changements d'utilisation des terres (LUCC) et du changement climatique (CC) sur divers aspects hydrologiques (débits d'étiage Q95, débit journalier moyen q mean, et débits de crue Q5) pour les horizons 2040-2060 et 2080-2100, en utilisant le modèle hydrologique SWAT. Les projections d'utilisation des sols, modélisées via l'approche Cellular Automata-Markov chain, prédisent une légère réduction du couvert forestier hors des zones protégées d'ici 2050 et 2100. Parallèlement, les projections climatiques, issues de cinq modèles climatiques régionaux (CCLM4, RCA4, HIRHAM5, RACMO22T, REMO2009) selon les scénarios RCP 4.5 et RCP 8.5, anticipent une augmentation des précipitations, particulièrement marquée durant la saison des pluies. Cette évolution s'accompagne d'une hausse des températures maximum et minimum. L'analyse révèle que les LUCC seuls n'entraînent pratiquement aucune modification des caractéristiques des débits, à l'exception d'un léger impact sur la fréquence des débits de crue. En revanche, l'impact du CC, qu'il soit considéré seul ou combiné aux LUCC, s'avère prépondérant, indiquant une interaction limitée entre ces deux facteurs. Ainsi, le changement climatique apparaît comme le principal moteur des modifications hydrologiques du bassin, surpassant très largement l'influence minime des changements d'utilisation des terres. Ces conclusions soulignent l'importance cruciale d'intégrer les projections climatiques dans la planification à long terme de la gestion des ressources en eau.

9.2. Limites et forces méthodologiques

9.2.1. Limites

L'étude a rencontré plusieurs défis méthodologiques, inhérents à la recherche hydrologique en milieu tropical. La principale limitation réside dans la disponibilité restreinte de données à long terme (Bonell 2005; Sivapalan et al. 2003), en particulier dans le bassin d'Ankavia. Cette contrainte a significativement impacté notre analyse, notamment en réduisant la période d'étude à seulement dix mois ou trois ans pour certaines analyses (Chapitres 5, 7 et 8), et à deux ans pour l'évaluation des produits satellitaires (Chapitre 4). Cette durée relativement courte peut potentiellement

limiter notre capacité à appréhender pleinement les variations saisonnières et les tendances pluriannuelles.

Dans le chapitre 4, l'étude s'est concentrée sur IMERG pour l'évaluation à différentes échelles temporelles en raison de sa performance supérieure à l'échelle quotidienne. Cependant, il est crucial de noter que la performance relative des produits satellitaires peut varier selon l'échelle temporelle considérée. Par exemple, l'étude récente d'Olivier et al. (2023) a démontré que WFDEI-GPCC surpasse IMERG à l'échelle mensuelle dans la partie nord-est de Madagascar sur une période plus longue (2007-2016). Ces résultats soulignent l'importance d'adapter le choix des produits satellitaires en fonction des objectifs spécifiques de l'étude et des caractéristiques des précipitations à analyser (Sun et al. 2018).

La rareté des bassins versants indépendants jaugés ou disposant de mesures de débit dans la région a nécessité l'inclusion du quatrième bassin d'Ankavia englobant les trois autres (Chapitre 5). Cette configuration imbriquée complexifie l'interprétation des résultats et exige une prudence accrue dans les conclusions. Par ailleurs, la sélection des ressources pour l'analyse a été guidée par des considérations méthodologiques spécifiques. Ainsi, malgré la disponibilité d'images à haute résolution pour les sols (ISDASoil, 30m) et l'occupation des sols (ESA Worldcover, 10m), le choix s'est porté sur des données à plus faible résolution (Globcover 300m et SoilGRIDS 250m). Cette décision méthodologique repose sur deux raisons principales : d'une part, Globcover fournit des images remontant à 1992, essentielles pour l'analyse de la déforestation traitée au chapitre 8 ; d'autre part, l'utilisation d'images à haute résolution aurait introduit des complications supplémentaires dans la caractérisation des bassins, notamment en raison du plus grand nombre de classes d'occupation du sol et de types de sol qu'elles impliquent. Cette approche permet de maintenir une cohérence analytique tout en facilitant la comparaison entre les différents bassins étudiés, malgré les contraintes liées à la disponibilité des données hydrologiques.

L'utilisation des produits IMERG, malgré leurs limitations connues dans la modélisation hydrologique, s'est avérée incontournable (Chapitres 7 et 8). Cette démarche a certes introduit une incertitude supplémentaire dans notre analyse, mais elle était nécessaire pour pallier le manque d'observations au sol. Les données IMERG, bien qu'essentielles, présentent des biais dans l'estimation des précipitations, particulièrement prononcés dans le bassin d'Ankavia. Ces imperfections dans les données d'entrée ont potentiellement influencé notre compréhension des processus hydrologiques et pourraient expliquer, en partie, les difficultés rencontrées dans l'interprétation de certains phénomènes observés. Néanmoins, l'intégration de ces données a permis une analyse plus complète, malgré les défis qu'elle a posés.

Les scénarios présentés au chapitre 8 comportent plusieurs limitations significatives. Concernant l'occupation des sols, les modèles employés, nécessairement simplifiés, ne peuvent capturer toute la complexité des changements futurs potentiels, en particulier les évolutions socio-économiques imprévues et les dynamiques non linéaires (Verburg et al. 2019). Les scénarios de changement climatique présentent, quant à eux, des incertitudes intrinsèques, notamment à l'échelle régionale, et ne couvrent pas nécessairement l'ensemble des futurs climatiques envisageables (Hawkins et Sutton 2009). Par ailleurs, l'étude s'est limitée aux précipitations et à la température comme paramètres climatiques, omettant d'autres facteurs essentiels tels que le rayonnement solaire, le vent et la pression atmosphérique. Cette restriction à deux paramètres risque d'entraîner une évaluation biaisée des impacts hydrologiques futurs, négligeant les interactions complexes entre les différentes composantes du climat (Milly et al. 2008). Par conséquent, les projections hydrologiques doivent être interprétées avec prudence, considérant qu'elles représentent une première approximation qui nécessite des études complémentaires plus exhaustives. Ces limitations soulignent l'importance d'adopter une approche plus holistique dans les futures recherches, intégrant un éventail plus large de paramètres climatiques et des scénarios plus diversifiés pour améliorer la robustesse des projections hydrologiques.

9.2.2. Forces

Cette étude apportait une contribution significative à la compréhension des dynamiques hydrologiques en milieu tropical humide, se concentrant sur la région SAVA de Madagascar, peu étudiée auparavant. L'approche multiscalaire adoptée englobe la complexité des interactions entre l'occupation du sol, les propriétés pédologiques et les régimes hydrologiques à différentes échelles. De plus, pour surmonter les défis liés aux données limitées, l'intégration de données satellitaires avec des mesures au sol représente une avancée méthodologique importante dans ces régions aux réseaux de mesure restreints. La comparaison de produits satellitaires de précipitations fournit des lignes directrices précieuses pour leur utilisation dans des contextes similaires.

Le modèle SWAT a été adapté et affiné pour mieux prendre en compte les spécificités locales des sous-bassins, améliorant ainsi la résolution spatiale de la compréhension des processus hydrologiques dans le Nord-Est de Madagascar, et par extension, dans d'autres milieux tropicaux humides. Le modèle a également été ajusté pour une simulation à pas de temps journalier, évaluant sa capacité à simuler de manière fiable les processus hydrologiques à une échelle temporelle plus fine.

L'approche interdisciplinaire adoptée a aussi fourni une vision holistique des défis liés à la gestion de l'eau dans ce contexte tropical humide, complétant l'analyse de l'influence des facteurs environnementaux sur les régimes hydrologiques.

9.3. Implications et perspectives de recherche

9.3.1. Implications pour la gestion des ressources en eau

Cette recherche a mis en lumière des implications cruciales pour la gestion des ressources en eau dans la région SAVA et potentiellement dans d'autres zones tropicales humides. Les résultats soulignent la nécessité d'adopter une approche intégrée de la gestion de l'eau, prenant en compte l'interaction complexe entre plusieurs facteurs.

L'étude met en évidence la complexité du rôle de la couverture forestière dans la régulation des débits en milieu tropical, s'alignant avec le concept émergent de "nouvelle hydrologie forestière tropicale" proposé par van Noordwijk et al. (2017). Contrairement à la perception traditionnelle d'un rôle uniformément bénéfique des forêts, les observations révèlent une dynamique plus nuancée, où les effets varient selon les échelles spatiales et temporelles. Cette approche reconnaît l'importance de l'évapotranspiration forestière, qui peut parfois réduire les débits disponibles, particulièrement en saison sèche. Elle souligne également la variabilité des impacts sur l'infiltration, la recharge des nappes, et les débits de crue et d'étiage, en fonction des caractéristiques locales du sol et du climat. Ces résultats remettent en question certains paradigmes de la gestion forestière tropicale et appellent à une approche plus contextuelle et adaptative dans les stratégies de conservation et de restauration des écosystèmes, tenant compte de la complexité des interactions entre forêts et cycles hydrologiques.

L'évaluation des produits satellitaires pour l'estimation des précipitations ouvre de nouvelles perspectives pour la modélisation hydrologique dans la région. Cependant, les résultats soulignent également l'importance de maintenir et d'optimiser les réseaux de mesure au sol, en particulier pour la détection des événements extrêmes. Cette conclusion s'inscrit dans la continuité des travaux de Satgé et al. (2020) sur l'évaluation des produits de précipitation par satellite en milieu tropical, tout en apportant des spécificités propres à la région d'étude.

Enfin, le constat de la prédominance des impacts du changement climatique sur l'hydrologie future du bassin, par rapport aux changements d'utilisation des terres, souligne l'urgence d'intégrer l'adaptation au changement climatique dans toutes les politiques de gestion de l'eau. Cela implique non seulement une planification à long terme, mais aussi le développement d'une flexibilité accrue dans les pratiques de gestion pour faire face à l'incertitude croissante liée aux changements climatiques.

9.3.2. Perspectives de recherche

Pour les recherches futures, il est recommandé de :

- Approfondir la recherche sur la dynamique des sédiments dans les cours d'eau. Cela comprend l'étude des processus d'érosion, de transport et de sédimentation, ainsi que leur impact sur la morphologie des rivières et la qualité de l'eau. Cette recherche pourrait contribuer à améliorer la gestion des barrages et des réservoirs.
- Évaluer le potentiel multifonctionnel des cours d'eau de la région en adoptant une approche holistique qui considère l'ensemble des services écosystémiques et des utilisations potentielles. Cette étude approfondie examinerait notamment, mais sans s'y limiter, les possibilités d'hydroélectricité et de navigation fluviale, tout en explorant d'autres aspects cruciaux tels que l'irrigation agricole, l'approvisionnement en eau potable et les opportunités récréotouristiques. En prenant en compte les contraintes environnementales, sociales et économiques, ainsi que les interactions complexes entre ces différentes fonctions, l'étude chercherait à identifier des synergies et des compromis optimaux. L'objectif serait de développer une stratégie de gestion intégrée des ressources hydriques qui préserve l'intégrité écologique des systèmes fluviaux tout en maximisant les bénéfices socio-économiques pour les communautés locales et régionales, assurant ainsi un développement durable et résilient du territoire.
- Approfondir la compréhension des interactions entre l'occupation du sol et les processus hydrologiques, en particulier les mécanismes d'infiltration et les écoulements de subsurface (SSF) et hortoniens (HOF). Cette recherche viserait à améliorer la représentation de ces processus dans les modèles hydrologiques, permettant ainsi une meilleure prédiction des débits et une gestion plus efficace des ressources en eau.
- Analyser l'impact des changements climatiques sur la qualité de l'eau et les services hydrologiques. Cette étude devrait prendre en compte les modifications potentielles de la température de l'eau, de sa composition chimique et de son régime

d'écoulement, ainsi que leurs conséquences sur les écosystèmes et les activités humaines dépendantes de l'eau.

En définitive, cette étude représente une avancée significative dans notre compréhension des dynamiques hydrologiques en milieu tropical humide, fournissant des informations cruciales pour la mise en œuvre effective d'une gestion intégrée des ressources en eau dans la région SAVA. Elle souligne l'importance d'une approche holistique, prenant en compte les interactions complexes entre le climat, le bassin versant et l'hydrologie. Nos résultats mettent également en lumière la nécessité de repenser certaines approches traditionnelles de gestion des ressources en eau et des terres, en intégrant les nouvelles connaissances sur les impacts du changement climatique et l'importance des réseaux de mesure au sol. Les perspectives de recherche identifiées ouvrent la voie à des études futures qui pourront approfondir et étendre nos connaissances, contribuant ainsi à une gestion plus durable et résiliente des ressources en eau dans les régions tropicales.

10. Références bibliographiques

Abbaspour, K. C., S. A. Vaghefi, and R. Srinivasan. 2017. “A guideline for successful calibration and uncertainty analysis for soil and water assessment: a review of papers from the 2016 international SWAT conference.” *Water*, 10 (1): 6. MDPI.

Abbott, M. B., J. C. Bathurst, J. A. Cunge, P. E. O’Connell, and J. Rasmussen. 1986. “An introduction to the European Hydrological System — Systeme Hydrologique Europeen, ‘SHE’, 1: History and philosophy of a physically-based, distributed modelling system.” *Journal of Hydrology*, 87 (1): 45–59. https://doi.org/10.1016/0022-1694(86)90114-9.

Abdulkareem, J. H., B. Pradhan, W. N. A. Sulaiman, and N. R. Jamil. 2019. “Development of lag time and time of concentration for a tropical complex catchment under the influence of long-term land use/land cover (LULC) changes.” *Arab J Geosci*, 12 (3): 101. https://doi.org/10.1007/s12517-019-4253-z.

Abdulkareem, J. H., W. N. A. Sulaiman, B. Pradhan, and N. R. Jamil. 2018. “Relationship between design floods and land use land cover (LULC) changes in a tropical complex catchment.” *Arab J Geosci*, 11 (14): 376. https://doi.org/10.1007/s12517-018-3702-4.

Abe, C., F. Lobo, Y. Dibike, M. Costa, V. Dos Santos, and E. Novo. 2018a. “Modelling the Effects of Historical and Future Land Cover Changes on the Hydrology of an Amazonian Basin.” *Water*, 10 (7): 932. https://doi.org/10.3390/w10070932.

Abe, C., F. Lobo, Y. Dibike, M. Costa, V. Dos Santos, and E. Novo. 2018b. “Modelling the Effects of Historical and Future Land Cover Changes on the Hydrology of an Amazonian Basin.” *Water*, 10 (7): 932. https://doi.org/10.3390/w10070932.

Abreu, M. C., M. de S. Fraga, L. T. de Almeida, F. B. Silva, R. A. Cecílio, G. B. Lyra, and R. C. Delgado. 2022. “Streamflow in the Sapucaí River watershed, Brazil: Probabilistic modeling, reference streamflow, and regionalization.” *Physics and Chemistry of the Earth, Parts A/B/C*, 126: 103133. https://doi.org/10.1016/j.pce.2022.103133.

Adamson, P. T., I. D. Rutherfurd, M. C. Peel, and I. A. Conlan. 2009. “The hydrology of the Mekong River.” *The Mekong*, 53–76. Elsevier.

Addor, N., G. Nearing, C. Prieto, A. J. Newman, N. Le Vine, and M. P. Clark. 2018. “A Ranking of Hydrological Signatures Based on Their Predictability in Space.” *Water Resour. Res.*, 54 (11): 8792–8812. https://doi.org/10.1029/2018WR022606.

Addor, N., and J. Seibert. 2014. “Bias correction for hydrological impact studies-beyond the daily perspective.” *Hydrological Processes*, 28 (17).

Adeyewa, Z. D., and K. Nakamura. 2003. “Validation of TRMM radar rainfall data over major climatic regions in Africa.” *Journal of Applied Meteorology*, 42 (2): 331–347.

Adhikary, S. K., A. G. Yilmaz, and N. Muttil. 2015. “Optimal design of rain gauge network in the Middle Yarra River catchment, Australia.” *Hydrological Processes*, 29 (11): 2582–2599. https://doi.org/10.1002/hyp.10389.

AFD. 2005. “Madagascar - Rural Drinking Water Supply and Sanitation Programme - Appraisal Report.” 75.

Agarwal, D. K., J. A. Silander Jr, A. E. Gelfand, R. E. Dewar, and J. G. Mickelson Jr. 2005. “Tropical deforestation in Madagascar: analysis using hierarchical, spatially explicit, Bayesian regression models.” *Ecological modelling*, 185 (1): 105–131. Elsevier.

Ageet, S., A. H. Fink, M. Maranan, J. E. Diem, J. Hartter, A. L. Ssali, and P. Ayabagabo. 2021. “Validation of Satellite Rainfall Estimates over Equatorial East Africa.” *Journal of Hydrometeorology*.

Akoko, G., T. H. Le, T. Gomi, and T. Kato. 2021. “A review of SWAT model application in Africa.” *Water*, 13 (9): 1313. Multidisciplinary Digital Publishing Institute.

Aldegheri. 1960. “Etat actuel des etudes hydrologiques sur le territoire de la republique malgache.”

Aldegheri, M. 1972. “Rivers and Streams on Madagascar.” *Biogeography and Ecology in Madagascar*, R. Battistini and G. Richard-Vindard, eds., 261–310. Dordrecht: Springer Netherlands.

Alegre, J. C., and D. K. Cassel. 1996. “Dynamics of soil physical properties under alternative systems to slash-and-burn.” *Agriculture, Ecosystems & Environment*, 58 (1): 39–48. Elsevier.

Ali, M. Z. M., and F. Othman. 2018. “Raingauge network optimization in a tropical urban area by coupling cross-validation with the geostatistical technique.” *Hydrological Sciences Journal*, 63 (3): 474–491. Taylor & Francis. https://doi.org/10.1080/02626667.2018.1437271.

Allen, R. G., L. S. Pereira, D. Raes, and M. Smith. 1998. “Crop evapotranspiration-Guidelines for computing crop water requirements-FAO Irrigation and drainage paper 56.” *Fao, Rome*, 300 (9): D05109.

Aloysius, N., and J. Saiers. 2017. “Simulated hydrologic response to projected changes in precipitation and temperature in the Congo River basin.” *Hydrology and Earth System Sciences*, 21 (8): 4115–4130. Copernicus GmbH.

Ambroise, B. 1999. “La dynamique du cycle de l’eau dans un bassin versant: processus, facteurs, modèles.” HGA Bucharest, Romania.

Andréassian, V. 2004. “Waters and forests: from historical controversy to scientific debate.” *Journal of Hydrology*, 291 (1–2): 1–27. https://doi.org/10.1016/j.jhydrol.2003.12.015.

Andriambeloson, J. A., A. Paris, S. Calmant, and S. Rakotondraompiana. 2020. “Re-initiating depth-discharge monitoring in small-sized ungauged watersheds by combining remote sensing and hydrological modelling: a case study in Madagascar.” *Hydrological Sciences Journal*, 65 (16): 2709–2728. Taylor & Francis. https://doi.org/10.1080/02626667.2020.1833013.

Aragaw, H. M., S. K. Mishra, and M. K. Goel. 2022. “Responses of water balance component to land use/land cover and climate change using geospatial and hydrologic modeling in the Gidabo watershed, Ethiopia.” *Geocarto International*, 1–26. Taylor & Francis.

Arias, M. E., E. Lee, F. Farinosi, F. F. Pereira, and P. R. Moorcroft. 2018a. “Decoupling the effects of deforestation and climate variability in the Tapajós river basin in the Brazilian Amazon.” *Hydrological Processes*, 32 (11): 1648–1663. https://doi.org/10.1002/hyp.11517.

Arias, M. E., E. Lee, F. Farinosi, F. F. Pereira, and P. R. Moorcroft. 2018b. “Decoupling the effects of deforestation and climate variability in the T apajós river basin in the B razilian A mazon.” *Hydrological Processes*, 32 (11): 1648–1663. Wiley Online Library.

Arnell, N. W., D. A. Hudson, and R. G. Jones. 2003. “Climate change scenarios from a regional climate model: Estimating change in runoff in southern Africa.” *Journal of Geophysical Research: Atmospheres*, 108 (D16). Wiley Online Library.

Arnell, N. W., and B. Lloyd-Hughes. 2014. “The global-scale impacts of climate change on water resources and flooding under new climate and socio-economic scenarios.” *Climatic change*, 122 (1): 127–140. Springer.

Arnold, J. G., D. N. Moriasi, P. W. Gassman, K. C. Abbaspour, M. J. White, R. Srinivasan, C. Santhi, R. D. Harmel, A. Van Griensven, and M. W. Van Liew. 2012. “SWAT: Model use, calibration, and validation.” *Transactions of the ASABE*, 55 (4): 1491–1508. American Society of Agricultural and Biological Engineers.

Arnold, J. G., R. Srinivasan, R. S. Muttiah, and J. R. Williams. 1998. “Large area hydrologic modeling and assessment part I: model development 1.” *JAWRA Journal of the American Water Resources Association*, 34 (1): 73–89. Wiley Online Library.

Asadullah, A., N. McINTYRE, and M. Kigobe. 2008. “Evaluation of five satellite products for estimation of rainfall over Uganda / Evaluation de cinq produits satellitaires pour l’estimation des précipitations en Ouganda.” *Hydrological Sciences Journal*, 53 (6): 1137–1150. https://doi.org/10.1623/hysj.53.6.1137.

Ashouri, H., K.-L. Hsu, S. Sorooshian, D. K. Braithwaite, K. R. Knapp, L. D. Cecil, B. R. Nelson, and O. P. Prat. 2015. "PERSIANN-CDR: Daily Precipitation Climate Data Record from Multisatellite Observations for Hydrological and Climate Studies." *Bulletin of the American Meteorological Society*, 96 (1): 69–83. https://doi.org/10.1175/BAMS-D-13-00068.1.

Atiah, W. A., L. K. Amekudzi, J. N. A. Aryee, K. Preko, and S. K. Danuor. 2020. "Validation of satellite and merged rainfall data over Ghana, West Africa." *Atmosphere*, 11 (8): 859. Multidisciplinary Digital Publishing Institute.

Aubert, S., S. Razafiarison, and A. Bertrand. 2003. *Déforestation et systèmes agraires à Madagascar: les dynamiques des tavy sur la côte orientale*. Editions Quae.

Auvet, B., B. Lidon, B. Kartiwa, Y. Le Bissonnais, and J.-C. Poussin. 2015. "Modeling runoff and erosion risk in a~small steep cultivated watershed using different data sources: from on-site measurements to farmers' perceptions." *Hydrology and Earth System Sciences Discussions*, 12 (9): 9701–9740. https://doi.org/10.5194/hessd-12-9701-2015.

Awessou, K. G. B., C. Peugeot, A. Rocheteau, L. Seguis, F. C. Do, S. Galle, M. Bellanger, E. Agbossou, and J. Seghieri. 2017. "Differences in transpiration between a forest and an agroforestry tree species in the Sudanian belt." *Agroforestry systems*, 91: 403–413. Springer.

Ayral, P.-A., and S. Sauvagnargues. 2005. "Contribution à la spatialisation du modèle opérationnel de prévision des crues éclair ALTHAÏR." 32.

Barasa, B., V. Kakembo, and F. Mugagga. 2018. "Effects of diversified land use/cover types on rainfall-runoff generation in a rural catchment in Uganda." *Geosciences*, 8 (1): 7–13.

Barral, M. T., M. Arias, and J. Guérif. 1998. "Effects of iron and organic matter on the porosity and structural stability of soil aggregates." *Soil and Tillage Research*, 46 (3): 261–272. https://doi.org/10.1016/S0167-1987(98)00092-0.

Bates, B., Z. W. Kundzewicz, and IPCC (Eds.). 2008. *Climate change and water*. IPCC Technical Paper; 6.

Bauer, W., G. J. Walsh, B. De Waele, R. J. Thomas, M. S. Horstwood, L. Bracciali, D. I. Schofield, U. Wollenberg, D. J. Lidke, and I. T. Rasaona. 2011. "Cover sequences at the northern margin of the Antongil Craton, NE Madagascar." *Precambrian Research*, 189 (3–4): 292–312. Elsevier.

Baumann, J. 2011. "Tropical Watersheds, Hydrological Processes." *Encyclopedia of Agrophysics*, J. Gliński, J. Horabik, and J. Lipiec, eds., 937–938. Dordrecht: Springer Netherlands.

Bayat, B., K. Hosseini, M. Nasseri, and H. Karami. 2019. "Challenge of rainfall network design considering spatial versus spatiotemporal variations." *Journal of Hydrology*, 574: 990–1002. Elsevier.

Beck, H. E., M. Pan, T. Roy, G. P. Weedon, F. Pappenberger, A. I. Van Dijk, G. J. Huffman, R. F. Adler, and E. F. Wood. 2019a. “Daily evaluation of 26 precipitation datasets using Stage-IV gauge-radar data for the CONUS.” *Hydrology and Earth System Sciences*, 23 (1): 207–224. Copernicus GmbH.

Beck, H. E., E. F. Wood, M. Pan, C. K. Fisher, D. G. Miralles, A. I. Van Dijk, T. R. McVicar, and R. F. Adler. 2019b. “MSWEP V2 global 3-hourly 0.1 precipitation: methodology and quantitative assessment.” *Bulletin of the American Meteorological Society*, 100 (3): 473–500. American Meteorological Society.

Beck, H. E., N. E. Zimmermann, T. R. McVicar, N. Vergopolan, A. Berg, and E. F. Wood. 2018. “Present and future Köppen-Geiger climate classification maps at 1-km resolution.” *Scientific data*, 5 (1): 1–12. Nature Publishing Group.

Benzaghta, M. A., T. A. Mohammed, A. H. Ghazali, and M. A. M. Soom. 2012. “Prediction of evaporation in tropical climate using artificial neural network and climate based models.” *Scientific Research and Essays*, 7 (36): 3133–3148.

Bernard, B., K. Vincent, and M. Frank. 2018. “Effects of Diversified Land Use/Cover Types on Rainfall-runoff Generation in a Rural Catchment in Uganda.” *Geosciences*, 8 (1): 7–13. Scientific & Academic Publishing.

Bertolina, C., M. Farotto, S. Crivellari, F. Giacchero, C. Grasso, M. Bertolotti, and A. Maconi. 2023. “Summary of the 2016 World Health Organization Report and 2021 Compendium on environmental diseases.” *Working Paper of Public Health*, 11 (1).

Beven, K. 2004. “Robert E. Horton’s perceptual model of infiltration processes.” *Hydrological Processes*, 18 (17): 3447–3460. https://doi.org/10.1002/hyp.5740.

Beven, K., and P. Germann. 1982. “Macropores and water flow in soils.” *Water Resources Research*, 18 (5): 1311–1325. https://doi.org/10.1029/WR018i005p01311.

Beven, K., and P. Germann. 2013. “Macropores and water flow in soils revisited: REVIEW.” *Water Resour. Res.*, 49 (6): 3071–3092. https://doi.org/10.1002/wrcr.20156.

Beven, K. J., and M. J. Kirkby. 1979. “A physically based, variable contributing area model of basin hydrology / Un modèle à base physique de zone d’appel variable de l’hydrologie du bassin versant.” *Hydrological Sciences Bulletin*, 24 (1): 43–69. Taylor & Francis. https://doi.org/10.1080/02626667909491834.

Beven, K. J., E. F. Wood, and M. Sivapalan. 1988. “On hydrological heterogeneity—catchment morphology and catchment response.” *Journal of hydrology*, 100 (1–3): 353–375. Elsevier.

Bezerra, M. O., D. Vollmer, N. J. Souter, K. Shaad, S. Hauck, M. C. Marques, S. Mtshali, N. Acero, Y. Zhang, and E. Mendoza. 2023. “Stakeholder engagement and

knowledge co-production for better watershed management with the Freshwater Health Index." *Current Research in Environmental Sustainability*, 5: 100206. Elsevier.

Bieger, K., J. G. Arnold, H. Rathjens, M. J. White, D. D. Bosch, P. M. Allen, M. Volk, and R. Srinivasan. 2017. "Introduction to SWAT+, A Completely Restructured Version of the Soil and Water Assessment Tool." *JAWRA Journal of the American Water Resources Association*, 53 (1): 115–130. https://doi.org/10.1111/1752-1688.12482.

Bigot, S., D. Dumas, T. Y. Brou, R. Ramboarison, S. Razanaka, and N. Philippon. 2021. "Studying recent hydroclimatic variability in Madagascar despite deficient measurement networks: use of CHIRPS and GRACE data at the scale of the Mahajunga province." *Proceedings of IAHS*, 43–48. Copernicus GmbH.

Birkel, C., and A. C. Barahona. 2019. "Rainfall-runoff modeling: a brief overview." *Reference Module in Earth Systems and Environmental Sciences*.

Birkel, C., A. Correa-Barahona, M. Martinez-Martinez, S. Granados-Bolaños, N. Venegas-Cordero, K. Gutiérrez-García, S. Blanco-Ramírez, R. Quesada-Mora, V. Solano-Rivera, and J. Mussio-Mora. 2020. "Headwaters drive streamflow and lowland tracer export in a large-scale humid tropical catchment." *Hydrological Processes*, 34 (18): 3824–3841. Wiley Online Library.

Birkel, C., C. Soulsby, and D. Tetzlaff. 2011. "Modelling catchment-scale water storage dynamics: reconciling dynamic storage with tracer-inferred passive storage." *Hydrological Processes*, 25 (25): 3924–3936. https://doi.org/10.1002/hyp.8201.

Blöschl, G., S. Ardoin-Bardin, M. Bonell, M. Dorninger, D. Goodrich, D. Gutknecht, D. Matamoros, B. Merz, P. Shand, and J. Szolgay. 2007. "At what scales do climate variability and land cover change impact on flooding and low flows?" *Hydrological processes*, 21 (9): 1241–1247.

Blöschl, G., and M. Sivapalan. 1995. "Scale issues in hydrological modelling: a review." *Hydrological processes*, 9 (3–4): 251–290. Wiley Online Library.

Blöschl, G., M. Sivapalan, H. Savenije, T. Wagener, and A. Viglione. 2013a. *Runoff prediction in ungauged basins: synthesis across processes, places and scales*. Cambridge University Press.

Blöschl, G., M. Sivapalan, and T. Wagener. 2013b. "Runoff Prediction in Ungauged Basins." 492.

Blöschl, G., C. White, and K. K. Yilmaz. 2019. "Twenty-three unsolved problems in hydrology (UPH) – a community perspective." *Hydrological Sciences Journal*, 64 (10): 1141–1158. Taylor & Francis. https://doi.org/10.1080/02626667.2019.1620507.

Bonell, M. 1993. "Progress in the understanding of runoff generation dynamics in forests." *Journal of Hydrology*, 150 (2–4): 217–275. Elsevier.

Bonell, M. 2005a. “Runoff generation in tropical forests.” *Forests, Water and People in the Humid Tropics: Past, Present and Future Hydrological Research for Integrated Land and Water Management*, 314–406.

Bonell, M. 2005b. “Runoff generation in tropical forests.” *Forests, Water and People in the Humid Tropics: Past, Present and Future Hydrological Research for Integrated Land and Water Management*, 314–406.

Bonell, M., and J. Williams. 1986. “The two parameters of the Philip infiltration equation: their properties and spatial and temporal heterogeneity in a red earth of tropical semi-arid Queensland.” *Journal of Hydrology*, 87 (1–2): 9–31. Elsevier.

Bonsor, H. 2010. “A review of continent scale hydrological datasets available for Africa.” 28.

Bontemps, S., P. Defourny, E. Van Bogaert, E. S. A. Team, O. Arino, V. Kalogirou, and J. R. Perez. 2009. “GLOBCOVER 2009 Products Description and Validation Report.”

Bosch, J. M., and J. D. Hewlett. 1982. “A review of catchment experiments to determine the effect of vegetation changes on water yield and evapotranspiration.” *Journal of hydrology*, 55 (1–4): 3–23.

Boughton, W. C. 1989. “A review of the USDA SCS curve number method.” *Soil Research*, 27 (3): 511–523. CSIRO Publishing.

Brandon, K. 2014. “Ecosystem services from tropical forests: review of current science.” *Center for Global Development Working Paper*, (380).

Bruijnzeel, L. A. 1983. “Evaluation of runoff sources in a forested basin in a wet monsoonal environment: A combined hydrological and hydrochemical approach.”

Bruijnzeel, L. A. 1988. “(De)forestation and dry season flow in the tropics: A closer look.” *J. Trop. For. Sci.*, 1: 229–243.

Bruijnzeel, L. A. 1989. “forestation and dry season flow in the tropics: A closer look.” *Journal of Tropical Forest Science*, 229–243. JSTOR.

Bruijnzeel, L. A. 2004a. “Hydrological functions of tropical forests: not seeing the soil for the trees?” *Agriculture, ecosystems & environment*, 104 (1): 185–228. Elsevier.

Bruijnzeel, L. A. 2004b. “Hydrological functions of tropical forests: not seeing the soil for the trees?” *Agriculture, Ecosystems & Environment*, 104 (1): 185–228. https://doi.org/10.1016/j.agee.2004.01.015.

Burgess, M. G., J. Ritchie, J. Shapland, and R. Pielke. 2020. “IPCC baseline scenarios have over-projected CO2 emissions and economic growth.” *Environ. Res. Lett.*, 16 (1): 014016. IOP Publishing. https://doi.org/10.1088/1748-9326/abcdd2.

Burgy, R. H., and J. N. Luthin. 1956. “A test of the single-and double-ring types of infiltrometers.” *Eos, Transactions American Geophysical Union*, 37 (2): 189–192. Wiley Online Library.

Burt, T. P., and J. J. McDonnell. 2015. “Whither field hydrology? The need for discovery science and outrageous hydrological hypotheses.” *Water Resources Research*, 51 (8): 5919–5928. https://doi.org/10.1002/2014WR016839.

Burton, J. 2003. *Integrated water resources management on a basin level: a training manual*. Paris; Sainte-Foy (Québec): UNESCO ; Éditions MultiMondes.

Cai, W., M. J. McPhaden, A. M. Grimm, R. R. Rodrigues, A. S. Taschetto, R. D. Garreaud, B. Dewitte, G. Poveda, Y.-G. Ham, and A. Santoso. 2020. “Climate impacts of the El Niño–southern oscillation on South America.” *Nature Reviews Earth & Environment*, 1 (4): 215–231. Nature Publishing Group UK London.

Calder, I. R., and B. Aylward. 2006. “Forest and Floods: Moving to an Evidence-based Approach to Watershed and Integrated Flood Management.” *Water International*, 31 (1): 87–99. Routledge. https://doi.org/10.1080/02508060608691918.

Camberlin, P., G. Barraud, S. Bigot, O. Dewitte, F. M. Imwangana, J.-C. M. Mateso, N. Martiny, E. Monsieurs, V. Moron, T. Pellarin, N. Philippon, M. Sahani, and G. Samba. 2019. “Evaluation of remotely sensed rainfall products over Central Africa.” *Quarterly Journal of the Royal Meteorological Society*, 145 (722): 2115–2138. https://doi.org/10.1002/qj.3547.

Campling, P., A. Gobin, and J. Feyen. 2002. “Logistic Modeling to Spatially Predict the Probability of Soil Drainage Classes.” *Soil Science Society of America Journal*, 66 (4): 1390–1401. https://doi.org/10.2136/sssaj2002.1390.

Caravaggio, N., and M. Iorio. 2016. “Management of Water Resources in the Amazon Region.” *Sustainable Ecological Engineering Design*, M. Dastbaz and C. Gorse, eds., 279–292. Cham: Springer International Publishing.

Carlyle-Moses, D. E., S. Iida, S. Germer, P. Llorens, B. Michalzik, K. Nanko, A. Tischer, and D. F. Levia. 2018. “Expressing stemflow commensurate with its ecohydrological importance.” *Advances in Water Resources*, 121: 472–479. Elsevier.

Carrière, S. D., T. Health, P. F. M. Rakotomandrindra, C. Ollivier, R. E. Rajaomahefasoa, H. A. Rakoto, J. Lapègue, Y. E. Rakotoarison, M. Mangin, J. Kempf, T. Razakamanana, and K. Chalikakis. 2021. “Long-term groundwater resource observatory for Southwestern Madagascar.” *Hydrological Processes*, 35 (3): e14108. https://doi.org/10.1002/hyp.14108.

Carrière, S. D., A. Olioso, and L. Oudin. 2024. *Exploring the physical consistency of evapotranspiration estimates over Madagascar using remote sensing.* Copernicus Meetings.

Carrière, S. D., P. F. M. Rakotomandrindra, T. Heath, K. Chalikakis, M. Gillon, M. Leblanc, and S. Tweed. 2023. “Water mixing processes in a complex multi-layer hydrosystem in southwestern Madagascar: a combined isotopic and piezometry approach.” *Hydrogeol J*, 31 (8): 2337–2346. https://doi.org/10.1007/s10040-023-02731-5.

Cassalho, F., S. Beskow, M. M. Vargas, M. M. de Moura, L. F. Ávila, and C. R. de Mello. 2017. “Hydrological regionalization of maximum stream flows using an approach based on L-moments.” *RBRH*, 22 (0). https://doi.org/10.1590/2318-0331.021720160064.

Castellarin, A., G. Botter, D. A. Hughes, S. Liu, T. Ouarda, J. Parajka, D. A. Post, M. Sivapalan, C. Spence, and A. Viglione. 2013. “Prediction of flow duration curves in ungauged basins.” *Runoff prediction in ungauged basins: Synthesis across processes, places and scales*, 135–162. University Press Cambridge.

Chadwick, R., P. Good, G. Martin, and D. P. Rowell. 2016. “Large rainfall changes consistently projected over substantial areas of tropical land.” *Nature Climate Change*, 6: 177–181. https://doi.org/10.1038/nclimate2805.

Change, I. P. O. C. 2007. “Climate change 2007: The physical science basis.” Geneva.

Chaperon et al., C. (Ed.). 1974. *Fleuves et rivières de Madagascar*. Monographies hydrologiques ORSTOM. Paris: Office de la recherche scientifique et technique outre-mer.

Chaperon, P., J. Danloux, and L. Ferry. 1993. “Fleuves et rivières de Madagascar.” *Monographies hydrologiques ORSTOM*, (10): 14–854.

Chappell, N. A., M. Sherlock, K. Bidin, R. Macdonald, Y. Najman, and G. Davies. 2007. “Runoff Processes in Southeast Asia: Role of Soil, Regolith, and Rock Type.” *Forest Environments in the Mekong River Basin*, H. Sawada, M. Araki, N. A. Chappell, J. V. LaFrankie, and A. Shimizu, eds., 3–23. Tokyo: Springer Japan.

Chen, J., F. P. Brissette, and R. Leconte. 2011. “Uncertainty of downscaling method in quantifying the impact of climate change on hydrology.” *Journal of hydrology*, 401 (3–4): 190–202. Elsevier.

Chou, C., J. C. Chiang, C.-W. Lan, C.-H. Chung, Y.-C. Liao, and C.-J. Lee. 2013. “Increase in the range between wet and dry season precipitation.” *Nature Geoscience*, 6 (4): 263–267. Nature Publishing Group UK London.

Choubin, B., K. Solaimani, F. Rezanezhad, M. Habibnejad Roshan, A. Malekian, and S. Shamshirband. 2019. “Streamflow regionalization using a similarity approach in ungauged basins: Application of the geo-environmental signatures in the Karkheh River Basin, Iran.” *CATENA*, 182: 104128. https://doi.org/10.1016/j.catena.2019.104128.

Christensen, J. H., K. K. Kanikicharla, E. Aldrian, S. I. An, I. F. A. Cavalcanti, M. de Castro, W. Dong, P. Goswami, A. Hall, and J. K. Kanyanga. 2013. “Climate phenomena and their relevance for future regional climate change.” *Climate change 2013 the physical science basis: Working group I*

contribution to the fifth assessment report of the intergovernmental panel on climate change, 1217–1308. Cambridge University Press.

Ciampalini, A., W. Frodella, C. Margottini, and N. Casagli. 2019. "Rapid assessment of geo-hydrological hazards in Antananarivo (Madagascar) historical centre for damage prevention." *Geomatics, Natural Hazards and Risk*, 10 (1): 1102–1124. Taylor & Francis. https://doi.org/10.1080/19475705.2018.1564375.

Clark, M. 2012. "Deforestation in Madagascar: Consequences of population growth and unsustainable agricultural processes." *Global Majority E-Journal*, 3 (1): 61–71.

Collins, A. S., and B. F. Windley. 2002. "The tectonic evolution of central and northern Madagascar and its place in the final assembly of Gondwana." *The Journal of geology*, 110 (3): 325–339. The University of Chicago Press.

CPGU. 2012. "Atlas de la vulnérabilité sectorielle de la région SAVA."

CREAM. 2013. "Monographie de la région SAVA."

Cresswell, H. P., T. W. Green, and N. J. McKenzie. 2008. "The Adequacy of Pressure Plate Apparatus for Determining Soil Water Retention." *Soil Science Soc of Amer J*, 72 (1): 41–49. https://doi.org/10.2136/sssaj2006.0182.

Cui, X., H.-F. Graf, B. Langmann, W. Chen, and R. Huang. 2007. "Hydrological impacts of deforestation on the southeast Tibetan plateau." *Earth Interactions*, 11 (15): 1–18.

Dahri, Z. H., F. Ludwig, E. Moors, S. Ahmad, B. Ahmad, M. Shoaib, I. Ali, M. S. Iqbal, M. S. Pomee, and A. G. Mangrio. 2021. "Spatio-temporal evaluation of gridded precipitation products for the high-altitude Indus basin." *International Journal of Climatology*. Wiley Online Library.

Dai, Q., M. Bray, L. Zhuo, T. Islam, and D. Han. 2017. "A Scheme for Rain Gauge Network Design Based on Remotely Sensed Rainfall Measurements." *Journal of Hydrometeorology*, 18 (2): 363–379. American Meteorological Society. https://doi.org/10.1175/JHM-D-16-0136.1.

D'Almeida, C., C. J. Vörösmarty, G. C. Hurtt, J. A. Marengo, S. L. Dingman, and B. D. Keim. 2007. "The effects of deforestation on the hydrological cycle in Amazonia: a review on scale and resolution." *International Journal of Climatology: A Journal of the Royal Meteorological Society*, 27 (5): 633–647.

Danloux, J. 1983. "Crues d'origine cyclonique dans l'Océan Indien (Madagascar) et le Pacifique Sud (Nouvelle-Calédonie et Tahiti)."

Danloux, J. 1991. "Etude des crues." Rapport scientifiques et techniques.

Danloux, J., and F. Danloux. 1990. "Madagascar : étude et gestion de la ressource en eau : analyse bibliographique des travaux récents (1968-1989)." 72.

Davidson, E. A., C. J. R. de Carvalho, A. M. Figueira, F. Y. Ishida, J. P. H. Ometto, G. B. Nardoto, R. T. Sabá, S. N. Hayashi, E. C. Leal, and I. C. G. Vieira. 2007.

"Recuperation of nitrogen cycling in Amazonian forests following agricultural abandonment." *Nature*, 447 (7147): 995–998. Nature Publishing Group UK London.

Davies, J. 2009. "Hydrogeological mapping of north-central Madagascar using limited data." conference. Cape Town, South Africa.

Deckers, J., F. Nachtergaele, and O. Spaargaren. 2010. "Tropical soils in the classification systems of USDA, FAO and WRB." *Evolution of Tropical Soil Science*, 79.

Derin, Y., P.-E. Kirstetter, and J. J. Gourley. 2021. "Evaluation of IMERG Satellite Precipitation over the Land–Coast–Ocean Continuum. Part I: Detection." *Journal of Hydrometeorology*, 22 (11): 2843–2859. American Meteorological Society. https://doi.org/10.1175/JHM-D-21-0058.1.

Desbureaux, S., and R. Damania. 2018. "Rain, forests and farmers: Evidence of drought induced deforestation in Madagascar and its consequences for biodiversity conservation." *Biological Conservation*, 221: 357–364. https://doi.org/10.1016/j.biocon.2018.03.005.

Dey, P., and A. Mishra. 2017. "Separating the impacts of climate change and human activities on streamflow: A review of methodologies and critical assumptions." *Journal of Hydrology*, 548: 278–290. Elsevier.

Dezfuli, A. K., C. M. Ichoku, G. J. Huffman, K. I. Mohr, J. S. Selker, N. van de Giesen, R. Hochreutener, and F. O. Annor. 2017. "Validation of IMERG Precipitation in Africa." *J. Hydrometeor.*, 18 (10): 2817–2825. https://doi.org/10.1175/JHM-D-17-0139.1.

Di Baldassarre, G., A. Montanari, H. Lins, D. Koutsoyiannis, L. Brandimarte, and G. Blöschl. 2010. "Flood fatalities in Africa: from diagnosis to mitigation." *Geophysical Research Letters*, 37 (22). Wiley Online Library.

Di Marco, M., T. D. Harwood, A. J. Hoskins, C. Ware, S. L. Hill, and S. Ferrier. 2019. "Projecting impacts of global climate and land-use scenarios on plant biodiversity using compositional-turnover modelling." *Global change biology*, 25 (8): 2763–2778. Wiley Online Library.

Dinku, T., S. Chidzambwa, P. Ceccato, S. J. Connor, and C. F. Ropelewski. 2008. "Validation of high-resolution satellite rainfall products over complex terrain." *International Journal of Remote Sensing*, 29 (14): 4097–4110. Taylor & Francis.

Dinku, T., C. Funk, P. Peterson, R. Maidment, T. Tadesse, H. Gadain, and P. Ceccato. 2018. "Validation of the CHIRPS satellite rainfall estimates over eastern Africa." *Quarterly Journal of the Royal Meteorological Society*, 144: 292–312. Wiley Online Library.

Ditthakit, P., S. Nakrod, N. Viriyanantavong, A. D. Tolche, and Q. B. Pham. 2021. "Estimating Baseflow and Baseflow Index in Ungauged Basins Using Spatial Interpolation Techniques: A Case Study of the Southern River Basin of

Thailand." *Water*, 13 (21): 3113. Multidisciplinary Digital Publishing Institute. https://doi.org/10.3390/w13213113.

Djaman, K., P. M. Ndiaye, K. Koudahe, A. Bodian, L. Diop, M. O'Neill, and S. Irmak. 2018. "Spatial and temporal trend in monthly and annual reference evapotranspiration in Madagascar for the 1980–2010 period." *Int. J. Hydrol*, 2 (2): 95–105.

Döll, P., and H. M. Schmied. 2012. "How is the impact of climate change on river flow regimes related to the impact on mean annual runoff? A global-scale analysis." *Environmental Research Letters*, 7 (1): 014037. IOP Publishing.

Dorling, D. 2021. "World population prospects at the UN: our numbers are not our problem?" *The struggle for social sustainability*, 129–154. Policy Press.

Dos Santos, S. 2012. "L'accès à l'eau en Afrique subsaharienne: la mesure est-elle cohérente avec le risque sanitaire?" *Environnement, Risques & Santé*, 11 (4): 282–286.

Douglas-Mankin, K. R., R. Srinivasan, and J. G. Arnold. 2010. "Soil and Water Assessment Tool (SWAT) model: Current developments and applications." *Transactions of the ASABE*, 53 (5): 1423–1431. American Society of Agricultural and Biological Engineers.

Dunne, T. 1983. "Relation of field studies and modeling in the prediction of storm runoff." *Journal of hydrology*, 65 (1–3): 25–48. Elsevier.

Dunne, T., and R. D. Black. 1970. "An Experimental Investigation of Runoff Production in Permeable Soils." *Water Resources Research*, 6 (2): 478–490. https://doi.org/10.1029/WR006i002p00478.

Earth Resources Observation And Science (EROS) Center. 2017. "Shuttle Radar Topography Mission (SRTM) 1 Arc-Second Global." U.S. Geological Survey.

Eckhardt, K. 2005. "How to construct recursive digital filters for baseflow separation." *Hydrological Processes: An International Journal*, 19 (2): 507–515. Wiley Online Library.

Eckhardt, K. 2008. "A comparison of baseflow indices, which were calculated with seven different baseflow separation methods." *Journal of Hydrology*, 352 (1–2): 168–173. Elsevier.

Eckhardt, K. 2012. "Technical note: Analytical sensitivity analysis of a two parameter recursive digital baseflow separation filter." *Hydrology and Earth System Sciences*, 16 (2): 451–455. https://doi.org/10.5194/hess-16-451-2012.

Eckhardt, K., S. Haverkamp, N. Fohrer, and H.-G. Frede. 2002. "SWAT-G, a version of SWAT99. 2 modified for application to low mountain range catchments." *Physics and Chemistry of the Earth, Parts A/B/C*, 27 (9–10): 641–644. Elsevier.

Eckstein, D., V. Künzel, and L. Schäfer. 2021. "Global climate risk index 2021." *Who Suffers Most from Extreme Weather Events*, 2000–2019.

Egashira, K., M. N. A. Gusmao, and K. Kurosawa. 2006. “The present and future land management in East Timor - From ‘slush and burn’ to ‘slush and mulch.’” *Journal of the Faculty of Agriculture, Kyushu University*, 51 (2): 367–372.

El Ghoul, I., H. Sellami, S. Khlifi, and M. Vanclooster. 2024. “Assessing Spatio-Temporal Hydrological Impacts of Climate Change in the Siliana Watershed, Northwestern Tunisia.” *Atmosphere*, 15 (10): 1209. Multidisciplinary Digital Publishing Institute. https://doi.org/10.3390/atmos15101209.

Elsenbeer, H. 2001. “Hydrologic flowpaths in tropical rainforest soilscapes—a review.” *Hydrological Processes*, 15 (10): 1751–1759. https://doi.org/10.1002/hyp.237.

Elsenbeer, H., and R. A. Vertessy. 2000. “Stormflow generation and flowpath characteristics in an Amazonian rainforest catchment.” *Hydrol. Process.*, 14 (14): 2367–2381. https://doi.org/10.1002/1099-1085(20001015)14:14<2367::AID-HYP107>3.0.CO;2-H.

Eltahir, E. A. B., and P. J. -F. Yeh. 1999. “On the asymmetric response of aquifer water level to floods and droughts in Illinois.” *Water Resources Research*, 35 (4): 1199–1217. https://doi.org/10.1029/1998WR900071.

Emmanouil, S., A. Langousis, E. I. Nikolopoulos, and E. N. Anagnostou. 2021. “An ERA-5 derived CONUS-wide high-resolution precipitation dataset based on a refined parametric statistical downscaling framework.” *Water Resources Research*, n/a (n/a): e2020WR029548. https://doi.org/10.1029/2020WR029548.

Ewen, J., G. Parkin, and P. E. O’Connell. 2000. “SHETRAN: Distributed River Basin Flow and Transport Modeling System.” *J. Hydrol. Eng.*, 5 (3): 250–258. https://doi.org/10.1061/(ASCE)1084-0699(2000)5:3(250).

FAO and UNEP. 2020. *The State of the World’s Forests 2020: Forests, biodiversity and people*. The State of the World’s Forests (SOFO). Rome, Italy: FAO and UNEP.

Fatichi, S., E. R. Vivoni, F. L. Ogden, V. Y. Ivanov, B. Mirus, D. Gochis, C. W. Downer, M. Camporese, J. H. Davison, and B. Ebel. 2016. “An overview of current applications, challenges, and future trends in distributed process-based models in hydrology.” *Journal of Hydrology*, 537: 45–60. Elsevier.

Ferry, L. 1987. “Bibliographie pouvant intéresser les recherches hydrologiques et climatologiques et les aménagements hydrauliques à Madagascar.” 107.

Ferry, L. 1995. “Banques de données hydrologiques et pluviometriques de Madagascar.”

Ferry, L., M. Mietton, L. Robison, and J. Erismann. 2009. “Le lac Alaotra à Madagascar-Passé, Présent et Futur.” *Annales De Géomorphologie/Annals of Geomorphology/Zeitschrift Für Geomorphologie*, 53 (3): 299–318.

Fox, J., D. M. Truong, A. T. Rambo, N. P. Tuyen, L. T. Cuc, and S. Leisz. 2000. “Shifting cultivation: a new old paradigm for managing tropical forests.” *BioScience*, 50 (6): 521–528.

Freeze, R. A., and J. A. Cherry. 1979. “Groundwater prentice-hall.” *Englewood Cliffs, NJ*, 176: 161–177.

Freitas, E. da S., V. H. R. Coelho, Y. Xuan, D. de C. D. Melo, A. N. Gadelha, E. A. Santos, C. de O. Galvão, G. M. Ramos Filho, L. R. Barbosa, G. J. Huffman, W. A. Petersen, and C. das N. Almeida. 2020. “The performance of the IMERG satellite-based product in identifying sub-daily rainfall events and their properties.” *Journal of Hydrology*, 589: 125128. https://doi.org/10.1016/j.jhydrol.2020.125128.

Fritsch, J.-M. 1986. “L’augmentation du ruissellement après défrichement mécanisé de la forêt amazonienne: les bassins versants" ECEREX" en Guyane Française.”

Fritsch, J.-M. 1992. “Les effets du défrichement de la forêt amazonienne et de la mise en culture sur l’hydrologie de petits bassins versants.” *ORSTOM éditions, Paris*, 392.

Fritsch, J.-M. 1995. “Les effets hydrologiques du déboisement de la forêt amazonienne et d’utilisations alternatives du sol.” *Colloques et séminaires-Institut français de recherche scientifique pour le développement en coopération*, 411–424.

Frodella, W., D. Spizzichino, A. Ciampalini, C. Margottini, and N. Casagli. 2021. “Hydrography and geomorphology of Antananarivo High City (Madagascar).” *Journal of Maps*, 17 (4): 215–226. Taylor & Francis. https://doi.org/10.1080/17445647.2020.1721343.

Funk, C., P. Peterson, M. Landsfeld, D. Pedreros, J. Verdin, S. Shukla, G. Husak, J. Rowland, L. Harrison, and A. Hoell. 2015. “The climate hazards infrared precipitation with stations—a new environmental record for monitoring extremes.” *Scientific data*, 2 (1): 1–21. Nature Publishing Group.

Furukawa, K., E. Wolanski, and H. Mueller. 1997. “Currents and sediment transport in mangrove forests.” *Estuarine, Coastal and Shelf Science*, 44 (3): 301–310. Elsevier.

Gabiri, G., B. Diekkrüger, K. Näschen, C. Leemhuis, R. van der Linden, J.-G. M. Majaliwa, and J. A. Obando. 2020. “Impact of Climate and Land Use/Land Cover Change on the Water Resources of a Tropical Inland Valley Catchment in Uganda, East Africa.” *Climate*, 8 (7): 83. Multidisciplinary Digital Publishing Institute. https://doi.org/10.3390/cli8070083.

Gade, D. W. 1996. “Deforestation and its effects in highland Madagascar.” *Mountain Research and Development*, 101–116.

Ganzhorn, J. U., P. P. Lowry, G. E. Schatz, and S. Sommer. 2001. “The biodiversity of Madagascar: one of the world’s hottest hotspots on its way out.” *Oryx*, 35 (4): 346–348. https://doi.org/10.1046/j.1365-3008.2001.00201.x.

Gardner, C. J., F. U. Gabriel, F. A. S. John, and Z. G. Davies. 2016. “Changing livelihoods and protected area management: a case study of charcoal production in south-west Madagascar.” *Oryx*, 50 (3): 495–505. Cambridge University Press.

Gasse, F., E. Cortijo, J.-R. Disnar, L. Ferry, E. Gibert, C. Kissel, F. Laggoun-Défarge, E. Lallier-Vergès, J.-C. Miskovsky, and B. Ratsimbazafy. 1994. “A 36 ka environmental record in the southern tropics: Lake Tritrivakely (Madgascar).” *Comptes rendus de l’Académie des sciences. Série IIa, Sciences de la terre et des planètes*, 318: 1513–1519.

Gassman, P. W., M. R. Reyes, C. H. Green, and J. G. Arnold. 2007. “The soil and water assessment tool: historical development, applications, and future research directions.” *Transactions of the ASABE*, 50 (4): 1211–1250. American Society of Agricultural and Biological Engineers.

Gay-des-Combes, J. M., B. J. M. Robroek, D. Hervé, T. Guillaume, C. Pistocchi, R. T. E. Mills, and A. Buttler. 2017. “Slash-and-burn agriculture and tropical cyclone activity in Madagascar: Implication for soil fertility dynamics and corn performance.” *Agriculture, Ecosystems & Environment*, 239: 207–218. https://doi.org/10.1016/j.agee.2017.01.010.

Gebere, S., T. Alamirew, B. Merkel, and A. Melesse. 2015. “Performance of High Resolution Satellite Rainfall Products over Data Scarce Parts of Eastern Ethiopia.” *Remote Sensing*, 7 (9): 11639–11663. https://doi.org/10.3390/rs70911639.

van Genderen, J. L. 2011. “Advances in Environmental Remote Sensing: Sensors, Algorithms, and Applications.” *International Journal of Digital Earth*, 4 (5): 446–447. https://doi.org/10.1080/17538947.2011.598701.

Gentine, P., A. Massmann, B. R. Lintner, S. Hamed Alemohammad, R. Fu, J. K. Green, D. Kennedy, and J. Vilà-Guerau de Arellano. 2019. “Land–atmosphere interactions in the tropics–a review.” *Hydrology and Earth System Sciences*, 23 (10): 4171–4197. Copernicus Publications Göttingen, Germany.

Germer, S., C. Neill, A. V. Krusche, and H. Elsenbeer. 2010. “Influence of land-use change on near-surface hydrological processes: undisturbed forest to pasture.” *Journal of hydrology*, 380 (3–4): 473–480.

Getirana, A., D. Kirschbaum, F. Mandarino, M. Ottoni, S. Khan, and K. Arsenault. 2020. “Potential of GPM IMERG Precipitation Estimates to Monitor Natural Disaster Triggers in Urban Areas: The Case of Rio de Janeiro, Brazil.” *Remote Sensing*, 12 (24): 4095. Multidisciplinary Digital Publishing Institute. https://doi.org/10.3390/rs12244095.

Ghimire, C. P., L. A. Bruijnzeel, M. Bonell, N. Coles, M. W. Lubczynski, and D. A. Gilmour. 2014. “The effects of sustained forest use on hillslope soil hydraulic conductivity in the Middle Mountains of Central Nepal.” *Ecohydrology*, 7 (2): 478–495. https://doi.org/10.1002/eco.1367.

Ghimire, C. P., L. A. Bruijnzeel, M. W. Lubczynski, M. Ravelona, B. W. Zwartendijk, and H. I. van Meerveld. 2017. “Measurement and modeling of rainfall interception by two differently aged secondary forests in upland eastern Madagascar.” *Journal of hydrology*, 545: 212–225. Elsevier.

Ghimire, C. P., H. I. van Meerveld, B. W. Zwartendijk, M. Ravelona, J. Lahitiana, H. Razakamanarivo, M. W. Lubczynski, L. S. Bruijnzeel, and J. Jones. 2015. “Effects of reforestation on the partitioning of precipitation into evapotranspiration, overland flow and recharge in eastern Madagascar.”

Ghimire, U., A. Agarwal, N. K. Shrestha, P. Daggupati, G. Srinivasan, and H. H. Than. 2020. “Applicability of Lumped Hydrological Models in a Data-Constrained River Basin of Asia.” *J. Hydrol. Eng.*, 25 (8): 05020018. https://doi.org/10.1061/(ASCE)HE.1943-5584.0001950.

Ghosh, P., A. Mukhopadhyay, A. Chanda, P. Mondal, A. Akhand, S. Mukherjee, S. K. Nayak, S. Ghosh, D. Mitra, T. Ghosh, and S. Hazra. 2017. “Application of Cellular automata and Markov-chain model in geospatial environmental modeling- A review.” *Remote Sensing Applications: Society and Environment*, 5: 64–77. https://doi.org/10.1016/j.rsase.2017.01.005.

Giertz, S., and B. Diekkrüger. 2003. “Analysis of the hydrological processes in a small headwater catchment in Benin (West Africa).” *Physics and Chemistry of the Earth, Parts A/B/C*, 28 (33–36): 1333–1341. Elsevier.

Giertz, S., B. Junge, and B. Diekkrüger. 2005. “Assessing the effects of land use change on soil physical properties and hydrological processes in the sub-humid tropical environment of West Africa.” *Physics and Chemistry of the Earth, Parts A/B/C*, 30 (8–10): 485–496.

Godinez-Madrigal, J., N. Van Cauwenbergh, and P. van der Zaag. 2019. “Production of competing water knowledge in the face of water crises: Revisiting the IWRM success story of the Lerma-Chapala Basin, Mexico.” *Geoforum*, 103: 3–15. https://doi.org/10.1016/j.geoforum.2019.02.002.

Godsey, S., and H. Elsenbeer. 2002. “The soil hydrologic response to forest regrowth: a case study from southwestern Amazonia.” *Hydrological Processes*, 16 (7): 1519–1522. https://doi.org/10.1002/hyp.605.

Godsey, S., H. Elsenbeer, and R. Stallard. 2004. “Overland flow generation in two lithologically distinct rainforest catchments.” *Journal of Hydrology*, 295 (1–4): 276–290. Elsevier.

Gómez-Delgado, F., O. Roupsard, G. Le Maire, S. Taugourdeau, A. Pérez, M. Van Oijen, P. Vaast, B. Rapidel, J.-M. Harmand, and M. Voltz. 2011. “Modelling

the hydrological behaviour of a coffee agroforestry basin in Costa Rica." *Hydrology and earth system sciences*, 15 (1): 369–392. Copernicus GmbH.

Gordon, D. A. R., M. Coenders-Gerrits, B. A. Sellers, S. M. Sadeghi, and J. T. Van Stan II. 2019. "Rainfall interception and redistribution by a common North American understory and pasture forb, Eupatorium capillifolium (Lam. dogfennel)." *Hydrology and Earth System Sciences Discussions*, 2019: 1–22. Göttingen, Germany.

Gosset, M., J. Viarre, G. Quantin, and M. Alcoba. 2013. "Evaluation of several rainfall products used for hydrological applications over West Africa using two high-resolution gauge networks." *Quarterly Journal of the Royal Meteorological Society*, 139 (673): 923–940. https://doi.org/10.1002/qj.2130.

Grayson, R. B., A. W. Western, F. H. S. Chiew, and G. Blöschl. 1997. "Preferred states in spatial soil moisture patterns: Local and nonlocal controls." *Water Resources Research*, 33 (12): 2897–2908. https://doi.org/10.1029/97WR02174.

Grillot, J.-C., and L. Ferry. 1990. "Approche des échanges surface-souterrain en milieu cristallin altéré aquifère." *Hydrol. Continent*, 5 (1): 3–12.

Grinand, C., F. Rakotomalala, V. Gond, R. Vaudry, M. Bernoux, and G. Vieilledent. 2013. "Estimating deforestation in tropical humid and dry forests in Madagascar from 2000 to 2010 using multi-date Landsat satellite images and the random forests classifier." *Remote Sensing of Environment*, 139: 68–80. Elsevier.

Group, A. H., C. Vörösmarty, A. Askew, W. Grabs, R. G. Barry, C. Birkett, P. Döll, B. Goodison, A. Hall, and R. Jenne. 2001. "Global water data: A newly endangered species." *Eos, Transactions American Geophysical Union*, 82 (5): 54–58. Wiley Online Library.

Gudmundsson, L., J. Boulange, H. X. Do, S. N. Gosling, M. G. Grillakis, A. G. Koutroulis, M. Leonard, J. Liu, H. Müller Schmied, L. Papadimitriou, Y. Pokhrel, S. I. Seneviratne, Y. Satoh, W. Thiery, S. Westra, X. Zhang, and F. Zhao. 2021. "Globally observed trends in mean and extreme river flow attributed to climate change." *Science*, 371 (6534): 1159–1162. https://doi.org/10.1126/science.aba3996.

Guo, H., A. Bao, T. Liu, F. Ndayisaba, D. He, A. Kurban, and P. De Maeyer. 2017. "Meteorological drought analysis in the Lower Mekong Basin using satellite-based long-term CHIRPS product." *Sustainability*, 9 (6): 901. Multidisciplinary Digital Publishing Institute.

Guzha, A. C., R. L. B. Nobrega, K. Kovacs, J. Rebola-Lichtenberg, R. S. S. Amorim, and G. Gerold. 2015. "Characterizing rainfall-runoff signatures from micro-catchments with contrasting land cover characteristics in southern Amazonia." *Hydrological Processes*, 29 (4): 508–521. https://doi.org/10.1002/hyp.10161.

Guzha, A. C., M. C. Rufino, S. Okoth, S. Jacobs, and R. L. B. Nóbrega. 2018. “Impacts of land use and land cover change on surface runoff, discharge and low flows: Evidence from East Africa.” *Journal of Hydrology: Regional Studies*, 15: 49–67. Elsevier.

Hannah, L., R. Dave, P. P. Lowry, S. Andelman, M. Andrianarisata, L. Andriamaro, A. Cameron, R. Hijmans, C. Kremen, J. MacKinnon, H. H. Randrianasolo, S. Andriambololonera, A. Razafimpahanana, H. Randriamahazo, J. Randrianarisoa, P. Razafinjatovo, C. Raxworthy, G. E. Schatz, M. Tadross, and L. Wilmé. 2008. “Climate change adaptation for conservation in Madagascar.” *Biol. Lett.*, 4 (5): 590–594. https://doi.org/10.1098/rsbl.2008.0270.

Harper, G. J., M. K. Steininger, C. J. Tucker, D. Juhn, and F. Hawkins. 2007. “Fifty years of deforestation and forest fragmentation in Madagascar.” *Environmental conservation*, 34 (4): 325–333.

Harrington, L. J., P. Wolski, I. Pinto, A. M. Ramarosandratana, R. Barimalala, R. Vautard, S. Philip, S. Kew, R. Singh, D. Heinrich, J. Arrighi, E. Raju, L. Thalheimer, T. Razanakoto, M. Van Aalst, S. Li, R. Bonnet, W. Yang, F. E. L. Otto, and G. J. Van Oldenborgh. 2022. “Limited role of climate change in extreme low rainfall associated with southern Madagascar food insecurity, 2019–21.” *Environ. Res.: Climate*, 1 (2): 021003. https://doi.org/10.1088/2752-5295/aca695.

van der Harst, G. G., and W. P. Stakman. 1961. *The use of the Sandbox-apparatus to determine pF-curves in the range pF 0.4 tot 2.7*. Instituut voor Cultuurtechniek en Waterhuishouding.

Hawkins, E., and R. Sutton. 2009. “The potential to narrow uncertainty in regional climate predictions.” *Bulletin of the American Meteorological Society*, 90 (8): 1095–1108. American Meteorological Society.

Hecht, S., M. Schmink, R. Abers, E. Assad, D. Humphreys Bebbington, B. Eduaro, F. Costa, A. M. Durán Calisto, P. M. Fearnside, and R. Garrett. 2021. “The Amazon in motion: Changing politics, development strategies, peoples, landscapes, and livelihoods.” *Amazon Assessment Report 2021, Part II*, 14–2. ETH Zurich.

Hengl, T., J. Mendes de Jesus, G. B. M. Heuvelink, M. Ruiperez Gonzalez, M. Kilibarda, A. Blagotić, W. Shangguan, M. N. Wright, X. Geng, B. Bauer-Marschallinger, M. A. Guevara, R. Vargas, R. A. MacMillan, N. H. Batjes, J. G. B. Leenaars, E. Ribeiro, I. Wheeler, S. Mantel, and B. Kempen. 2017. “SoilGrids250m: Global gridded soil information based on machine learning.” *PLoS ONE*, (B. Bond-Lamberty, ed.), 12 (2): e0169748. https://doi.org/10.1371/journal.pone.0169748.

Herman, A., V. B. Kumar, P. A. Arkin, and J. V. Kousky. 1997. “Objectively determined 10-day African rainfall estimates created for famine early warning systems.”

International Journal of Remote Sensing, 18 (10): 2147–2159. Taylor & Francis. https://doi.org/10.1080/014311697217800.

Hersbach, H., B. Bell, P. Berrisford, S. Hirahara, A. Horányi, J. Muñoz-Sabater, J. Nicolas, C. Peubey, R. Radu, D. Schepers, A. Simmons, C. Soci, S. Abdalla, X. Abellan, G. Balsamo, P. Bechtold, G. Biavati, J. Bidlot, M. Bonavita, G. De Chiara, P. Dahlgren, D. Dee, M. Diamantakis, R. Dragani, J. Flemming, R. Forbes, M. Fuentes, A. Geer, L. Haimberger, S. Healy, R. J. Hogan, E. Hólm, M. Janisková, S. Keeley, P. Laloyaux, P. Lopez, C. Lupu, G. Radnoti, P. De Rosnay, I. Rozum, F. Vamborg, S. Villaume, and J. Thépaut. 2020. "The ERA5 global reanalysis." *Quart J Royal Meteoro Soc*, 146 (730): 1999–2049. https://doi.org/10.1002/qj.3803.

Hijmans, R. J., S. E. Cameron, J. L. Parra, P. G. Jones, and A. Jarvis. 2005. "Very high resolution interpolated climate surfaces for global land areas." *International Journal of Climatology: A Journal of the Royal Meteorological Society*, 25 (15): 1965–1978. John Wiley & Sons, Ltd. Chichester, UK.

Hillel, D., and R. S. Baker. 1988. "A descriptive theory of fingering during infiltration into layered soils." *Soil Science*, 146 (1): 51–56. LWW.

Hohmann, C., G. Kirchengast, S. O, W. Rieger, and U. Foelsche. 2020. "Runoff sensitivity to spatial rainfall variability: A hydrological modeling study with dense rain gauge observations." *Hydrology and Earth System Sciences Discussions*, 1–28. Copernicus GmbH. https://doi.org/10.5194/hess-2020-453.

Hong, Y., K. Hsu, and S. Sorooshian. 2004. "Precipitation estimation from remotely sensed imagery using an artificial neural network cloud classification system." *J. Appl. Meteor*, 43: 1834–1853.

Horton, R. E. 1932a. "Drainage-basin characteristics." *Trans. AGU*, 13 (1): 350. https://doi.org/10.1029/TR013i001p00350.

Horton, R. E. 1932b. "Drainage-basin characteristics." *Trans. AGU*, 13 (1): 350. https://doi.org/10.1029/TR013i001p00350.

Hossain, F., and E. N. Anagnostou. 2006. "A two-dimensional satellite rainfall error model." *IEEE transactions on geoscience and remote sensing*, 44 (6): 1511–1522. IEEE.

Hou, A. Y., R. K. Kakar, S. Neeck, A. A. Azarbarzin, C. D. Kummerow, M. Kojima, R. Oki, K. Nakamura, and T. Iguchi. 2014. "The global precipitation measurement mission." *Bulletin of the American meteorological Society*, 95 (5): 701–722. American Meteorological Society.

Hou, Y., M. Zhang, Z. Meng, S. Liu, P. Sun, and T. Yang. 2018. "Assessing the impact of forest change and climate variability on dry season runoff by an improved single watershed approach: A comparative study in two large watersheds, China." *Forests*, 9 (1): 46. MDPI.

Houze, R. A. 2012. “Orographic effects on precipitating clouds.” *Reviews of Geophysics*, 50 (1): 2011RG000365. https://doi.org/10.1029/2011RG000365.

Hrdinka, T., O. Novickỳ, E. Hanslík, and M. Rieder. 2012. “Possible impacts of floods and droughts on water quality.” *Journal of Hydro-environment Research*, 6 (2): 145–150. Elsevier.

Hu, S., and P. Shrestha. 2020. “Examine the impact of land use and land cover changes on peak discharges of a watershed in the midwestern United States using the HEC-HMS model.” *Papers in Applied Geography*, 6 (2): 101–118. https://doi.org/10.1080/23754931.2020.1732447.

Huffman, G. J., D. T. Bolvin, D. Braithwaite, K.-L. Hsu, R. J. Joyce, C. Kidd, E. J. Nelkin, S. Sorooshian, E. F. Stocker, and J. Tan. 2020. “Integrated Multi-satellite Retrievals for the Global Precipitation Measurement (GPM) Mission (IMERG).” *Satellite Precipitation Measurement*, 343–353. Springer.

Huffman, G. J., D. T. Bolvin, and E. J. Nelkin. 2015. “Integrated Multi-satellitE Retrievals for GPM (IMERG) technical documentation.” *NASA/GSFC Code*, 612: 47.

Huffman, G. J., D. T. Bolvin, E. J. Nelkin, D. B. Wolff, R. F. Adler, G. Gu, Y. Hong, K. P. Bowman, and E. F. Stocker. 2007. “The TRMM Multisatellite Precipitation Analysis (TMPA): Quasi-Global, Multiyear, Combined-Sensor Precipitation Estimates at Fine Scales.” *Journal of Hydrometeorology*, 8 (1): 38–55. https://doi.org/10.1175/JHM560.1.

INSTAT. 2020. “Résultats globaux du recensement général de la population et de l’habitation de 2018 de Madagascar.” Accessed November 21, 2022. https://madagascar.unfpa.org/sites/default/files/pub-pdf/resultat_globaux_rgph3_tome_01.pdf.

Iroumé, A., A. Huber, and K. Schulz. 2005. “Summer flows in experimental catchments with different forest covers, Chile.” *Journal of Hydrology*, 300 (1–4): 300–313. Elsevier.

Islam, A. R. M. T., A. Al Mamun, M. N. Rahman, M. Y. Akter, M. A. Chisty, G. M. Alam, J. Mallick, and M. S. Sohel. 2024. “A cost-benefit analysis of flood early warning system: Evidence from lower Brahmaputra River Basin, Bangladesh.” *International Journal of Disaster Risk Reduction*, 104: 104380. Elsevier.

Jalilibal, Z., A. Amiri, P. Castagliola, and M. B. C. Khoo. 2021. “Monitoring the coefficient of variation: A literature review.” *Computers & Industrial Engineering*, 161: 107600. https://doi.org/10.1016/j.cie.2021.107600.

Janeau, J.-L., L.-C. Gillard, S. Grellier, P. Jouquet, T. P. Q. Le, T. N. M. Luu, Q. A. Ngo, D. Orange, D. R. Pham, and D. T. Tran. 2014. “Soil erosion, dissolved organic carbon and nutrient losses under different land use systems in a small

catchment in northern Vietnam." *Agricultural water management*, 146: 314–323. Elsevier.

Jayapadma, J., T. N. Wickramaarachchi, G. Silva, H. Ishidaira, J. Magome, and K. Souma. 2022. "Impact of land use change on flood peak discharges and runoff volumes at the catchment scale." *18th Annual Meeting of the Asia Oceania Geosciences Society: Proceedings of the 18th Annual Meeting of the Asia Oceania Geosciences Society (AOGS 2021)*, 79–81. World Scientific.

Jiang, L., and P. Bauer-Gottwein. 2019. "How do GPM IMERG precipitation estimates perform as hydrological model forcing? Evaluation for 300 catchments across Mainland China." *Journal of Hydrology*, 572: 486–500. Elsevier.

Jiang, Q., W. Li, Z. Fan, X. He, W. Sun, S. Chen, J. Wen, J. Gao, and J. Wang. 2021. "Evaluation of the ERA5 reanalysis precipitation dataset over Chinese Mainland." *Journal of Hydrology*, 595: 125660. https://doi.org/10.1016/j.jhydrol.2020.125660.

Jiang, S., L. Ren, C.-Y. Xu, B. Yong, F. Yuan, Y. Liu, X. Yang, and X. Zeng. 2018. "Statistical and hydrological evaluation of the latest Integrated Multi-satellitE Retrievals for GPM (IMERG) over a midlatitude humid basin in South China." *Atmospheric Research*, 214: 418–429. https://doi.org/10.1016/j.atmosres.2018.08.021.

Joly, F. 1941. "Les climats de Madagascar." *L'Information Géographique*, 5 (4): 76–80. Persée - Portail des revues scientifiques en SHS. https://doi.org/10.3406/ingeo.1941.5092.

Jury, M. R., S. M. Goodman, and J. P. Benstead. 2003. "The climate of Madagascar."

Jury, M. R., B. A. Parker, N. Raholijao, and A. Nassor. 1995. "Variability of summer rainfall over Madagascar: climatic determinants at interannual scales." *International journal of climatology*, 15 (12): 1323–1332. Wiley Online Library.

Kaba, A. J. 2020. "Explaining Africa's Rapid Population Growth, 1950 to 2020: Trends, Factors, Implications, and Recommendations." *Sociology Mind*, 10 (4): 226–268. Scientific Research Publishing. https://doi.org/10.4236/sm.2020.104015.

Karthe, D., S. Chalov, and D. Borchardt. 2015. "Water resources and their management in central Asia in the early twenty first century: status, challenges and future prospects." *Environmental Earth Sciences*, 73: 487–499. Springer.

Kassin, K. E., K. Doffangui, B. Kouamé, G. Yoro, and A. Assa. 2008. "Variabilité pluviométrique et perspectives pour la replantation cacaoyère dans le Centre Ouest de la Côte d'Ivoire." *Journal of Applied biosciences*, 12: 633–641.

Katimon, A., and A. K. A. Wahab. 2003. "Hydrologic Characteristics of a Drained Tropical Peat Catchment: Runoff Coefficients, Water Table and Flow

Duration Curves." *Jurnal Teknologi*, 39â€“54-39â€“54. https://doi.org/10.11113/jt.v38.487.

Kayitesi, N. M., A. C. Guzha, and G. Mariethoz. 2022. "Impacts of land use land cover change and climate change on river hydro-morphology- a review of research studies in tropical regions." *Journal of Hydrology*, 615: 128702. https://doi.org/10.1016/j.jhydrol.2022.128702.

Kazemzadeh, M., and A. Malekian. 2018. "Homogeneity analysis of streamflow records in arid and semi-arid regions of northwestern Iran." *J. Arid Land*, 10 (4): 493–506. https://doi.org/10.1007/s40333-018-0064-4.

Khan, S. 2019. "Evaluating High-Resolution Satellite Precipitation Products Globally Over Land and Oceans." PhD Thesis. George Mason University.

Khodadoust Siuki, S., B. Saghafian, and S. Moazami. 2017. "Comprehensive evaluation of 3-hourly TRMM and half-hourly GPM-IMERG satellite precipitation products." *International Journal of Remote Sensing*, 38 (2): 558–571. Taylor & Francis. https://doi.org/10.1080/01431161.2016.1268735.

Khomsiati, N. L., N. Suryoputro, A. Yulistyorini, G. Idfi, and N. E. B. Alias. 2021. "The effect of forest area change in tropical islands towards baseflow and streamflow." *IOP Conf. Ser.: Earth Environ. Sci.*, 847 (1): 012032. https://doi.org/10.1088/1755-1315/847/1/012032.

Kidd, C., A. Becker, G. J. Huffman, C. L. Muller, P. Joe, G. Skofronick-Jackson, and D. B. Kirschbaum. 2017. "So, how much of the Earth's surface is covered by rain gauges?" *Bulletin of the American Meteorological Society*, 98 (1): 69–78. American Meteorological Society.

Kidd, C., and V. Levizzani. 2011. "Status of satellite precipitation retrievals." *Hydrology and Earth System Sciences*, 15 (4): 1109–1116. Copernicus GmbH.

Kilpatrick, F. A., and V. R. Schneider. 1983. *Use of flumes in measuring discharge*. Techniques of Water-Resources Investigations. Report.

Kong, M., J. Zhao, C. Zang, Y. Li, and J. Deng. 2023. "Characteristics and Driving Mechanism of Water Resources Trend Change in Hanjiang River Basin." *International Journal of Environmental Research and Public Health*, 20 (4): 3764. MDPI.

Koppen, W. 1936. "Das geographische System de Klimate." *Handbuch der klimatologie*.

Kraemer, H. C. 2015. "Kappa Coefficient." *Wiley StatsRef: Statistics Reference Online*, R. S. Kenett, N. T. Longford, W. W. Piegorsch, and F. Ruggeri, eds., 1–4. Wiley.

Krause, P., D. P. Boyle, and F. Bäse. 2005. “Comparison of different efficiency criteria for hydrological model assessment.” *Advances in Geosciences*, 5: 89–97. https://doi.org/10.5194/adgeo-5-89-2005.

Kull, C. A. 2004. *Isle of fire: the political ecology of landscape burning in Madagascar*. University of Chicago press.

Kummerow, C., W. Barnes, T. Kozu, J. Shiue, and J. Simpson. 1998. “The tropical rainfall measuring mission (TRMM) sensor package.” *Journal of atmospheric and oceanic technology*, 15 (3): 809–817.

Lacombe, G., O. Ribolzi, A. de Rouw, A. Pierret, K. Latsachak, N. Silvera, R. Pham Dinh, D. Orange, J.-L. Janeau, B. Soulileuth, H. Robain, A. Taccoen, P. Sengphaathith, E. Mouche, O. Sengtaheuanghoung, T. Tran Duc, and C. Valentin. 2016. “Contradictory hydrological impacts of afforestation in the humid tropics evidenced by long-term field monitoring and simulation modelling.” *Hydrology and Earth System Sciences*, 20 (7): 2691–2704. Copernicus GmbH. https://doi.org/10.5194/hess-20-2691-2016.

Lathuillière, M. J., M. T. Coe, and M. S. Johnson. 2016. “A review of green-and blue-water resources and their trade-offs for future agricultural production in the Amazon Basin: what could irrigated agriculture mean for Amazonia?” *Hydrology and Earth System Sciences*, 20 (6): 2179–2194. Copernicus GmbH.

Lee, S., and S. U. Kim. 2017. “Quantification of Hydrological Responses Due to Climate Change and Human Activities over Various Time Scales in South Korea.” *Water*, 9 (1): 34. Multidisciplinary Digital Publishing Institute. https://doi.org/10.3390/w9010034.

Leigh, E. G. 1975. “Structure and climate in tropical rain forest.” *Annual review of ecology and systematics*, 67–86. JSTOR.

Lenton, T. M., H. Held, E. Kriegler, J. W. Hall, W. Lucht, S. Rahmstorf, and H. J. Schellnhuber. 2008. “Tipping elements in the Earth’s climate system.” *Proc. Natl. Acad. Sci. U.S.A.*, 105 (6): 1786–1793. https://doi.org/10.1073/pnas.0705414105.

Levia, D. F., I. F. Creed, D. M. Hannah, K. Nanko, E. W. Boyer, D. E. Carlyle-Moses, N. Van de Giesen, D. Grasso, A. J. Guswa, and J. E. Hudson. 2020. “Homogenization of the terrestrial water cycle.” *Nature geoscience*, 13 (10): 656–658. Nature Publishing Group UK London.

Li, G., Z. Yu, W. Wang, Q. Ju, and X. Chen. 2021. “Analysis of the spatial Distribution of precipitation and topography with GPM data in the Tibetan Plateau.” *Atmospheric Research*, 247: 105259. https://doi.org/10.1016/j.atmosres.2020.105259.

Li, N., G. Tang, P. Zhao, Y. Hong, Y. Gou, and K. Yang. 2017. “Statistical assessment and hydrological utility of the latest multi-satellite precipitation analysis

IMERG in Ganjiang River basin." *Atmospheric Research*, 183: 212–223. https://doi.org/10.1016/j.atmosres.2016.07.020.

Li, W., D. Li, and Z. N. Fang. 2023. "Intercomparison of automated near-real-time flood mapping algorithms using satellite data and DEM-Based methods: a case study of 2022 Madagascar flood." *Hydrology*, 10 (1): 17. MDPI.

Li, X., L. Zou, J. Xia, M. Dou, H. Li, and Z. Song. 2022. "Untangling the effects of climate change and land use/cover change on spatiotemporal variation of evapotranspiration over China." *Journal of Hydrology*, 612: 128189. https://doi.org/10.1016/j.jhydrol.2022.128189.

Lim, K. J., B. A. Engel, Z. Tang, J. Choi, K.-S. Kim, S. Muthukrishnan, and D. Tripathy. 2005. "Automated web GIS based hydrograph analysis tool, WHAT 1." *JAWRA Journal of the American Water Resources Association*, 41 (6): 1407–1416. Wiley Online Library.

Ling, T. 2022. "A global study about water crisis." *2021 International Conference on Social Development and Media Communication (SDMC 2021)*, 809–814. Atlantis Press.

Liu, C.-Y., P. Aryastana, G.-R. Liu, and W.-R. Huang. 2020. "Assessment of satellite precipitation product estimates over Bali Island." *Atmospheric Research*, 244: 105032. https://doi.org/10.1016/j.atmosres.2020.105032.

Love, T. B., V. Kumar, P. Xie, and W. Thiaw. 2004. "P5. 4 A 20-year daily Africa precipitation climatology using satellite and gauge data." *14th Conference on Applied Climatology*. Citeseer.

Lozano-Baez, S. E., M. Cooper, S. Frosini de Barros Ferraz, R. Ribeiro Rodrigues, M. Castellini, and S. Di Prima. 2019. "Recovery of soil hydraulic properties for assisted passive and active restoration: assessing historical land use and forest structure." *Water*, 11 (1): 86. MDPI.

Machado, R. E., T. O. Cardoso, and M. H. Mortene. 2022. "Determination of runoff coefficient (C) in catchments based on analysis of precipitation and flow events." *International Soil and Water Conservation Research*, 10 (2): 208–216. https://doi.org/10.1016/j.iswcr.2021.09.001.

Macron, C., Y. Richard, T. Garot, M. Bessafi, B. Pohl, A. Ratiarison, and A. Razafindrabe. 2016. "Intraseasonal Rainfall Variability over Madagascar." *Mon. Wea. Rev.*, 144 (5): 1877–1885. American Meteorological Society. https://doi.org/10.1175/MWR-D-15-0077.1.

Maggioni, V., and C. Massari. 2018. "On the performance of satellite precipitation products in riverine flood modeling: A review." *Journal of hydrology*, 558: 214–224. Elsevier.

Mahmoud, M. T., S. A. Mohammed, M. A. Hamouda, and M. M. Mohamed. 2021. "Impact of Topography and Rainfall Intensity on the Accuracy of IMERG Precipitation Estimates in an Arid Region." *Remote Sensing*, 13 (1): 13.

Multidisciplinary Digital Publishing Institute. https://doi.org/10.3390/rs13010013.

Maina, J., H. de Moel, J. E. Vermaat, J. Henrich Bruggemann, M. M. M. Guillaume, C. A. Grove, J. S. Madin, R. Mertz-Kraus, and J. Zinke. 2012. "Linking coral river runoff proxies with climate variability, hydrology and land-use in Madagascar catchments." *Marine Pollution Bulletin*, 64 (10): 2047–2059. https://doi.org/10.1016/j.marpolbul.2012.06.027.

Malhi, Y., L. E. O. C. Aragão, D. Galbraith, C. Huntingford, R. Fisher, P. Zelazowski, S. Sitch, C. McSweeney, and P. Meir. 2009. "Exploring the likelihood and mechanism of a climate-change-induced dieback of the Amazon rainforest." *Proceedings of the National Academy of Sciences*, 106 (49): 20610–20615. Proceedings of the National Academy of Sciences. https://doi.org/10.1073/pnas.0804619106.

Maraun, D., F. Wetterhall, A. M. Ireson, R. E. Chandler, E. J. Kendon, M. Widmann, S. Brienen, H. W. Rust, T. Sauter, M. Themeßl, V. K. C. Venema, K. P. Chun, C. M. Goodess, R. G. Jones, C. Onof, M. Vrac, and I. Thiele-Eich. 2010. "Precipitation downscaling under climate change: Recent developments to bridge the gap between dynamical models and the end user." *Rev. Geophys.*, 48 (3): RG3003. https://doi.org/10.1029/2009RG000314.

Marcus, R. R. 2007. "Where Community-Based Water Resource Management has Gone Too Far: Poverty and Disempowerment in Southern Madagascar." *Conservation and Society*, 5 (2): 202.

Mariotti, L., E. Coppola, M. B. Sylla, F. Giorgi, and C. Piani. 2011. "Regional climate model simulation of projected 21st century climate change over an all-Africa domain: Comparison analysis of nested and driving model results." *Journal of Geophysical Research: Atmospheres*, 116 (D15). Wiley Online Library.

Martinez, P., and I. F. Souza. 2020. "Genesis of pseudo-sand structure in Oxisols from Brazil – A review." *Geoderma Regional*, 22: e00292. https://doi.org/10.1016/j.geodrs.2020.e00292.

Masson-Delmotte, V., P. Zhai, A. Pirani, S. L. Connors, C. Péan, S. Berger, N. Caud, Y. Chen, L. Goldfarb, M. I. Gomis, M. Huang, K. Leitzell, E. Lonnoy, J. B. R. Matthews, T. K. Maycock, T. Waterfield, Ö. Yelekçi, R. Yu, and B. Zhou (Eds.). 2021. *Climate Change 2021: The Physical Science Basis. Contribution of Working Group I to the Sixth Assessment Report of the Intergovernmental Panel on Climate Change*. Cambridge, United Kingdom and New York, NY, USA: Cambridge University Press.

Matsuno, Y., K. Nakamura, T. Masumoto, H. Matsui, T. Kato, and Y. Sato. 2006. "Prospects for multifunctionality of paddy rice cultivation in Japan and other countries in monsoon Asia." *Paddy and Water Environment*, 4: 189–197. Springer.

Mayor, Y., I. Tereshchenko, M. Fonseca-Hernández, D. Pantoja, and J. Montes. 2017. "Evaluation of Error in IMERG Precipitation Estimates under Different Topographic Conditions and Temporal Scales over Mexico." *Remote Sensing*, 9 (5): 503. https://doi.org/10.3390/rs9050503.

McConnell, W. J. 2002. "Madagascar: Emerald Isle or Paradise Lost?" *Environment*, 44 (8): 10–22. https://doi.org/10.1080/00139157.2002.10544685.

McDonnell, J. J. 1990. "A Rationale for Old Water Discharge Through Macropores in a Steep, Humid Catchment." *Water Resources Research*, 26 (11): 2821–2832. https://doi.org/10.1029/WR026i011p02821.

McDonnell, J. J., M. Sivapalan, K. Vaché, S. Dunn, G. Grant, R. Haggerty, C. Hinz, R. Hooper, J. Kirchner, M. L. Roderick, J. Selker, and M. Weiler. 2007. "Moving beyond heterogeneity and process complexity: A new vision for watershed hydrology." *Water Resources Research*, 43 (7): 2006WR005467. https://doi.org/10.1029/2006WR005467.

McGinnis, S., D. Nychka, and L. O. Mearns. 2015. "A New Distribution Mapping Technique for Climate Model Bias Correction." *Machine Learning and Data Mining Approaches to Climate Science*, V. Lakshmanan, E. Gilleland, A. McGovern, and M. Tingley, eds., 91–99. Cham: Springer International Publishing.

McMillan, H., I. Westerberg, and F. Branger. 2017. "Five guidelines for selecting hydrological signatures." *Hydrological Processes*, 31 (26): 4757–4761. https://doi.org/10.1002/hyp.11300.

McNally, A., K. Verdin, L. Harrison, A. Getirana, J. Jacob, S. Shukla, K. Arsenault, C. Peters-Lidard, and J. P. Verdin. 2019. "Acute water-scarcity monitoring for Africa." *Water*, 11 (10): 1968. MDPI.

Mdee, A., A. D. Ofori, J. Cohen, M. Kjellén, E. Rooney, S. Singhal, J. Amezaga, A. Figueroa-Benítez, S. Gupta, and A. T. Haile. 2024. "Obscuring Complexity and Performing Progress: Unpacking SDG Indicator 6.5. 1 and the Implementation of IWRM." *Water Alternatives*, 17 (2): 2.

Medina, M. A. 2010. "Global Water Crisis and Climate Change." *Journal of Hydrologic Engineering*, 15 (3): 167–170. American Society of Civil Engineers. https://doi.org/10.1061/(ASCE)HE.1943-5584.0000203.

van Meerveld, H. J., J. P. Jones, C. P. Ghimire, B. W. Zwartendijk, J. Lahitiana, M. Ravelona, and M. Mulligan. 2021. "Forest regeneration can positively contribute to local hydrological ecosystem services: Implications for forest landscape restoration." *Journal of Applied Ecology*, 58 (4): 755–765. Wiley Online Library.

Mei, Y., E. N. Anagnostou, E. I. Nikolopoulos, and M. Borga. 2014. "Error Analysis of Satellite Precipitation Products in Mountainous Basins." *J. Hydrometeor.*, 15 (5): 1778–1793. https://doi.org/10.1175/JHM-D-13-0194.1.

Merz, R., G. Blöschl, and J. Parajka. 2006. “Regionalization methods in rainfall–runoff modelling using large catchment samples.” 9.

Michaelides, S., V. Levizzani, E. Anagnostou, P. Bauer, T. Kasparis, and J. E. Lane. 2009. “Precipitation: Measurement, remote sensing, climatology and modeling.” *Atmospheric Research*, 94 (4): 512–533. Elsevier.

Miller, S. J. 2006. “The method of least squares.” *Mathematics Department Brown University*, 8 (1).

Milly, P. C. D., J. Betancourt, M. Falkenmark, R. M. Hirsch, Z. W. Kundzewicz, D. P. Lettenmaier, and R. J. Stouffer. 2008. “Stationarity Is Dead: Whither Water Management?” *Science*, 319 (5863): 573–574. https://doi.org/10.1126/science.1151915.

Mishra, S. K., and V. P. Singh. 2013. *Soil conservation service curve number (SCS-CN) methodology*. Springer Science & Business Media.

Moazami, S., and M. R. Najafi. 2021. “A comprehensive evaluation of GPM-IMERG V06 and MRMS with hourly ground-based precipitation observations across Canada.” *Journal of Hydrology*, 594: 125929. https://doi.org/10.1016/j.jhydrol.2020.125929.

Modeste, M., K. Abdellatif, M. Nadia, and S. Mohamed. 2018. “Effects of land use and cover type on the risks of runoff and water erosion: infiltration tests in the Ourika watershed (High Atlas, Morocco).” *Euro-Mediterranean Journal for Environmental Integration*, 3 (1). https://doi.org/10.1007/s41207-017-0046-5.

Molina-Sanchis, I., R. Lázaro, E. Arnau Rosalén, and A. Calvo Cases. 2016. “Rainfall timing and runoff: The influence of the criterion for rain event separation.” *Journal Of Hydrology And Hydromechanics, 2016, vol. 64, num. 3, p. 226-236*.

Montanari, A., G. Young, H. H. G. Savenije, D. Hughes, T. Wagener, L. L. Ren, D. Koutsoyiannis, C. Cudennec, E. Toth, S. Grimaldi, G. Blöschl, M. Sivapalan, K. Beven, H. Gupta, M. Hipsey, B. Schaefli, B. Arheimer, E. Boegh, S. J. Schymanski, G. Di Baldassarre, B. Yu, P. Hubert, Y. Huang, A. Schumann, D. A. Post, V. Srinivasan, C. Harman, S. Thompson, M. Rogger, A. Viglione, H. McMillan, G. Characklis, Z. Pang, and V. Belyaev. 2013. “‘Panta Rhei—Everything Flows’: Change in hydrology and society—The IAHS Scientific Decade 2013–2022.” *Hydrological Sciences Journal*, 58 (6): 1256–1275. https://doi.org/10.1080/02626667.2013.809088.

Moriasi, D. N., N. Pai, J. L. Steiner, P. H. Gowda, M. Winchell, H. Rathjens, P. J. Starks, and J. A. Verser. 2019. “SWAT-LUT: A Desktop Graphical User Interface for Updating Land Use in SWAT.” *JAWRA Journal of the American Water Resources Association*, 55 (5): 1102–1115. https://doi.org/10.1111/1752-1688.12789.

Moron, V., A. W. Robertson, and Y. Swarinoto. 2009. “Seasonal predictability of daily rainfall statistics over Indramayu district, Indonesia.” Columbia University. https://doi.org/10.7916/D8NZ8J98.

Mpanano, T. 2019. “Assessment of Flood Hazard Areas in the Congo River Basin in the Democratic Republic of Congo: a case study of the N’djili River Sub-basin.” PhD Thesis. University of Nairobi.

Muñoz-Sabater, J., E. Dutra, A. Agustí-Panareda, C. Albergel, G. Arduini, G. Balsamo, S. Boussetta, M. Choulga, S. Harrigan, and H. Hersbach. 2021. *ERA5-Land: A state-of-the-art global reanalysis dataset for land applications, Earth Syst. Sci. Data Discuss*.

Musy, A. 2004. “Hydrology: A Science for Engineers.” 583.

Nainar, A., K. Bidin, R. P. Walsh, R. M. Ewers, and G. Reynolds. 2017. “Effects of different land-use on suspended sediment dynamics in Sabah (Malaysian Borneo)–a view at the event and annual timescales.” *Hydrological Research Letters*, 11 (1): 79–84. Japan Society of Hydrology and Water Resources (JSHWR)/Japanese Association ….

Nassor, A., and M. R. Jury. 1998. “Intra-seasonal climate variability of Madagascar. Part 1: Mean summer conditions.” *Meteorology and Atmospheric Physics*, 65 (1–2): 31–41. Springer.

Negishi, J. N., S. Noguchi, R. C. Sidle, A. D. Ziegler, and A. Rahim Nik. 2007. “Stormflow generation involving pipe flow in a zero-order basin of Peninsular Malaysia.” *Hydrological Processes*, 21 (6): 789–806. https://doi.org/10.1002/hyp.6271.

Neitsch, S. L., J. G. Arnold, J. R. Kiniry, and J. R. Williams. 2011. *Soil and water assessment tool theoretical documentation version 2009*. Texas Water Resources Institute.

Nguyen, P., M. Ombadi, S. Sorooshian, K. Hsu, A. AghaKouchak, D. Braithwaite, H. Ashouri, and A. R. Thorstensen. 2018. “The PERSIANN family of global satellite precipitation data: a review and evaluation of products.” *Hydrology and Earth System Sciences*, 22 (11): 5801–5816. Copernicus GmbH. https://doi.org/10.5194/hess-22-5801-2018.

Nippgen, F., B. L. McGlynn, L. A. Marshall, and R. E. Emanuel. 2011. “Landscape structure and climate influences on hydrologic response.” *Water Resources Research*, 47 (12). https://doi.org/10.1029/2011WR011161.

Nobre, A. D., L. A. Cuartas, M. Hodnett, C. D. Rennó, G. Rodrigues, A. Silveira, and S. Saleska. 2011. “Height Above the Nearest Drainage–a hydrologically relevant new terrain model.” *Journal of Hydrology*, 404 (1–2): 13–29. Elsevier.

Nobre, C., G. Sampaio, L. Borma, J. Castilla-Rubio, J. Silva, and M. Cardoso. 2016. “Land-use and climate change risks in the Amazon and the need of a novel sustainable development paradigm.” *Proceedings of the National Academy*

of Sciences of the United States of America, 113. https://doi.org/10.1073/pnas.1605516113.

Novella, N. S., and W. M. Thiaw. 2013. "African rainfall climatology version 2 for famine early warning systems." *Journal of Applied meteorology and Climatology*, 52 (3): 588–606.

Ntouda, J., F. Sikodf, M. Ibrahim, and I. Abba. 2013. "Access to drinking water and health of populations in Sub-Saharan Africa." *Comptes Rendus. Biologies*, 336 (5–6): 305–309.

Nunes, F. G., A. P. Fiori, and G. Firpo. 2011. "ESTIMATIVA DE COEFICIENTES DE ESCOAMENTO SUPERFICIAL NA BACIA HIDROGRÁFICA DO RIO ATUBA: CURITIBA E REGIÃO METROPOLITANA PARANÁ/BRASIL." *Boletim Paranaense de Geociências*, 65.

Ochoa-Tocachi, B. F., W. Buytaert, J. Antiporta, L. Acosta, J. D. Bardales, R. Célleri, P. Crespo, P. Fuentes, J. Gil-Ríos, and M. Guallpa. 2018. "High-resolution hydrometeorological data from a network of headwater catchments in the tropical Andes." *Scientific data*, 5 (1): 1–16. Nature Publishing Group.

Ochoa-Tocachi, B. F., W. Buytaert, and B. De Bièvre. 2016. "Regionalization of land-use impacts on streamflow using a network of paired catchments." *Water Resources Research*, 52 (9): 6710–6729. Wiley Online Library.

Ogden, F. L., T. D. Crouch, R. F. Stallard, and J. S. Hall. 2013. "Effect of land cover and use on dry season river runoff, runoff efficiency, and peak storm runoff in the seasonal tropics of Central Panama." *Water Resources Research*, 49 (12): 8443–8462. Wiley Online Library.

Ollivier, C. C., S. D. Carrière, T. Heath, A. Olioso, Z. Rabefitia, H. Rakoto, L. Oudin, and F. Satgé. 2023. "Ensemble precipitation estimates based on an assessment of 21 gridded precipitation datasets to improve precipitation estimations across Madagascar." *Journal of Hydrology: Regional Studies*, 47: 101400. https://doi.org/10.1016/j.ejrh.2023.101400.

Ombadi, M., P. Nguyen, S. Sorooshian, and K. Hsu. 2018. "Developing Intensity-Duration-Frequency (IDF) Curves From Satellite-Based Precipitation: Methodology and Evaluation." *Water Resources Research*, 54 (10): 7752–7766. https://doi.org/10.1029/2018WR022929.

Ombadi, M., P. Nguyen, S. Sorooshian, and K. Hsu. 2021. "Retrospective analysis and Bayesian model averaging of CMIP6 precipitation in the Nile River Basin." *Journal of Hydrometeorology*, 22 (1): 217–229.

O'Neill, B. C., C. Tebaldi, D. P. van Vuuren, V. Eyring, P. Friedlingstein, G. Hurtt, R. Knutti, E. Kriegler, J.-F. Lamarque, J. Lowe, G. A. Meehl, R. Moss, K. Riahi, and B. M. Sanderson. 2016. "The Scenario Model Intercomparison Project (ScenarioMIP) for CMIP6." *Geoscientific Model Development*, 9 (9): 3461–3482. Copernicus GmbH. https://doi.org/10.5194/gmd-9-3461-2016.

Ormsby, A., and K. Mannle. 2006. “Ecotourism benefits and the role of local guides at Masoala National Park, Madagascar.” *Journal of Sustainable Tourism*, 14 (3): 271–287.

Otto, F. E., M. Zachariah, P. Wolski, I. Pinto, R. Barimalala, B. Nhamtumbo, R. Bonnet, R. Vautard, S. Philip, and S. Kew. 2022. “Climate change increased rainfall associated with tropical cyclones hitting highly vulnerable communities in Madagascar, Mozambique & Malawi.” *Mozambique & Malawi*.

Palm, C. A., M. J. Swift, and P. L. Woomer. 1996. “Soil biological dynamics in slash-and-burn agriculture.” *Agriculture, Ecosystems & Environment*, 58 (1): 61–74. Elsevier.

Panofsky, H. A., and G. W. Brier. 1968. “Some applications of statistics to meteorology.” *(No Title)*.

Papa, F., J.-F. Crétaux, M. Grippa, E. Robert, M. Trigg, R. M. Tshimanga, B. Kitambo, A. Paris, A. Carr, and A. S. Fleischmann. 2023. “Water resources in Africa under global change: monitoring surface waters from space.” *Surveys in Geophysics*, 44 (1): 43–93. Springer.

Paré, N., A. Biarnès, J.-M. Barbier, and M. Voltz. 2010. “Impact of land management on hydrological functioning in cultivated landscapes: a coupled model of functional assessment.” *EGUGA*, 881.

Payraudeau, S. 2002. “Modélisation distribuée des flux d’azote sur des petits bassins versants méditerranéens.” phdthesis. ENGREF (AgroParisTech).

Peña-Arancibia, J. L., L. A. Bruijnzeel, M. Mulligan, and A. I. Van Dijk. 2019. “Forests as ‘sponges’ and ‘pumps’: Assessing the impact of deforestation on dry-season flows across the tropics.” *Journal of Hydrology*, 574: 946–963. Elsevier.

Pereira, D. dos R., A. Q. de Almeida, M. A. Martinez, and D. R. Q. Rosa. 2014. “Impacts of deforestation on water balance components of a watershed on the Brazilian East Coast.” *Revista Brasileira de Ciência do Solo*, 38 (4): 1350–1358. SciELO Brasil.

Pereira, D. dos R., M. A. Martinez, F. F. Pruski, and D. D. da Silva. 2016. “Hydrological simulation in a basin of typical tropical climate and soil using the SWAT model part I: Calibration and validation tests.” *Journal of Hydrology: Regional Studies*, 7: 14–37. https://doi.org/10.1016/j.ejrh.2016.05.002.

Perrin, C. 2002. “Vers une amélioration d’un modèle global pluie-débit au travers d’une approche comparative.” *La Houille Blanche - Revue internationale de l’eau*, (6–7): 84–91. EDP Sciences. https://doi.org/10.1051/lhb/2002089.

Perrin, C., C. Michel, and V. Andréassian. 2003. “Improvement of a parsimonious model for streamflow simulation.” *Journal of hydrology*, 279 (1–4): 275–289. Elsevier.

Peterson, P., C. C. Funk, G. J. Husak, D. H. Pedreros, M. Landsfeld, J. P. Verdin, and S. Shukla. 2013. "The Climate Hazards group InfraRed Precipitation (CHIRP) with Stations (CHIRPS): Development and Validation." *AGUFM*, 2013: H33E-1417.

Phillips, J. V., and S. Tadayon. 2006. *Selection of Manning's roughness coefficient for natural and constructed vegetated and non-vegetated channels, and vegetation maintenance plan guidelines for vegetated channels in central Arizona*. US Geological Survey.

Piman, T., T. Lennaerts, and P. Southalack. 2013. "Assessment of hydrological changes in the lower Mekong Basin from Basin-Wide development scenarios." *Hydrological Processes*, 27 (15): 2115–2125. https://doi.org/10.1002/hyp.9764.

PNUD. 2015. "pnud_bilan_diagnostic_hydraulique_rurale_situation_agences_bassins_nord_madagascar_gire.pdf."

Poff, N. L., C. M. Brown, T. E. Grantham, J. H. Matthews, M. A. Palmer, C. M. Spence, R. L. Wilby, M. Haasnoot, G. F. Mendoza, and K. C. Dominique. 2016. "Sustainable water management under future uncertainty with eco-engineering decision scaling." *Nature Climate Change*, 6 (1): 25–34. Nature Publishing Group UK London.

Puri, P., and V. Puri. 2022. "The 'First climate change famine' from 2017–2022?-An analysis of the economics and geography of great SUD drought of Madagascar (1901–2021)." *ACADEMICIA: An International Multidisciplinary Research Journal*, 12 (3): 100–113. South Asian Academic Research Journals.

Qazi, N. 2020. "Hydrological functioning of forested catchments, Central Himalayan Region, India." *Forest Ecosystems*, 7 (1): 63. https://doi.org/10.1186/s40663-020-00275-8.

Rabefitia, Z. 2008. "Le changement climatique à Madagascar."

Rabezanahary, M. F., and M. H. Andrianarimanana. 2024. "Projection of future drought characteristics in the Great South of Madagascar using CMIP6 and bias-correction spatial disaggregation method." *Theor Appl Climatol*, 155 (3): 1871–1883. https://doi.org/10.1007/s00704-023-04727-3.

Rabezanahary, M. F., M. H. Rahaman, and J. Zhai. 2021. "Assessment of the future impact of climate change on the hydrology of the Mangoky River, Madagascar using ANN and SWAT." *Water*, 13 (9): 1239. MDPI.

Rahmawati, N., and M. W. Lubczynski. 2018. "Validation of satellite daily rainfall estimates in complex terrain of Bali Island, Indonesia." *Theoretical and applied climatology*, 134 (1–2): 513–532. Springer.

Rakotoarimanana, H., and I. Hiroshi. 2022. "Analysis of River Basin Management in Madagascar and Lessons Learned from Japan." *Water*, 14 (3): 449.

Multidisciplinary Digital Publishing Institute. https://doi.org/10.3390/w14030449.

Rakotoarimanana, H., I. Hiroshi, R. Z. M. Harivelo, M. Jun, S. Kazuyoshi, and M. Keiichi. 2024a. "Assessing future intra-basin water availability in madagascar: Accounting for climate change, population growth, and land use change." *Water Research*, 257: 121711. Elsevier.

Rakotoarimanana, H., I. Hiroshi, S. Kazuyoshi, M. Jun, R. Z. M. Harivelo, and C. A. Fernández-Palomino. 2024b. "Multi-gauge calibration comparison for simulating streamflow across the Major River Basins in Madagascar: SWAT+ Toolbox, R-SWAT, and SWAT+ Editor Hard calibration." *Hydrology Research*, nh2024188. IWA Publishing.

Rakotoarimanana, H., R. Zy Misa Harivelo, I. Hiroshi, M. Jun, and S. Kazuyoshi. 2022. "A Systematic Review of Water Resources Assessment at a Large River Basin Scale: Case of the Major River Basins in Madagascar." *Sustainability*, 14 (19): 12237. https://doi.org/10.3390/su141912237.

Rakotoarimanana, R. Z., I. Hiroshi, S. Kazuyoshi, M. Jun, R. Z. M. Harivelo, and C. A. Fernández-Palomino. 2024c. "Multi-gauge calibration comparison for simulating streamflow across the Major River Basins in Madagascar: SWAT + Toolbox, R-SWAT, and SWAT + Editor Hard calibration." *Hydrology Research*, 55 (3): 412–430. https://doi.org/10.2166/nh.2024.188.

Rakotoarisoa, M. M., C. Fleurant, A. N. Taïbi, M. Rouan, S. Caillault, T. Razakamanana, and A. Ballouche. 2018. "Un modèle multi-agents pour évaluer la vulnérabilité aux inondations : le cas des villages aux alentours du Fleuve Fiherenana (Madagascar)." *Cybergeo: European Journal of Geography*. CNRS-UMR Géographie-cités 8504. https://doi.org/10.4000/cybergeo.29144.

Ralaingita, M., G. Ennis, J. Russell-Smith, K. Sangha, and T. Razanakoto. 2022. "The Kere of Madagascar: a qualitative exploration of community experiences and perspectives." *Ecology and Society*, 27 (1). The Resilience Alliance. https://doi.org/10.5751/ES-12975-270142.

Ramahaimandimby, Z., A. Randriamaherisoa, F. Jonard, M. Vanclooster, and C. L. Bielders. 2022. "Reliability of Gridded Precipitation Products for Water Management Studies: The Case of the Ankavia River Basin in Madagascar." *Remote Sensing*, 14 (16): 3940. Multidisciplinary Digital Publishing Institute. https://doi.org/10.3390/rs14163940.

Ramahaimandimby, Z., A. Randriamaherisoa, M. Vanclooster, and C. L. Bielders. 2023. "Driving Factors of the Hydrological Response of a Tropical Watershed: The Ankavia River Basin in Madagascar." *Water*, 15 (12): 2237. Multidisciplinary Digital Publishing Institute. https://doi.org/10.3390/w15122237.

Ramahaimandimby, Z., A. Randriamaherisoa, M. Vanclooster, and C. L. Bielders. (under review). "Raingauge vs IMERG Precipitation Data: Balancing

Accuracy and Cost for a Reliable Hydrological Observatory in a Tropical River Basin." Preprints.

Ramaroson, V. H., T. Becquer, S. O. Sá, H. Razafimahatratra, J. L. Delarivière, D. Blavet, P. R. S. Vendrame, L. Rabeharisoa, and A. F. M. Rakotondrazafy. 2018. "Mineralogical analysis of ferralitic soils in Madagascar using NIR spectroscopy." *CATENA*, A Tribute to Ewart A. FitzPatrick (1926-2018), a life for Pedology and Morphology of Soils, 168: 102–109. https://doi.org/10.1016/j.catena.2017.07.016.

Rana, G., and N. Katerji. 2000. "Measurement and estimation of actual evapotranspiration in the field under Mediterranean climate: a review." *European Journal of agronomy*, 13 (2–3): 125–153. Elsevier.

Rana, S. S., S. A. Habib, M. N. H. Sharifee, N. Sultana, and S. H. Rahman. 2024. "Flood risk mapping of the flood-prone Rangpur division of Bangladesh using remote sensing and multi-criteria analysis." *Natural Hazards Research*, 4 (1): 20–31. Elsevier.

Randriamahefasoa, T. S. M., and C. J. C. Reason. 2017. "Interannual variability of rainfall characteristics over southwestern Madagascar." *Theoretical and applied climatology*, 128: 421–437. Springer.

Randriamaherisoa, A., and M. Binard. 1992. "Régionalisation des paramètres du modèle maillé: impact de la déforestation sur le régime hydrologique de la Lokoho (Madagascar)." *Acte des VIII Journées hydrologiques de l'ORSTOM: Régionalisation en hydrologie-Application au développement*, 223–232. ORSTOM.

Randriamaherisoa, A., M. Binard, and E. Persoons. 1993. "Use of GIS and remote sensing in hydrological model for impact study of land cover change in a Malagasy rural basin." *EARSeL Advances in Remote Sensing*, 2 (3). EARSeL.

Randriatsara, H. H. H., Z. Hu, X. Xu, B. Ayugi, K. T. C. L. K. Sian, R. Mumo, and V. Ongoma. 2022a. "Evaluation of gridded precipitation datasets over Madagascar." *Intl Journal of Climatology*, 42 (13): 7028–7046. https://doi.org/10.1002/joc.7628.

Randriatsara, H. H. H., Z. Hu, X. Xu, B. Ayugi, K. T. C. L. K. Sian, R. Mumo, V. Ongoma, and E. Holtanova. 2023. "Performance evaluation of CMIP6 HIGHRESMIP models in simulating precipitation over Madagascar." *Intl Journal of Climatology*, 43 (12): 5401–5421. https://doi.org/10.1002/joc.8153.

Randriatsara, H. H.-R. H., Z. Hu, B. Ayugi, E. K. Makula, F. Vuguziga, and A. Nkunzimana. 2022b. "Interannual characteristics of rainfall over Madagascar and its relationship with the Indian Ocean sea surface temperature variation." *Theor Appl Climatol*. https://doi.org/10.1007/s00704-022-03950-8.

Rasolofomanana, L. H. 2016. "Vilatily&Vulnerability of water resources in Madagascar." Accessed March 11, 2022.

https://www.pseau.org/outils/ouvrages/wateraid_vitality_and_vulnerability_of_water_ressources_in_madagascar_2016_en.pdf.

Rasolofoson, R. A., P. J. Ferraro, C. N. Jenkins, and J. P. Jones. 2015. "Effectiveness of community forest management at reducing deforestation in Madagascar." *Biological Conservation*, 184: 271–277. Elsevier.

Rasolomanana, E. harilala. 1997. "Reconnaissance hydrogéologique par méthodes électrique et électromagnétique dans la région du Lac Ihotry, Sud-Ouest de Madagascar."

Rawls, W. J., D. L. Brakensiek, and N. Miller. 1983. "Green-ampt Infiltration Parameters from Soils Data." *J. Hydraul. Eng.*, 109 (1): 62–70. https://doi.org/10.1061/(ASCE)0733-9429(1983)109:1(62).

Rodriguez, D. A., J. Tomasella, and C. Linhares. 2010. "Is the forest conversion to pasture affecting the hydrological response of Amazonian catchments? Signals in the Ji-Paraná Basin." *Hydrological Processes: An International Journal*, 24 (10): 1254–1269. Wiley Online Library.

Rodriguez-Martínez, J., and M. Santiago. 2017. *The effects of forest cover on base flow of streams in the mountainous interior of Puerto Rico, 2010*. *Scientific Investigations Report*. U.S. Geological Survey.

Rogger, M., M. Agnoletti, A. Alaoui, J. C. Bathurst, G. Bodner, M. Borga, V. Chaplot, F. Gallart, G. Glatzel, J. Hall, J. Holden, L. Holko, R. Horn, A. Kiss, S. Kohnová, G. Leitinger, B. Lennartz, J. Parajka, R. Perdigão, S. Peth, L. Plavcová, J. N. Quinton, M. Robinson, J. L. Salinas, A. Santoro, J. Szolgay, S. Tron, J. J. H. Van Den Akker, A. Viglione, and G. Blöschl. 2017. "Land use change impacts on floods at the catchment scale: Challenges and opportunities for future research." *Water Resources Research*, 53 (7): 5209–5219. https://doi.org/10.1002/2017WR020723.

Roose, É., H. Duchaufour, and G. de Noni. 2012. "Lutte antiérosive, réhabilitation des sols tropicaux et protection contre les pluies exceptionnelles." IRD éd.

Ross, C. W., L. Prihodko, J. Anchang, S. Kumar, W. Ji, and N. P. Hanan. 2018. "HYSOGs250m, global gridded hydrologic soil groups for curve-number-based runoff modeling." *Scientific data*, 5: 180091. Nature Publishing Group.

Rossi, G. 1979. "L'érosion à Madagascar: l'importance des facteurs humains." *Cahiers d'outre-mer*, 32 (128): 355–370.

Rozante, J. R., E. R. Gutierrez, A. de A. Fernandes, and D. A. Vila. 2020. "Performance of precipitation products obtained from combinations of satellite and surface observations." *International Journal of Remote Sensing*, 41 (19): 7585–7604. Taylor & Francis. https://doi.org/10.1080/01431161.2020.1763504.

Sabater, M. 2019. "ERA5-Land hourly data from 1981 to present." *Copernicus Climate Change Service (C3S) Climate Data Store (CDS)*.

Sahlu, D., E. I. Nikolopoulos, S. A. Moges, E. N. Anagnostou, and D. Hailu. 2016. “First Evaluation of the Day-1 IMERG over the Upper Blue Nile Basin.” *Journal of Hydrometeorology*, 17 (11): 2875–2882. American Meteorological Society. https://doi.org/10.1175/JHM-D-15-0230.1.

Savenije, H. H. 2004. “The importance of interception and why we should delete the term evapotranspiration from our vocabulary.”

Sawicz, K., T. Wagener, M. Sivapalan, P. A. Troch, and G. Carrillo. 2011. “Catchment classification: empirical analysis of hydrologic similarity based on catchment function in the eastern USA.” *Hydrology & Earth System Sciences Discussions*, 8 (3).

Scales, I. R. 2014. “The drivers of deforestation and the complexity of land use in Madagascar.” *Conservation and environmental management in Madagascar*, 105–126. Routledge.

Schlesinger, W. H., and S. Jasechko. 2014. “Transpiration in the global water cycle.” *Agricultural and Forest Meteorology*, 189: 115–117. Elsevier.

Schumm, S. A. 1956. “EVOLUTION OF DRAINAGE SYSTEMS AND SLOPES IN BADLANDS AT PERTH AMBOY, NEW JERSEY.” *Geol Soc America Bull*, 67 (5): 597. https://doi.org/10.1130/0016-7606(1956)67[597:EODSAS]2.0.CO;2.

Sellami, H., S. Benabdallah, I. La Jeunesse, and M. Vanclooster. 2016. “Quantifying hydrological responses of small Mediterranean catchments under climate change projections.” *Science of The Total Environment*, 543: 924–936. https://doi.org/10.1016/j.scitotenv.2015.07.006.

Sellami, H., I. La Jeunesse, S. Benabdallah, and M. Vanclooster. 2013. “Parameter and rating curve uncertainty propagation analysis of the SWAT model for two small Mediterranean catchments.” *Hydrological Sciences Journal*, 58 (8): 1635–1657. https://doi.org/10.1080/02626667.2013.837222.

Serele, C., A. Pérez-Hoyos, and F. Kayitakire. 2020. “Mapping of groundwater potential zones in the drought-prone areas of south Madagascar using geospatial techniques.” *Geoscience Frontiers*, 11 (4): 1403–1413. https://doi.org/10.1016/j.gsf.2019.11.012.

Shamsuddin, S. A., Z. Yusop, and S. Noguchi. 2014. “Influence of Plantation Establishment on Discharge Characteristics in a Small Catchment of Tropical Forest.” *International Journal of Forestry Research*, 2014: e408409. Hindawi. https://doi.org/10.1155/2014/408409.

Sivakumar, B. 2017. *Chaos in Hydrology*. Dordrecht: Springer Netherlands.

Sivapalan, M., K. Takeuchi, S. W. Franks, V. K. Gupta, H. Karambiri, V. Lakshmi, X. Liang, J. J. McDONNELL, E. M. Mendiondo, P. E. O’Connell, T. Oki, J. W. Pomeroy, D. Schertzer, S. Uhlenbrook, and E. Zehe. 2003. “IAHS Decade on Predictions in Ungauged Basins (PUB), 2003–2012: Shaping an exciting future for the hydrological sciences.” *Hydrological Sciences Journal*, 48 (6): 857–880. https://doi.org/10.1623/hysj.48.6.857.51421.

Sklash, M. G., and R. N. Farvolden. 1979. “The role of groundwater in storm runoff.” *Journal of Hydrology*, 43 (1–4): 45–65. Elsevier.

Slater, D. 2019. “Water scarcity in Brazil: a case study.” *Expeditions with MCUP*, 2019 (1): 1–42. Marine Corps University Press.

Sloan, P. G., and I. D. Moore. 1984. “Modeling subsurface stormflow on steeply sloping forested watersheds.” *Water Resources Research*, 20 (12): 1815–1822. https://doi.org/10.1029/WR020i012p01815.

Soesbergen, A. van, and M. Mulligan. 2018. “Uncertainty in data for hydrological ecosystem services modelling: potential implications for estimating services and beneficiaries for the CAZ Madagascar.” *Ecosystem Services*, 33 (Part B): 175–186. Elsevier B.V.

Song, X., P. Wang, L. Van Zwieten, N. Bolan, H. Wang, X. Li, K. Cheng, Y. Yang, M. Wang, T. Liu, and F. Li. 2022. “Towards a better understanding of the role of Fe cycling in soil for carbon stabilization and degradation.” *carbon res*, 1 (1): 5. https://doi.org/10.1007/s44246-022-00008-2.

Sophocleous, M. 2002. “Interactions between groundwater and surface water: the state of the science.” *Hydrogeology journal*, 10: 52–67. Springer.

Sorribas, M. V., R. C. Paiva, J. M. Melack, J. M. Bravo, C. Jones, L. Carvalho, E. Beighley, B. Forsberg, and M. H. Costa. 2016. “Projections of climate change effects on discharge and inundation in the Amazon basin.” *Climatic change*, 136 (3): 555–570. Springer.

Stampoulis, D., Z. S. Haddad, and E. N. Anagnostou. 2014. “Assessing the drivers of biodiversity in Madagascar by quantifying its hydrologic properties at the watershed scale.” *Remote Sensing of Environment*, 148: 1–15. https://doi.org/10.1016/j.rse.2014.03.005.

Stockfisch, N., T. Forstreuter, and W. Ehlers. 1999. “Ploughing effects on soil organic matter after twenty years of conservation tillage in Lower Saxony, Germany.” *Soil and Tillage Research*, 52 (1): 91–101. https://doi.org/10.1016/S0167-1987(99)00063-X.

Strahler, A. N. 1952. “HYPSOMETRIC (AREA-ALTITUDE) ANALYSIS OF EROSIONAL TOPOGRAPHY.” *GSA Bulletin*, 63 (11): 1117–1142. https://doi.org/10.1130/0016-7606(1952)63[1117:HAAOET]2.0.CO;2.

Strahler, A. N. 1957. “Quantitative analysis of watershed geomorphology.”

Styger, E., H. M. Rakotondramasy, M. J. Pfeffer, E. C. M. Fernandes, and D. M. Bates. 2007. “Influence of slash-and-burn farming practices on fallow succession and land degradation in the rainforest region of Madagascar.” *Agriculture, Ecosystems & Environment*, 119 (3–4): 257–269. https://doi.org/10.1016/j.agee.2006.07.012.

Su, J., X. Li, W. Ren, H. Lü, and D. Zheng. 2021. “How reliable are the satellite-based precipitation estimations in guiding hydrological modelling in South China?”

Journal of Hydrology, 602: 126705. https://doi.org/10.1016/j.jhydrol.2021.126705.

Sun, L. 2024. "Physical Mechanisms Driving Local Precipitation over the Tropical Oceans from the Perspective of Moisture Convergence." PhD Thesis. ResearchSpace@ Auckland.

Sun, Q., C. Miao, Q. Duan, H. Ashouri, S. Sorooshian, and K. Hsu. 2018. "A Review of Global Precipitation Data Sets: Data Sources, Estimation, and Intercomparisons." *Rev. Geophys.*, 56 (1): 79–107. https://doi.org/10.1002/2017RG000574.

Sungmin, O., U. Foelsche, G. Kirchengast, J. Fuchsberger, J. Tan, and W. A. Petersen. 2017. "Evaluation of GPM IMERG Early, Late, and Final rainfall estimates using WegenerNet gauge data in southeastern Austria." *Hydrology & Earth System Sciences*, 21 (12).

Tabary, P., P. DUPUY, G. L'HENAFF, C. GUEGUEN, L. Moulin, and O. LAURANTIN. 2012. "A 10-year (1997—2006) reanalysis of Quantitative Precipitation Estimation over France: methodology and first results." *IAHS-AISH publication*, (351): 255–260.

Tadross, M., L. Randriamarolaza, Z. Rabefitia, and K. Y. Zheng. 2008. "Climate change in Madagascar; recent past and future." *Washington, DC: World Bank*, 18.

Tallman, P. S., S. Collins, G. Salmon-Mulanovich, B. Rusyidi, A. Kothadia, and S. Cole. 2023. "Water insecurity and gender-based violence: A global review of the evidence." *WIREs Water*, 10 (1): e1619. https://doi.org/10.1002/wat2.1619.

Tan, J., G. J. Huffman, D. T. Bolvin, and E. J. Nelkin. 2019a. "Diurnal Cycle of IMERG V06 Precipitation." *Geophysical Research Letters*, 46 (22): 13584–13592. https://doi.org/10.1029/2019GL085395.

Tan, M. L., and Z. Duan. 2017. "Assessment of GPM and TRMM Precipitation Products over Singapore." *Remote Sensing*, 9 (7): 720. Multidisciplinary Digital Publishing Institute. https://doi.org/10.3390/rs9070720.

Tan, M. L., P. W. Gassman, R. Srinivasan, J. G. Arnold, and X. Yang. 2019b. "A review of SWAT studies in Southeast Asia: applications, challenges and future directions." *Water*, 11 (5): 914. MDPI.

Tan, M. L., and H. Santo. 2018. "Comparison of GPM IMERG, TMPA 3B42 and PERSIANN-CDR satellite precipitation products over Malaysia." *Atmospheric Research*, 202: 63–76. Elsevier.

Tan, W. J., J. F. Khor, L. Ling, and Y. F. Huang. 2018. "Misuse of Lambda (λ) in NRCS-CN Model." *E3S Web of Conferences*, 07006. EDP Sciences.

Tang, G., Y. Ma, D. Long, L. Zhong, and Y. Hong. 2016a. "Evaluation of GPM Day-1 IMERG and TMPA Version-7 legacy products over Mainland China at

multiple spatiotemporal scales." *Journal of Hydrology*, 533: 152–167. https://doi.org/10.1016/j.jhydrol.2015.12.008.

Tang, G., Z. Zeng, D. Long, X. Guo, B. Yong, W. Zhang, and Y. Hong. 2016b. "Statistical and hydrological comparisons between TRMM and GPM level-3 products over a midlatitude basin: Is day-1 IMERG a good successor for TMPA 3B42V7?" *Journal of Hydrometeorology*, 17 (1): 121–137.

Tangang, F., S. Supari, J. X. Chung, F. Cruz, E. Salimun, S. T. Ngai, L. Juneng, J. Santisirisomboon, J. Santisirisomboon, and T. Ngo-Duc. 2018. "Future changes in annual precipitation extremes over Southeast Asia under global warming of 2 C." *APN Science Bulletin*, 8 (1).

Tapiador, F. J., F. J. Turk, W. Petersen, A. Y. Hou, E. García-Ortega, L. A. Machado, C. F. Angelis, P. Salio, C. Kidd, and G. J. Huffman. 2012. "Global precipitation measurement: Methods, datasets and applications." *Atmospheric Research*, 104: 70–97. Elsevier.

Tarasova, L., S. Basso, M. Zink, and R. Merz. 2018. "Exploring controls on rainfall-runoff events: 1. Time series-based event separation and temporal dynamics of event runoff response in Germany." *Water Resources Research*, 54 (10): 7711–7732. Wiley Online Library.

Tarigan, S., K. Wiegand, Sunarti, and B. Slamet. 2018. "Minimum forest cover required for sustainable water flow regulation of a watershed: a case study in Jambi Province, Indonesia." *Hydrology and Earth System Sciences*, 22 (1): 581–594. Copernicus GmbH. https://doi.org/10.5194/hess-22-581-2018.

Taufik, M. 2022. "Baseflow Index Analysis for Bengawan Solo River, Indonesia." *Agromet*, 36 (2): 70–78.

Teale, N. G., H. Mahan, S. Bleakney, A. Berger, N. Shibley, O. W. Frauenfeld, S. M. Quiring, A. D. Rapp, E. B. Roark, and R. Washington-Allen. 2014. "Impacts of Vegetation and Precipitation on Throughfall Heterogeneity in a Tropical Pre-Montane Transitional Cloud Forest." *Biotropica*, 46 (6): 667–676. https://doi.org/10.1111/btp.12166.

Telle, A. 2024. "Basin organization and members' development agenda in the Global South." *Water International*, 49 (3–4): 298–309. https://doi.org/10.1080/02508060.2024.2321775.

Teuling, A. J., E. A. De Badts, F. A. Jansen, R. Fuchs, J. Buitink, A. J. Hoek van Dijke, and S. M. Sterling. 2019. "Climate change, reforestation/afforestation, and urbanization impacts on evapotranspiration and streamflow in Europe." *Hydrology and Earth System Sciences*, 23 (9): 3631–3652. Copernicus GmbH.

Thanapakpawin, P., J. Richey, D. Thomas, S. Rodda, B. Campbell, and M. Logsdon. 2007. "Effects of landuse change on the hydrologic regime of the Mae Chaem river basin, NW Thailand." *Journal of Hydrology*, 334 (1–2): 215–230. Elsevier.

Thiemig, V., R. Rojas, M. Zambrano-Bigiarini, V. Levizzani, and A. D. Roo. 2012. "Validation of Satellite-Based Precipitation Products over Sparsely Gauged African River Basins." *Journal of Hydrometeorology*, 13 (6): 1760–1783. American Meteorological Society. https://doi.org/10.1175/JHM-D-12-032.1.

Thompson, I., B. Mackey, S. McNulty, and A. Mosseler. 2009. "Forest resilience, biodiversity, and climate change." *Secretariat of the Convention on Biological Diversity, Montreal. Technical Series no. 43. 1-67.*, 1–67.

Tian, F., S. Hou, L. Yang, H. Hu, and A. Hou. 2018. "How Does the Evaluation of the GPM IMERG Rainfall Product Depend on Gauge Density and Rainfall Intensity?" *Journal of Hydrometeorology*, 19 (2): 339–349. American Meteorological Society. https://doi.org/10.1175/JHM-D-17-0161.1.

Uamusse, M. M., K. Tussupova, and K. M. Persson. 2020. "Climate change effects on hydropower in Mozambique." *Applied Sciences*, 10 (14): 4842. MDPI.

UPDR, D. 2003. "Monographie de la SAVA." 115.

Urban, M. C., G. Bocedi, A. P. Hendry, J.-B. Mihoub, G. Pe'er, A. Singer, J. R. Bridle, L. G. Crozier, L. De Meester, W. Godsoe, A. Gonzalez, J. J. Hellmann, R. D. Holt, A. Huth, K. Johst, C. B. Krug, P. W. Leadley, S. C. F. Palmer, J. H. Pantel, A. Schmitz, P. A. Zollner, and J. M. J. Travis. 2016. "Improving the forecast for biodiversity under climate change." *Science*, 353 (6304): aad8466. https://doi.org/10.1126/science.aad8466.

Vallet-Coulomb, C., F. Gasse, L. Robison, L. Ferry, E. Van Campo, and F. Chalié. 2006. "Hydrological modeling of tropical closed Lake Ihotry (SW Madagascar): Sensitivity analysis and implications for paleohydrological reconstructions over the past 4000 years." *Journal of Hydrology*, Water Resources in Regional Development: The Okavango River, 331 (1): 257–271. https://doi.org/10.1016/j.jhydrol.2006.05.026.

Van De Giesen, N. C., T. J. Stomph, and N. De Ridder. 2000. "Scale effects of Hortonian overland flow and rainfall-runoff dynamics in a West African catena landscape." *Hydrol. Process.*, 14 (1): 165–175. https://doi.org/10.1002/(SICI)1099-1085(200001)14:1<165::AID-HYP920>3.0.CO;2-1.

Van Genuchten, M. van, F. J. Leij, and S. R. Yates. 1991. "The RETC code for quantifying the hydraulic functions of unsaturated soils." Citeseer.

Van Soesbergen, A., and M. Mulligan. 2018. "Uncertainty in data for hydrological ecosystem services modelling: Potential implications for estimating services and beneficiaries for the CAZ Madagascar." *Ecosystem services*, 33: 175–186. Elsevier.

Vecchia, R. P., and J. Eunhea. 2019. "Understanding the Variability of Hydro Meteorological Extremes in an Evolving Climate in Madagascar." 한국대기환경학회 학술대회논문집, 95–95.

Veldkamp, T. I. E., Y. Wada, J. Aerts, P. Döll, S. N. Gosling, J. Liu, Y. Masaki, T. Oki, S. Ostberg, and Y. Pokhrel. 2017. "Water scarcity hotspots travel downstream due to human interventions in the 20th and 21st century." *Nature communications*, 8 (1): 15697. Nature Publishing Group UK London.

Veloria, A., G. J. Perez, G. Tapang, and J. Comiso. 2021. "Improved Rainfall Data in the Philippines through Concurrent Use of GPM IMERG and Ground-Based Measurements." *Remote Sensing*, 13 (15): 2859. Multidisciplinary Digital Publishing Institute. https://doi.org/10.3390/rs13152859.

Verburg, P. H., P. Alexander, T. Evans, N. R. Magliocca, Z. Malek, M. D. Rounsevell, and J. Van Vliet. 2019. "Beyond land cover change: towards a new generation of land use models." *Current Opinion in Environmental Sustainability*, 38: 77–85. Elsevier.

Villarini, G., W. F. Krajewski, G. J. Ciach, and D. L. Zimmerman. 2009. "Product-error-driven generator of probable rainfall conditioned on WSR-88D precipitation estimates." *Water Resources Research*, 45 (1). Wiley Online Library.

van Vuuren, D. P., J. Edmonds, M. Kainuma, K. Riahi, A. Thomson, K. Hibbard, G. C. Hurtt, T. Kram, V. Krey, J.-F. Lamarque, T. Masui, M. Meinshausen, N. Nakicenovic, S. J. Smith, and S. K. Rose. 2011. "The representative concentration pathways: an overview." *Climatic Change*, 109 (1): 5. https://doi.org/10.1007/s10584-011-0148-z.

Wang, J., Y. Liu, B. Li, Z. Li, Y. Zhang, S. Zhang, Y. Pan, and F. Zhang. 2024. "The Throughfall, Stemflow, and Canopy Interception Loss in Corn and Soybean Fields in Northeast China." *Water*, 16 (2): 253. Multidisciplinary Digital Publishing Institute. https://doi.org/10.3390/w16020253.

Wang, W., H. Lu, T. Zhao, L. Jiang, and J. Shi. 2017a. "Evaluation and Comparison of Daily Rainfall From Latest GPM and TRMM Products Over the Mekong River Basin." *IEEE J. Sel. Top. Appl. Earth Observations Remote Sensing*, 10 (6): 2540–2549. https://doi.org/10.1109/JSTARS.2017.2672786.

Wang, X., Y. Zhang, R. Hu, Y. Pan, and R. Berndtsson. 2012. "Canopy storage capacity of xerophytic shrubs in Northwestern China." *Journal of Hydrology*, 454: 152–159. Elsevier.

Wang, Z., R. Zhong, C. Lai, and J. Chen. 2017b. "Evaluation of the GPM IMERG satellite-based precipitation products and the hydrological utility." *Atmospheric Research*, 196: 151–163. https://doi.org/10.1016/j.atmosres.2017.06.020.

Whipkey, R. Z. 1978. "Flow within the soil." *Hillslope hydrology*. John WILEY and sons.

Wilk, J., L. Andersson, and V. Plermkamon. 2001. "Hydrological impacts of forest conversion to agriculture in a large river basin in northeast Thailand." *Hydrological Processes*, 15 (14): 2729–2748. Wiley Online Library.

Winter, T. C. 2000. *Ground water and surface water: a single resource*. Diane Publishing.

WMO. 1987. “Tropical hydrology.”

WMO. 2022. “Climate change increased extreme rainfall in Southeast Africa storms - Madagascar.” Accessed October 2, 2022. https://reliefweb.int/report/madagascar/climate-change-increased-extreme-rainfall-southeast-africa-storms.

Wohl, E., A. Barros, N. Brunsell, N. A. Chappell, M. Coe, T. Giambelluca, S. Goldsmith, R. Harmon, J. M. Hendrickx, and J. Juvik. 2012. “The hydrology of the humid tropics.” *Nature Climate Change*, 2 (9): 655–662. Nature Publishing Group.

Wu, Q., L. Ke, J. Wang, T. M. Pavelsky, G. H. Allen, Y. Sheng, X. Duan, Y. Zhu, J. Wu, and L. Wang. 2023. “Satellites reveal hotspots of global river extent change.” *Nature communications*, 14 (1): 1587. Nature Publishing Group UK London.

Wu, S., J. Zhao, H. Wang, and M. Sivapalan. 2021. “Regional Patterns and Physical Controls of Streamflow Generation Across the Conterminous United States.” *Water Resources Research*, 57 (6): e2020WR028086. https://doi.org/10.1029/2020WR028086.

Xu, J., Z. Ma, S. Yan, and J. Peng. 2022. “Do ERA5 and ERA5-land precipitation estimates outperform satellite-based precipitation products? A comprehensive comparison between state-of-the-art model-based and satellite-based precipitation products over mainland China.” *Journal of Hydrology*, 605: 127353. Elsevier.

Yeh, H.-C., Y.-C. Chen, C.-H. Chang, C.-H. Ho, and C. Wei. 2017. “Rainfall Network Optimization Using Radar and Entropy.” *Entropy*, 19 (10): 553. Multidisciplinary Digital Publishing Institute. https://doi.org/10.3390/e19100553.

Yuan, F., B. Wang, C. Shi, W. Cui, C. Zhao, Y. Liu, L. Ren, L. Zhang, Y. Zhu, T. Chen, S. Jiang, and X. Yang. 2018. “Evaluation of hydrological utility of IMERG Final run V05 and TMPA 3B42V7 satellite precipitation products in the Yellow River source region, China.” *Journal of Hydrology*, 567: 696–711. https://doi.org/10.1016/j.jhydrol.2018.06.045.

Zhang, M., N. Liu, R. Harper, Q. Li, K. Liu, X. Wei, D. Ning, Y. Hou, and S. Liu. 2017. “A global review on hydrological responses to forest change across multiple spatial scales: Importance of scale, climate, forest type and hydrological regime.” *Journal of Hydrology*, 546: 44–59. Elsevier.

Zhu, A. 2018. “Hot money, cold beer: Navigating the vanilla and rosewood export economies in northeastern Madagascar.” *American Ethnologist*, 45 (2): 253–267. https://doi.org/10.1111/amet.12636.

Ziegler, A. 2004. “Hydrological consequences of landscape fragmentation in mountainous northern Vietnam: evidence of accelerated overland flow generation.” *Journal of Hydrology*.

Zimmermann, B., and H. Elsenbeer. 2009. “The near-surface hydrological consequences of disturbance and recovery: a simulation study.” *Journal of Hydrology*, 364 (1–2): 115–127. Elsevier.

Zimmermann, B., H. Elsenbeer, and J. M. De Moraes. 2006. “The influence of land-use changes on soil hydraulic properties: Implications for runoff generation.” *Forest Ecology and Management*, 222 (1): 29–38. https://doi.org/10.1016/j.foreco.2005.10.070.

Zorzetto, E., and M. Marani. 2019. “Downscaling of rainfall extremes from satellite observations.” *Water Resources Research*, 55 (1): 156–174. Wiley Online Library.

Zubieta, R., A. Getirana, J. C. Espinoza, W. Lavado-Casimiro, and L. Aragon. 2017. “Hydrological modeling of the Peruvian–Ecuadorian Amazon Basin using GPM-IMERG satellite-based precipitation dataset.” *Hydrology and Earth System Sciences*, 21 (7): 3543–3555. Copernicus GmbH. https://doi.org/10.5194/hess-21-3543-2017.

Zwartendijk, B. W., H. J. van Meerveld, A. J. Teuling, C. P. Ghimire, and L. A. Bruijnzeel. 2023. “Rainfall-runoff responses and hillslope moisture thresholds for an upland tropical catchment in Eastern Madagascar subject to long-term slash-and-burn practices.” *Hydrological Processes*, 37 (8): e14937. https://doi.org/10.1002/hyp.14937.

Zwartendijk, B. W., H. J. Van Meerveld, C. P. Ghimire, L. A. Bruijnzeel, M. Ravelona, and J. P. G. Jones. 2017. “Rebuilding soil hydrological functioning after swidden agriculture in eastern Madagascar.” *Agriculture, ecosystems & environment*, 239: 101–111. Elsevier.

Zwartendijk, B. W., H. J. Van Meerveld, C. P. Ghimire, M. Ravelona, J. Lahitiana, and L. A. Bruijnzeel. 2020. “Soil water- and overland flow dynamics in a tropical catchment subject to long-term slash-and-burn agriculture.” *Journal of Hydrology*, 582: 124287. https://doi.org/10.1016/j.jhydrol.2019.124287.

11. Annexes

Annexe A : Modèle SWAT (Chapitre 2)

- Runoff volume: SCS Curve Number Procedure

The SCS curve number equation A.1 is :

$$Q_{surf} = \frac{(Rday - Ia)}{Rday - Ia + S} \qquad \text{A.1.}$$

where Q_{surf} is the accumulated runoff or rainfall excess (mm H_2O), R_{day} is the rainfall depth for the day (mm H_2O), I_a is the initial abstractions which includes surface storage, interception and infiltration prior to runoff (mm H_2O), and S is the retention parameter (mm H_2O).

The retention parameter varies spatially due to changes in soils, land use, management and slope and temporally due to changes in soil water content. The retention parameter is defined as (equation A.2):

$$S = \frac{1000}{CN} - 10 \qquad \text{A.2.}$$

where CN is the curve number for the day. The initial abstractions, Ia, is commonly approximated as 0.2S and equation A.1.

$$Q_{surf} = \frac{(R_{day} - 0.2S)^2}{(R_{day} + 0.8S)} \qquad \text{A.3.}$$

Runoff will only occur when $R_{day} > I_a$.

- Runoff volume: Green & Ampt infiltration method

The Green-Ampt Mein-Larson infiltration rate is defined as (Equation A.4):

$$f_{inf,t} = K_e \cdot \left(1 + \frac{\Psi_{wf} \cdot \Delta\theta_v}{F_{inf,t}}\right) \qquad \text{A.4.}$$

where f_{inf} is the infiltration rate at time t (mm h^{-1}), K_e is the effective hydraulic conductivity (mm h^{-1}), Ψ_{wf} is the wetting front matric potential (mm), $\Delta\Theta_v$ is the change in volumetric moisture content across the wetting front (mm mm^{-1}) and F_{inf} is the cumulative infiltration at time t (mm H_2O).

When the rainfall intensity is less than the infiltration rate, all the rainfall will infiltrate during the time period and the cumulative infiltration for that time period is calculated (equation A.5):

$$F_{inf,t} = F_{inf,t-1} + R_{\Delta t} \qquad \text{A.5.}$$

where $F_{inf,t}$ is the cumulative infiltration for a given time step (mm H_2O), $F_{inf,t-1}$ isthe cumulative infiltration for the previous time step (mm H_2O), and R_t is the amount of rain falling during the time step (mm H_2O).

The infiltration rate defined by equation A.6 is a function of the infiltrated volume, which in turn is a function of the infiltration rates in previous time steps. To avoid numerical errors over long time steps, f_{inf} is replaced by dF_{inf}/dt in equation A.5. and integrated to obtain equation A.6 :

$$F_{inf,t} = F_{inf,t-1} + K_e \cdot \Delta t + \Psi_{wf} \cdot \Delta\theta_v \cdot \ln\left[\frac{F_{inf,t} + \Psi_{wf} \cdot \Delta\theta_v}{F_{inf,t-1} + \Psi_{wf} \cdot \Delta\theta_v}\right] \qquad \text{A.6.}$$

Equation A.6 must be solved iteratively for $F_{inf,t}$, the cumulative infiltration at the end of the time step. A successive substitution technique is used.

The Green-Ampt effective hydraulic conductivity parameter, K_e, is approximately equivalent to one-half the saturated hydraulic conductivity of the soil, K_{sat} (Bouwer, 1969). Nearing et al. (1996) developed an equation to calculate the effective hydraulic conductivity as a function of saturated hydraulic conductivity and curve number. This equation A.7 incorporates land cover impacts into the calculated effective hydraulic conductivity. The equation for effective hydraulic conductivity is:

$$K_e = \frac{56.82 \cdot K_{sat}^{0.286}}{1 + 0.051 \cdot \exp(0.062 \cdot CN)} - 2 \qquad \text{A.7.}$$

where K_e is the effective hydraulic conductivity (mm h^{-1}), K_{sat} is the saturated hydraulic conductivity (mm h^{-1}), and CN is the curve number.

- Canopy storage in SWAT model

When calculating surface runoff, the SCS curve number method lumps canopy interception in the term for initial abstractions. This variable also includessurface storage and infiltration prior to runoff and is estimated as 20% of the retention parameter value for a given day. When the Green and Ampt infiltration equation is used to calculate surface runoff and infiltration, the interception of rainfall by the canopy must be calculated separately.

SWAT allows the maximum amount of water that can be held in canopy storage to vary from day to day as a function of the leaf area index:

$$can_{day} = can_{mx} \cdot \frac{LAI}{LAI_{mx}} \qquad \text{A.8.}$$

where can_{day} is the maximum amount of water that can be trapped in the canopy on a given day (mm H_2O), can_{mx} is the maximum amount of water that can be trapped in the canopy when the canopy is fully developed (mm H_2O), LAI is the leaf area index for a given day, and LAI_{mx} is the maximum leaf area index for the plant.

- Potential evapotraspiration

The three PET methods included in SWAT vary in the amount of required inputs. The Penman-Monteith method requires solar radiation, air temperature, relative humidity and wind speed. The Priestley-Taylor method requires solar radiation, air temperature and relative humidity. The Hargreaves method requires air temperature only.

Penman-Monteith

The Penman-Monteith equation combines components that account for energy needed to sustain evaporation, the strength of the mechanism required to remove the water vapor and aerodynamic and surface resistance terms. The Penman-Monteith equation A.9 is:

$$\lambda E = \frac{\Delta \cdot (H_{net} - G) + \rho_{air} \cdot c_p \cdot [e_z^o - e_z] / r_a}{\Delta + \gamma \cdot (1 + r_c / r_a)} \qquad \text{A.9.}$$

where λ*E* is the latent heat flux density (MJ m^{-2} d^{-1}), *E* is the depth rate evaporation (mm d^{-1}), Δ is the slope of the saturation vapor pressure-temperature curve, *de/dT* (kPa ˚C^{-1}), H_{net} is the net radiation (MJ m^{-2} d^{-1}), *G* is the heat flux density to the ground (MJ m^{-2} d^{-1}), ρ_{air} is the air density (kg m^{-3}), c_p is the specific heat at constant pressure (MJ kg^{-1} ˚C^{-1}), e_z is the saturation vapor pressure of air at height *z* (kPa), e_z is the water vapor pressure of air at height *z* (kPa), γ is the psychrometric constant (kPa ˚C^{-1}), r_c is the plant canopy resistance (s m^{-1}), and r_a is the diffusion resistance of the air layer (aerodynamic resistance) (s m^{-1}).

Priestley-Taylor method

Priestley and Taylor (1972) developed a simplified version of the combination equation for use when surface areas are wet. The aerodynamic component was removed and the energy component was multiplied by a coefficient, α_{pet} = 1.28, when the general surroundings are wet or under humid conditions (Equation A.10).

$$\lambda E_o = \alpha_{pet} \cdot \frac{\Delta}{\Delta + \gamma} \cdot (H_{net} - G) \qquad \text{A.10.}$$

where λ is the latent heat of vaporization (MJ kg^{-1}), Eo is the potential evapotranspiration (mm d^{-1}), αpet is a coefficient, Δ is the slope of the saturation vapor pressure-temperature curve, de/dT (kPa ˚C^{-1}), γ is the psychrometric constant (kPa ˚C^{-1}), Hnet is the net radiation (MJ m^{-2} d^{-1}), and G is the heat flux density to the ground (MJ m^{-2} d^{-1}).

Hargreaves method

The Hargreaves method was originally derived from eight years of cool-season Alta fescue grass lysimeter data from Davis, California. Several improvements were mad to the original equation and the form used in SWAT was published in 1985 (Equation A.11).

$$\lambda E_o = 0.0023 \cdot H_0 \cdot (T_{mx} - T_{mn})^{0.5} \cdot (\overline{T}_{av} + 17.8) \qquad \text{A.11.}$$

Where λ is the latent heat of vaporization (MJ kg^{-1}), E_o is the potential evapotranspiration (mm d^{-1}), H_0 is the extraterrestrial radiation (MJ m^{-2} d^{-1}), T_{mx} is the minimum air temprerature for a given day (°C), and T_{av} is the mean air temperature for a given day (°C).

- Perched water table

For an HRU with a seasonal high water table, if the soil profile becomes saturated to the point that percolation for upper soil layers to lower soil layers is inhibited, water will pond in the soil profile and create a perched water table.

SWAT allows the user to define the depth to an impervious layer for the HRU. If the depth to the impervious layer is in the soil profile, no water is allowed to percolate out of the soil profile. If the impervious layer is defined below the soil profile, percolation out of the soil profile is adjusted from the value determined with equation A.12 using:

$$w_{perc,btm} = w_{perc,btm,orig} \cdot \frac{depth_{diff}}{depth_{diff} + \exp\left[8.833 - 2.598 \cdot depth_{diff}\right]} \qquad \text{A.12.}$$

where $w_{perc,btm}$ is the amount of water percolating out of the soil profile on a given day (mm H_2O), $w_{perc,btm,orig}$ is the amount of water percolating out of the soil profile on a given day (mm H_2O), and $depth_{diff}$ is the distance from the bottom of the soil profile to the impervious layer (m).

- Lateral flow

Lateral flow will be significant in areas with soils having high hydraulic conductivities in surface layers and an impermeable or semipermeable layer at a shallow depth. In such a system, rainfall will percolate vertically until it encounters the impermeable layer. The water then ponds above the impermeable layer forming a saturated zone of water, i.e. a perched water table. This saturated zone is the source of water for lateral subsurface flow.

SWAT incorporates a kinematic storage model for subsurface flow developed by Sloan et al. (1983) and summarized by Sloan and Moore (1984). This model simulates subsurface flow in a two-dimensional cross-section along a flow path down a steep hillslope. The kinematic approximation was used in its derivation.

This model is based on the mass continuity equation, or mass water balance, with the entire hillslope segment used as the control volume. The hillslope segment has a permeable soil surface layer of depth D_{perm} and length L_{hill} with an impermeable soil layer or boundary below it as shown in Figure A1 and A2. The hillslope segment is oriented at an angle α_{hill} to the horizontal.

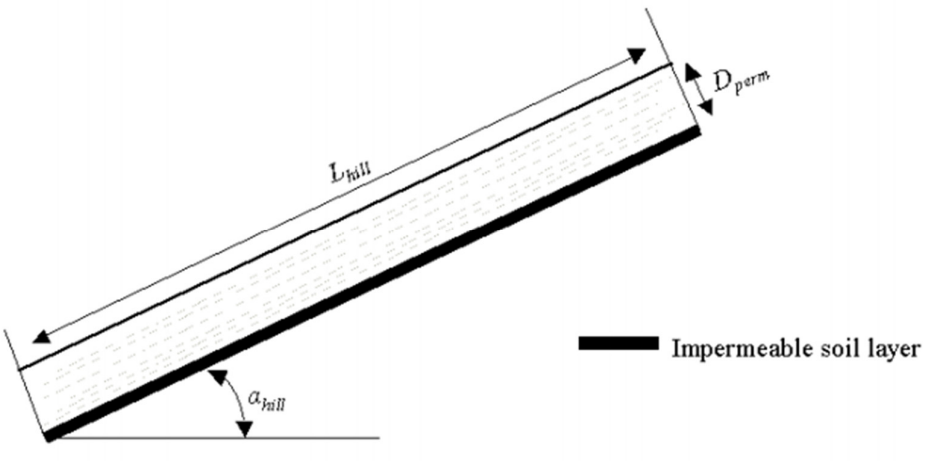

Figure A. 1. Conceptual representation of the hillslope segment.

The kinematic wave approximation of saturated subsurface or lateral flow assumes that the lines of flow in the saturated zone are parallel to the impermeable boundary and the hydraulic gradient equals the slope of the bed.

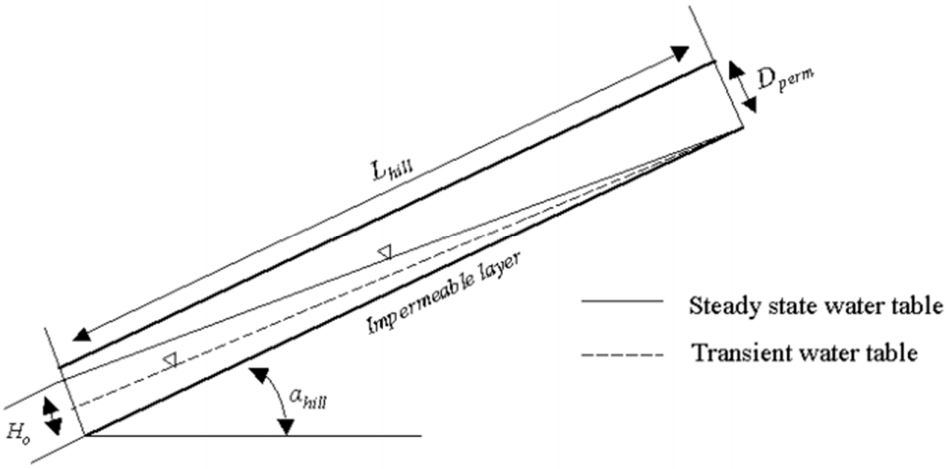

Figure A. 2. Behaviour of the water as assumed in the kinematic storage model.

Annexe B : Descripteurs de bassin versant (Chapitres 3 et 5)

Attributes	CD	WS1	WS2	WS3	WS4
Topography / Morphometry	Drainage area (A), km²	1116.0	623.9	197.1	69.9
	Perimeter (P), km	198.0	131.8	93.2	56.8
	Basin length (L_b), km	54.6	35.1	32.1	17.1
	Mean slope, °	16.3	18.4	18.9	18.2
	Elevation range (H_{min}, H_{max}), m	14, 1469	56, 1469	56, 1309	45, 1271
	Gravelius coefficient (K_G),	1.7	1.5	1.9	1.9
	Effective basin width (R_b), km	20.4	17.8	6.1	4.1
	Elongation ratio (R_e),	0.7	0.8	0.5	0.6
	Unit shape factor (R_u)	1.6	1.4	2.3	2.0
	Total relief (R_r)	1455	1413	1253	1226
	Relative relief (R_r), km	1.4	1.4	1.2	1.2
	Relief ratio (R_h)	0.03	0.04	0.04	0.07
	Total stream length (L_t)	1153.8	621.9	206.2	70.5
	Length of main stream (L_c), km	94.0	49.3	31.4	9.9
	Total number of stream segment (N_u)	5652.0	3647.0	1166.0	426.0
	Drainage density ($D_{d)}$, $km.km^{-2}$	1.03	1.00	1.05	1.00
	Constant of channel maintenance (C_m)	0.97	1.00	0.96	0.99
	Ruggedness number (R_n)	1.5	1.4	1.3	1.2
Land cover	M_Crop	35.6	15	36.3	40.8
	Mos	9.6	7.6	23.1	10.7
	Tree	54.7	77.4	40.6	48.4
	CN_est	63.3	58.7	64.1	64.5
Soil	Acrisols (Acri)	24.7	7.9	18.9	30.5
	Ferrasols (Ferra)	73.1	90.1	78.8	64.7
	Lixisols (Lixi)	1.7	1.2	2.3	4.7
	Cambisols (Cambi)	0.4	0.7	0	0.2
	Sandy-Clay (S-C)	0.5	0.4	0.8	0.0
	Clay-Loam (C-L)	28.4	29.0	42.0	47.5
	Sandy-Clay-Loam (S-C-L)	71.0	70.6	57.2	52.5
	Organic Carbon Density OC (g/dm^3)	362.2	371.7	383.7	373.4
	Dg (µm)	299.0	295.1	301.2	294.4
	Moderate runoff potential (H-C)	34.8	28.5	18.5	48.8
	High runoff potential (H-D)	65.2	71.5	81.5	51.2
Geology	Gneiss	14.3	22.6	0.0	0.9
	Gran	70.7	64.0	88.9	55.5
	Shales	6.4	1.8	0.0	43.6
	Quartz.	8.6	11.6	11.1	0.0

Annexe C : Localisation géographique des pluviomètres au sol et des exutoires (Chapitre 3)

Rain gauge	South Latitude (Decimal degrees)	Longitude (Decimal degrees)	Elevation (m)
Antalaha **A**	-14.90805556	50.27399167	83
Antsahamanenona **B**	-14.91933611	50.24931111	25
Ambohitsara **C**	-14.95564722	50.23177222	26
Antombana **D**	-14.99480278	50.17094722	35
Ambarabaha **E**	-14.99439167	50.10634722	91
Antsahoragna **F**	-14.98180833	50.09081667	152
Marofinaritra **G**	-15.03640556	50.11960833	87
Antsambalahy **H**	-15.11241389	50.10338056	151
Antakotako **I**	-15.16114722	50.08871667	153
Colline Antakotako **J**	-15.17621944	50.06073889	683
Manakambahiny **K**	-15.23339722	50.06914167	284
Antsahantitra **L**	-15.1498	50.01704722	165
Beravintsara **M**	-15.14563889	49.95935	208
Andranolavabe **N**	-15.14064722	49.93002778	233
Exutoires			
Ankavia	-14.91690278	50.24826667	14
Ankaviabe	-15.04353333	50.103975	60
Sahafihitry	-15.04523056	50.11056389	58
Antsahovy	-14.99601667	50.10306667	44

Annexe D : Grille de corrélation entre les pluviomètres (Chapitres 4 et 7).

	AMBARABAHA	AMBOHITSARA	ANDRANOLAVABE	ANTAKOTAKO	ANTALAHA	ANTOMBANA	ANTSAHAMENONA	ANTSAHANTITRA	ANTSAHORAGNA	ANTSAMBALAHY	BERAVINTSARA	COLLINE ANTAKOTAKO	MANAKAMBAHINY	MAROFINATRA
AMBARABAHA	**1.000**	0.749	0.508	0.635	0.646	0.690	0.708	0.668	0.914	0.736	0.603	0.690	0.659	0.705
AMBOHITSARA	0.749	**1.000**	0.487	0.575	0.850	0.861	0.900	0.616	0.799	0.628	0.528	0.642	0.663	0.679
ANDRANOLAVABE	0.508	0.487	**1.000**	0.697	0.382	0.501	0.414	0.738	0.543	0.697	0.841	0.756	0.659	0.541
ANTAKOTAKO	0.635	0.575	0.697	**1.000**	0.491	0.540	0.545	0.785	0.647	0.882	0.711	0.933	0.827	0.696
ANTALAHA	0.646	0.850	0.382	0.491	**1.000**	0.694	0.914	0.457	0.673	0.540	0.370	0.536	0.569	0.598
ANTOMBANA	0.690	0.861	0.501	0.540	0.694	**1.000**	0.737	0.631	0.743	0.646	0.569	0.626	0.637	0.681
ANTSAHAMENONA	0.708	0.900	0.414	0.545	0.914	0.737	**1.000**	0.518	0.734	0.596	0.432	0.582	0.602	0.624
ANTSAHANTITRA	0.668	0.616	0.738	0.785	0.457	0.631	0.518	**1.000**	0.700	0.753	0.828	0.807	0.699	0.669
ANTSAHORAGNA	0.914	0.799	0.543	0.647	0.673	0.743	0.734	0.700	**1.000**	0.724	0.655	0.734	0.721	0.646
ANTSAMBALAHY	0.736	0.628	0.697	0.882	0.540	0.646	0.596	0.753	0.724	**1.000**	0.715	0.879	0.779	0.752
BERAVINTSARA	0.603	0.528	0.841	0.711	0.370	0.569	0.432	0.828	0.655	0.715	**1.000**	0.768	0.648	0.603
COLLINE ANTAKOTAKO	0.690	0.642	0.756	0.933	0.536	0.626	0.582	0.807	0.734	0.879	0.768	**1.000**	0.864	0.653
MANAKAMBAHINY	0.659	0.663	0.659	0.827	0.569	0.637	0.602	0.699	0.721	0.779	0.648	0.864	**1.000**	0.620
MAROFINATRA	0.705	0.679	0.541	0.696	0.598	0.681	0.624	0.669	0.646	0.752	0.603	0.653	0.620	**1.000**

Annexe E : Matrice des distances entre les pluviomètres (Chapitres 3, 4 et 7).

	AMBARABAHA	AMBOHITSARA	ANDRANOLAVABE	ANTAKOTAKO	ANTALAHA	ANTOMBANA	ANTSAHAMENONA	ANTSAHANTITRA	ANTSAHORAGNA	ANTSAMBALAHY	BERAVINTSARA	COLLINE ANTAKOTAKO	MANAKAMBAHINY	MAROFINATRA
AMBARABAHA	**0.00**	14.16	24.93	18.55	20.41	6.95	17.48	19.69	2.17	13.06	23.02	20.71	26.75	4.86
AMBOHITSARA	14.16	**0.00**	38.36	27.45	6.95	7.85	4.44	31.54	15.44	22.17	36.06	30.56	35.36	15.01
ANDRANOLAVABE	24.93	38.36	**0.00**	17.21	45.06	30.52	42.17	9.41	24.65	18.89	3.20	14.59	18.13	23.42
ANTAKOTAKO	18.55	27.45	17.21	**0.00**	34.37	20.42	31.84	7.80	19.85	5.62	14.01	3.44	8.27	14.20
ANTALAHA	20.41	6.95	45.06	34.37	**0.00**	14.66	2.93	38.46	21.33	29.12	42.85	37.50	42.20	21.85
ANTOMBANA	6.95	7.85	30.52	20.42	14.66	**0.00**	11.87	23.83	8.74	14.90	28.22	23.31	28.58	7.19
ANTSAHAMENONA	17.48	4.44	42.17	31.84	2.93	11.87	**0.00**	35.69	18.40	26.51	39.99	34.91	39.78	19.04
ANTSAHANTITRA	19.69	31.54	9.41	7.80	38.46	23.83	35.69	**0.00**	20.21	10.16	6.22	5.53	10.81	16.70
ANTSAHORAGNA	2.17	15.44	24.65	19.85	21.33	8.74	18.40	20.21	**0.00**	14.51	22.99	21.75	27.94	6.79
ANTSAMBALAHY	13.06	22.17	18.89	5.62	29.12	14.90	26.51	10.16	14.51	**0.00**	15.91	8.42	13.88	8.59
BERAVINTSARA	23.02	36.06	3.20	14.01	42.85	28.22	39.99	6.22	22.99	15.91	**0.00**	11.41	15.28	21.05
COLLINE ANTAKOTAKO	20.71	30.56	14.59	3.44	37.50	23.31	34.91	5.53	21.75	8.42	11.41	**0.00**	6.39	16.71
MANAKAMBAHINY	26.75	35.36	18.13	8.27	42.20	28.58	39.78	10.81	27.94	13.88	15.28	6.39	**0.00**	22.46
MAROFINATRA	4.86	15.01	23.42	14.20	21.85	7.19	19.04	16.70	6.79	8.59	21.05	16.71	22.46	**0.00**

Annexe F : Méthode de polygone de Thiessen (Chapitre 4)

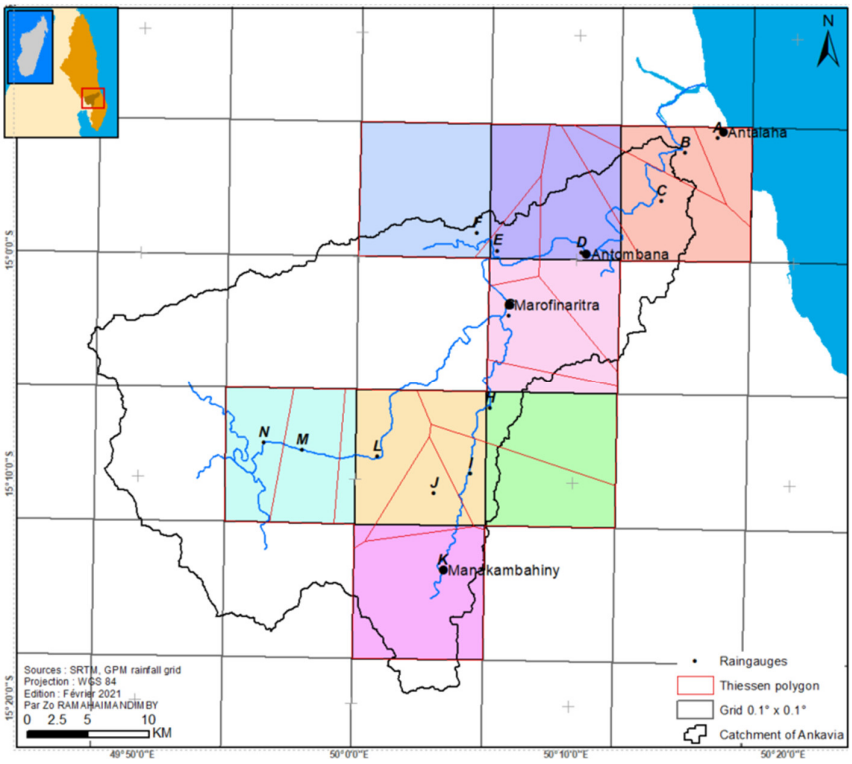

Annexe G : Séparation du débit de base (échelle journalière) (Chapitre 5) WS1 = Ankavia ; WS2 = Ankaviabe ; WS3 = Sahafihitry ; WS4 = Antsahovy

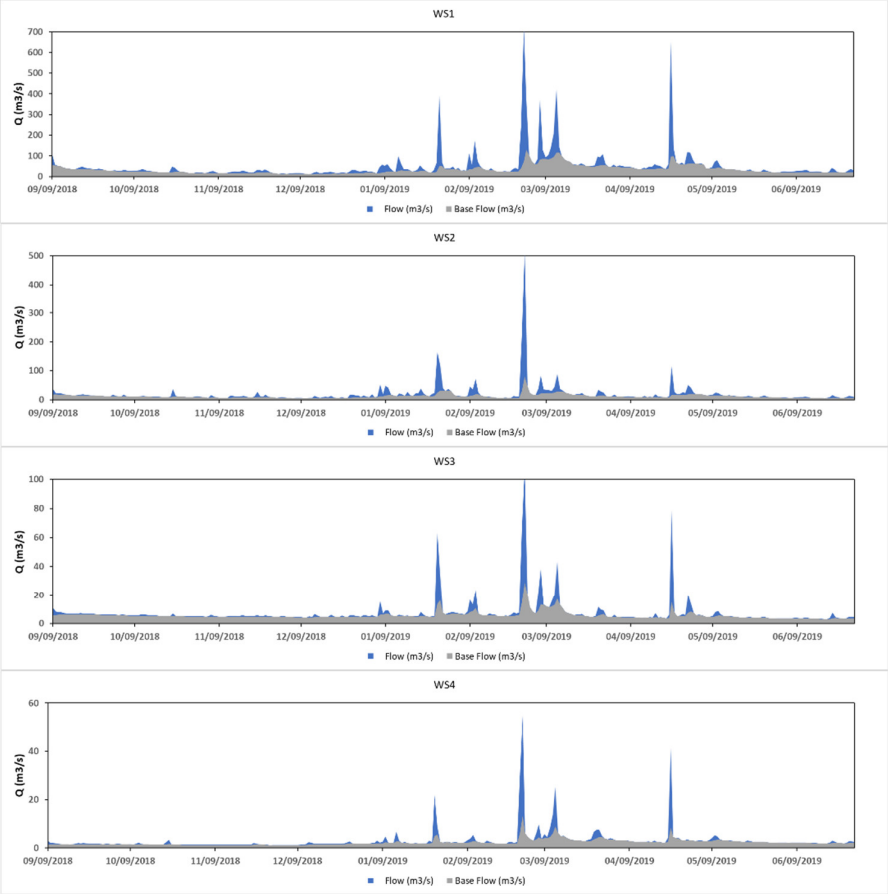

Annexe H : Signatures hydrologiques (Chapitre 5)

HSs	WS 1	WS 2	WS 3	WS 4
BFI [-]	0.63	0.60	0.68	0.68
Rc [-]	0.34	0.09	0.13	0.26
Qp [mm/h]	0.66	0.34	0.71	1.38
ts [h/km]	0.11	0.13	0.11	0.22
Q5 [mm/day]	8.65	5.72	6.05	7.4
Q95 [mm/day]	1.25	0.87	1.58	1.60
q_mean [mm/day]	3.93	2.80	3.22	3.78

Annexe I : Corrélation entre les CD et les HS sélectionnés WS1 (Ankavia) = vert ; WS2 (Ankaviabe) = rouge ; WS3 (Sahafihitry) = bleu ; WS4 (Antsahovy) = gris (Chapitre 5)

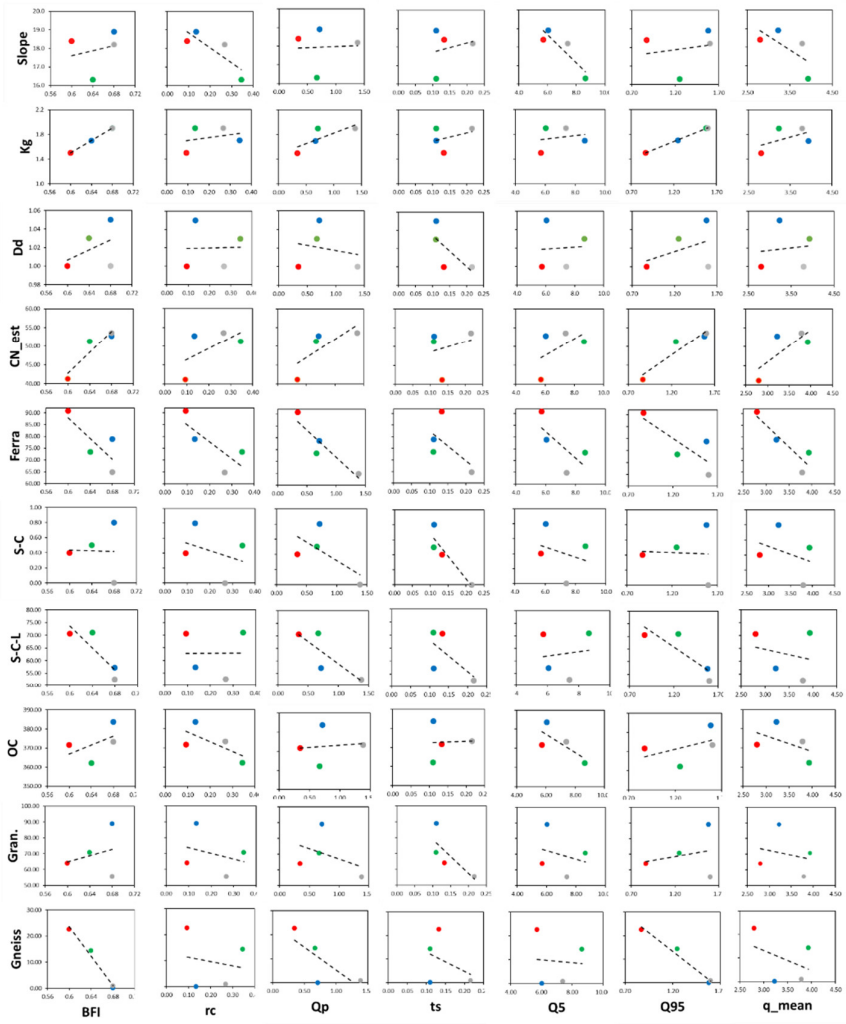

Limites : Faible significativité statistique, sensibilité aux valeurs extrêmes, faible représentativité

Annexe J : La charte des couleurs de Munsell (Chapitre 6)

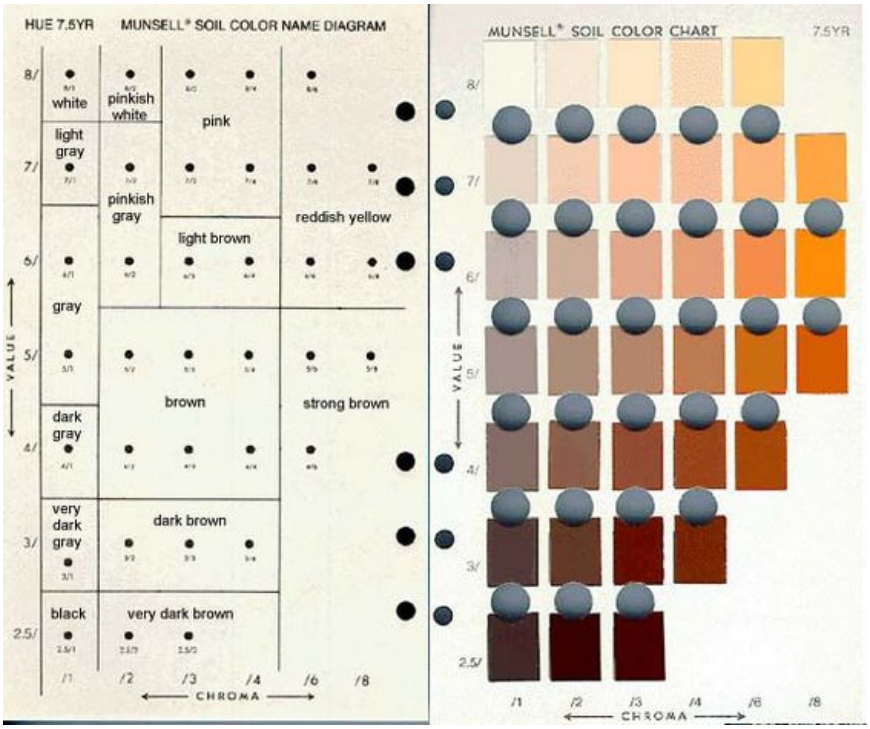

Annexe K : Séparation linéaire de l'hydrogramme telle que mise en œuvre dans l'outil Visuhydro (Rocha 2014) (Chapitre 6)

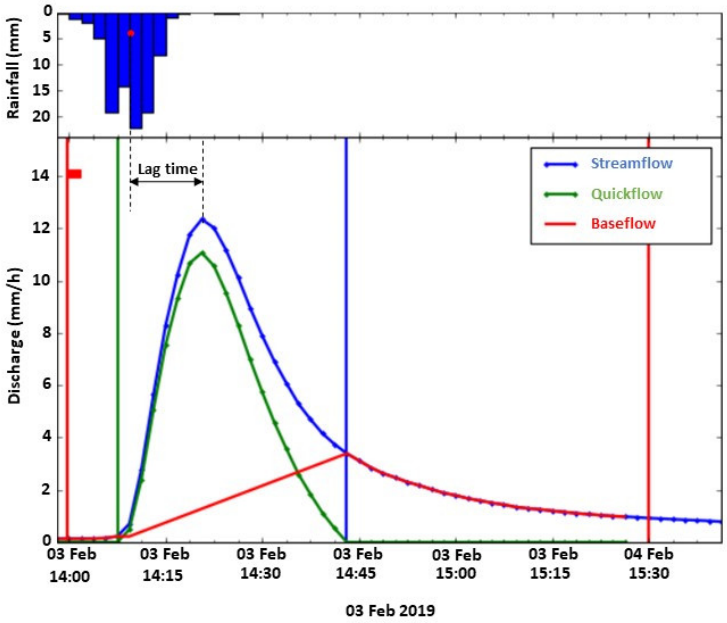

Annexe L : pH du sol sous chaque type de couvert végétal : prairie (ancienne rizière irriguée), jachère, forêt, terre cultivée (Chapitre 6)

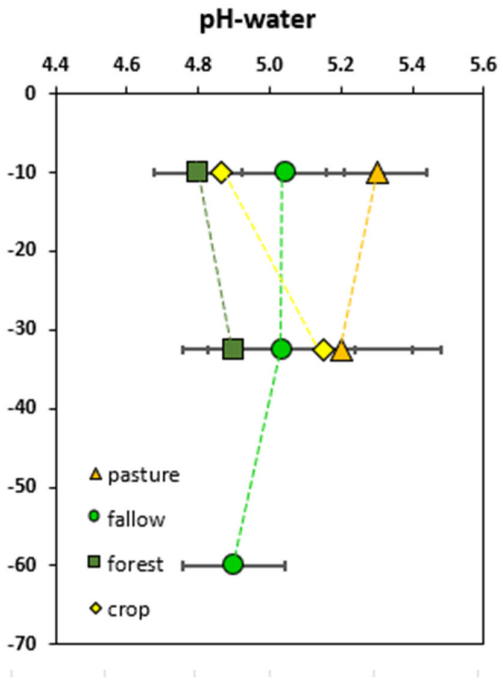

Publications et conférences

Publications dans des revues avec comité de lecture

Ramahaimandimby, Z., A. Randriamaherisoa, F. Jonard, M. Vanclooster, and C. L. Bielders. 2022. "Reliability of Gridded Precipitation Products for Water Management Studies: The Case of the Ankavia River Basin in Madagascar." *Remote Sensing*, 14 (16): 3940. Multidisciplinary Digital Publishing Institute. https://doi.org/10.3390/rs14163940.

Ramahaimandimby, Z., A. Randriamaherisoa, M. Vanclooster, and C. L. Bielders. 2023. "Driving Factors of the Hydrological Response of a Tropical Watershed: The Ankavia River Basin in Madagascar." *Water*, 15 (12): 2237. Multidisciplinary Digital Publishing Institute. https://doi.org/10.3390/w15122237.

Articles soumis ou à soumettre

Ramahaimandimby, Z., A. Randriamaherisoa, M. Vanclooster, and C. L. Bielders. "Raingauge vs IMERG precipitation data : Balancing Accuracy and Cost for a Reliable Hydrological Observatory in a Tropical River Basin." Submitted to *Hydrological Sciences Journal* in September 2024.

Ramahaimandimby, Z., A. Randriamaherisoa, M. Vanclooster, and C. L. Bielders. "Unraveling the impacts of land cover and climate changes on hydrological response of a tropical river basin: the case of the Sahafihitry catchment, Madagascar". To be submitted.

Ramahaimandimby, Z., A. Randriamaherisoa, M. Vanclooster, and C. L. Bielders. 'How Tropical Land Cover Shapes Streamflow: Insights from the Ankavia River Basin, Madagascar". To be submitted.

Communications orales

Ramahaimandimby, Z., A. Randriamaherisoa, M. Vanclooster, and C. L. Bielders. Unraveling the impacts of land cover and climate changes on hydrological response of a tropical river basin: the case of the Sahafihitry catchment, Madagascar. Circle U Knowledge Hub Climate&Louvain4water, Humboldt Universität zu Berlin, November 2024.

Ramahaimandimby, Z., A. Randriamaherisoa, M. Vanclooster, and C. L. Bielders. Etudes des altérations hydrologiques du bassin versant d'Ankavia et options de gestion dans une perspective de GIRE. Water symposium. Université catholique de Louvain, Louvain-la-Neuve, Belgique, April 2022.

Ramahaimandimby, Z., A. Randriamaherisoa, M. Vanclooster, and C. L. Bielders. Unraveling the impacts of land cover and climate changes on hydrological response of a tropical river basin: the case of the Sahafihitry catchment, Madagascar. SWAT Conference, Czech University of Life Sciences (CZU), Prague, July 2022.

Ramahaimandimby, Z., J. Benitsiafantoka and M. Vanclooster. Projet GIRE SAVA : Renforcement des capacités en Gestion Intégrée des Ressources en Eau de la région SAVA. World Water Day 2021, Sambava, Madagascar, April 2021.

Ramahaimandimby, Z., A. Randriamaherisoa, M. Vanclooster, and C. L. Bielders. Facteurs déterminants de la réponse hydrologique d'un bassin versant tropical : Le bassin de la rivière Ankavia à Madagascar. Health, Population, Environment day, Sambava, Madagascar, February 2021.

Ramahaimandimby, Z., A. Benitsiafantoka, H. Voahanginirina. Le bassin versant d'Ankavia, Madagascar. World Water Day 2019, Sambava, Madagascar, April 2019.

Ramahaimandimby, Z., A. Randriamaherisoa, M. Vanclooster, and C. L. Bielders. Projet GIRE SAVA : Quantification des ressources en eau de surface, Louvain4water, Université catholique de Louvain, Belgique, April 2018.

Posters

Ramahaimandimby, Z., A. Randriamaherisoa, F. Jonard, M. Vanclooster, and C. L. Bielders. Reliability of Gridded Precipitation Products for Water Management Studies: The Case of the Ankavia River Basin in Madagascar. Water accounting, IHE Delft, Netherlands, September 2022.

Ramahaimandimby, Z., A. Randriamaherisoa, F. Jonard, M. Vanclooster, and C. L. Bielders. Performance of Satellite-based Precipitation Products: The case of the Ankavia River Basin in Madagascar. ELIE event, Louvain-la-neuve, September 2022.

Ramahaimandimby, Z., A. Randriamaherisoa, F. Jonard, M. Vanclooster, and C. L. Bielders. Reliability of Satellite-based Precipitation Products: The case of the Ankavia River Basin in Madagascar. Tropentag 2022, Czech University of Life Sciences (CZU), Prague, July 2022.

Ramahaimandimby, Z., A. Randriamaherisoa, M. Vanclooster, and C. L. Bielders. Driving Factors of the Hydrological Response of a Tropical Watershed: The Ankavia River Basin in Madagascar. PHE Event, Centre Universitaire Régional de la SAVA, Madagascar, February 2021.

Biographie



UCLouvain

Faculté des bioingénieurs

Earth and Life Institute

Croix du Sud,2

Batiment de Serres

B – 1348 Louvain-la-neuve, Belgique

Tel. +261349234545

Email : zonirina.ramahaimandimby@gmail.com

Né le 03 juin 1990 à Antsirabe (Madagascar), Zonirina Ramahaimandimby obtient son diplôme d'ingénieur en géosciences à l'École Supérieure Polytechnique d'Antananarivo en 2014, puis son Master II en Économie et Gestion de l'Environnement à l'Université de Bordeaux en 2015. De 2015 à 2018, il travaille en tant qu'ingénieur de recherche à l'Institut de Recherche pour le Développement (IRD) à Madagascar. À partir de septembre 2019, grâce à une bourse de l'ARES-CCD, il entreprend une thèse de doctorat sur l'hydrologie des milieux tropicaux à l'UCLouvain (Belgique) sous la direction du Prof. Charles L. Bielders et du Dr. Alain Randriamaherisoa.